

Spectroscopy of Cold, Biomolecular Ions: Instrumentation and Application

THÈSE N° 5162 (2011)

PRÉSENTÉE LE 16 SEPTEMBRE 2011

À LA FACULTÉ SCIENCES DE BASE

LABORATOIRE DE CHIMIE PHYSIQUE MOLÉCULAIRE

PROGRAMME DOCTORAL EN CHIMIE ET GÉNIE CHIMIQUE

ÉCOLE POLYTECHNIQUE FÉDÉRALE DE LAUSANNE

POUR L'OBTENTION DU GRADE DE DOCTEUR ÈS SCIENCES

PAR

Ulrich LORENZ

acceptée sur proposition du jury:

Dr C. Wandrey, présidente du jury

Prof. T. Rizzo, directeur de thèse

Prof. O. Dopfer, rapporteur

Prof. Y. Tsybin, rapporteur

Prof. R. Wester, rapporteur



ÉCOLE POLYTECHNIQUE
FÉDÉRALE DE LAUSANNE

Suisse
2011

Abstract

In recent years, spectroscopic investigations of cold, biomolecular ions have started to provide new, detailed information about the structures of biomolecules in the gas phase. The present work comprises three major parts that describe the development of instrumentation for the preparation and manipulation of cold ions as well as its application to the spectroscopic study of a protonated amino acid dimer.

The first part describes the development of a tandem quadrupole mass spectrometer with a 22-pole ion trap, designed for the spectroscopic investigation of cold, biomolecular ions. Several new features improve the performance of the instrument in comparison with the previous generation of the setup. The instrument is characterized in detail, and a vibrational temperature of the ions of about 10 K is demonstrated.

In the second part, a novel multipole ion trap time-of-flight mass spectrometer is described, a hybrid instrument that uses a planar multipole trap as the extraction region of a reflectron. Its development is originally motivated in the context of the first part of the present work, as a tool to obtain a time-of-flight spectrum of the ions stored in the 22-pole. However, it may offer advantages for a range of different applications. The evolution of the mechanical design and the electronics are described, as well as the different setups that were used to test the instrument. Aided by numerical simulations, the characterization experiments shed light onto several subtleties of the principle of operation.

The third and last part describes the infrared (IR) and ultraviolet (UV) spectroscopic investigation of the protonated phenylalanine/serine dimer, using the instrument detailed in the first part. The isomer-specific IR spectra demonstrate that this small and apparently simple system is more complex than could have been anticipated from previous investigations of related systems. In particular, isotopic labeling experiments provide evidence for different protonation sites in different isomers. Using a UV-pump/IR-probe scheme, it is demonstrated how the lifetimes and the IR spectra of several excited state species can be obtained.

Keywords: cold ions, gas phase, buffer gas cooling, ion traps, time-of-flight mass spectrometry, IR spectroscopy, UV spectroscopy, amino acid, cluster, excited states

Zusammenfassung

Spektroskopische Untersuchungen von kalten biomolekularen Ionen haben in den vergangenen Jahren neue, detaillierte Informationen über die Struktur von Biomolekülen in der Gasphase geliefert. Die vorliegende Arbeit besteht aus drei Hauptteilen, die die Entwicklung von Instrumenten zur Herstellung und Manipulierung kalter Ionen und deren Anwendung für die Spektroskopie eines protonierten Aminosäure-Dimers beschreiben.

Der erste Teil erläutert die Entwicklung eines Tandem-Quadrupol-Massespektrometers mit 22-Pol-Falle für die spektroskopische Untersuchung von kalten, biomolekularen Ionen. Die Implementierung verschiedener neuer Methoden verbessert die Leistung des Setups im Vergleich mit der vorigen Generation. Das Instrument wird im Detail charakterisiert, und es wird gezeigt, daß die Ionen eine Vibrationstemperatur von 10 K besitzen.

Der zweite Teil beschreibt ein neues Multipol-Ionen-Fallen-Flugzeit-Massespektrometer, ein Hybridinstrument, in dem eine planare Multipol-Falle als Extraktionsregion eine Reflektrons benutzt wird. Ursprünglich ist die Entwicklung dieses Instruments aus dem Zusammenhang des ersten Teils dieser Arbeit motiviert, als Hilfsmittel, um ein Flugzeitspektrum der im 22-Pol gespeicherten Ionen zu erhalten. Es besitzt aber das Potential für eine breitere Anwendung in ganz verschiedenen Gebieten. Sowohl die Evolution der Konstruktion und die Elektronik werden beschrieben, als auch die verschiedenen Versuchsaufbauten, in denen das Gerät getestet wurde. Numerische Simulationen begleiten die Experimente zur Charakterisierung und erhellen verschiedene Details der Funktionsweise.

Der dritte und letzte Teil der vorliegenden Arbeit behandelt die Infrarot- (IR-) und Ultraviolett- (UV-)Spektroskopie des protonierten Phenylalanin/Serin-Dimers mit Hilfe des Instruments, das im ersten Teil beschrieben wird. Die isomeren-selektiven IR-Spektren zeigen, daß dieses kleine und scheinbar simple System komplexer ist, als man aus vorhergehenden Studien an verwandten Systemen hätte vermuten können. Insbesondere belegen Isotopen-Substitutionsexperimente verschiedene Protonierungsstellen in verschiedenen Isomeren. Es wird gezeigt, wie mit einer UV-Pump/IR-Probe-Technik die Lebensdauern und IR-Spektren verschiedener angeregter Zustände erhalten werden können.

Stichworte: kalte Ionen, Gasphase, Puffergaskühlung, Ionenfallen, Flugzeit-Massespektrometrie, IR-Spektroskopie, UV-Spektroskopie, Aminosäure, Cluster, angeregte Zustände

“Laboratorium im Sinne des Mittelalters, weitläufige, unbehülliche Apparate zu phantastischen Zwecken” (Szenenüberschrift in Goethes Faust II)

“Laboratory in the style of the middle ages; scattered, clumsy apparatus for fantastic purposes”
(stage direction in Goethe’s Faust II)

Contents

1	Introduction	1
2	Construction of a Tandem Quadrupole Mass Spectrometer with Cold 22-Pole Ion Trap	12
2.1	Motivation and State of the Art	12
2.2	Outline	13
2.3	Time sequence of a typical experiment	15
2.4	Overview of the ion source	15
2.5	Differential Pumping Stages	17
2.6	The Electrospray Source	17
2.7	RF Devices	20
2.7.1	The Quadrupole Mass Analyzers	20
2.7.2	The Adiabatic Approximation and the Effective Potential	22
2.7.3	Adiabaticity and Stability	24
2.7.4	Hexapole, Octopole and 22-Pole	26
2.7.5	The Ion Funnel	29
2.8	Ion Detection	33
2.9	Electronics and Data Acquisition	33
2.10	Characterization	37
2.10.1	Determining the Number of Trapped Ions – Detector Saturation	37
2.10.2	Low-Mass Cut-Off of the Ion Funnel	41
2.10.3	Ideas for the Normalization on Parent Ion Signal	42
2.10.4	22-Pole Trapping Time	44
2.10.5	Determination of the Ion Temperature	45
2.11	Conclusions and Outlook	46
3	Development of a Planar Multipole Ion Trap Time-of-Flight Mass Spectrometer	48
3.1	Motivation and State of the Art	48
3.2	Reflectron Time-of-Flight Mass Spectrometry	53
3.3	Planar Ion Traps	57

3.4	Combining a Planar Multipole Ion Trap with a Time-of-Flight Mass Spectrometer	58
3.5	Design Considerations	60
3.6	Realization	67
3.6.1	Construction of the Prototype	68
3.6.2	Construction of an Improved Version	68
3.6.3	The Test Setup	70
3.6.4	Coupling to the Tandem Quadrupole Mass Spectrometer	70
3.6.5	Electronics	72
3.7	Characterization	74
3.7.1	Experiments with the Test Setup	74
3.7.2	TOF Mass Spectra with and without Trapping	75
3.7.3	Background Signal	77
3.7.4	Local Minima of the Effective Potential	78
3.7.5	Extraction Phase	80
3.7.6	Trapping DC Voltage	84
3.7.7	Pressure	85
3.7.8	Ion Motion	86
3.7.9	RF Amplitude, Studied in the Test Setup	88
3.7.10	Trapping Time in the Test Setup	90
3.7.11	Experiments with the Trap Coupled to the Tandem Quadrupole Mass Spectrometer	91
3.7.12	Comparison of Quadrupole and TOF Mass Spectra	92
3.7.13	TOF Mass Spectra of Laser Induced Fragment Ions	94
3.7.14	RF Amplitude, Studied with the Trap Coupled to the Tandem Quadrupole Mass Spectrometer	95
3.7.15	Gas Pulse	96
3.7.16	Trapping Time of the Trap Coupled to the Tandem Quadrupole Mass Spectrometer	98
3.7.17	Trapping DC Voltage	99
3.8	Conclusions and Outlook	101
4	Spectroscopy of a Protonated Amino Acid Dimer	106
4.1	Motivation	106
4.2	Experimental Approach	109
4.3	Spectroscopic Techniques	109
4.4	Ground State Spectra	111
4.5	Quantum Chemical Calculations	120
4.6	Excited State Spectra	128

4.7 Conclusions and Outlook	137
5 Conclusions	139
Appendix	142
List of Figures	152
List of Tables	157
List of Abbreviations	158
Bibliography	160
Acknowledgments	175
Curriculum Vitae	177

Chapter 1

Introduction

“The problem of chemistry” solved The interaction of electrons and nuclei is fully described by quantum mechanics. It explains the structure of atoms, the nature of the chemical bond, and the dynamics and interactions of molecules. In this sense, the Schrödinger equation

$$i\hbar\dot{\Psi} = H\Psi \quad (1.1)$$

with the Hamiltonian operator H and the wave function Ψ solves “the problem of chemistry”. Heitler, one of the founding fathers of quantum chemistry, expressed this with the words that now, one could “eat chemistry with a spoon”.¹

Dirac, who generalized the Schrödinger equation to incorporate relativistic effects, stated the same idea in 1929, writing “The underlying physical laws necessary for the mathematical theory of a large part of physics and the whole of chemistry are thus completely known...”. However, he added “...and the difficulty is only that the exact application of these laws leads to equations much too complicated to be soluble.”²

Quantum chemistry is therefore based on the quest for suitable approximation methods for the Schrödinger equation. In his Nobel lecture, John Pople gives an overview of the history of quantum chemistry, starting in 1929, when Heitler and London first carried out quantum mechanical calculations of molecular hydrogen.³ Landmarks include the Hartree-Fock theory and the Roothaan equations; the introduction of approaches including electron correlation, like the configuration interaction method and the Møller–Plesset perturbation theory; or density functional theory (DFT),⁴ which has gained immense popularity in recent years. Thanks to the development of these methods and the ever increasing speed of modern computers, quantum chemical calculations have become a powerful tool to aid the interpretation of experimental findings.

Structures of flexible biomolecules in the gas phase As will be discussed in greater detail below, the larger aim of the present work is to determine the structures of flexible biomolecules in the gas phase. To this end, we record infrared (IR) spectra of the species of interest. Their corresponding structures can then be inferred by comparison with the results of quantum chem-

ical calculations. This process, however, also implies that the interpretation of the spectra will in most cases only be successful if the calculations would have given the right answer anyway. One might ask more generally and maybe a little naïvely if there is any point at all in carrying out the experiment if a complete theory exists that can predict all the measurable properties of a molecular system and this theory has not been disproved to date?

Certainly, as any other scientific theory, the validity of quantum mechanics needs to be put to a test. This is, for example, the goal of experiments testing whether entangled particles violate the Bell inequalities as quantum mechanics predicts⁵ or experiments designed to demonstrate the wave nature of ever bigger objects.⁶ The experimental method that forms the basis of the present work, however, is hardly suitable to provide a stringent test of quantum mechanics.

The computational effort of current quantum chemistry methods scales exponentially with the number of particles N (*e.g.* M^4 for Hartree-Fock in the large system limit, where M represents the basis set size⁷) so that the limited computing power restricts accurate calculations to small enough systems. (Another way of looking at this problem is that simulating a quantum system on a classical computer puts quantum chemists at an inherent disadvantage, while quantum simulation might in the future change the scaling laws.⁸) Therefore, one could argue that the experiment can give access to systems too big or too complex to be accurately calculated. However, in the special case of our experiment, successful modeling of the compound is essential in order to obtain the molecular structure from the recorded IR spectrum. Studying a large, complex system might then as well lead to results that cannot be interpreted or that give only indirect or qualitative structural information.

In this situation, the experimentalist is faced with a dilemma. While it may be of little interest to determine properties of molecules that can easily be calculated, so that the experiment only gives the obvious answer, studying a complex system might not yield any answer at all. Worse, a computational problem that can just be addressed with today’s capabilities might look trivial in a couple of years if Moore’s law should continue to provide ever faster computing speeds and if more powerful quantum chemical methods should be developed. One might ask why one should measure anything today that could easily be calculated tomorrow, when computers are bound to be faster?

The interplay of experiment and theory One reason is that experiments can be used to verify and improve the results of quantum chemical calculations. To this end, the experiments must provide a stringent test for the performance of different methods. As will be discussed below, we are confident that our experiment can, indeed, deliver an unprecedented detail of information, the accuracy of which presents a challenge for theoretical investigations, even of small systems.⁹

Dispersive interactions, for example, play an important role in determining the conformational preferences of biomolecules. Determining their structures experimentally can therefore

serve to evaluate different approaches for including dispersive corrections in DFT methods.¹⁰ Furthermore, flexible biomolecules frequently feature potential energy surfaces with a large number of local minima, and different strategies have been developed to predict the relevant conformations.^{11,12} Since our experiment can provide information about the global minimum and connected local minima conformations, it can also serve to evaluate the performance of different techniques to perform conformational searches.

Ideally, theory and experiment do not deliver redundant results but engage in a synergetic process, in which experimental techniques and theoretical methods are iteratively refined. At the end of the process, theory would be accurate enough to predict the properties of large systems, so that, for example, the interactions of an enzyme with a drug could be studied and novel drugs could be developed merely from calculations.

Extending the experimental toolbox and curiosity-driven research From the viewpoint of an experimentalist, the prospect of doing experiments for the sole purpose of advancing theory and finally rendering experiments superfluous might be little attractive.

However, to speak with Asher Peres, "...quantum phenomena do not occur in a Hilbert space, they occur in a laboratory."⁸ Trying to do ever more detailed and more sophisticated experiments will help to extend our experimental toolbox and our capabilities to investigate and manipulate molecular systems. This includes the development of novel spectroscopic techniques and new kinds of scientific instruments. In fact, a large part of the present work has been devoted to the latter goal.

In his essay "The future of chemical physics"¹³ Ahmed Zewail illustrates this point with the example of the laser. Starting out as a mere intellectual curiosity and "a solution looking for a problem", the laser has enabled technological breakthroughs in a variety of fields in the past 50 years and continues to have a profound impact on our society.

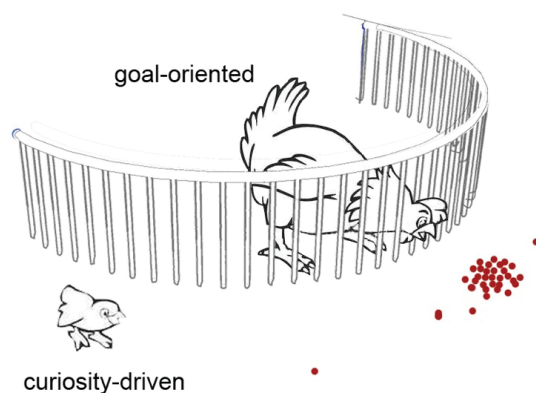


Figure 1.1: The merits of curiosity-driven research (from Theodor Hänsch's Nobel lecture in 2005¹⁴).

Ahmed Zewail argues that the primary objective of chemical physics is "to provide the fundamental concepts and the new tools that enable understanding and control of the systems

behavior, from molecules to cells” and thereby underlines the fruitful interplay of theory and experiments. He concludes by advising chemical physicists to continue to “look ahead with intellectual curiosity to examine the fundamentals of nature”.

Seeking a detailed understanding of proteins Proteins perform a large variety of tasks in living organisms, including the catalysis of chemical transformations, the transport of chemical species through membranes, cell signaling, gene transcription, and structural functions.¹⁵ They constitute the molecular machinery of the cell that carries out the tasks encoded in the DNA. The plethora of different functions is seemingly contrasted by the fact that proteins are initially synthesized in the ribosomes as a simple linear polymer of 20 standard amino acids (that may afterwards undergo posttranslational modifications). However, the protein is inactive until it folds into the three-dimensional structure that determines its functions. Misfolded proteins, on the other hand, have been found to be involved in the formation of aggregates that are, for example, at the origin of Alzheimer’s and Parkinson’s diseases.¹⁶

The folding is a spontaneous process, in which most proteins “self-assemble” into their correct shape. This process is driven by the hydrophobic effect, which favors conformations in which amino acids with hydrophobic side chains are placed in the inside of the protein; the formation of intramolecular hydrogen bonds; and the weaker van der Waals interactions. However, it is not understood in detail and on the molecular level how these interactions determine the structure.

These weak interactions also govern molecular recognition and determine, for example, how an enzyme recognizes its specific substrate, how antibodies bind to a pathogen, or how a cellular receptor recognizes a chemical signal. Understanding these processes on a fundamental level could allow one, for example, to design artificial proteins to catalyze specific reactions. While molecular nano-machines are an active field of research,¹⁷ it has not been possible so far to harness the power of proteins. Similarly, for the development of novel drugs, pharmaceutical companies still largely rely on the tedious process of screening large libraries of chemical compounds. A better understanding of intermolecular interactions, however, could pave the way towards the successful *in silico* design of novel drugs.

Peptides in the gas phase X-ray crystallography and NMR spectroscopy are currently the most powerful tools to investigate the structure of proteins. NMR spectroscopy probes the structure of proteins directly in solution and can deliver dynamic information.¹⁸ Under the premise that a protein can be crystallized and its structure is not altered by the crystal packing, X-ray crystallography gives access to even larger systems.¹⁹

However, most proteins are far too large to be amenable to high-level *ab initio* quantum chemical calculations, which are required to accurately describe intramolecular interactions. The necessity to model the interaction with the solvent further aggravates the problem. In order to arrive at a greater detail of understanding, one is therefore forced to drastically reduce

the size and complexity of the system, which is the motivation for studies on (microsolvated) amino acids and small peptides in the gas phase.

While NMR spectroscopy is not sensitive enough for gas phase studies because of the low number densities in gases, diffraction techniques have so far been limited to smaller systems.^{20–25} Structural information on gas-phase ions can also be obtained with mass spectrometric techniques. However, different dissociation rates in blackbody infrared radiative dissociation (BIRD) experiments,^{26–29} different H/D exchange rates,^{30–38} or different collision induced dissociation (CID) behavior can only yield indirect information about the structures involved.^{30,39–41} Ion mobility measurements provide a more direct probe of the conformation of an ion by determining its collision cross section in collisions with an inert gas, usually helium.^{33,42–46} Due to their different cross sections, helical and globular structures of polyalanine containing peptides can, for example, be distinguished with this technique, so that it has been possible to deduce different parameters that influence the propensity for helix formation in the gas phase.^{47–49} However, in ion mobility measurements, the detail of structural information that can be obtained is necessarily limited, since all the information is essentially contained in a single observable.

Spectroscopy of neutral peptides in the gas phase Optical spectra on the other hand can provide a more direct link to the molecular structure and are therefore better suited to study the conformations of small peptides in the gas phase, as will be argued in the following.

The history of the study of gas-phase biomolecules (see also reference⁵⁰ and references therein) begins with the ultraviolet (UV) spectroscopy of the neutral amino acid tryptophan.^{51–54} In these experiments, tryptophan was volatilized by heating and entrained in a molecular beam. Resonance enhanced two photon ionization (R2PI) spectra showed a different saturation behavior of different UV transitions, indicating the presence of several ground state conformations of tryptophan in the molecular beam. Furthermore, different dispersed fluorescence spectra obtained by pumping the different conformers provided evidence that several distinct conformations are also present in the excited state, which do not interconvert on the time scale of the fluorescence lifetime.

In order to extend studies to larger systems that possess insufficient vapor pressure and cannot be volatilized by heating without significant decomposition, laser desorption (LD) in combination with cooling in a molecular beam⁵⁵ was introduced.^{56–58} The largest systems investigated with this technique possess up to 15 amino acids.^{59,60}

Several multi-resonance techniques have been developed to gain additional spectral information. With UV/UV and IR/UV hole burning, different UV transitions can be more easily assigned to different conformers, and the UV spectrum of a single species can be obtained.^{61–64} IR/UV depletion experiments yield conformer-selective IR spectra,^{59,60,62,63,65,66,66–72} and even an IR/IR/UV scheme has been employed to achieve conformer-selectivity despite overlapping UV transitions.⁷³ IR spectra offer valuable structural information, since they are a sensitive

probe for the conformation of a peptide. The hydrogen bonding pattern, which largely determines the three-dimensional structure, is encoded in the characteristic shifts of NH and OH stretch vibrations, which, fortunately, also possess large transition dipole moments. Furthermore, NH bending and C=O stretch vibrations can serve as fingerprints of the structure of a peptide. IR spectra of excited states have been recorded using the excited-state fluorescence dip technique.^{74,75}

As one further addition to the spectroscopic toolbox, Zwier and co-workers introduced IR and UV population transfer spectroscopy,^{76–78} in which the high gas densities at an early point in a molecular beam expansion are used to recool molecules after absorption of an IR or UV photon, respectively. With this technique, the transfer of population between different conformations could be observed. Barrier heights for the interconversion could also be determined when stimulated emission pumping (SEP) was used in the initial excitation step of the scheme.^{79,80}

IR spectroscopy of protonated peptides at room temperature With the advent of matrix assisted laser desorption ionization (MALDI)⁸¹ and electrospray ionization (ESI),^{82–84} the soft ionization and transfer into the gas phase of large biomolecules has become possible. While the spectroscopy of ions suffers from lower number densities, it offers the advantage that the species of interest can be mass-selected, so that, for example, decomposition products can be eliminated. (Moreover, ion mobility experiments allow for the preselection of conformational families.⁸⁵) Furthermore, protonated or metalated species, as they are typically generated with MALDI or ESI, resemble the *in vivo* state of peptides, since many biomolecules exist as ions under physiological conditions.¹⁵

ESI and its variants are currently the preferred approach for the mild ionization of the largest biomolecules and biomolecular complexes accessible.⁸⁶ Moreover, with ESI, peptide molecular ions can be sampled from their native environment. Together with the fact that ESI usually shows smaller shot-to-shot signal fluctuations than MALDI, this has made ESI generated peptide ions a popular target for spectroscopic investigations.

IR spectroscopic studies of a wide range of electro-sprayed systems, ranging from single protonated amino acids and their clusters^{87–91} to peptides^{92–95} and even entire proteins,^{96,97} have been carried out that had previously not been accessible. Two action-spectroscopic schemes have been employed. While some small, weakly-bound clusters already dissociate upon absorption of a single IR photon (IR photodissociation, IRPD),²⁹ several IR photons are required to fragment larger and covalently-bound systems (IR multiple photon dissociation, IRMPD).^{98,99} In particular the advent of IR free electron lasers (FELs),^{100,101} capable of delivering high photon fluxes, has fuelled numerous IRMPD studies in the fingerprint region. Different tandem mass spectrometers have been employed in these experiments, including 3D Paul traps,^{102,103} Fourier transform ion cyclotron resonance mass spectrometers (FT-ICRs),^{98,104} and tandem quadrupole mass spectrometers.²⁹

In these setups, the ion internal temperature is usually close to room temperature. Under these conditions, IR transitions typically show a width of about 30 cm^{-1} , so that in small systems, resolved spectral features are obtained that can yield structural information. The interpretation of IRMPD spectra by means of quantum chemical calculations is complicated by the intricate dynamics and nonlinearity of the IRMPD process, which can, for example, lead to shifts of the band positions or largely different relative band intensities compared with linear spectra.¹⁰⁵ Moreover, the room-temperature UV spectra of peptides with aromatic side chains are usually broad,¹⁰⁶ so that IR/UV double-resonance methods cannot be applied to obtain conformer-selective spectra. If several conformers are present, the obtained IR spectrum consequently represents a thermal average, which renders the assignment of structures difficult.

Spectroscopy of cold protonated peptides in the gas phase At the origin of the broad UV spectra of peptides at room temperature is a statistical effect. Especially for large systems, many states are populated at $\sim 300\text{ K}$, so that the UV spectrum is the sum of the different spectra of a large number of eigenstates. In order to obtain a resolved UV spectrum and render conformer-selective techniques possible, one would have to force the ensemble into a small number of states, which is most easily achieved by cooling.

However, there is no obvious way how electrosprayed ions could be cooled in a molecular beam without losing a majority of them in the expansion. Moreover, large systems, which possess higher internal energies at room temperature, cannot be sufficiently cooled in a molecular beam due to the limited number of collisions with the carrier gas. This ultimately also limits the size of laser-desorbed neutrals which can be studied with double-resonance techniques.⁶⁰

The development of methods for the generation of cold molecules is an active field of research. Applications range from ultracold chemistry, high precision measurements, and fundamental tests of physics to quantum information processing.¹⁰⁷ However, the only method available to date to internally cool large, gas-phase ions is buffer gas cooling. (Electrosprayed ions have also been captured in helium droplets, which makes even lower temperatures accessible than is currently possible with buffer gas cooling.^{108,109} However, with this technique, it is not possible so far to prepare isolated cold species.) For the purpose of buffer gas cooling, ions are stored in an ion trap and translationally and internally cooled in collisions with a bath gas. Weinkauff and co-workers first applied this technique to the spectroscopy of a biomolecular ion, when they stored protonated tryptophan in a liquid nitrogen-cooled Paul trap.¹¹⁰ The recorded UV photofragment spectrum was broad and showed little structure. However, as could be demonstrated later, the broadening is not due to insufficient cooling of the ions, but rather to the ultrafast dissociation dynamics following electronic excitation in protonated tryptophan.¹¹¹

Using a cryogenic 22-pole ion trap,¹¹² Rizzo and co-workers demonstrated in the following the cooling of protonated tyrosine to $\sim 12\text{ K}$, so that a sharp UV spectrum with transitions as narrow as 2.7 cm^{-1} could be recorded.¹⁰⁶ Well-resolved electronic spectra laid the basis for

conformer-selective IR/UV double-resonance spectroscopy, which was demonstrated in the following for protonated tyrosine and phenylalanine¹¹³ as well as protonated dipeptides containing tyrosine.¹¹⁴ These experiments showed how detailed structural information could be obtained about the lowest lying minima of the potential energy surface (PES), when the conformer-selective IR spectra were compared with the predictions of quantum chemical calculations. Subsequent studies on the propensity of polyalanine containing peptides to form helices in the gas phase demonstrated that the technique can be extended to larger peptides.^{115,116}

The more recent work on the cyclic decapeptide Gramicidin S can serve to illustrate the power of the experimental approach for the study of larger systems.^{9,117} IR depletion spectra of laser-desorbed neutral Gramicidin peptides in a molecular beam had previously been reported. For molecules of this size, broad UV spectra were obtained, most probably due to insufficient cooling, so that no conformer selectivity could be achieved.⁶⁰ The fingerprint IRMPD spectrum of doubly protonated Gramicidin S at room temperature had also been recorded.⁹² It features broad, overlapping absorptions, assigned to amide I and amide II vibrations. Although some qualitative structural information could be obtained, it could, for example, not be determined how many conformations contribute to the observed spectrum. When Gramicidin S ions were cooled to ~ 12 K in a 22-pole ion trap, a resolved UV spectrum could be obtained, which allowed for the identification of at least four different conformers. Conformer-selective IR depletion spectra could be recorded in the mid-IR region, which show distinctly different features. However, it was noted at the same time that the interpretation of the detailed information contained in the spectra is a formidable challenge with the currently available quantum chemical methods.⁹

Two further developments should also be noted here. Although proteins undergo conformational changes during folding or as part of their function, the determination of the structure of a peptide can only give a static view. However, it could be demonstrated that population transfer spectroscopy, which uses conformational isomerization to reveal connections between different minima of the PES, can also be performed with ions stored in a 22-pole trap, although the lower number densities and reduced sensitivity render the experiment challenging.¹¹⁸

The complex behavior of peptides is also linked to their size. In our current experimental approach, however, the investigation of large systems is hampered by their lower UV fragmentation yield. It was demonstrated that this problem can be alleviated by using a scheme termed IR laser assisted photofragmentation spectroscopy (IRLAPS). By irradiating the ions with a CO₂ laser pulse following UV excitation, the photofragmentation yield was shown to increase by as much as two orders of magnitude. With this technique, it was possible to obtain well-resolved UV and IR spectra of a 17 amino acid peptide.^{119,120}

Summary The goal set out above, to gain a more detailed understanding of the fundamental interactions that govern proteins, and the experimental strategy proposed in the following might appear incompatible. An unsolvated, short peptide fragment in the gas phase at 10 K certainly

bears little resemblance to a large *in vivo* protein at body temperature. Did we get side-tracked?

We have certainly fallen prey to our initial goal, to gain detailed and fundamental insights into the properties of proteins. Especially the requirement to study systems that are tractable with current quantum chemical methods made a number of simplifications necessary. The higher level of detail comes at the expense of the complexity of the investigated system. Conversely, the complex behavior of proteins arises only from the interplay of a large number of these fundamental interactions. Complexity should be easier to grasp once the elementary steps are understood.

The experiments summarized above on the spectroscopy of cold, biomolecular ions are surely exciting from the point of view of molecular spectroscopy. But do they possess any relevance at all for the understanding of a living system? A peptide at 10 K is certainly a bad model for the same molecule in solution at room temperature.^{42,49,117} This, however, would mean to misunderstand the idea of the experiment. Rather, the low temperature is an experimental prerequisite for mapping out the PES of the system, which is a fundamental property of the molecule and also applies to the system at higher temperature. Moreover, the lowest energy minima and the connecting pathways between them are likely also going to be most relevant at physiological temperatures.

With an improvement of the tools of quantum chemistry, larger and more complex systems will lend themselves to high level *ab initio* calculations. At the same time, the insights into the challenges and the limitations of the current experiments will lead to new and improved methods. To resume a thought from the beginning of this chapter — with a fruitful interplay of theory and experiment, it will be possible to gradually understand the complex behavior of proteins.

Outline This document has the following structure. While chapters 2 and 3 describe the development of instrumentation for the spectroscopy of cold, biomolecular ions, chapter 4 discusses the spectroscopic findings for a simple system, a protonated cluster containing one serine and phenylalanine molecule. Chapter 5 summarizes and concludes.

Chapter 2 describes the development of a tandem quadrupole mass spectrometer featuring a 22-pole ion trap, designed for the spectroscopic investigation of cold, biomolecular ions. After laying out the various design goals and giving an overview of the system, the most important components of the setup are described in more detail, including the ion source, the various radio frequency (RF) devices, the ion detectors, the electronics, and the data acquisition software. A special emphasis is put on the theory and principle of operation of the RF devices, since two of them play a central role: The 22-pole is the heart of the instrument, while the ion funnel is crucial in obtaining a high ion transmission in the source. Subsequently, the characterization of the instrument is described, and most importantly, the vibrational temperature of the ions

is determined. The chapter closes with a summary and an outlook for possible future developments of the system.

Chapter 3 describes a novel multipole ion trap time-of-flight mass spectrometer. Its development was originally motivated in the context of chapter 2 by the goal of detecting the ions stored in the 22-pole with a time-of-flight method. First, different existing approaches for this technical challenge are summarized, and their advantages and drawbacks are discussed. Subsequently, the theory of reflectron time-of-flight mass spectrometers and of planar multipole ion traps is laid out. The concept of a multipole ion trap time-of-flight mass spectrometer is described, a hybrid instrument that uses a planar trap as the extraction region of a reflectron; and its possible advantages for the purpose of obtaining a time-of-flight spectrum of the ions stored in the 22-pole are outlined.

Different considerations for the design of such an instrument are then discussed, and its experimental realization is described. Two generations of the trap were developed and tested, using ions generated by laser ionization inside the trap volume. Subsequently, the trap was coupled to the tandem quadrupole mass spectrometer described in chapter 2 to explore the injection of externally generated ions.

The characterization of this novel instrument in combination with numerical simulations of ion trajectories refines the understanding of its principle of operation. Finally, the results of this chapter are summarized, remaining challenges are outlined, and future directions are suggested. To conclude, possible applications of the instrument, quite independent of its original purpose, are discussed.

Chapter 4 describes the IR and UV spectroscopic investigation of the protonated phenylalanine/serine heterodimer,¹ using the instrument detailed in chapter 2. Isomer-specific IR spectra demonstrate the presence of at least five different species, whose spectral signatures point to structures that are dominated by several intermolecular hydrogen bonds with the ammonium group. Isotopic labeling experiments show that serine, the less basic amino acid, carries the excess proton in two of the five isomers.

In order to assign structures to these species, quantum chemical calculations were carried out, following the established strategy of exploring the PES on the force field level and refining the obtained structures in DFT calculations. Unfortunately, this approach fails for the present system. A detailed analysis reveals that the employed search algorithm does not sample the PES efficiently. Nevertheless, some additional, qualitative structural information is gained.

Initial investigations of the spectroscopic properties and dynamics of the excited states of the dimers are presented. Finally, the results of this chapter are summarized, and further ex-

¹Strictly speaking, a complex consisting of two different subunits, here phenylalanine and serine, is not a dimer. However, in the field of gas phase spectroscopy, the designations “heterodimer” and “dimer” are frequently used to denote this kind of cluster.

periments are suggested to answer several open questions. The importance of the findings for the gas-phase spectroscopy of protonated amino acid dimers and larger biomolecular ions is discussed.

Finally, chapter 5 summarizes the results of the present work and makes an attempt to draw conclusions for the broader context of the research field.

Chapter 2

Construction of a Tandem Quadrupole Mass Spectrometer with Cold 22-Pole Ion Trap

2.1 Motivation and State of the Art

The broader context of the present work is the spectroscopy of molecular ions and ionic clusters in the gas phase. The early experiments by Y. T. Lee, whose influence on the development of the field has been reviewed,¹²¹ may serve to illustrate the basic experimental approach that is used here. His breakthrough idea was to combine mass spectrometry and IR spectroscopy with narrow-band lasers to obtain action spectra of mass-selected ionic clusters.^{122–124} In his original setup, ionic clusters are generated in a corona discharge source. The parent ions are selected in a magnetic sector and stored in an octopole trap, where the ions interact with the IR laser. Fragments generated by vibrational predissociation are then selected in a quadrupole filter. By monitoring the fragment intensity as a function of the IR wavelength, a spectrum is obtained.

A variety of different tandem mass spectrometer setups have since been employed for the spectroscopic study of ions, including tandem time-of-flight (TOF) mass spectrometers,^{125–127} Fourier transform ion cyclotron resonance (FT-ICR) mass spectrometers,^{128–130} Paul traps,¹¹⁰ and hybrid Paul trap/TOF instruments.¹⁰⁵

The introduction of the 22-pole ion trap by D. Gerlich added a new dimension to the field,¹³¹ since it allowed for the study of ions with their translational and internal degrees of freedom cooled to cryogenic temperatures. Especially for large systems, the ability to prepare the ion in a very limited number of quantum states facilitates its spectroscopy and gives access to new kinds of information.⁵⁰ Although a tandem TOF configuration has also been developed,¹³² most instruments with cold 22-pole ion traps use a tandem quadrupole configuration.^{106, 133–135}

This is also the case for the instrument described in the present work.¹³⁶ It builds upon the experience of our research group gained with the first generation setup,¹⁰⁶ but was conceived with the goal in mind to implement a number of distinct improvements that would allow new kinds of experiments.

In comparison with neutrals, molecular ions offer the advantage that they can be selected by their mass over charge ratio, filtered according to their ion mobility,⁴³ and trapped in order to cool them to cryogenic temperatures. However, the spectroscopy of ions always faces the complication of lower number densities, which are limited by space charge to about $10^5 - 10^6$ ions/cm³. For population transfer experiments^{76,79} in a 22-pole ion trap, for example, achieving a good signal to noise ratio is a formidable challenge.¹¹⁸ It was therefore one of the goals to increase the number of ions stored in the 22-pole during one experimental cycle (the length of which is determined by the laser repetition rate). To this end, an ion funnel¹³⁷ was incorporated into the ion source to replace the skimmer in the previous setup. Ion funnels had been shown to improve the transfer efficiency of the ions into the vacuum chamber by an order of magnitude (see section 2.7.5).

A prerequisite for obtaining conformer-selective IR spectra of peptides by means of IR/UV double resonance experiments¹¹³ are well-separated transitions in the UV spectrum. However, with the size of the peptide, the number of possible conformations increases, which frequently leads to spectral congestion and overlapping bands.¹²⁰ Adding an ion mobility stage to the instrument could solve this problem, as drift tube ion mobility measurements have been shown to be able to resolve different conformational families according to their different collisional cross sections.⁴² As a first step in this direction, the instrument was designed with a front end that would be able to accommodate a high-field asymmetric waveform ion mobility spectrometer¹³⁸ (FAIMS) by Thermo Fisher (usually operated with a conventional ESI source instead of a nano-spray source).

A number of smaller changes were also introduced. The machine was designed with a shorter laser axis to facilitate laser alignment in multiple laser experiments. A flexible structure of the machine was envisioned that would allow the addition of further instruments later on (see chapter 3). With the new helium cryostat specified to reach temperatures as low as 4 K (previously 6 K), we also expected to obtain slightly colder ions. Finally, the electronics of the system and the computer interface were completely redesigned in order to provide better stability and a greater ease of operation.

2.2 Outline

Figure 2.1 shows a horizontal cross section of the mass spectrometer, which features a tandem quadrupole configuration with a cold 22-pole ion trap. Ions are produced by nano-electrospray (nano-ESI) and enter the vacuum chamber via the transfer capillary (section 2.6). An ion funnel (section 2.7.5) refocusses the ions exiting the capillary and guides them into a hexapole ion guide (section 2.7.4). In the following quadrupole analyzer (section 2.7.1) the parent mass/charge ratio is selected and transmitted to a quadrupole bender, where the ion beam is turned by 90° and enters an octopole guide (section 2.7.4). After a second quadrupole bender the ions are focused by a lens stack and injected into a cryogenically cooled 22-pole ion trap (section 2.7.4). After

the interaction with the laser(s), the ions are ejected from the trap, pass another lens stack and a third quadrupole bender, and enter the second analyzing quadrupole, which selects the mass over charge ratio of the fragment ions. These are finally detected by a channeltron detector (section 2.8).

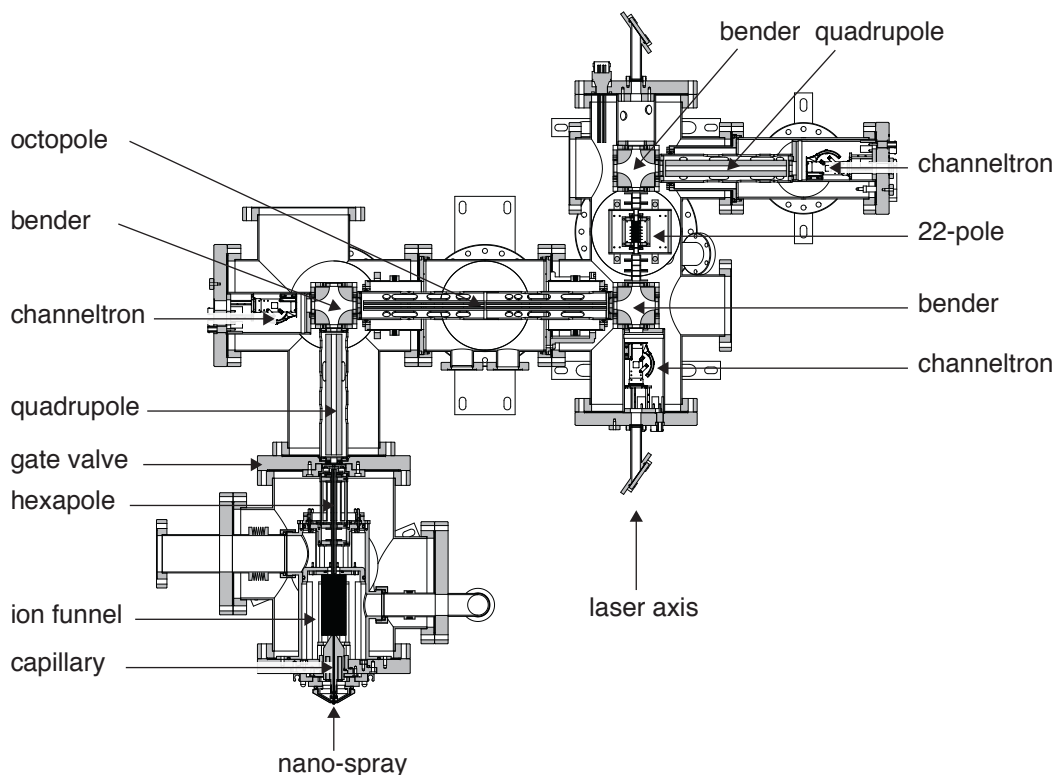


Figure 2.1: Overview of the tandem mass spectrometer with 22-pole ion trap.

The setup owes its zigzag shape to the three quadrupole benders. The first one (which follows the first quadrupole) serves to separate the ion beam from any directed flow of neutral gas that passes through the bender in a straight line and strikes a turbomolecular pump. The other two benders surround the 22-pole and thus reduce the length of the optical axis of the machine. This facilitates laser alignment through the laser ports, especially in multiple laser experiments.

Two further channeltron detectors are placed at the first and second bender. With the polarity of the poles of these benders reversed, ions can be detected with these additional detectors, which is useful for analytical purposes. The benders also render the design of the machine more flexible for the purpose of future extensions. The unoccupied sides of the second and third bender could, for example, be used to extend the instrument by a further ion trap or a time-of-flight analyzer.

2.3 Time sequence of a typical experiment

The time sequence of a typical experiment is schematically depicted in Fig. 2.2. For experiments with a pulsed UV or IR laser, the continuous ion beam produced by the nanospray source has to be converted into discrete packages. To this end, ions are stored in the hexapole by raising the potential on the hexapole exit lens. They are periodically released by pulsing the exit lens to a lower voltage and injected into the 22-pole. Alternatively, the ions can be pretrapped in the octopole by leaking helium into this section (raising the pressure to $\sim 1\text{e-4}$ mbar) and switching the octopole exit lens in the same fashion. About 1 ms before the arrival of the ions, helium is pulsed into the 22-pole, which serves to decelerate the injected ions and cool them to the (cryogenic) temperature of the walls of the trap. Several ms later, the lasers are fired. The ions are subsequently ejected from the trap by lowering the voltage on the 22-pole exit lens, mass selected in the second quadrupole, and detected with the channeltron detector.

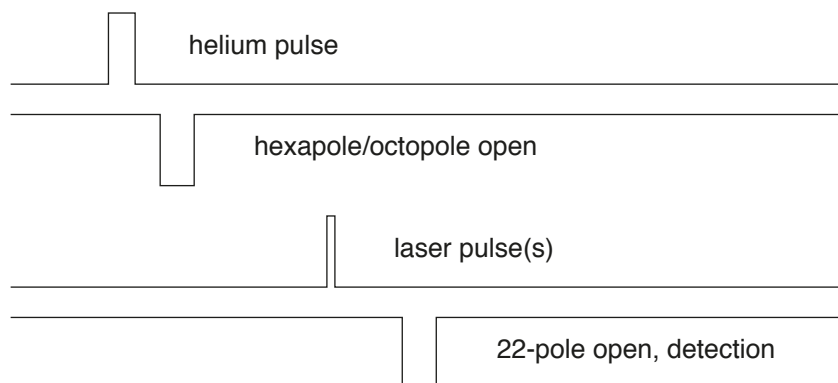


Figure 2.2: Time sequence of a typical experiment.

2.4 Overview of the ion source

A considerable effort was devoted to the design and construction of the ion source, which houses the capillary, ion funnel, and hexapole. Three differential pumping stages (the ion funnel comprising one and the hexapole spanning two stages, see section 2.5) had to be accommodated in one chamber. Furthermore, we sought a design that would allow one to easily clean and service the RF devices and ion optics. Figure 2.3 shows a section view of our design.

The source is housed in a six-way cross and terminated by a gate valve, which is based on a design by O’Conner and co-workers.¹³⁹ It allows one to evacuate the machine while the source is at atmospheric pressure and thus facilitates the work with the instrument and decreases pump-out times. The gate valve blade can be moved by a linear manipulator that protrudes from the top of the flange on which the gate valve is mounted (Fig. 2.3). In its closed state, the blade presses against an o-ring and thus seals off the remainder of the machine from the source, while in its open state, it functions as an electrostatic lens, to which a DC potential is applied. The

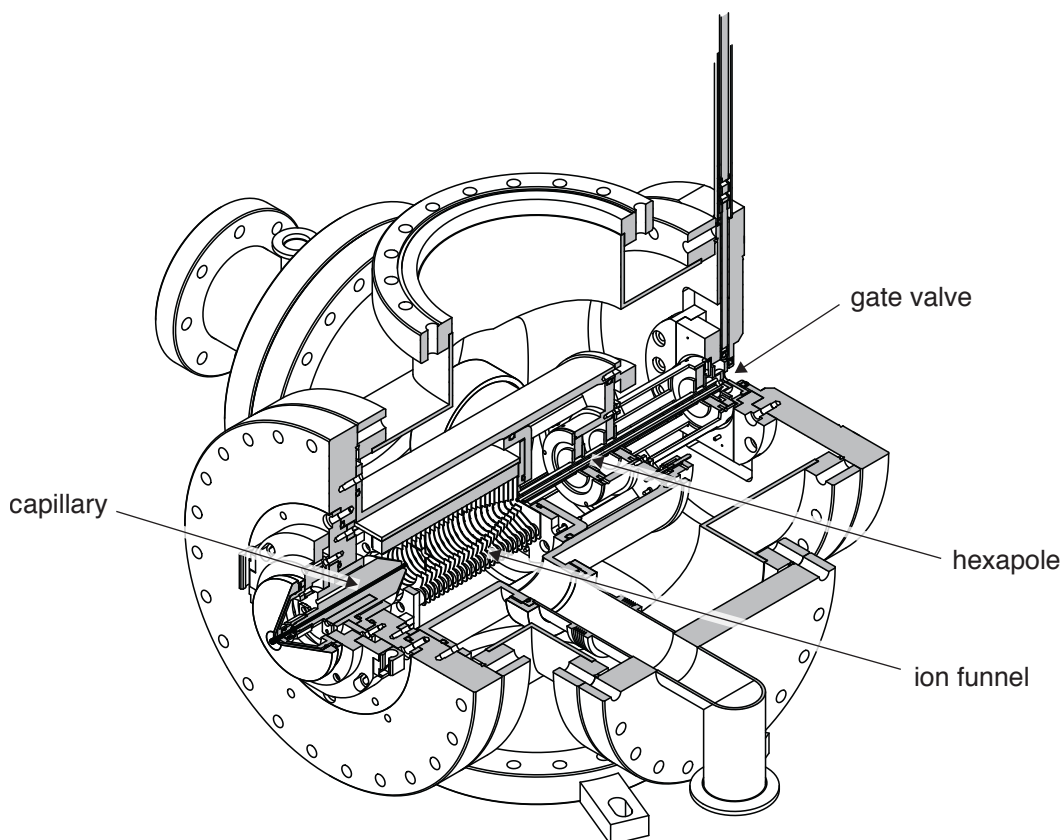


Figure 2.3: The ion source. (Only every fourth plate of the ion funnel is shown.)

housing of the first quadrupole (not shown) inserts into the gate valve flange from the other side. This way, the distance is kept short in which the ion beam is only guided by the potential of the blade.

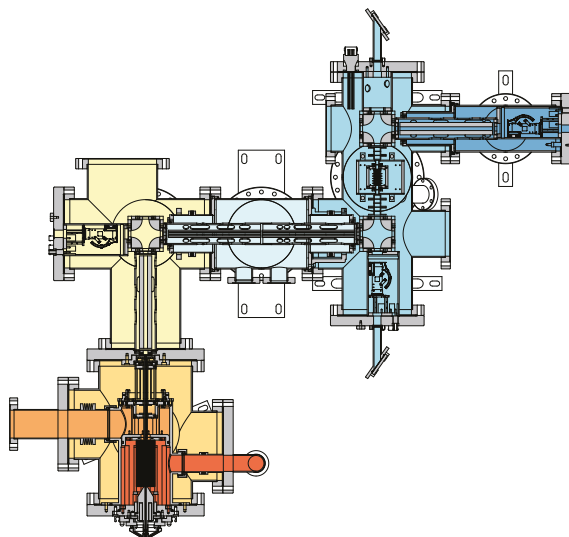
The capillary, ion funnel, and hexapole are mounted on a separate assembly that can easily be removed from the vacuum chamber for cleaning purposes. It inserts into the front flange of the machine and a cylindrical inner chamber, which houses the first two vacuum stages. The end of the hexapole is enclosed in a cylindrical structure, which fits into a counter piece in the gate valve, so that the relative alignment is ensured. In Fig. 2.3, the tubes are visible that connect the two sections of the inner chamber to pump ports on the flanges of the six-way cross. The third stage (the second half of the hexapole) is pumped from a turbomolecular pump on the flange below the chamber. None of the RF and DC voltages for the ion funnel and hexapole have to be connected or disconnected manually. Pins on the source assembly push onto spring-loaded counter pieces on the inner chamber that carry the electrical signals.

Figure 2.3 also shows two concentric cones that surround the capillary entrance. They direct the counter-flow gas and are designed to match a high-field asymmetric waveform ion mobility spectrometer¹³⁸ (FAIMS) by Thermo Fisher, which can be connected to the front end of the machine to additionally select ions by their differential cross section.

2.5 Differential Pumping Stages

The instrument comprises seven differential pumping stages, which are illustrated in Fig. 2.4 and listed in table 2.1 together with the corresponding pressures and the pumps that are being used. In brief, the ion funnel constitutes the first pumping stage, with its exit electrode forming

Figure 2.4: Illustration of the pumping stages of the tandem quadrupole mass spectrometer.



the conductance limiting orifice. The hexapole spans the following two stages. Its rods are mounted on three ceramic collars. By enclosing the first two collars in a cylinder, the gas load in the third stage could be reduced (see Fig. 2.3). In the fourth stage, which contains the first quadrupole and the first bender, the pressure is already decreased to 2×10^{-7} mbar. The octopole and 22-pole (together with the last two benders) are each placed in a pumping stage of their own, where pressures of 1×10^{-8} mbar and 2×10^{-9} mbar are reached, respectively. If ions are trapped in the octopole, a helium pressure of $\sim 1 \times 10^{-4}$ mbar is maintained in this section. For efficient trapping and cooling, helium is pulsed into the 22-pole which raises the pressure to $\sim 1 \times 10^{-5}$ mbar in the corresponding stage. The second quadrupole mass analyzer finally occupies the last pumping stage together with the detector.

2.6 The Electrospray Source

Principle of operation The studies on cold biomolecular ions by Rizzo and co-workers⁵⁰ have received considerable attention. Their appeal is to no small extent due to the size of the peptides under investigation for which detailed spectroscopic information could be obtained. Peptides of up to 20 amino acids are still far smaller than most naturally occurring enzymes. However, they were shown to exhibit features of secondary structure that occur in much larger systems.

The study of large molecules in the gas phase encounters the challenge that they possess low vapor pressures and decompose upon heating. In 2002, the Nobel Prize was awarded for

two soft ionization techniques, electrospray ionization (ESI)⁸² and matrix assisted laser desorption/ionization (MALDI),⁸¹ that made it possible to transfer large molecules to the gas phase and ionize them without significant decomposition.

The previous setup of our group as well as the setup which is being described here both use ESI^{82–84} to generate a continuous beam of gaseous ions. The process¹⁴⁰ is illustrated in Fig. 2.5. High voltage is applied between a sampling orifice (usually the transfer capillary which

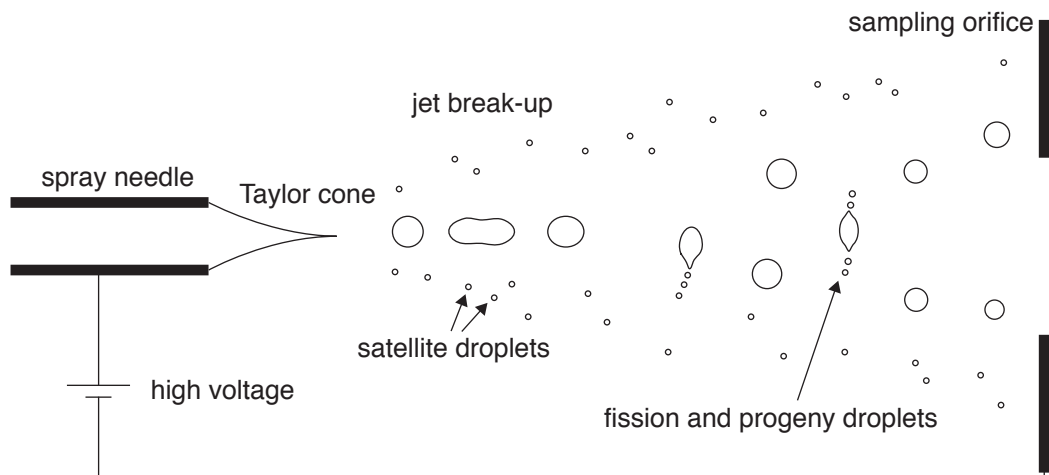


Figure 2.5: The ESI process.

constitutes the entrance to the vacuum system) and the ESI needle, which contains a (slightly pressurized) solution of the analyte. In case of a positive high voltage, the solution is oxidized and due to the action of the electric field forms a cone-shaped liquid meniscus at the capillary exit, a so-called Taylor cone. Because of charge repulsion, a highly charged liquid jet is emitted,

no	section	pressure	pump	forepump
1	ion funnel	1.5 mbar	60 m ³ /h rotary vane (Alcatel)	
2	hexapole (1)	7e-3 mbar	60 l/s turbomolecular pump (Pfeiffer, TMU 071 P)	5 m ³ /h rotary vane pump (Pfeiffer, DUO 5)
3	hexapole (2)	1e-5 mbar	500 l/s turbomolecular pump (Pfeiffer TMU 521 P)	0.9 m ³ /h membrane pump (Pfeiffer, MVP 015-4)
4	quadrupole 1	2e-7 mbar	500 l/s turbomolecular pump (Pfeiffer, TMU 521 P)	0.9 m ³ /h membrane pump (Pfeiffer, MVP 015-4)
5	octopole	1e-8 mbar	500 l/s turbomolecular pump (Pfeiffer, TMU 521 P)	0.9 m ³ /h membrane pump (Pfeiffer, MVP 015-4)
6	22-pole	2e-9 mbar	500 l/s turbomolecular pump (Pfeiffer, TMU 521 P)	5 m ³ /h scroll pump (Edwards, XDS5)
7	quadrupole 2	2e-9 mbar	260 l/s turbomolecular pump (Pfeiffer TMU 261 P)	5 m ³ /h scroll pump (Edwards, XDS5)

Table 2.1: Differential pumping stages of the tandem mass spectrometer with 22-pole ion trap. If helium is pulsed into the 22-pole, the pressure in sections 6 and 7 will rise to $\sim 1e-5$ mbar and $\sim 1e-8$ mbar, respectively. Similarly, if ions are pretrapped in the octopole, the helium pressure is maintained at $\sim 1e-4$ mbar in this part.

which subsequently breaks up into the larger primary droplets and smaller satellite droplets, which occupy the periphery of the spray.

Because of the electric field, the droplets move to the sampling orifice and finally enter the mass spectrometer. Due to collisions with gas, they continuously evaporate neutral solvent molecules. While they shrink in size, the charge repulsion in the droplets approaches the magnitude of their surface tension, so that they become unstable. The critical limit at which both forces become equal in a spherical droplet is called the Rayleigh limit. Different mechanisms have been proposed how the analyte molecules are subsequently liberated from these droplets.¹⁴¹

According to the ion evaporation model, single ions are detached from the surface of the droplet as the Coulomb repulsion overcomes the surface tension. In this process, the analyte ions are directly liberated and can be sampled.

The charged residue model, on the other hand, assumes that asymmetric droplet fission occurs at about 70% of the Rayleigh limit, in which the primary droplet emits a number of smaller droplets. These progeny droplets were found to carry about 2% of the mass and 15% of the parent droplet charge. Microphotographs of these events showed that emission occurred from one or two conical protrusions in the primary droplet in a direction orthogonal to the electric field, and aerodynamic effects have been suggested to explain these observations.¹⁴² However, it is not clear how many fission cycles the droplets undergo before single analyte ions are liberated. It is also conceivable that smaller progeny droplets could rather detach ions in agreement with the ion evaporation model than undergo further fissions.

Depending on the spray conditions, different processes can lead to the formation of charged analyte ions. In the case of peptides and operation in positive ESI mode, protonation predominates. If metal ions are present in the sample, the formation of adducts can also be observed. In both cases, closed-shell species are produced.

In our setup, ions are generated by nano-ESI,^{143,144} an ESI-variant that uses spray needles whose orifice has a diameter of several μm only. Under these conditions, the liquid ionizes by the sole action of the applied electric field. Without the need to pressurize the solution, very low flow rates of 20-50 nl/min can be achieved, which renders the method sensitive for the analysis of picomolar amounts of sample. The low sample consumption is particularly advantageous for our application, since we frequently work on expensive synthetic peptides. Furthermore, pure water solutions can be sprayed, which is difficult with conventional ESI due to the high surface tension of the solvent. Since nano-ESI produces smaller primary droplets (typical 150 nm diameter as compared with 1.5 μm for conventional ESI), fewer fission cycles are required, so that more analyte ions are finally available for mass analysis. This leads to a further sensitivity gain, especially for hydrophilic molecules that tend to be suppressed in ESI.

Realization The nano-ESI source (Proxeon, ES070) uses metalized borosilicate needles (1 μm inner diameter of the tip) that are mounted on a microtranslational stage and connected to a

programmable high voltage power supply (1-1000 V, EMCO High Voltage Corporation). For precise positioning of the needle with respect to the transfer capillary and monitoring of the spray, two cameras are used.

The stainless-steel transfer capillary is 11.5 cm long and possesses an inner and outer diameter of 0.5 mm and 2 mm, respectively. It is surrounded by a copper block, which can be heated to 250 °C by two 100 W cartridge heaters (Prang+Partner AG). Its potential is defined with a programmable DC power supply (Spectrum Solutions, TD 1400).

2.7 RF Devices

The principal purpose of the experimental setup that is being described in this chapter is the study of the interaction of cold, gaseous ions with laser radiation. To this end, ions are cooled in collisions with a cold buffer gas, which requires the manipulation and storage of slow ions (on the order of a few eV). This is generally difficult to achieve with electrostatic potentials, which only allow for the creation of saddle points in space, but no true minima. This is a consequence of Laplace's equation

$$\Delta\Phi = -4\pi\rho \quad (2.1)$$

(with the the electrical potential Φ , and the charge density ρ), which in the absence of space charge becomes

$$\Delta\Phi = 0. \quad (2.2)$$

Space charge and the presence of a buffer gas will generally render the problem more difficult. However, slow ions can be guided and trapped by means of inhomogenous RF fields. The experimental setup makes use of several of these RF devices: the ion funnel, hexapole and octopole, the mass analyzing quadrupoles, and the 22-pole. The following sections explain their principle of operation and give details on their experimental realization.

2.7.1 The Quadrupole Mass Analyzers

Principle of Operation Among the earliest realizations of RF devices are linear quadrupoles, which can be used for ion guiding, storage, and mass selection.¹⁴⁵ Four hyperbolic or circular electrodes are used to approximate the ideal potential $\Phi(x, y)$ of an infinitely long quadrupole

$$\Phi(x, y) = \frac{\Phi_0}{r_0^2}(x^2 - y^2), \quad (2.3)$$

with $\Phi(r_0, 0) = \Phi_0$. $\Phi_0 = U + V_0 \cos \Omega t$ is composed of a DC component U and a RF component $V \cos \Omega t$ with amplitude V and angular frequency Ω . These are applied as illustrated in Fig. 2.6. The resulting equation of motion of a charged particle of mass m and charge q can be separated for the coordinates x and y to give

$$m\ddot{x} = -2q \frac{(U + V \cos \Omega t)}{r_0^2} x \quad (2.4)$$

$$m\ddot{y} = -2q \frac{-(U + V \cos \Omega t)}{r_0^2} y. \quad (2.5)$$

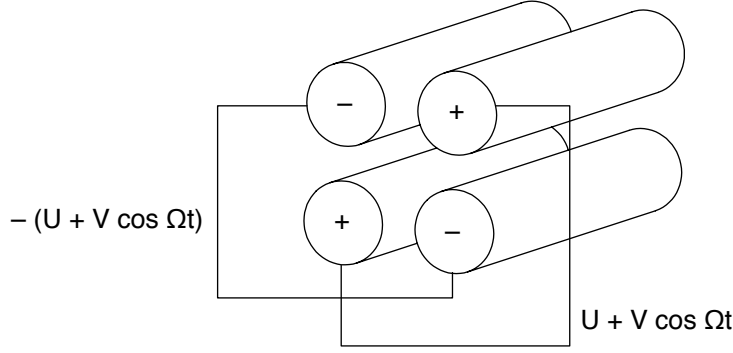


Figure 2.6: Waveforms and wiring diagram for a quadrupole mass filter.

These are special cases of the Mathieu Equation

$$\frac{d^2u}{d\xi^2} + (a_u - 2q_u \cos 2\xi)u = 0. \quad (2.6)$$

Comparison with Eqn. 2.4 yields

$$u = x, \quad (2.7)$$

$$\xi = \frac{\Omega t}{2}, \quad (2.8)$$

$$q_x = \frac{-4qV}{mr_0^2\Omega^2}, \quad (2.9)$$

$$\text{and } a_x = \frac{8qU}{mr_0^2\Omega^2}. \quad (2.10)$$

For the purposes of ion transmission and mass filtering, it is of interest to identify combinations of q_x and a_x ($q_y = -q_x$ and $a_y = -a_x$) for which ion trajectories are simultaneously stable in the x and y directions, *i.e.* for which ions of a given mass are transmitted rather than ejected. Several such regions of stability exist. Figure 2.7 displays the region in which quadrupoles are usually operated. For a given ratio of the DC and AC voltages U/V different masses lie on a straight line, with the heavier masses at lower (q_u, a_u) values. In Fig. 2.7, the mass m_2 lies within the stability region and is transmitted while the heavier mass m_1 and the lighter mass m_3 are ejected.

By simultaneously increasing U and V while keeping U/V is constant (*i.e.* scanning the quadrupole), the different m/z ratios shift along the straight line to higher (q_u, a_u) values, so that m_2 will leave the stable region and at a later point, m_1 will enter. This way, a mass spectrum can be obtained. It is obvious that by increasing the slope of the straight line in Fig. 2.7 (*i.e.* increasing U/V), the mass resolution is being increased while sacrificing sensitivity.

Realization The two quadrupole analyzers that are used to select parent and fragment ion m/z ratios were purchased from Extrel. They possess 20 cm long, 9.27 mm diameter rods on a 8.2 mm inscribed diameter and are equipped with entrance and exit lenses. They are driven at 1.2 MHz by an Extrel power supply and provide a scan range of 2-2000 amu (for singly charged ions). Analog control voltages are used to set the mass command, resolution and pole bias.

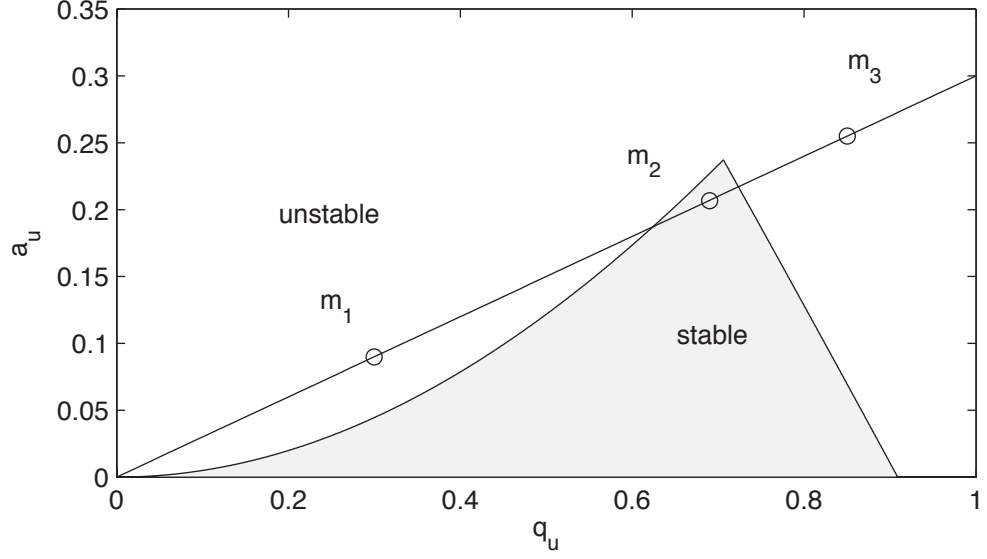


Figure 2.7: Stability diagram for the operation of a quadrupole, with the Mathieu parameters a_u and q_u . For a given ratio U/V different masses ($m_1 > m_2 > m_3$) lie on a straight line.

2.7.2 The Adiabatic Approximation and the Effective Potential

For higher order multipoles¹ and other geometries and arrangements of the RF electrodes, the resulting equations of motion

$$m\ddot{\mathbf{r}} = q\mathbf{E}_0(\mathbf{r}) \cos \Omega t \quad (2.11)$$

(with particle mass m , position vector \mathbf{r} , particle charge q , electric field amplitude \mathbf{E}_0 , the angular frequency Ω of the RF, and time t) are generally nonlinear and coupled, so that analytical solutions are not available. In this sense, the quadrupole potential represents a special case. Many properties of RF devices can nevertheless be understood within the adiabatic approximation (D. Gerlich),¹¹² which will be elaborated in the following.

Figure 2.8 shows the simulated trajectory of an ion that is trapped in an RF only octopole. The ion trajectory apparently consists of a slow drift motion superimposed by a fast wiggling motion, which increases in amplitude close to the electrodes.

For this kind of trajectory, it therefore appears sensible to describe the ion motion $\mathbf{r}(t)$ as a sum of a smooth drift $\mathbf{R}_0(t)$ and a fast oscillation $\mathbf{R}_1(t)$

$$\mathbf{r}(t) = \mathbf{R}_0(t) + \mathbf{R}_1(t), \quad (2.12)$$

with

$$\mathbf{R}_1(t) = -\mathbf{a}(t) \cos \Omega t, \quad (2.13)$$

¹This also holds for “lower order multipoles”, *i.e.* tripoles, which have been theoretically explored.^{146, 147}

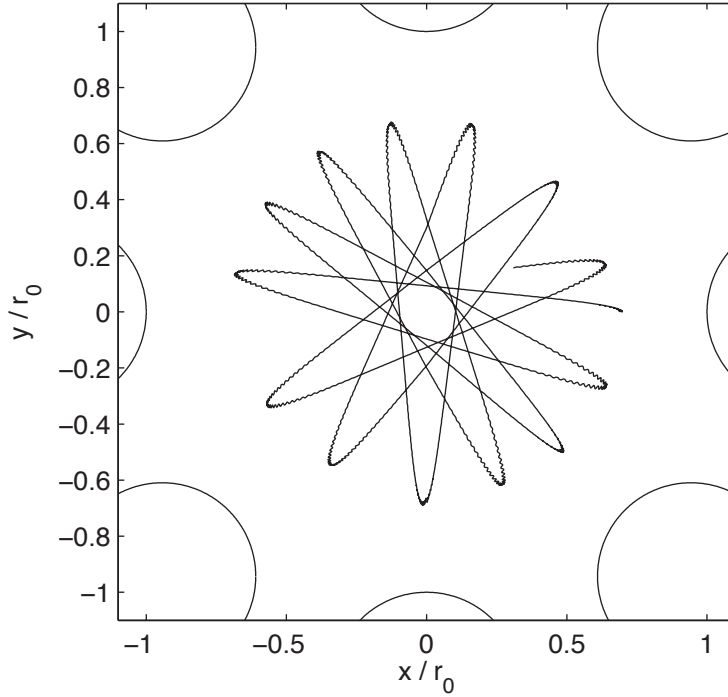


Figure 2.8: Simulated ion trajectory in an ideal, two-dimensional octopole RF field.

where $\mathbf{a}(t)$ is the amplitude of the micro-oscillations.

This will certainly be a good approximation if \mathbf{E}_0 changes only slightly during one micro-oscillation. This is the case if \mathbf{E}_0 varies smoothly and the amplitude of the wiggling motion is small (the latter holds for high Ω , see below). Under these conditions, it is justified to keep only the first two terms of the expansion of \mathbf{E}_0

$$\mathbf{E}_0(\mathbf{R}_0 - \mathbf{a}(t) \cos \Omega t) = \mathbf{E}_0(\mathbf{R}_0) - (\mathbf{a}(t) \cdot \nabla) \mathbf{E}_0(\mathbf{R}_0) \cos \Omega t + \dots \quad (2.14)$$

If one substitutes Eqns. 2.12 and 2.14 into Eqn. 2.11 and assumes a slow time variation of $\mathbf{a}(t)$, so that $\dot{\mathbf{a}}(t)$ can be neglected, one obtains

$$m\ddot{\mathbf{R}}_0 + m\Omega^2 \mathbf{a}(t) \cos \Omega t = q\mathbf{E}_0(\mathbf{R}_0) \cos \Omega t - q(\mathbf{a}(t) \cdot \nabla) \mathbf{E}_0(\mathbf{R}_0) \cos^2 \Omega t. \quad (2.15)$$

One can assume that the wiggling amplitude $\mathbf{a}(t)$ changes only as a function of \mathbf{R}_0 and can therefore be replaced by $\mathbf{a}(\mathbf{R}_0)$. A particle in a homogeneous field $\mathbf{E}_0 \cos \Omega t$ oscillates with an amplitude $\mathbf{a} = \frac{q\mathbf{E}_0}{m\Omega^2}$. For a small wiggling motion in a slowly varying electric field, the amplitude $\mathbf{a}(\mathbf{R}_0)$ can therefore be approximated by

$$\mathbf{a}(\mathbf{R}_0) = \frac{q\mathbf{E}_0(\mathbf{R}_0)}{m\Omega^2} \quad (2.16)$$

so that one obtains

$$m\ddot{\mathbf{R}}_0 = -\frac{q^2}{m\Omega^2} (\mathbf{E}_0(\mathbf{R}_0) \cdot \nabla) \mathbf{E}_0(\mathbf{R}_0) \cos^2 \Omega t. \quad (2.17)$$

Using a vector analysis identity and $\nabla \times \mathbf{E}_0 = 0$

$$(\mathbf{E}_0 \cdot \nabla) \mathbf{E}_0 = \frac{1}{2} \nabla E_0^2 - \mathbf{E}_0 \times (\nabla \times \mathbf{E}_0) = \frac{1}{2} \nabla E_0^2, \quad (2.18)$$

so that

$$m\ddot{\mathbf{R}}_0 = -\frac{q^2}{2m\Omega^2}\nabla E_0(\mathbf{R}_0)^2 \cos^2 \Omega t. \quad (2.19)$$

By replacing $\cos^2 \Omega t$ by its average $\frac{1}{2}$, one obtains a differential equation for the slow drift motion \mathbf{R}_0

$$m\ddot{\mathbf{R}}_0 = -\frac{q^2}{4m\Omega^2}\nabla E_0(\mathbf{R}_0)^2. \quad (2.20)$$

The motion occurs in a pseudo potential $\frac{q^2}{4m\Omega^2}E_0(\mathbf{R}_0)^2$, which is created by the time-averaged action of the oscillating electric field. This pseudo potential is proportional to the square of charge and the square of the electric field, so that particles experience a *field gradient force*, which accelerates them towards lower fields.

Taking into account an electrostatic field

$$\mathbf{E}_s(\mathbf{R}_0) = -\nabla\Phi_s(\mathbf{R}_0) \quad (2.21)$$

that can be superimposed on the oscillating electric field, one can define an *effective potential*

$$V^*(\mathbf{R}_0) = \frac{q^2 E_0(\mathbf{R}_0)^2}{4m\Omega^2} + q\Phi_s(\mathbf{R}_0) \quad (2.22)$$

so that the equation of motion becomes

$$m\ddot{\mathbf{R}}_0 = -\nabla V^*(\mathbf{R}_0). \quad (2.23)$$

It is instructive to consider the total energy E_{tot} of the system

$$E_{tot} = \frac{1}{2}m\dot{\mathbf{R}}_0^2 + \frac{q^2 E_0(\mathbf{R}_0)^2}{4m\Omega^2} + q\Phi_s(\mathbf{R}_0). \quad (2.24)$$

The total energy E_{tot} is an adiabatic constant of the drift motion \mathbf{R}_0 , so that kinetic energy $\frac{1}{2}m\dot{\mathbf{R}}_0^2$ is transferred into effective potential energy $\frac{q^2 E_0(\mathbf{R}_0)^2}{4m\Omega^2}$ and electrostatic energy $q\Phi_s(\mathbf{R}_0)$ during the ion motion. The nature of the effective potential energy term is further elucidated by realizing that it is identical to the average kinetic energy of the wiggling motion.

$$\left\langle \frac{1}{2}m\dot{\mathbf{R}}_1^2 \right\rangle = \frac{q^2 E_0(\mathbf{R}_0)^2}{4m\Omega^2} \quad (2.25)$$

The properties of RF devices can now be interpreted in terms of the effective potential, as will be done in the following sections for ion funnels and linear multipoles.

2.7.3 Adiabaticity and Stability

The derivation of the effective potential in the previous section assumes a fast, small-amplitude oscillatory motion of the ion around an average position within a slowly varying electric field. The wiggling motion can thus be separated from the drift motion and treated as if it took place in a homogeneous electric field, whose magnitude only varies slowly as a function of the average position of the ion. Under these conditions, the total average ion energy is an adiabatic constant of the ion motion.

It is, however, obvious that non-adiabatic conditions can exist, under which the oscillating electric field continuously increases the total energy of the ion, so that unstable trajectories result. Such an example is presented in Fig. 2.9 where the amplitude of the oscillations of the ion in the trap is increased by the RF field until the ion is lost on an electrode. It is therefore

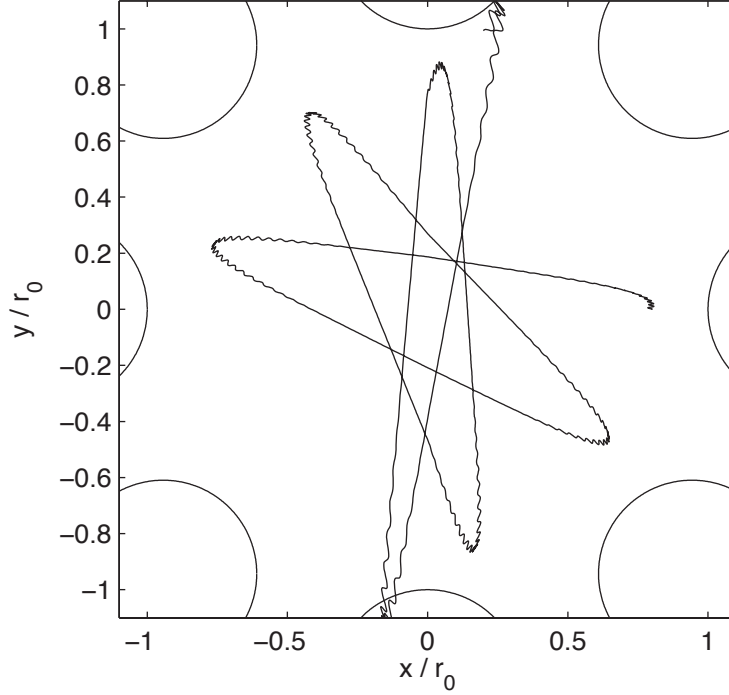


Figure 2.9: Simulated ion trajectory in an ideal, two-dimensional octopole RF field. Non-adiabatic behavior leads to the loss of the ion on the electrode surface.

desirable to find a strict mathematical criterion for adiabaticity.

D. Gerlich defines an adiabaticity parameter η , based on the idea that the change of the electric field during a full micro-oscillation, *i.e.* over $2\mathbf{a}$, should be small compared with the electric field at the average position

$$|2(\mathbf{a} \cdot \nabla) \mathbf{E}_0(\mathbf{R}_0)| < |\mathbf{E}_0(\mathbf{R}_0)|. \quad (2.26)$$

The adiabaticity parameter η is then given as the ratio of both quantities

$$\eta = \frac{|2(\mathbf{a} \cdot \nabla) \mathbf{E}_0(\mathbf{R}_0)|}{|\mathbf{E}_0(\mathbf{R}_0)|}, \quad (2.27)$$

which with Eqns. 2.16 and 2.18 becomes

$$\eta = \frac{2q|\nabla E_0(\mathbf{R}_0)|}{m\Omega^2}. \quad (2.28)$$

The adiabaticity parameter η represents a scalar field and is proportional to the gradient of the electric field. No mathematical procedure is available to determine the maximum allowed value of η along the ion trajectory. However, Gerlich and co-workers determined an empirical rule for safe operation of RF devices within the adiabatic approximation based on numerical simulations

of ion trajectories in several RF devices. It requires that the maximum value of the adiabaticity parameter along an ion trajectory η_{max} should be smaller than 0.3

$$\eta_{max} < 0.3. \quad (2.29)$$

For $\eta_{max} > 0.3$, non-adiabatic behavior is observed, *i.e.* the average total ion energy fluctuates or increases continuously over time, leading to ion loss. From investigations of the evaporation of chlorine anions from a 22-pole ion trap, Wester and co-workers experimentally determined the effective trapping volume, within which adiabatic ion motion is preserved, and deduced $\eta_{max} < 0.36 \pm 0.02$.¹³²

Under conditions for which the adiabatic approximation holds, the volume that is accessible to a trapped ion is limited by the condition that its effective potential energy $V^*(\mathbf{r})$ cannot exceed its total average energy E_{tot}

$$V^*(\mathbf{r}) = \frac{q^2 E_0(\mathbf{r})^2}{4m\Omega^2} + q\Phi_s(\mathbf{r}) \leq E_{tot}. \quad (2.30)$$

Stable trapping can thus be achieved if this volume does not exceed the physical limits of the device and $\eta_{max} < 0.3$ within this volume. Within the limits of the adiabatic approximation, this represent a sufficient condition for stable confinement of the ion. However, this does not exclude that stable ion motion exists outside of this limit, and, indeed, stable orbits with $\eta_{max} > 0.3$ can be demonstrated in numerical simulations.

2.7.4 Hexapole, Octopole and 22-Pole

In the experimental setup, a hexapole and octopole are used to guide, thermalize, and pretrap ions, while the 22-pole trap constitutes the heart of the instrument, where ions are stored, cooled, and interact with laser radiation. The potential of an ideal, infinitely long multipole $V(r, \phi)$ of order n is described by

$$V(r, \phi) = V_0 \hat{r}^n \cos n\phi, \quad (2.31)$$

with the cylindrical coordinates r and ϕ , the reduced variable $\hat{r} = \frac{r}{r_0}$ and $V(r_0, \phi) = V_0 \cos n\phi$. The effective potential (Eqn. 2.22) in the absence of static electric fields is obtained as¹¹²

$$V^* = \frac{n^2 q^2 V_0^2}{4m\Omega^2 r_0^2} \hat{r}^{2n-2}. \quad (2.32)$$

Figure 2.10 displays the effective potentials of quadrupoles, hexapoles, octopoles, and 22-poles. Instead of hyperbolic electrodes that follow the equipotential lines of the ideal multipole potential, circular rods are frequently used, which are more readily available. This leads to higher order multipole terms in the potential, which, however, do not have any negative influence on the performance of RF-only devices.

Realization of the hexapole and octopole The 17 cm long hexapole with 2 mm diameter rods on an inscribed radius of 2 mm is purchased from Analytica of Branford. It is driven by a

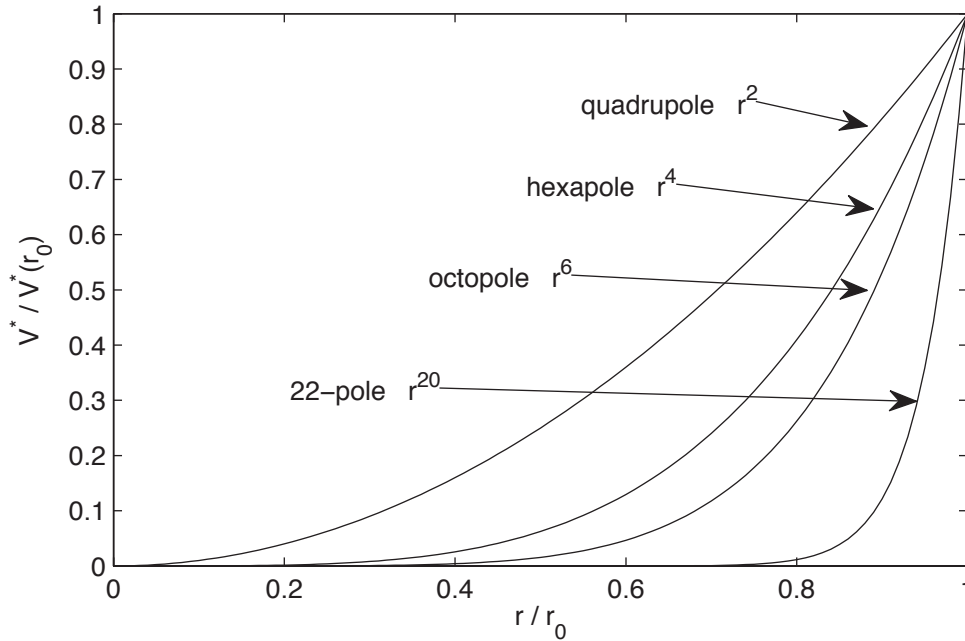


Figure 2.10: Effective potentials V^* for quadrupoles, hexapoles, octopoles, and 22-poles.

4 MHz RF power supply (CGC instruments, RFG50-10) that is based on a design by Cermak *et al.*¹⁴⁸ but does not use an air coil to couple the RF onto the rods. The ends of the secondary coil of the transformer are directly connected to the load, which simplifies the instrument and drastically reduces its power consumption, while maintaining sufficient purity of the waveforms. The RF amplitude (usually 100–200 V_{0-p}) is determined by an external computer controlled DC power supply (FuG Elektronik GmbH, NTN 35-35), while the pole bias is supplied through a programmable DC voltage (Spectrum Solutions, TD 1400).

The 40 cm long octopole with 3.18 mm diameter rods on a 9.52 mm inscribed diameter, equipped with an exit and entrance lens, is driven by a 2.1 MHz power supply (all Extrel). The RF amplitude and pole bias are controlled by analog programming voltages.

Buffer gas cooling of ions and the 22-pole The only known method to date to generate translationally as well as the internally cold gas phase molecules is buffer gas cooling. With the technology of current cryostats, a bath gas (mostly helium) can be cooled to temperatures as low as 4 K. Given sufficient interaction time, a molecule or molecular ion will thermalize to the buffer gas temperature. Simulations showed that only about five collisions are necessary to translationally cool a 4 amu ion starting from an initial temperature of 300 K to a helium bath temperature of 18 K. The number increases with the ion mass, so that around 60 collisions are necessary for a 150 amu ion.¹⁴⁹ Since the cross section for inelastic collisions is frequently smaller than that for elastic collisions, it is estimated that 10–10'000 collisions are necessary to cool the internal degrees of freedom of a molecular ion.¹⁵⁰

Ions offer the advantage over neutrals that they can easily be stored using RF traps so that

sufficiently long cooling times can be realized. However, while under adiabatic operating conditions no net transfer of energy from the RF trapping field to the ion occurs the additional presence of buffer gas can lead to so-called RF heating. While the ion undergoes micro-oscillations energetic collisions with the buffer gas can occur which increase the translational and the internal temperature of the ions. In a quadrupole ion trap operated at room temperature the ion translational temperature was, for example, shown to be in the range of 1180 – 1690 K.¹⁵¹

However, simulations show how the ion temperature successively approaches the bath gas temperature when the number of poles of the trap is increased.^{149, 150, 152} This behavior can be understood in terms of the larger field-free region of the higher order multipoles (see Fig. 2.10), where the ions do not exhibit micromotion and can be successfully cooled. RF heating is limited to a narrow region close to the steep reflecting walls of the effective potential.

Based upon this insight D. Gerlich introduced the now widely used 22-pole ion trap¹³¹ in which translational, rotational and vibrational temperatures of the stored ions were shown to approach the bath gas temperature.^{50, 133, 135} The choice of the exact number of poles has technical reasons. A multipole potential can be approximated with circular electrodes when their diameter d and the inscribed trap radius r_0 are related by

$$r_0 = (n - 1)d/2 \quad (2.33)$$

where n is the order of the multipole.¹¹² With 1 mm diameter rods one therefore obtains a convenient inscribed diameter of 10 mm for a 22-pole ion trap.

The understanding of the mechanisms that can lead to RF heating in 22-poles has been improved in a number of experiments and accompanying simulations. It was found that a mass-mismatch, *i.e.* a light ion and a heavy buffer gas, leads to increased RF heating.¹⁴⁹ For H_3^+ ions stored in a 22-pole at 55 K with argon as buffer gas a translational temperature of 170 K and a rotational temperature of 140-150 K was determined.¹⁵³ Furthermore, space charge or excessive end cap potentials heat the ions by forcing them into the RF walls. While field distortions can have a similar effect misalignments of the trap only seem to play a minor role.¹⁴⁹ Finally, the ion temperature was found to be largely independent of the buffer gas density, RF frequency and amplitude within the usual operating ranges.^{149, 150}

Realization of the 22-pole The 22-pole is the central element and the heart of the setup presented here. Its design (Fig. 2.11) closely follows the original design of D. Gerlich.^{131, 154} The copper housing of the 22-pole is mounted onto the second stage of a closed cycle helium refrigerator (Sumitomo Heavy Industries, SRDK-408D-W71D) and is enclosed by an aluminum heat shield, connected to the first stage. A solenoid valve (Parker Hannifin, General Valve) is used to pulse helium into the 22-pole through a teflon tube (not drawn), connected to the copper housing and reaching through the heat shield. The temperature of the 22-pole housing can be adjusted between 4 and 320 K. It is controlled by means of a silicon diode and a 50 W

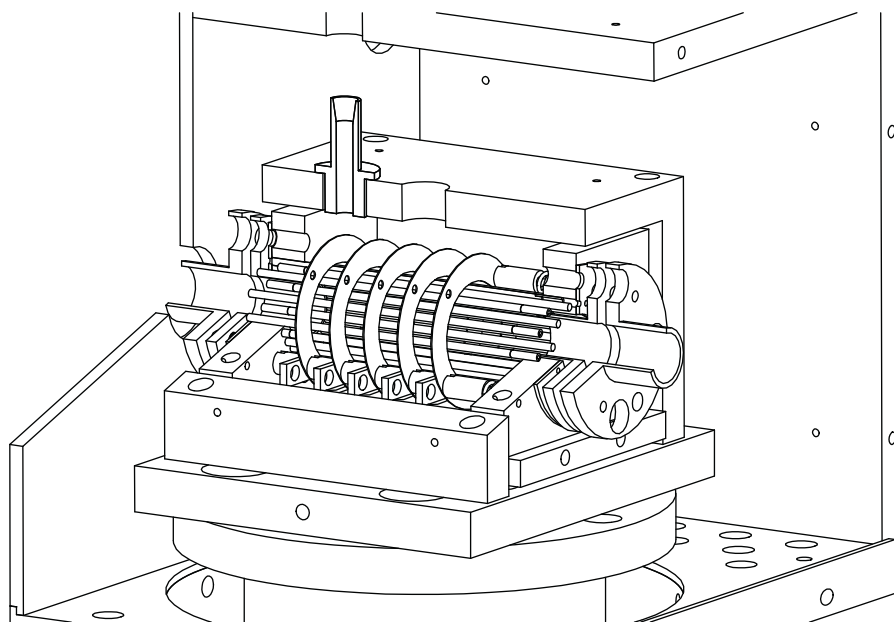


Figure 2.11: Drawing of the 22-pole mounted on the cold head.

cartridge heater (Lakeshore, DT-670B-CU and HTR-50), which are attached to the outside of the housing and connected to a Lakeshore Model 331S temperature controller.

The 22-pole is constructed from 1 mm diameter, 41 mm long stainless-steel rods and has an inscribed diameter of 10 mm. They are held in place by a circular hole pattern in the front and the end plate of the housing to which the two RF phases are applied. Ceramic sleeves insulate the rods from either the front or the end plate so that neighboring poles carry opposite RF phases. The plates are electrically insulated from the remainder of the housing while good thermal contact is provided through 1 mm thick sapphire plates. In order to further improve the thermal conductance 0.1 mm thick indium foils are inserted in between the sapphire plates and copper parts. Similarly, an indium foil ensures a good contact between the cold head and the base plate of the 22-pole housing.

On the outside of the housing, the end plates carry two electrostatic lenses each. The inner two lenses protrude in between the rods and serve as trapping electrodes. On the inside, the end plates are used to mount an assembly of five 0.15 mm thick ring electrodes of 13 mm inner diameter, spaced at a distance of 6 mm, which surround the rods of the 22-pole and can be used to shape the ion cloud along the trap axis. All electrical connections are tied to the heat shield in order to reduce the heat load on the 22-pole.

2.7.5 The Ion Funnel

Principle of operation The ion funnel¹⁵⁵ addresses a problem that arises when ions created in a high pressure source have to be introduced into the vacuum region of a mass spectrometer. This is the case for ESI, which is normally performed at atmospheric pressure. Ions then usually enter the mass spectrometer through a capillary, which serves to limit the gas flow

into the system, and subsequently pass further conductance limiting orifices that separate the differential pumping stages. The first pumping stage is usually held at several mbar, and the gas exits the capillary in the form of a mild molecular beam expansion. A divergent ion beam results that is hard to refocus, since it is entrained in the jet of neutrals.

In many setups, including the one that has previously been used in our group,¹⁰⁶ a skimmer follows the capillary, which limits the gas flow to the following stage and only transmits the central, less divergent part of the expansion. It is obvious that important ion losses result.

In 1997, Smith and co-workers presented the first design of an ion funnel,¹⁵⁶ a device designed to replace the skimmer and refocus the expanding ion beam to a small aperture, thus improving ion transmission by an order of magnitude. Figure 2.12 illustrates their latest design.¹³⁷

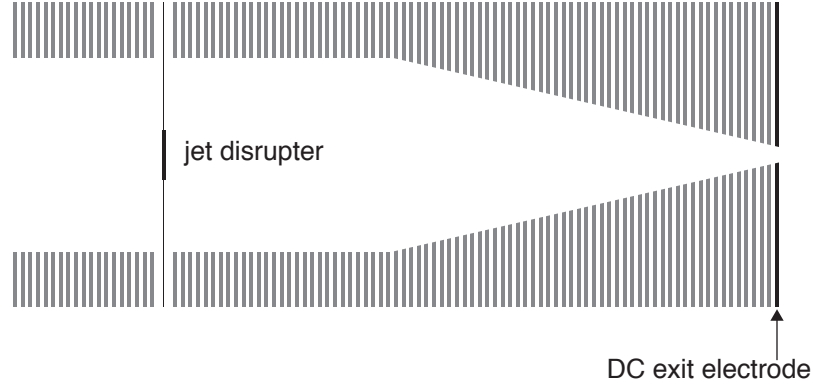


Figure 2.12: Schematic representation of an ion funnel with ring electrodes (grey), jet disrupter, and DC exit electrode.

It uses a stack of ring electrodes in which alternating electrodes are connected to the two phases of a RF. In this basic feature, it resembles D. Gerlich's design of a ring electrode trap (RET).¹¹² In the design shown in Fig. 2.12, ions first enter a section of ring electrodes with constant inner diameter. A second section follows in which the inner diameter of the electrodes slowly decreases, so that the ions are focussed to the exit aperture. Ion funnels are usually operated in the range of 1-30 mbar, where gas-dynamic effects play an important role. A DC gradient is therefore superimposed on the RF that actively drags the ions to the exit. (Similarly, in their design of a RET, Asmis and co-workers use a pulsed gradient to efficiently extract ions.¹⁵⁷)

Figure 2.13 displays a SIMION¹⁵⁸ simulation of the effective potential V^* (Eqn. 2.22) of an ion funnel with 27 electrodes; only the contribution from the RF field is shown, while the DC gradient is omitted for clarity. In the first section, the effective potential closely resembles that of a RET: A large field free space in the center is surrounded by steep RF walls. As in a RET, the effective potential is approximately proportional to $\sim e^r$.^{112,159} Closer to the walls, it is furthermore modulated with a period that equals the spacing of the ring electrodes. In the section of decreasing inner diameter, the RF walls close in on the central axis, making the effective potential indeed appear like a funnel. If one adds the DC gradient that is applied across

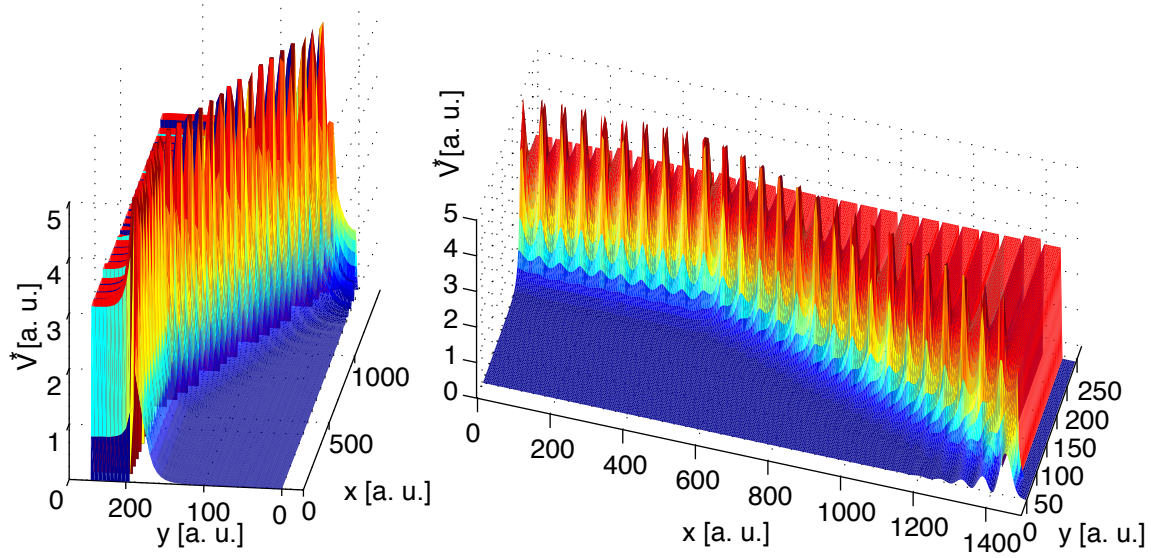


Figure 2.13: Simulation of the effective potential V^* of an ion funnel with 27 electrodes. Contributions from the DC gradient are omitted.

the electrodes, one obtains a funnel-shaped potential that is steeply pointing down towards the exit. By analyzing the effective potential, the principle of operation of ion funnels thus becomes immediately evident in a qualitative fashion. However, some important modifications to this simple picture have to be taken into account.

Due to the cylindrical symmetry of the ion funnel, the angular momentum of the ions with respect to axis is conserved.¹¹² Without the presence of gas and the resulting damping of the motion through collisions, ions would simply be reflected. Ion funnels are usually operated at elevated pressures, where a high collision frequency generally leads to an effective reduction of the confining potential. At even higher pressures, where ion funnels can still be operated efficiently, the ions experience drag forces from the bath gas and move in phase with the RF field, while the adiabatic approximation assumes out-of-phase oscillations and thus breaks down under these conditions. Furthermore, space charge effects will occur especially at the exit of the ion funnel and modify the behavior of the device. Detailed simulations that took these effects into account improved the understanding of the operation of the ion funnel and led to improvements of the design.¹⁵⁹

An early design of the ion funnel exhibited a discrimination of low masses and a mass-dependent optimum of the RF amplitude.¹⁶⁰ This behavior was shown to result from axial potential wells at the funnel exit, which are created if the inner diameter of the electrodes becomes comparable to the electrode spacing. The simulated funnel potential in Fig. 2.13 clearly demonstrates this behavior. Since the effective potential V^* (Eqn. 2.22) is inversely proportional to the mass over charge ratio, the effect is more pronounced for ions with low m/z ratio. They will be trapped and accumulated in these wells, until space charge forces them towards the electrodes. This effect is aggravated by the fact that for regions of comparable

inner diameter and electrode spacing a high adiabaticity parameter η results, which is again inversely proportional to the ion mass over charge ratio (Eqn. 2.28). Ions with low m/z ratio are therefore likely to have unstable trajectories.

An obvious solution to this problem is to increase the inner diameter at the funnel exit. This, however, leads to a higher gas load in the following differential pumping sections. Therefore, in subsequent designs of the ion funnel, the electrode spacing was instead reduced, which improved the low mass transmission and reduced the dependence of the optimum transmission efficiency of different masses on the RF amplitude.¹⁶¹ Further improvements can be obtained by increasing the RF angular frequency Ω because of the inverse dependence of the adiabaticity parameter η on the square of Ω (Eqn. 2.28).

Figure 2.12 also shows a so-called jet disrupter.¹⁶² It is a small conductive plate that is suspended in the center of the ion funnel, about 2 cm away from the capillary. It is biased such that ions will flow around it while the directed jet of neutrals hits it and is disrupted. The jet disrupter thus reduces the gas load on subsequent pumping stages.

The DC exit electrode (Fig. 2.12) terminates the ion funnel and represents the conductance limit. With an appropriate bias voltage applied, it can be used as a low-mass filter.¹⁶³

Realization The design of our ion funnel closely follows that of Smith and co-workers.¹³⁷ The funnel consists of a stack of 100 stainless steel electrodes mounted on four ceramic rods. They are 0.5 mm thick and 0.5 mm apart. Four teflon spacers ensure the right distance between adjacent plates. The first section comprises 57 ring electrodes with a constant inner diameter of 25.4 mm. The 20th plate is used as the jet disrupter and features a 6.5 mm diameter disc in its center, which is held in place by four 0.5 mm thick rods. In the second section of 42 electrodes, the inner diameter is linearly reduced to 2.5 mm. The 100th and last plate is the DC exit electrode, which constitutes the conductance limit with an inner diameter of 1.5 mm.

To ensure precise alignment, the electrodes of each section were simultaneously cut out of a stack of stainless steel plates by electrical discharge machining. In the same process, the electrode surface was reduced as much as possible in order to lower the capacitance of the ion funnel. The jet disrupter and exit electrode were cut separately. Before mounting, the sharp edges in the conical section of the funnel were removed to prevent discharges.

Pins on the RF electrodes insert into a custom zero-insertion-force (ZIF) connector, which connects the electrodes to a printed circuit board (PCB) (Fig. 2.14). In order to accommodate the circuit on a single PCB, the electrodes of each RF phase are connected to a separate resistor chain of 1 M Ω resistors, which determines the bias of the electrodes and establishes the DC gradient across the funnel. The DC potentials at the funnel entrance and exit (DC_{entrance} and DC_{exit}) are connected to the ends of the resistor chains. The RF (RF(+)) and RF(-) is coupled onto the plates by means of 10 nF capacitors. The DC potentials on the jet disrupter and on the exit electrode are supplied separately.

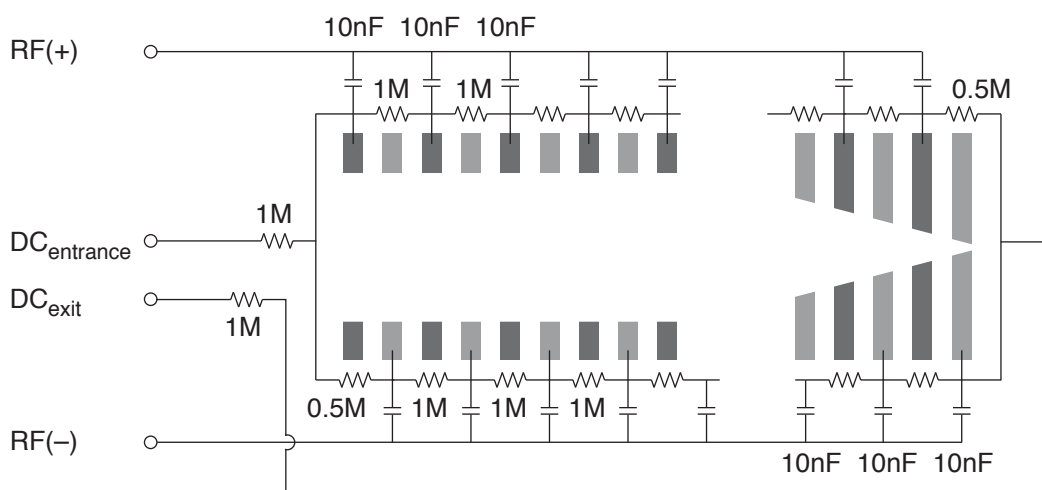


Figure 2.14: Circuit diagram of the in-vacuum PCB of the ion funnel.

The total ion funnel capacitance of 1.77 nF is driven by a 500 kHz RF power supply (CGC instruments) with the same design as for the hexapole (section 2.7.4).¹⁴⁸ The RF amplitude (usually 30–90 V_{0-p}) is determined by an external computer-controlled DC power supply (FuG Elektronik GmbH, NTN 35-35); the voltages at the funnel entrance and exit, on the jet disrupter and the DC exit electrode are delivered by a programmable DC power supply (Spectrum Solutions, TD 1400).

2.8 Ion Detection

Ions are detected with a channel electron multiplier (DeTech, 402-A-H). Positive ions first impinge on the conversion dynode which is usually held at -5 kV. The resulting secondary electrons are attracted to the entrance of the channeltron which is biased to -1.7 kV. In a cascade of impacts, secondary electrons move to the grounded end of the channeltron, where the amplified current is collected.

The high voltages (for positive and negative mode ion detection) are provided from three programmable power supplies (Applied Kilovolts, AK0072 and AK0002). A fast preamplifier (Advanced Research Instruments, COMBO-100) is used that combines a pulse preamplifier with a current amplifier and thus allows for simultaneous analog and counting mode detection.

2.9 Electronics and Data Acquisition

The instrument control/data acquisition system was designed with the objective to computer-control as many parameters and instrument features as possible and make them accessible over a simple user interface. In an experiment with over 100 instrument parameters, this would simplify and speed up the work, ensure the repeatability and reproducibility of experiments and allow for the automation of time-consuming tasks.

Table 2.2 lists the instrument control and data acquisition hardware that is being used. It comprises a PXI (“PCI eXtensions for Instrumentation”) chassis with real time controller and data acquisition cards (National Instruments) and an external delay generator (Berkeley Nucleonics 565), which provides the master clock of the experiment and is used to trigger the lasers.

instrument	function
NI PXI-1044	12-slot PXI chassis
NI PXI-8145 RT	real time controller
NI PXI-6602	8 timers/CTRs (80 MHz), 8 DI/DO
NI PXI-6052E	16 multiplexed AI (16 bit, 333 kS/s), 2 AO (16 bit, 333 kS/s)
NI PXI-6711	4 AO (12 bit, 1 MS/s/channel)
NI PXI-6723 (2x)	32 AO (13 bit, static)
NI PXI-6704	16 AO (16 bit, static)
NI PXI-8430/8	8 serial ports
NI PXI-6132	4 AI (14 bit, 2.5 MS/s/channel)
BNC 565	8 channel delay generator (500 ps resolution)

Table 2.2: Hardware for instrument control and data acquisition, comprising a PXI chassis with real time controller and data acquisition cards and an external delay generator. For multi-purpose data acquisition cards only the main functions are listed. AO (analog output), AI (analog input), DO (digital output), DI (digital input), CTR (counter).

The large number of data acquisition cards alone made it necessary to use the PXI platform, the 12-slot chassis leaving room for future extensions. The real time controller is a dedicated, separate computer that carries out the data acquisition and transfers the data to the host PC, which provides the graphical user interface and displays and stores the data.

The real time operating system on the remote target allows for deterministic code execution. This means that time critical tasks (such as reading out an analog trace before it is overwritten in the following experimental cycle) are carried out with accurate timing, so that, for example, no loss of data can occur. Other tasks (like data transfer or reading back voltages) are then carried out once the time critical tasks have completed. For this purpose, the tasks are assigned priorities, and the real time operating system ensures immediate execution of the task with the highest priority. The programmer then has to make sure that in between the execution of time critical tasks, sufficient time is available to complete the remaining tasks.

The structure of the software, written in LabView 8 (National Instruments), is illustrated in Fig. 2.15. The white boxes in the top row represent programs running on the host PC. They communicate with programs that are executed on the real time controller (grey boxes), which in turn control the hardware resources and perform various tasks for instrument control and data acquisition.

The program is subdivided into several modules that carry out independent tasks. Three separate programs on the host computer provide a graphical user interface for setting static

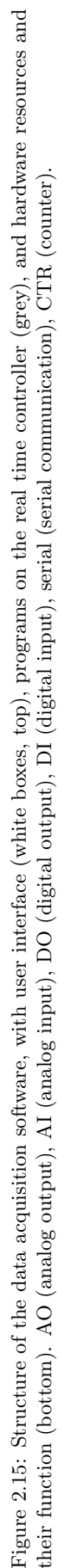


Figure 2.15: Structure of the data acquisition software, with user interface (white boxes, top), programs on the real time controller (grey), and hardware resources and their function (bottom). AO (analog output), AI (analog input), DO (digital output), DI (digital input), serial (serial communication), CTR (counter).

parameters and delays and running different kinds of experiments. A fourth program records and displays the acquired data.

Static parameters All static instrument parameters are controlled from a single window. These include 60 static voltages (delivered by three programmable DC power supplies, Spectrum Solutions, TD 1400), the programmable high voltages for the spray needle and the detectors, the quadrupole and octopole parameters, the RF amplitudes of the ion funnel, hexapole and 22-pole, and the settings for the 22-pole temperature controller (references for the instruments in the corresponding sections). Readbacks are available for most of these parameters as well as for the pressures in the different pumping stages.

Delays All timing parameters are set in a second window, which also provides a graphical representation of the time structure of the experiment. The parameters of the external delay generator are fully controlled over the user interface and transmitted via serial communication. It triggers the lasers and provides the master clock of the experiment. The parameters of the PXI timers are accessible from the same window. They are synchronized to the delay generator and are used for tasks that do not require more accurate timing. These include the switching of voltages on the exit lenses of the hexapole, octopole, and 22-pole with home-built metal-oxide-semiconductor field-effect transistor (MOSFET) switches in push-pull configuration; the helium pulse for the 22-pole; the gates for ion counting and analog detection; and the quenching of the RF on the 22-pole at the end of the machine cycle.

Experiments Four different operation modes of the instrument are currently implemented, which are accessible via the tabs of a third window. A fifth tab serves to display the analog traces of the ion signal and pyroelectric detector (normalization on laser power) for the purpose of testing and adjusting the analog acquisition parameters. It controls a program on the real time controller that accesses the fast analog inputs (AI) of the PXI-6132 card.

The first tab allows the user to record “continuous” mass spectra (*i.e.* no trapping in either of the multipoles) of the ion beam exiting the source. Once the acquisition is started, a program on the controller repeatedly scans the first quadrupole, simultaneously counts the ions arriving on the detector, and transfers the data to the host PC, where the resulting mass spectra are recorded and displayed.

Three further data acquisition modes are designed for experiments with trapped ions. In the simplest and most general case, the ion signal that results for a given set of instrument parameters (and laser settings) is recorded and displayed. This mode is used to optimize operating conditions (*e.g.* optimum static parameters and delays, laser wavelength and beam overlap) and to obtain statistics for a given set of parameters.

In order to determine the fragmentation patterns that result from collision induced dissociation (CID) or laser induced dissociation (LID), a CID/LID scan is performed. While the first

quadrupole selects the mass of the parent ions, the second quadrupole probes a fragment mass and is slowly scanned across a specified mass range in subsequent experiments.

A laser spectrum can be recorded in the laser scan mode. Here, the ion signal is monitored as a function of the laser wavelength with fixed parent and fragment masses.

In these three modes, the data acquisition cycle is synchronized to the master clock (usually 10 or 20 Hz). The ion signal is simultaneously measured by counting and analog detection, and the laser power can be recorded by the integrating the signal of a pyroelectric detector. A shot-to-shot normalization on the number of parent ions can be performed by switching the second quadrupole between fragment mass (“on cycle”) and parent mass (“off cycle”) in alternating experiments. A digital input (DI) uses a signal from the external delay generator to determine the cycle, and the mass command of the second quadrupole (as given by an analog output, AO) is changed accordingly. The communication with the lasers is performed via serial ports and digital lines. At the end of each experiment, the user is prompted to save the acquired data together with the various experimental parameters.

2.10 Characterization

2.10.1 Determining the Number of Trapped Ions – Detector Saturation

One of the major differences between the first-generation tandem mass spectrometer setup of our research group⁵⁰ and the instrument, which is described in this chapter, is the incorporation of an ion funnel (see section 2.7.5). The expected improvement in ion transmission by an order of magnitude would render the experiment more sensitive and make studies possible that were previously not feasible due to the limited signal to noise. One of our first goals was therefore to establish the number of ions that could be trapped in the 22-pole within a 10 or 20 Hz cycle, which corresponds to the repetition rate of our lasers.

On the other hand, an increased number of ions in the 22-pole could potentially cause space charge to push ions into the outer regions of the trap, where RF heating occurs, leading to a higher ion temperature.¹⁴⁹ Determining the number of ions in the 22-pole was therefore also necessary in order to verify if these effects could be relevant in our setup.

The amino acid tyrosine was used for test experiments, and the protonated species ($m/z = 182$) was monitored. With the previous setup, 10'000 to 20'000 ions could typically be counted in a 50 ms cycle. However, with the new setup, only $\sim 12'000$ counts were obtained in the initial experiments, despite extensive efforts to optimize ion transmission.

We subsequently switched to a preamplifier (Advanced Research Instruments, COMBO-100, section 2.8) that allows for simultaneous analog detection and counting in order to verify whether detector saturation could be playing a role. Figure 2.16 shows a scatter plot of the integrated analog signal versus the counts per ms that were simultaneously measured on the second detector for a continuous ion beam and various ion currents. In this experiment, ions

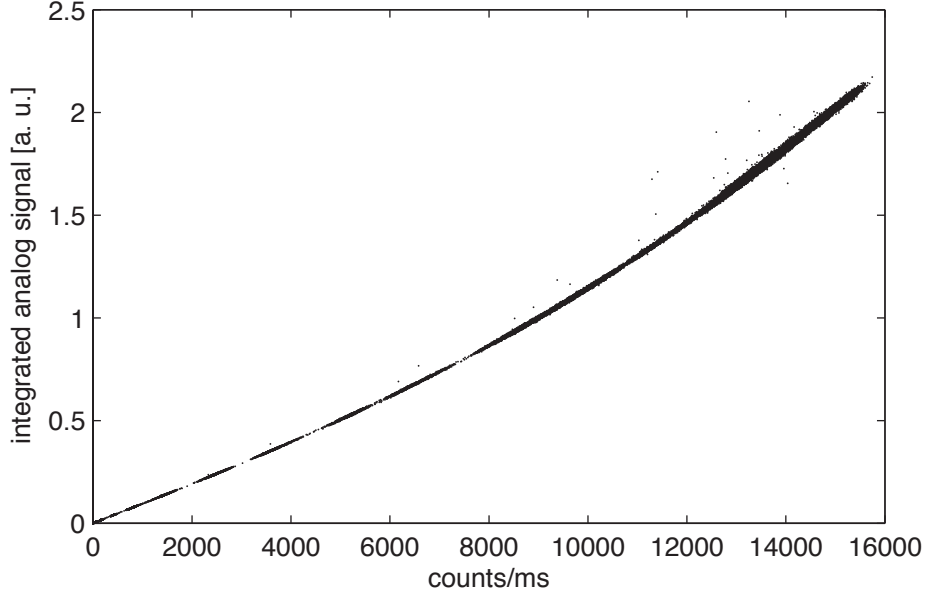


Figure 2.16: Analog ion signal versus ion counts per ms for a continuous ion beam.

were not trapped in either the hexapole or octopole, but gated with the octopole exit lens. The ions that arrived on the detector within a 35 ms window were counted, and the corresponding analog signal was integrated. The ion current was varied by changing the jet disrupter voltage.

Up to 5000 counts per ms, both signals are proportional in good approximation. For higher ion currents, however, the slope of the curve increases, indicating that in counting mode, too few events are detected in order to account for the measured current in the channeltron.

This effect is expected due to the limited pulse pair resolution of the counting preamplifier of 20 ns (50'000 counts per ms). Even at lower rates of 5000 counts per ms, a certain probability exists that two ions will arrive within 20 ns and will only be counted as a single event. For higher count rates, this probability increases, leading to observed behavior.

When ions are released from an ion trap as a dense package, the effect should be even more severe. Figure 2.17 shows the same correlation of integrated analog signal and ion counts for ions that were trapped in the octopole (3.35×10^{-4} mbar helium pressure), periodically released in a 2 ms long package, and detected on the second detector. Again, the number of trapped ions was varied by changing the jet disrupter voltage. Most notably, the number of counts shows a maximum at about 36'500, while an even higher analog signal leads to a lower number of detected events. It appears that this behavior is observed when ions arrive on the detector with such a high frequency that several consecutive events will be counted as only one, even though they occur over a time span longer than the minimum pulse pair resolution. This is the case if during a train of pulses, the current is permanently above the detection threshold, so that the pulses appear like a single long pulse.

Since the ion counts go through a maximum, it becomes impossible to calibrate the analog signal such that the true number of ions arriving on the detector could be calculated. The ion

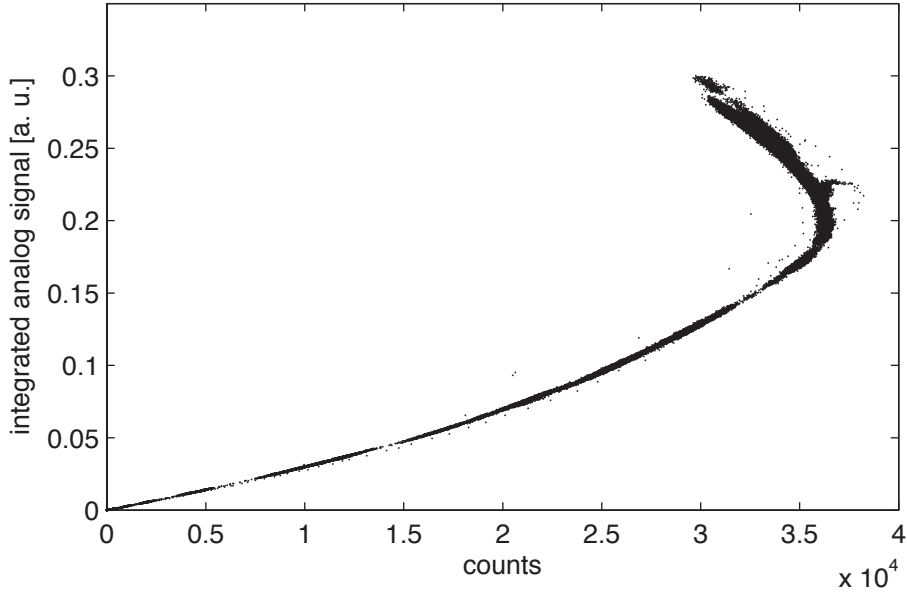


Figure 2.17: Analog ion signal versus number of ion counts for a 2 ms ion package released from the octopole.

package leaving the 22-pole typically has a width of 1–2 ms. If one could stretch this package out over a much longer time span, an accurate count could be obtained. Attempts to find parameters that would generate stretched-out ion packages initially failed and succeeded only after the entire section between the second and third bender was carefully realigned. With long ion pulses spanning 30–40 ms, counts of $\gtrsim 100'000$ ions trapped in the 22-pole in a 20 Hz cycle could be achieved, which demonstrated indeed the signal levels we were hoping to achieve.

Figure 2.18 compares the analog signal from a short ion package ejected from the 22-pole (left) to the signal from a long ion package (right) recorded with a digital oscilloscope (LeCroy WaveSurfer 24Xs-A). In a 250 ms cycle, the ions were pre-trapped in the octopole, injected into the 22-pole (~ 4 K), stored for 3 ms, and released.

Long pulses were generated by using a low RF amplitude of ~ 50 V_{0-p}, setting the second and third lens following the 22-pole to -400 V, and raising the “open voltage” on the 22-pole exit lens until the maximum number of counts could be obtained in a 150 ms detection window. All remaining parameters of the elements following the 22-pole were optimized for maximum signal.

These long pulses actually consist of a sequence of discrete ~ 0.5 –1 ms long packages. Within the first 40 ms, they appear with a regular period of 3.5 ms, while at later times, they arrive more randomly. This could point to coherent axial ion motion, which has previously been reported for ions in an octopole trap.¹⁶⁴ However, since the ion signal is very sensitive to the stability of the voltage on the exit lens as well as to some other parameters, this pattern could also simply reflect electronic noise.

Figure 2.19 compares the ion signal obtained with a short and a long ion package in both

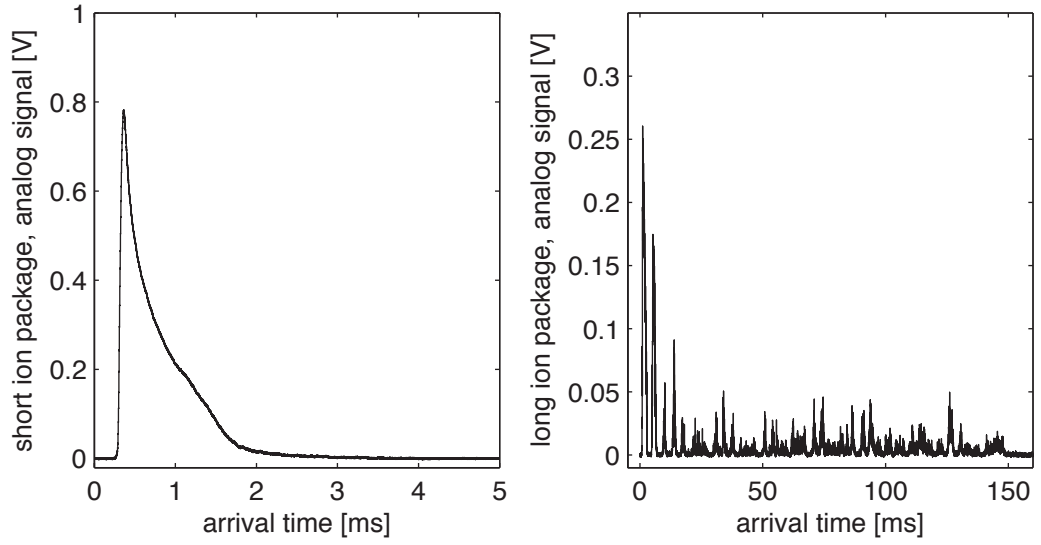


Figure 2.18: Analog signal of a short ion package (left) and a stretched-out ion package (right) released from the cold 22-pole.

counting (top) and analog mode (bottom). In this experiment, the ion current was again varied by means of the jet disrupter voltage and alternately recorded with the settings optimized for a short or a long ion package.

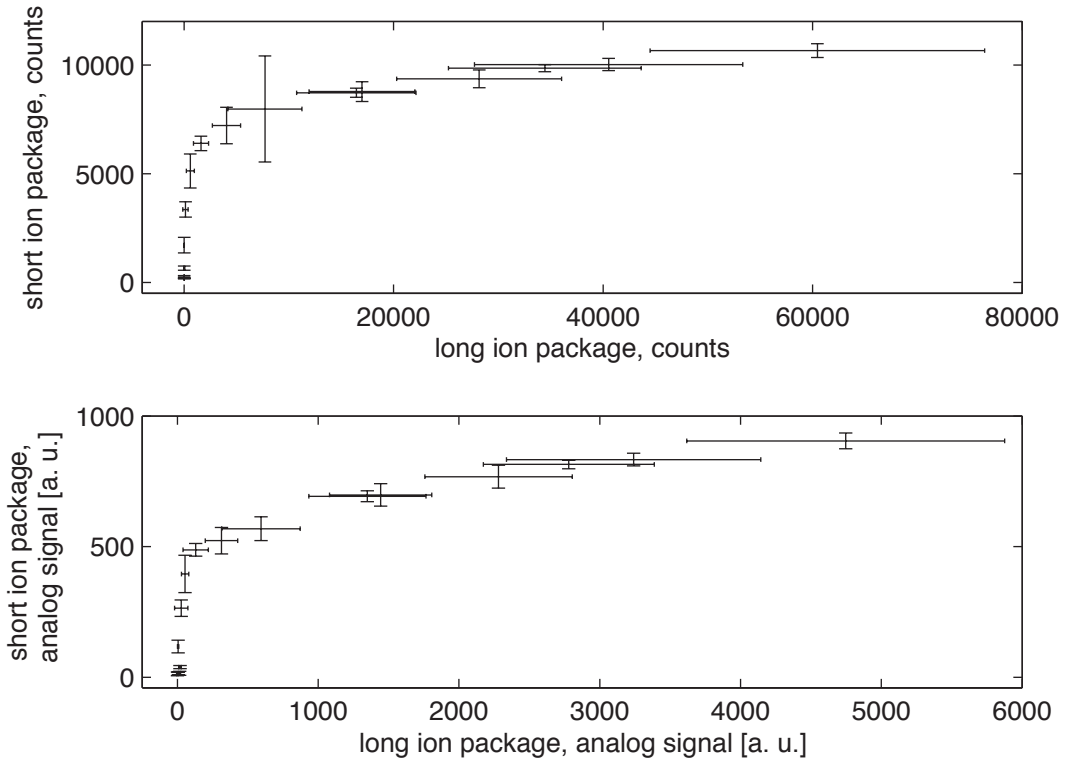


Figure 2.19: Signal level of a short ion package versus signal level of a long ion package released from the 22-pole in counting and analog detection mode.

Both curves show a similar behavior. At low ion currents, the signal measured with a short package is 5–10 times as large as the signal of a long package, indicating a low extraction

efficiency in long pulse mode, which is probably due to the low velocities at which the ions initially exit the 22-pole. This also means that the count numbers obtained in long pulse mode represent lower limits for the number of ions stored in the 22-pole.

At larger ion currents, the signal recorded with a short ion package starts to level off. Since the same behavior is also observed in the analog trace, this strongly suggests that at high ion numbers and with short pulses, the channeltron itself starts to saturate. Unlike in Fig. 2.17, the counting signal does not go through a maximum, indicating that ions were arriving on the detector with a lower maximum frequency than in the previous experiment.

In summary, this section discussed the technical difficulty of accurately determining the number of ions stored in the 22-pole, which is due to different saturation effects. The counting signal saturates as soon as the ions arrive at the detector with a frequency higher than the count rate of the preamplifier. Analog detection can circumvent this problem. However, when ions are ejected from the 22-pole in a narrow package, evidence is found for the saturation of the channeltron. Releasing the ions in a stretched-out ion package can avoid this problem. The significantly higher ion numbers which are obtained with this approach, however, only represent a lower limit for the number of ions stored in the 22-pole, since under these conditions the extraction of the ions is less efficient than with a short pulse.

The practical implication of these findings is that saturation affects the reading for the parent ion signal and can render it difficult to optimize parameters for maximum ion transmission. However, for the detection of a small number of laser induced fragments, these considerations do not play any role. For a small number of ions, the highest count numbers are recorded when a short ion package is used.

2.10.2 Low-Mass Cut-Off of the Ion Funnel

As detailed in section 2.7.5, ion funnels have been shown to possess a lower-mass cut-off, and the origins of the observed mass discrimination have been investigated. The design of the ion funnel implemented in this setup was specifically chosen to avoid this flaw, so that studies of low molecular weight species could be conducted with a similar sensitivity. While it is difficult to obtain quantitative information about the transfer efficiency of different masses in the ion funnel, the following experiment was carried out to yield at least some qualitative insight.

Figure 2.20 shows the mass spectrum of a solution of a mixture of primary amines RNH_2 in methanol, with R = methyl, ethyl, *n*-propyl, *n*-butyl and *n*-hexyl. The spectrum was obtained by scanning the first quadrupole and detecting a continuous signal on the first channeltron detector.

It was found that the signal intensity of the different masses depends on the choice of several parameters, especially the ion funnel and hexapole RF amplitudes. However, as the spectrum in Fig. 2.20 demonstrates, suitable parameters can be found so that a wide range of masses down to $m/z \approx 40$ can be transmitted with good efficiency, while ions with $m/z \approx 30$ can at

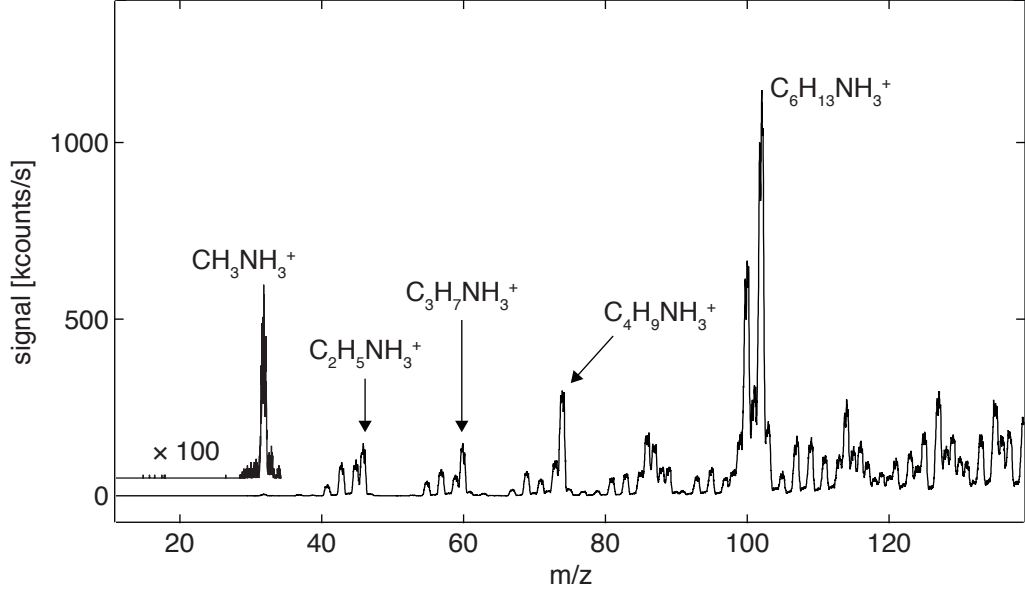


Figure 2.20: Mass spectrum of a mixture of protonated primary amines, demonstrating the transmission of low masses through the ion funnel.

least be detected.

2.10.3 Ideas for the Normalization on Parent Ion Signal

Shot-to-shot variations of the parent ion signal arise mainly from instabilities of the nano-ESI source and, to a lesser extent, from electronic noise and mechanical vibrations induced from the operation of the cold head. In order to account for these fluctuations, UV spectra are usually recorded such that in successive machine cycles, the parent and fragment ions are alternately monitored. The UV signal S_{UV} is obtained by dividing the fragment signal recorded in one cycle $S_{\text{fragment}}^{\text{cycle 1}}$ by the number of parent ions detected in the subsequent cycle $S_{\text{parent}}^{\text{cycle 2}}$

$$S_{UV} = \frac{S_{\text{fragment}}^{\text{cycle 1}}}{S_{\text{parent}}^{\text{cycle 2}}}. \quad (2.34)$$

For IR/UV depletion experiments, a similar scheme is employed. Here, the fragment mass is monitored in both cycles, while the IR laser is only fired in every other cycle. The depletion signal $S_{\text{depletion}}$ is obtained as the difference of the ion count in both cycles $S_{\text{IRon}}^{\text{cycle 1}} - S_{\text{IRoff}}^{\text{cycle 2}}$ normalized to the UV-only signal $S_{\text{IRoff}}^{\text{cycle 2}}$

$$S_{\text{depletion}} = \frac{S_{\text{IRon}}^{\text{cycle 1}} - S_{\text{IRoff}}^{\text{cycle 2}}}{S_{\text{IRoff}}^{\text{cycle 2}}}. \quad (2.35)$$

Obviously, it would be advantageous to record parent and fragment ions in the same shot, which is not possible with a quadrupole mass analyzer. However, by extracting the ions simultaneously out of both ends of the 22-pole, one can record the fragment ion count on the third detector and the parent ion intensity on the second detector within the same cycle. If the partitioning of the ions between both detectors does not fluctuate, the normalized UV signal

can be calculated from the signals on the second detector $S_{\text{det } 2}$ and on the third detector $S_{\text{det } 3}$ in the same cycle as

$$S_{\text{UV}} = \frac{S_{\text{det } 3}}{S_{\text{det } 2}}. \quad (2.36)$$

The depletion signal can be obtained from the signals in alternate cycles with IR laser $S_{\text{det } 2,3}^{\text{cycle } 1}$ and without $S_{\text{det } 2,3}^{\text{cycle } 2}$ as

$$S_{\text{depletion}} = \frac{S_{\text{det } 3}^{\text{cycle } 1}}{S_{\text{det } 2}^{\text{cycle } 1}} - \frac{S_{\text{det } 3}^{\text{cycle } 2}}{S_{\text{det } 2}^{\text{cycle } 2}}. \quad (2.37)$$

In order to test this idea, protonated tyrosine ions were stored in the 22-pole at room temperature and then released from both ends. For this purpose, the voltage on both end cap electrodes was simultaneously lowered to the same potential such that a long ion package could be recorded on both detectors using analog detection in a 30 ms window. It should be noted that no laser induced fragments were generated. Instead, the parent ion signal was recorded on both detectors. With Eqn. 2.36, one should obtain a constant value that corresponds to the partitioning of the ions between the two detectors, while with Eqn. 2.37, one should obtain zero under ideal conditions. The same experiment was repeated with the usual detection scheme, allowing for the same acquisition time and, likewise, using a long ion package. Here, the signals were obtained from Eqns. 2.34 and 2.35.

As a measure of the signal to noise ratio, table 2.3 lists the standard deviations of the signals $\sigma(S_{\text{UV}})$ and $\sigma(S_{\text{depletion}})$ normalized to the average signal $\langle S_{\text{UV}} \rangle$ for the usual acquisition mode (“normal”) and the acquisition mode using two detectors (“two detectors”).

	normal	two detectors
$\sigma(S_{\text{UV}})/\langle S_{\text{UV}} \rangle$	7.6%	9.6%
$\sigma(S_{\text{depletion}})/\langle S_{\text{UV}} \rangle$	7.6%	13%

Table 2.3: Signal to noise ratios for two different acquisition modes, using one detector (“normal”) or two detectors (“two detectors”) for the normalization on parent ion signal.

As can be seen, detecting parent and fragment ions simultaneously on two different detectors is unfortunately afflicted with an even higher noise level. Obviously, the fact that twice as many data points can be recorded in the same amount of time when two detectors are being used is more than compensated by the smaller number of ions that reach either detector. Moreover, it appears that the signals recorded simultaneously on both detectors do not correlate well, which is probably due to electronic noise that affects the partitioning. As noted above, when long ion packages are released from the 22-pole, the signal level is particularly sensitive to small changes in the parameters, especially the exit lens voltage.

At 4 K, even larger fluctuations of the relative signals on both detectors were observed. The situation could slightly be improved when a high voltage on one of ring electrodes of the 22-pole was used to split the ion cloud into two physically separated packages before ejection. However, the increase in the noise level was still more pronounced than reported in table 2.3 for the analogous experiment at room temperature.

In summary, while the suggested scheme of detecting parent and fragment ions at the same time can easily be put into practice, it does not offer an advantage under the current experimental conditions. Obviously, the shot-to-shot fluctuation of the signal has an important contribution from electronic noise, especially when long ion packages are used to avoid detector saturation. However, unlike for fluctuations of the number of ions stored in the 22-pole, this kind of noise will become even more important in the proposed scheme.

2.10.4 22-Pole Trapping Time

Figure 2.21 displays the signal of protonated tyrosine ($m/z = 182$) as a function of the trapping time in the 22-pole at room temperature. In this experiment, ions were accumulated in the octopole during a 5 s machine cycle. Subsequently, a package of reduced intensity was injected into the 22-pole. After they had been stored for a variable amount of time, the ions were counted in a long ion package optimized to fill a 350 ms window in order to limit saturation effects. The 22-pole was operated with an amplitude of ~ 50 V, while 3.2 and 5.5 V were applied to the entrance and exit lens, respectively.

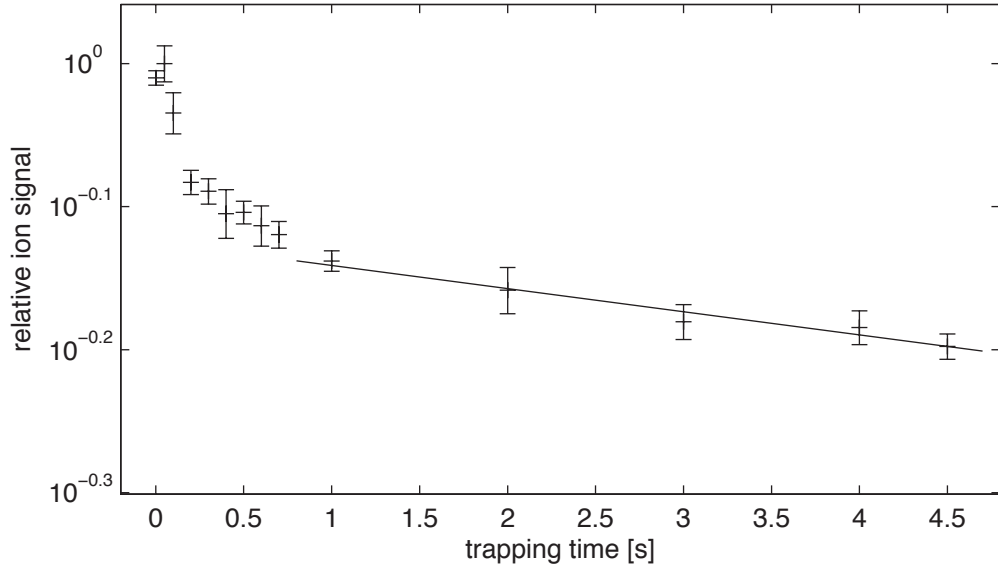


Figure 2.21: Ion signal of protonated tyrosine as a function of storage time in the 22-pole. From the fit for times > 1 s, a $1/e$ time of 26.8 ± 3.1 s is determined.

The signal drops sharply within the first ~ 500 ms to about 80% of its initial value. The 22-pole is initially loaded with about 180'000 ions so that it can be expected that the signal is slightly saturated for short times. It is possible that the initial drop reflects ion losses due to an overfilling of the trap. However, a similar time dependence has also been observed in the previous instrument, where the number of stored ions is generally smaller.¹⁶⁵ For times > 1 s an exponential decay is observed, and a $1/e$ trapping time of 26.8 ± 3.1 s can be determined, which indicates the correct alignment and functioning of the trap.

2.10.5 Determination of the Ion Temperature

When protonated tyrosine ions ($m/z = 182$) are stored in the 22-pole at 4 K, the formation of helium clusters can be observed (Fig. 2.22, bottom), which already points to a low internal energy of the ions.¹⁶⁵

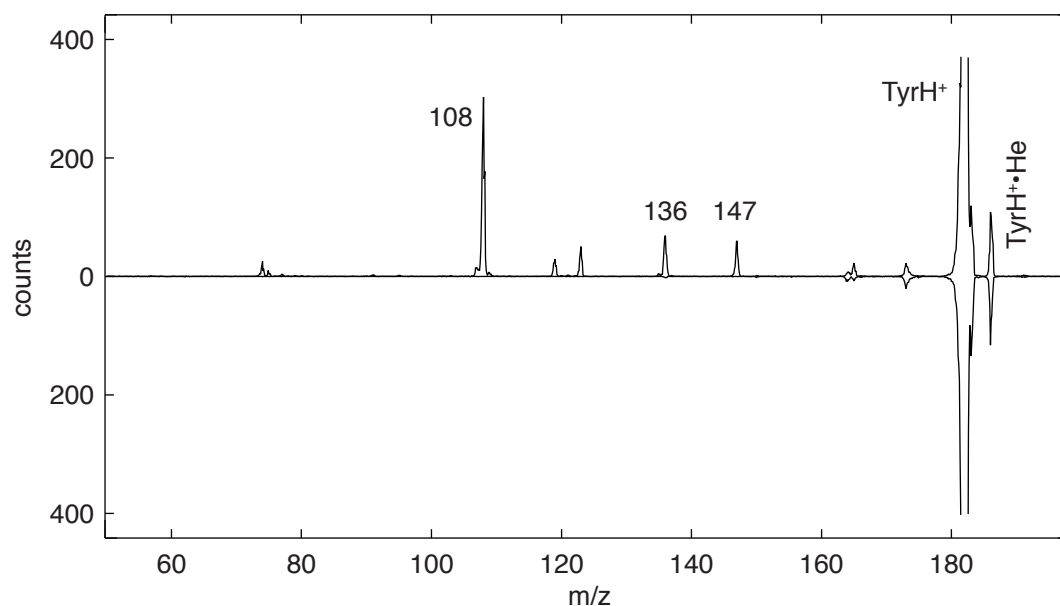


Figure 2.22: Mass spectra obtained when protonated tyrosine is stored in the 22-pole at 4 K (bottom) and after laser irradiation at 35081 cm^{-1} (top).

In order to determine their temperature more precisely, the UV spectrum of protonated tyrosine was recorded.¹¹³ Irradiation at 35081 cm^{-1} (the band origin of conformer A in the nomenclature of reference¹¹³) produces a range of fragment ions (see Fig. 2.22, top). Thanks to the better sensitivity in this experiment, it is now possible to accurately determine the mass of the dominant channel as $m/z = 108$, which corresponds to the protonated side chain radical, while $m/z = 107$ ¹¹³ is also observed, although with much lower intensity.

The UV spectrum recorded while monitoring $m/z = 108$ is depicted in Fig. 2.23. It agrees well with the previously published spectrum,¹¹³ and the band origins or conformers A–D are labeled as assigned there. Hot band transitions of conformers A and B, labeled A_1^0 and B_1^0 , can be observed 40 cm^{-1} and 46 cm^{-1} to the red of the respective band origins. Under the assumption that a hot band and the first progression band of the same vibration have similar Franck-Condon factors, their intensity ratio can be used to estimate the ion temperature from a Boltzmann distribution. Here, a vibrational temperature of $\sim 10\text{ K}$ is obtained. Evidently, despite the large number of ions stored in the 22-pole ($\sim 10^5$), space charge induced heating of the ion cloud¹⁴⁹ does not yet limit the achievable ion temperature. Spectra measured with a reduced number of parent ions regularly show comparable temperatures.

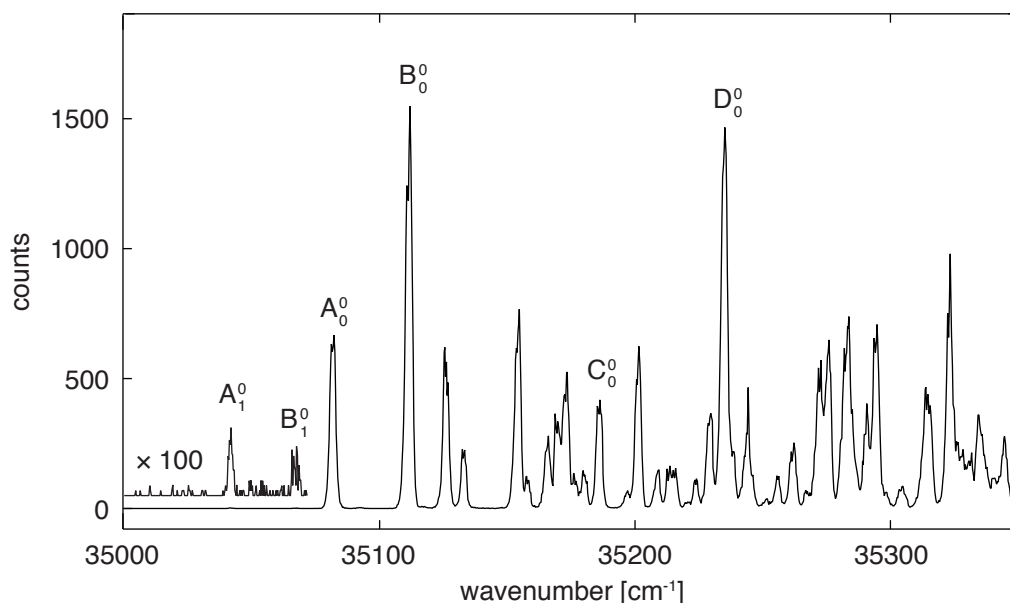


Figure 2.23: UV spectrum of protonated tyrosine recorded in the $m/z = 108$ fragment channel.

2.11 Conclusions and Outlook

This chapter described the development and characterization of a new tandem quadrupole mass spectrometer for the spectroscopy of cold, gas-phase biomolecular ions. The most important results are summarized in the following, and an outlook for possible future developments of the setup is given.

It was shown that the implementation of an ion funnel led to an improvement of the sensitivity of the instrument. Specifically, the recorded ion counts were about one order of magnitude higher than those that have been reported for the previous setup. (It is, however, not clear whether the count numbers observed there are equally affected by detector saturation.) At the same time, the low-mass cut-off of the ion funnel was determined to set in at $m/z \approx 40$, which is lower than necessary for the study of most biologically relevant molecules.

Difficulties were encountered to accurately determine the large number of ions stored in the 22-pole during one experimental cycle due to detector saturation. By stretching out the ion package leaving the 22-pole, saturation effects can be reduced. This way, a lower estimate for the number of trapped ions could be obtained.

The determination of the ion vibrational temperature from the UV spectrum of protonated tyrosine yielded ~ 10 K, about 2 K lower than in the previous setup. This finding also demonstrates that the temperature of the protonated tyrosine ions is not yet affected by space charge induced RF heating, despite their large number ($\geq 100'000$).

The instrument has proved easy to use in everyday operation. This includes the facile servicing of the 22-pole and the cleaning of the source, where the gate valve is of great practical value. (While the design does not allow us to vent the source separately, it is possible to evacuate

the high vacuum section of the machine independently, when both parts are initially at atmospheric pressure.) The software interface provides a simple overview and an easy control of the vast majority of the experimental parameters and allows one to modify or reload settings and to control experiments with a mouse click. Operating conditions have generally been found to be very stable and reproducible.

Chapter 3 describes the addition of a planar trap/TOF mass spectrometer to the instrument, which will in the future allow one to routinely record TOF spectra of parent and fragment ions. As will be argued there, this device also has the potential to replace the 22-pole entirely and greatly simplify the setup.

Experiments using the FAIMS ion mobility filter have not yet been carried out with this setup. However, for ultimate resolution, the addition of a classical ion mobility drift tube appears as the logical next step.

Chapter 3

Development of a Planar Multipole Ion Trap Time-of-Flight Mass Spectrometer

3.1 Motivation and State of the Art

The tandem quadrupole mass spectrometer described in chapter 2 was designed with the goal in mind to later add a time-of-flight (TOF) mass spectrometer¹⁶⁶ to the instrument. When ions are released from the 22-pole in a package that is typically several hundred μs long, only a single mass can be detected in the second quadrupole, while TOF mass analysis of the ion population in the 22-pole could potentially yield the entire mass spectrum at once. The benefits of the multiplexing capability of TOF mass spectrometry for the purpose of cold ion spectroscopy are immediately evident if one, for example, considers the large number of different UV photofragments of larger peptide ions¹²⁰ and the fact that the fragmentation pattern can be conformer-specific.¹¹³

TOF mass spectrometers are popular, as they can provide good mass resolution over a large mass range and good ion transmission, while their construction and operation are comparably simple.¹⁶⁷ While this made a TOF analyzer the obvious choice for our application, it is challenging to record a TOF mass spectrum of the population of a multipole ion trap with both good resolution and detection efficiency, as will be discussed in the following.

TOF mass spectra of ions ejected from the 22-pole When ions are ejected through the exit lens of a linear ion trap, they are all imparted with (roughly) the same energy, and consequently, different masses will reach a detector placed at a distance at different times. However, only a moderate mass resolution can be obtained with this approach, since the ions start with a large spatial distribution inside the trap, and the necessarily inhomogeneous extraction fields do not allow for good space focusing. A resolution of $m/\Delta m = 5 - 10$ was obtained when ions were simply released from a linear quadrupole trap,¹⁶⁸ and for ions ejected from a 22-pole and

a ring electrode trap, linear TOF mass spectra could be recorded with a resolution of 40 and 50, respectively.^{132, 169} In all three experiments, the ion cloud was compressed at the exit of the trap before ejection in order to improve resolution.

Multipass reflectrons Even when ion extraction leads to a broad ion package, a high resolution could be obtained if a considerably longer flight path could be realized. This is the principle of multipass reflectrons,^{170–174}

which achieve an increase in mass resolution by reflecting ions multiple times in between two ion mirrors. One realization of such a multipass reflectron, consisting of two opposite ion mirrors and two Einzel lenses in between, is frequently termed Zajfman trap.¹⁷⁵ With these devices, “self-bunching” of the ion cloud was observed to occur under certain operation conditions. It results from the Coulombic interaction of the ions and prevents the dephasing of the circulating ion packages even after prolonged storage, so that resolutions up to $\sim 140'000$ could be obtained.^{176–179}

Wester and co-workers recently employed such a trap to record high resolution TOF mass spectra of ions ejected from a 22-pole.¹⁸⁰ A drawback of this elegant solution lies in the low trapping efficiencies that result unless ions are injected in a narrow, well-collimated beam.¹⁸¹ Furthermore, when the trap is opened in order to release ions onto a micro channel plate (MCP) detector, different masses may have completed a different number of round trips. Consequently, ions of higher and lower mass can appear in the spectrum at similar times. Multi-pass reflectrons or the alternative multi-turn instruments¹⁸² represent a general tool to improve the TOF mass resolution that can be obtained with a limited available flight path length in any instrument.

Orthogonal acceleration While an ion beam released from a multipole trap necessarily has a large spatial and velocity spread in the extraction direction, it can have a small diameter and be well collimated. Consequently, TOF extraction orthogonal to the flight direction of the beam should improve the resolution. Since the ion package leaving the trap is long compared to the typical size of a TOF extraction region, this approach resembles the task of sampling a continuous ion beam, which is a much studied problem of TOF mass spectrometry. Indeed, orthogonal acceleration^{183, 184} is the method of choice to obtain TOF mass spectra of (semi-) continuous ion beams as they are produced, for example, in ESI sources^{185, 186} or ion mobility measurements with drift tubes.⁴³ Frequently, a quadrupole guide or mass filter precedes the extraction region of the TOF. The corresponding instruments are sometimes referred to as qTOF devices.¹⁸⁷ Using orthogonal acceleration, commercial reflectron instruments obtain a resolution of up to $40'000$.¹⁸⁸

The high mass resolution, however, comes at the expense of the ion utilization efficiency, since ions that pass the extraction region while a TOF spectrum is being recorded will be lost. A 3 eV ion beam of 100 amu ions, for example, travels at a speed of about 2.4 km/s. During the

time of flight of $100\ \mu\text{s}$, it traverses a distance of about 24 cm. With a large extraction region of 2.5 cm diameter, a duty cycle of $2.5\ \text{cm}/24\ \text{cm} \approx 10\%$ results. Working with slower ion beams could in principle enhance the duty cycle, but constitutes a challenge in itself.

Multiplexing techniques Multiplexing techniques like Fourier transform¹⁸⁹ or Hadamard transform TOF mass spectrometry^{190,191} have been suggested, the latter of which has been explored more thoroughly. Here, a continuous ion beam is modulated with a pseudo-random on-off-sequence, and the TOF spectrum is reconstructed from the complex signal that results through an inverse Hadamard transformation. While this technique makes better use of the available ions and thus leads to a gain in signal, it also introduces transform noise, which would reduce the sensitivity of our experiment, which frequently relies on the background-free detection of a few UV fragments. Moreover, while the ion beam ejected from a 22-pole trap is typically only several hundred μs long, it changes its composition over time, since light ions travel faster and reach the extraction region earlier, which will increase the noise in the reconstructed spectrum.¹⁹²

Synchronized ejection of short ion packages and TOF extraction If an ion package released from an ion trap is too long to be efficiently sampled with orthogonal extraction, it appears that injecting several shorter packages into the extraction region could solve the problem. Such a scheme has, for example, been implemented for qTOF instruments.^{187,193} However, as mentioned above, mass separation of the ions inevitably occurs on their way to the extraction region, so that a mass window is observed, which depends on the relative timing of ion ejection and extraction. While a 100% duty cycle can be achieved for a single species for which the timing has been optimized, other masses may even be absent from the spectrum.

Two schemes were reported that alleviate this problem by mass-selectively ejecting ions from a linear quadrupole in the axial direction. In the first case, a quadrupolar DC potential is created along the axis of the ion trap, so that a specific mass can be resonantly ejected, trapped in a second quadrupole, and separately injected into a TOF analyzer, which is synchronized to the arrival of this specific mass.¹⁹⁴ In the second approach, an effective RF potential is created at the exit of a linear quadrupole, which prevents the ions from escaping. When this axial trapping potential is ramped down, heavier ions are ejected before the lighter ones because of the inverse dependence of the effective potential on the mass (Eqn. 2.22). If the ramp is properly adjusted, heavy and light ions reach the extraction region at the same time.

Both methods are complicated, since they essentially include a mass selection step that precedes the recording of the TOF spectrum. Careful consideration also shows that for the second approach, it will be technically challenging to focus all masses simultaneously to a small volume within the extraction plates in order to obtain a good resolution and detection efficiency.

Quadrupole ion trap TOF mass spectrometers If ions could be accumulated within the extraction region — or in other words if the extraction region could be used as an ion trap — all masses could indeed be focussed to a small volume prior to extraction. While linear multipoles provide poor extraction fields, as noted above, the Paul trap^{195,196} has successfully been employed as an “ion trap storage/time-of-flight mass spectrometer”.¹⁹⁷ Commercial instruments achieve resolutions of up to 12’000 in reflectron mode.¹⁹⁸ These hybrid instruments have successfully been coupled with a wide range of ionization techniques, such as laser ionization,¹⁹⁹ electron impact (EI) and chemical ionization (CI),²⁰⁰ glow discharge,²⁰¹ ESI,²⁰² and matrix assisted laser desorption ionization (MALDI).²⁰³ The RF is usually applied to the ring electrode, while the extraction pulse is applied to the end caps. A higher resolution is obtained in bipolar mode, *i.e.* for positive ions, a positive pulse is applied to the “repeller”, and a negative pulse is applied to the “extractor” end cap electrode, which improves the homogeneity of the extraction fields.^{200,204,205}

As the Paul trap does not possess a field-free region, the ion cloud changes its shape and its velocity distribution during the RF period,²⁰⁶ so that the extraction efficiency and resolution depend on the RF phase.^{197,200,207} In order to avoid this effect, the RF is shut down before the extraction pulse is applied. However, residual RF oscillations can still lead to peak broadening.^{151,200} When the extraction pulse is delayed with respect to the clamping of the RF, the amplitude of these oscillations and their detrimental effect on the resolution can be reduced. After the RF is switched off, the ion cloud expands, which also decreases the resolution, so that a compromise has to be found that balances both effects.²⁰⁵

The absence of a field-free region in the Paul trap also causes RF heating and increases the velocity spread of the ions prior to extraction, leading to a decrease in resolution.¹¹² For ions stored at room temperature with helium as a buffer gas, translational temperatures of 1180–1690 K have been measured.¹⁵¹

The achievable resolution is furthermore limited by the inhomogeneity of the extraction fields, which is a consequence of the trap geometry. Along the trap axis, ions experience a variation of the field strength which leads to a different space focus for different masses and a stronger dependence of the flight time on the axial position of the ion at the moment of extraction.²⁰⁵ Furthermore, curved equipotential lines inside the trap lead to different times of flight for ions originating from different radial positions.²⁰⁴

Homogeneous extraction fields can be achieved in a cylindrical ion trap in which the ring electrode is replaced by two flat rings (to which the RF is applied) and the end caps consist of flat plates.²⁰⁸ The trapping fields resemble those of a Paul trap, but also contain contributions from higher order multipoles. The ions are stored in the center of the trap in between the two rings. Since all electrodes are flat, homogeneous extraction fields can be achieved when separate high voltage pulses are applied to all four electrodes.

This electrode geometry, however, shares another drawback with the Paul trap/TOF mass

spectrometers, which severely restricts its utility for our application. Externally generated ions are usually injected axially, *i.e.* through a hole in one of the end caps.²⁰⁹ With the RF present on the ring electrode, most ions are either reflected before they enter the trap volume or cannot be decelerated in collisions with the trapping gas and are lost. Efficient trapping can only be achieved in a narrow window of RF phases that depends on the ion kinetic energy.²⁰⁵ Moreover, the trapping efficiency is mass dependent.²¹⁰

Trapping efficiencies of 3%²¹¹ (the value representing an upper limit, as ions were neglected that are reflected before entering the trapping volume²¹²) and 1-5%²¹⁰ have been measured. It was calculated that a continuous ion beam can be trapped at 1 mTorr helium pressure with an efficiency 0.2%, while near 100% efficiency was obtained at 10 Torr.²¹³ However, such high pressures are difficult to realize and will degrade the TOF resolution.²¹⁴ Another numerical study found a trapping efficiency of 3% for 100 amu ions at 1.5 mTorr helium pressure and of 23% for 1522 amu ions.²¹⁵

It was also suggested to inject 280 ns long ion pulses that are synchronized to the RF while applying a short decelerating DC pulse to the entrance end cap electrode. A 100% trapping efficiency was calculated for this method with parameters optimized for a specific mass, while a mass window is observed for the simultaneous injection of several different masses.²¹³ Moreover, achieving such a sequence of short ion pulses with ions ejected from a 22-pole meets obvious experimental difficulties.

Higher efficiencies can be obtained if the RF is ramped up during injection²¹⁶ or is allowed to even overshoot its final amplitude (“matched dynamic trapping”).^{211,217} However, the dependence of the injection efficiency on the RF phase and ion kinetic energy cannot be completely eliminated.²¹² For matched dynamic trapping of a short ion package generated by MALDI, an efficiency of 39% was reported,²¹¹ which likewise should be considered an upper limit.²¹² Moreover, one should note that this technique is only applicable for ion pulses that are considerably shorter than the time required for ramping up the RF, which is on the order of 200 μ s.²¹¹

Radial extraction out of linear multipoles The low duty cycle is the major drawback of a scheme in which a Paul trap is used to pretrap ions released from the 22-pole and then extract them in order to obtain a TOF spectrum. In linear multipoles, on the other hand, ions can be trapped with near 100% efficiency at moderate pressures,²¹⁸ while the mass discrimination is much less pronounced.²¹⁹ This difference can be explained in terms of the region of low field on the axis of a linear multipole. Ions injected along this axis will mostly travel in this low-field region as they are guided to the DC exit electrode and reflected, which gives them sufficient time to lose their kinetic energy in collisions. In contrast, in a 3D quadrupole trap ions necessarily start out in a region of strong oscillating fields. Under these conditions trajectories, that lead to successful trapping, exist only in a narrow window of initial RF phases.

The C-trap²²⁰ is a c-shaped quadrupole trap which is used to inject short ion packages into

an orbitrap mass analyzer. Ions are injected into the trap along its axis, accumulated, focused to the center of the trap, and extracted in the radial direction. Passing through a hole in the innermost of the curved quadrupole rods, they reach the entrance of the orbitrap as a narrow package.

It is, however, conceivable that using a linear multipole as the extraction region of a time-of-flight analyzer would be accompanied by certain disadvantages. Even if the multipole rods are sandwiched by a set of extraction plates,²²¹ inhomogeneous extraction fields will result because of the finite width of the multipole rods.

Concluding remarks In this section, I have given an overview of existing experimental techniques that could be used to obtain a TOF spectrum of the ion population of a 22-pole ion trap. Achievable resolution and detection efficiency restrict the utility of most of these methods for our purposes, as has been argued above. This chapter describes the development of a novel hybrid ion trap/TOF instrument, which combines several of the advantages of the much investigated Paul trap/TOF devices, while eliminating some of its drawbacks, as will be outlined in section 3.4.

3.2 Reflectron Time-of-Flight Mass Spectrometry

Time-of-flight (TOF) mass spectrometry is based on the principle that ions of the same kinetic energy Uq , but of different mass m travel at different speeds. Starting simultaneously at the same point, they will reach a detector at different flight times. In the most simple arrangement (Fig. 3.1, top), ions are accelerated in a homogeneous electric field U/a in between two flat electrodes. They leave the acceleration region after a time

$$t_a = a\sqrt{\frac{2m}{Uq}} \quad (3.1)$$

and drift in a field-free region for a time

$$t_c = c\sqrt{\frac{m}{2Uq}}, \quad (3.2)$$

before they reach the detector at a time $t = t_a + t_c$.

In this simple layout, the mass spectral resolution is limited by several factors. Since the ion package starts with a finite width, ions of the same mass will start at different points in the extraction region and travel with different kinetic energies in the drift region. In Fig. 3.1, top, this is illustrated for three ions. Ions lagging behind in the acceleration region acquire higher kinetic energies and catch up with the slower ions in the field-free region at a distance of $c = 2a$, where the ion cloud is brought to a (first-order) space focus. Subsequently, the ion cloud spreads out again, with the fast ions reaching the detector before the slow ones, which leads to a loss in resolution. It would therefore be best to place the detector in the space focus. However, this does not allow one to realize long drift times, which is necessary to obtain a good resolution.

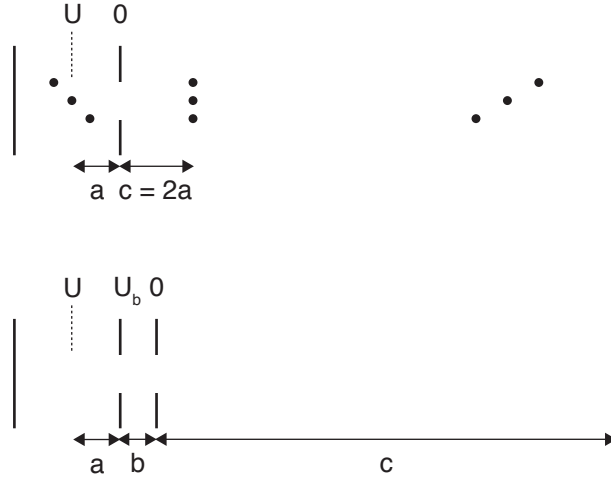


Figure 3.1: Schematic representation of a simple two-electrode ion source (top) and a Wiley-McLaren type acceleration region comprising three electrodes (bottom). (Adapted from reference ²²².)

Adding a third electrode to the extraction region²²³ introduces the potential U_b on this element as a new parameter, which allows one to freely choose the length of the (first-order) space focus (see Fig. 3.1, bottom). The total flight time is now a sum of the flight times in the extraction region, t_a and t_b , and the drift time t_c

$$t = t_a + t_b + t_c. \quad (3.3)$$

As before, t_c is given by Eqn. 3.2, while $U_a = U - U_b$ replaces U in Eqn. 3.1

$$t_a = a \sqrt{\frac{2m}{U_a q}}. \quad (3.4)$$

t_b is given by

$$t_b = \sqrt{\frac{2m}{q}} \frac{b}{U_b} (\sqrt{U} - \sqrt{U_a}). \quad (3.5)$$

Expanding t with respect to U_a and substituting $\Delta U_a/U = r$ yields²²²

$$t = A[2a + 2bD(B^{-\frac{1}{2}} - 1) + cB^{\frac{1}{2}}] \quad (3.6)$$

$$+ A\frac{r}{2}[2a + 2bD(B^{\frac{1}{2}} - 1) - cB^{\frac{3}{2}}] \quad (\text{first order}) \quad (3.7)$$

$$- A\frac{r^2}{8}[2a + 2bD(B^{\frac{3}{2}} - 1) - 3cB^{\frac{5}{2}}] \quad (\text{second order}) \quad (3.8)$$

$$+ A\frac{r^3}{16}[2a + 2bD(B^{\frac{5}{2}} - 1) - 5cB^{\frac{7}{2}}] \dots \quad (\text{third order}) \quad (3.9)$$

$$\text{with } A = \sqrt{\frac{m}{2Uq}}, B = \frac{U_a}{U} \text{ and } D = \frac{U_a}{U_b}. \quad (3.10)$$

If the first-order term is set to zero, the conditions for a first-order space focus are obtained. It was also shown that second-order compensation can be realized (both the first and second-order terms are zero). However, the position of this second-order space focus is fixed for a given geometry and cannot be adjusted with the voltages applied to the electrodes.²²⁴

While space focusing can be realized with a two-stage ion source, it can only insufficiently compensate for the initial velocity distribution of the ions. This effect is sometimes referred

to as “turn around time”, from the amount of time that elapses before an ion initially moving with a velocity opposite to the extraction direction returns to its starting point. Since ions with different initial velocities arrive at the detector at different times, a decrease in resolution results.

The “turn around time” can be reduced when high extraction fields are used. This places the space focus at a short distance from the source. Ions pass this point after a short flight time with little temporal spread, but with a large distribution of velocities. Placing the detector in this point, however, is undesirable because of the short drift times that can be realized. The reflectron solves this dilemma by means of an ion mirror, which images this point onto the detector, so that long drift times can be realized while maintaining the small temporal spread of the ion package in the space focus of the source.^{222,225–227}

Figure 3.2 illustrates this principle. The space focus of a two-stage ion source with acceleration and drift lengths a_s, b_s and c_s can be considered as a new (virtual) ion source, from which ions originate with a small temporal spread but a large spread of velocities. When the ions reach the ion mirror, the slow ions are reflected at an early point while the fast ions penetrate more deeply into the reflector. Thus, higher velocities can be compensated with a longer flight path, so that all ions reach the detector at the same time. To sum up, the reflectron offers the

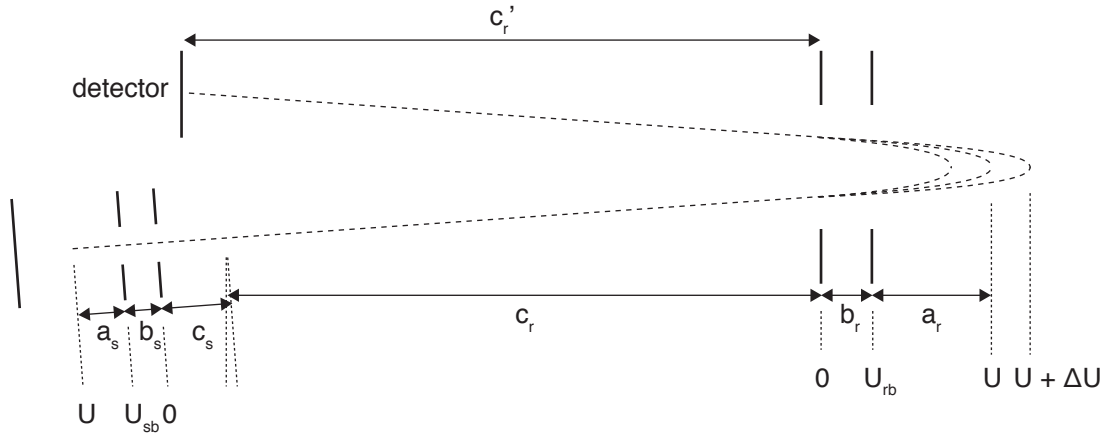


Figure 3.2: Schematic representation of a two-stage reflectron setup. The ion mirror is usually composed of a stack of electrodes (to better define the reflecting potentials), which is omitted here for clarity. (Adapted from reference ²²².)

advantage that the source can be independently optimized to reduce the “turn around time” effect while the ion reflector takes care of the resulting velocity spread.

Ideal energy compensation could be achieved in an ion mirror with a plane parabolic potential $U_{mirror} = kx^2$, with a constant k and the coordinate of ion motion x . The flight time in such a potential

$$t = 2 \int_0^{x_{max}} \frac{dx}{\sqrt{\frac{2q}{m}(U - ax^2)}} = \frac{\pi}{\sqrt{\frac{2qa}{m}}} \quad (3.11)$$

with the turning point of the ion $x_{max} = \sqrt{U/a}$, is independent of the initial ion kinetic

energy U .²²⁶ However, constructing or even approximating such an ideal ion mirror²²⁸ meets experimental difficulties. Field-free drift regions are necessary in order to accommodate ion optical elements and the detector. Moreover, Laplace's equation demands that a parabolic field defined by ring shaped electrodes has a curvature in the radial direction, which limits the acceptance angle of the reflectron.¹⁵¹ Therefore, a design as shown in Fig. 3.2 is frequently adopted that comprises two field-free drift regions of length c_r and c'_r between the ion mirror on the one side and the virtual source and detector, respectively. Here, a two-stage reflectron is shown that features two different deceleration/reflection fields U_{rb}/b_r and $(U - U_{rb})/a_r$.

The properties and principle of operation of a two-stage reflectron can be understood in terms of Eqns. 3.6–3.10, which describe a two-stage ion source.²²² Let us assume for the moment that $c_r = c'_r$. The reflectron can now be considered as a large (virtual) ion source whose (second-order) space focus can be adjusted to coincide with the space focus of the real ion source and the detector. The inclination of the real ion source serves to separate the trajectories of incoming and reflected ions. It is now conceivable how ions originating from the space focus of the real ion source will all reverse their flight direction in the ion mirror at the same time, with the ions spread out along the axis of the reflectron stack, depending on their initial kinetic energy. Obviously, the time of flight of the ions will not change when $c_r \neq c'_r$ as long as $c_r + c'_r = \text{const.}$ The picture given above changes only slightly for different drift lengths in that ions of different energy are no longer reflected at the same time.

With a two-stage ion source and a two-stage ion mirror adjusted for second-order energy compensation, the TOF resolution is now only limited by the following factors. Although the “turn around time” can be decreased by high extraction potentials, as noted above, it remains one of the most important contributions to the peak width. Therefore, by reducing the velocity spread of the ions, *e.g.* in a molecular beam or by other techniques for ion cooling, the resolution can be further improved. Another contribution to the peak width results from the third-order term of the ion energy, for which the ion mirror does not compensate. This effect is more important if high extraction potentials are used, which results in a large spread of the ion energies. The second-order term for the space focus of the ion source, on the other hand, is negligible because of the short flight times, so that adjusting the ion source for second-order compensation does not lead to an improvement.

Apart from these inherent limitations, several experimental restrictions exist, like the finite detector rise time, for example. If ions are created by laser ionization, the finite laser pulse length leads to different ion times of birth and, consequently, different arrival times at the detector. The occurrence of space charge effects in the extraction region or at the space focus of the source will deviate ion trajectories and broaden the peaks, as will the use of grids in the reflectron. Since ions enter the ion mirror at an angle, a large ion beam diameter or any divergence of the beam will lead to different lengths of the ion trajectories and, consequently, different times of flight. Finally, flight paths of different length also result if the ion transmission is optimized

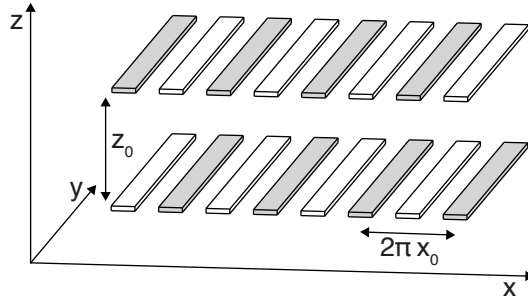
using deflection plates or an Einzel lens following the source.²²²

3.3 Planar Ion Traps

In order to store ions, they have to be spatially confined in all three dimensions over a prolonged period of time. Ion traps therefore usually feature a three-dimensional assembly of RF and DC electrodes. In recent years, however, several designs based on planar electrode arrays have been developed. This has in part been motivated by the goal to manufacture miniaturized ion traps with high precision, which can be achieved when standard microfabrication techniques are used to pattern electrodes onto a flat substrate. Examples include planar “halo”,²²⁹ quadrupole,²³⁰ and “coaxial” traps,²³¹ which create quadrupolar or toroidal RF trapping fields by means of suitable patterns of planar RF electrodes to which different RF amplitudes are applied. The development of surface ion traps, which store ions above the plane of a printed circuit board, is part of a larger effort to implement scalable quantum computing.^{232, 233}

The present work builds upon the design of a planar multipole trap developed by Wester and co-workers, who used microelectromechanical systems (MEMS) technology to plate gold electrodes onto the surface of two opposite, flat glass substrates, between which the ions are stored.²³⁴ The trap features two planar arrays of 16 RF electrodes each (schematically depicted in Fig. 3.3) with a width and distance of 0.5 mm. The arrays are spaced at a distance of 5 mm from each other and confine ions in the z direction, while trapping in the xy plane is achieved with sets of DC electrodes (not shown). The two RF phases are applied to alternating electrodes as indicated by the shading.

Figure 3.3: RF electrode geometry of the planar multipole trap of Wester and co-workers²³⁴. Grey and white electrodes carry opposite RF phases.



The principle of operation of this trap can be understood if one considers that each of the RF electrode arrays functions as an ion mirror, as had been demonstrated previously.^{235, 236} The potential $\Phi(\hat{x}, \hat{z})$ of an infinitely large electrode array can be approximated when the actual potential on the electrodes is substituted by the first term of its Fourier series to give the boundary condition for Laplace’s equation. One obtains

$$\Phi(\hat{x}, \hat{z}) = \Phi_0 \exp(-\hat{z}) \cos \hat{x} \quad (3.12)$$

with $\hat{x} = x/x_0$, $\hat{z} = z/x_0$ and $\Phi_0 = 8\sqrt{2}/\pi^2 U_0$, where U_0 is the voltage applied to the electrodes.^{112, 234} In contrast to the multipole potentials (Eqn. 2.31), Φ decreases exponentially

with the distance from the plane of the array and is modulated in the direction orthogonal to the electrodes. The potential Φ of two opposite electrode arrays is given by

$$\Phi(\hat{x}, \hat{z}) = \Phi_0 \sinh(\hat{z}) \cos(\hat{x}), \quad (3.13)$$

where $\Phi_0 = 8\sqrt{2}/\pi^2 U_0 / \sinh[z_0/(2x_0)]$ and U_0 is the RF amplitude. For the effective potential V^* (Eqn. 2.22), one obtains²³⁴

$$V^*(\mathbf{r}) = \frac{q^2 (\frac{8\sqrt{2}}{\pi^2} U_0)^2}{4m\Omega^2 x_0^2} \frac{\cosh(2\hat{z}) + \cos(2\hat{x})}{\cosh \frac{z_0}{x_0} - 1}. \quad (3.14)$$

With their planar trap, Wester and co-workers demonstrated the storage of up to 3000 ions (created by electron impact inside the trap) and determined a storage time of 16 s. Evidence for a charging up of the glass substrate was found, and a concomitant reduction of the storage time was observed.²³⁴ They subsequently incorporated an improved version of the trap into a tandem TOF mass spectrometer.²³⁷ Mass-selected protonated water clusters were injected into the trap and decelerated in collisions with helium that had been pulsed into the trap prior to the arrival of the ions. The injection efficiency was estimated to be higher than 70% for clusters with $m/z \geq 37$ and about 30% lower for the lower masses. Storage times of 2.9 s for H_3O^+ to 12.0 s for $\text{H}^+(\text{H}_2\text{O})_4$ were measured. In order to obtain a TOF spectrum, the ions were extracted along the x direction, which is analogous to extracting ions out of a linear multipole along its axis and is therefore afflicted with similar limitations for the resolution (see section 3.1).

This biplanar multipole ion trap has several appealing features that render it interesting for a number of purposes. As a true multipole trap, it can be used for the buffer gas cooling of ions. Unlike linear multipole traps, which are usually employed for that purpose, its open geometry offers easy access to the trapping volume for both particle and laser beams. It was furthermore suggested that with electrodes manufactured from transparent indium tin oxide, the trap could be overlapped with a magneto optical trap for ultracold neutral atoms to study the interaction between a Bose-Einstein condensate and a single charge. Finally, its planar geometry makes it amenable to microfabrication techniques, which allow one to manufacture the electrodes with high precision and achieve better trapping fields.^{234, 237} Most important for the present work is the fact that planar electrodes can be used to create homogeneous DC extraction fields as they are necessary in TOF mass spectrometers to achieve a good mass resolution.

3.4 Combining a Planar Multipole Ion Trap with a Time-of-Flight Mass Spectrometer

The original motivation for the work presented in this chapter was to find a method to record a TOF spectrum of the ions stored in the 22-pole ion trap of the tandem mass spectrometer described in chapter 2. However, most existing techniques suffer either from a low detection efficiency or insufficient mass spectral resolution (see section 3.1).

The basic idea of this chapter is to develop a novel hybrid mass spectrometer for this purpose in which ions can be stored in a planar multipole ion trap and subsequently extracted in the direction orthogonal to the planar RF electrodes in order to record a TOF spectrum. As will be argued in the following, such an instrument would allow one to transfer the ions from the 22-pole into the multipole trap with a high efficiency and extract them to obtain a well-resolved TOF spectrum.

Like a linear multipole, the trap possesses a large field-free region in its center, so that it should be possible to inject ions with near 100% efficiency and little mass discrimination. (For a planar RF trap, an efficiency of more than 70% has been reported for ions with $m/z > 37$.)²³⁷ Furthermore, the RF fields and the potentials of the DC electrodes surrounding the trap allow focusing the ion cloud in the z direction and the xy plane, respectively. As in all high-order multipolar ion traps, ions will spend most of their time in the field-free region, where no RF heating occurs, and thus have a translational temperature close to that of the buffer gas. It should therefore be possible to create an ion package with a narrow spatial and velocity distribution prior to extraction, which is necessary to achieve good mass resolution. Moreover, the phase space distribution of the ions will be largely independent of the RF phase, such that the extraction efficiency and resolution should not depend on the extraction phase and the ion mass. Finally, homogeneous extraction fields can be created with planar trap electrodes, which should help to obtain a good mass resolution.

Disadvantages of the design include the possible difficulty to develop suitable electronics capable of supplying a RF to the trapping electrodes, switching it off within one oscillation, and finally applying a high voltage pulse with short rise time. Furthermore, the collision gas needed for efficient trapping will inevitably lead to a loss of resolution if it cannot be pumped away before extraction. With solid electrodes, the maximum transmission efficiency would be limited to 50%. However, a different design of the electrodes could improve the extraction efficiency.

Since the multipole trap could also be used for buffer gas cooling of trapped ions, it could actually replace the 22-pole of the instrument described in chapter 2 entirely. This way, one ion transfer step would be saved, and the complexity of the experiment could be reduced. The advantages of the open structure of the trap for the purposes of laser spectroscopy, such as easy access for laser beams, have already been noted above. As a positive side effect, cooling the ions would also reduce their spatial and velocity distribution further and could be a means to improve the mass resolution. However, it was beyond the scope of this work to couple the trap to a cryostat and implement this idea.

Quite apart from its original purpose, a planar multipole ion trap/TOF mass spectrometer could find a number of different applications, and some ideas are noted below (see section 3.8). The following sections describe design, development and characterization of the multipole ion trap/TOF mass spectrometer.

3.5 Design Considerations

The design of the planar multipole trap was guided by SIMION¹⁵⁸ simulations of potentials and ion trajectories. Figure 3.4 shows one layer of RF and DC electrodes of the trap in its final design. The RF is applied to two interlacing combs of eight 30 mm long and 1 mm wide poles each, with a spacing of 1 mm between the poles. This structure is surrounded by four 5 mm wide DC electrodes, which confine the ions in the x and y direction.

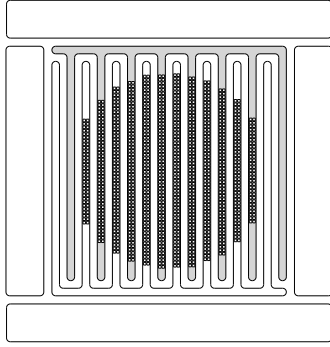


Figure 3.4: Electrode geometry of the planar multipole trap, one set of trap electrodes as realized in the final design, scale 1:1. The interlacing RF combs (8 poles of each phase, 30 mm long, 1 mm wide, and 1 mm apart) are surrounded by DC electrodes (5 mm wide and spaced by 1 mm).

The trap is composed of two such arrays placed opposite each other at a distance of 5 mm (Fig. 3.5). Ions are stored between these arrays and ejected in the z direction in order to obtain a time-of-flight spectrum. Two plates sandwich the structure at a distance of 2 mm, which are usually kept at the voltage of the pole bias during trapping and serve to provide better fields during extraction, as described below.

Figure 3.6 displays calculated potentials for a two-dimensional ion trap. They resemble closely those that one obtains from a cut through the center of the actual three-dimensional trap along the xz plane (see Fig. 3.5). However, two-dimensional simulations require less computational effort while capturing the essential features of the trap geometry.

The potential Φ of the DC electrodes (1 V applied) is shown in the top of Fig. 3.6. It is used to confine the ions in the x direction, while trapping in the z direction is achieved by means of the RF electrodes. The effective potential V^* that an ion of mass 93 experiences if a 3.2 MHz RF of 60 V amplitude is applied to the comb structure is depicted in the lower part of Fig. 3.6. V^* is set to zero in regions where the adiabaticity parameter η exceeds 0.3, so that stable trapping cannot be achieved (see section 2.7.3). The trap depth is therefore determined by the areas with $\eta < 0.3$.

In the case of linear multipoles, the trap depth initially rises with increasing RF amplitude because the effective potential is proportional to the square of the RF amplitude (Eqn. 2.32). However, stronger fields also increase the adiabaticity parameter η , so that the critical radius within which $\eta < 0.3$ finally becomes smaller than the physical radius of the trap. At even higher RF amplitudes, the volume in which (stable) trapping is possible shrinks, so that the trap depth decreases.¹³² This behavior is depicted in Fig. 3.7 (left), where the trap depth for a 93 amu ion in a 20-pole and a 10-pole of 5 mm inscribed diameter is shown as a function of

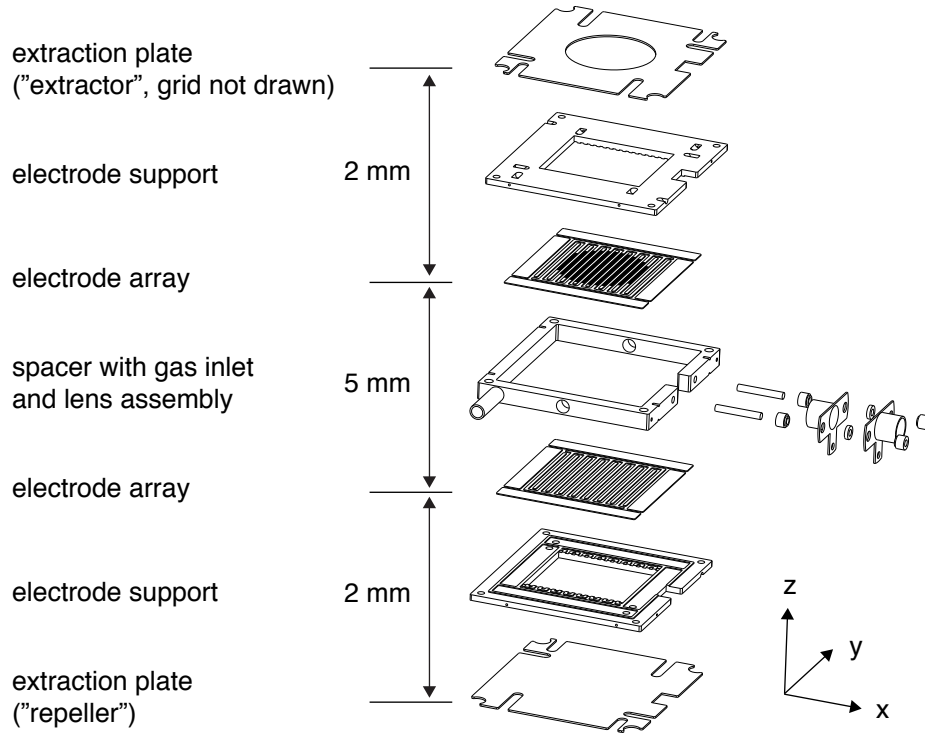


Figure 3.5: Exploded view of the planar multipole trap in its final design. From the top to the bottom: Upper extraction plate (“extractor”, grid covering the extraction hole not drawn), upper electrode support, upper array of RF and DC electrodes, spacer with gas inlet and injection lens assembly, lower array of RF and DC electrodes, lower electrode support, lower extraction plate (“repeller”). Ions are stored in between the two electrode arrays and then extracted through the hole in the top plate.

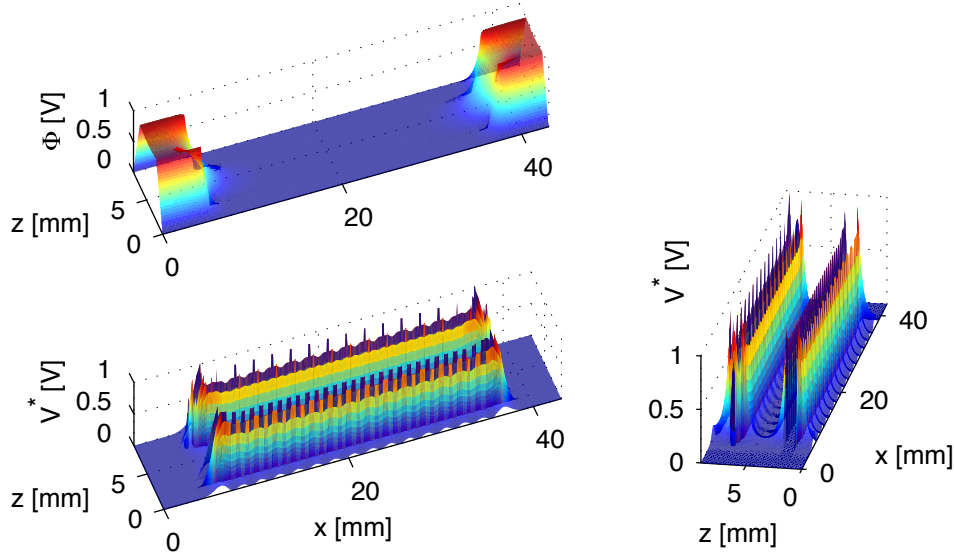


Figure 3.6: Simulated potentials of a two-dimensional planar multipole trap: Electrostatic potential Φ of the surrounding DC electrodes (1 V applied, top) and effective potential V^* created by the RF electrodes (bottom) for a 93 amu ion and a 3.2 MHz RF of 60 V amplitude. The effective potential is set to zero for regions with $\eta > 0.3$.

the amplitude of the 3.2 MHz trapping RF. For a lower order multipole with the same inscribed diameter, a higher trap depth can be achieved, while the field-free region in the center of the

trap is smaller (Fig. 2.10).

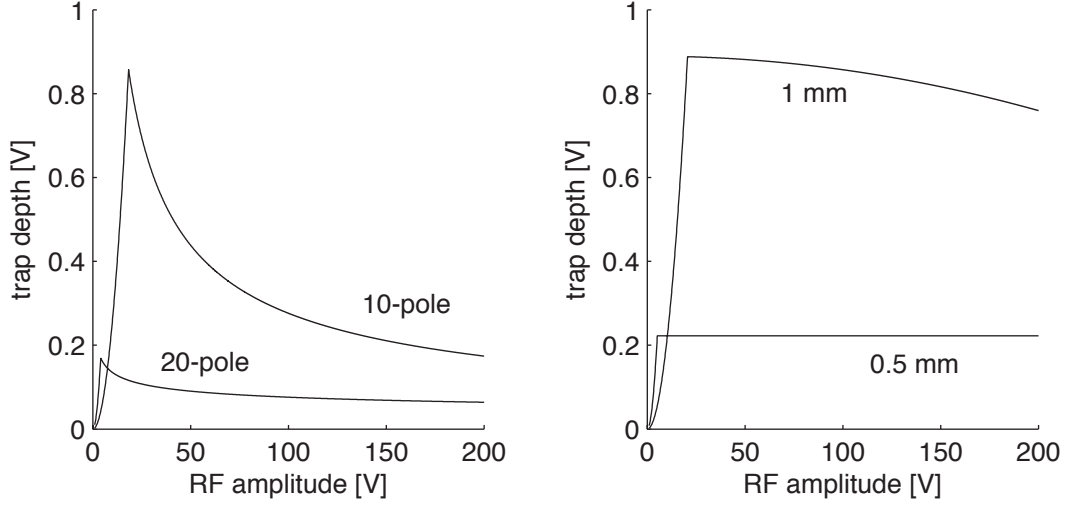


Figure 3.7: Comparison of the trap depths of linear multipoles and planar traps as a function of the RF amplitude. The trap depths of a 20-pole and a 10-pole with 5 mm inscribed diameter (left) and a planar multipole ion trap with 0.5 mm and 1 mm electrode width and a distance between the RF combs of 5 mm (right) are shown.

The same analysis can be performed for planar multipole traps using the approximations for the potential and effective potential (Eqns. 3.13 and 3.14) and likewise assuming a trapping RF of 3.2 MHz. Figure 3.7 (right) depicts the trap depth as a function of the RF amplitude for planar traps with a distance of 5 mm between the two layers of RF electrodes and an electrode width of 0.5 mm and 1 mm. The behavior is similar to the case of linear multipoles. Initially, the trap depth increases because the effective potential is proportional to the square of the RF amplitude (Eqn. 3.14). Upon further increase of the RF amplitude, η starts to exceed 0.3 in regions close the electrodes, which reduces the volume in which adiabatic ion motion is possible and consequently the trap depth. In this regime the trap depth is described by

$$\Phi_{\text{trap depth}} = \frac{\eta_{\text{max}}^2 m \Omega^2 x_0^2}{16} - \frac{q^2 \left(\frac{8\sqrt{2}}{\pi^2} U_0 \right)^2}{4m\Omega^2 x_0^2 \left(\sinh \frac{z_0}{2x_0} \right)^2} \quad (3.15)$$

with the maximum allowed adiabaticity parameter η_{max} . The maximum trap depth

$$\Phi_{\text{trap depth}}^{\text{max}} = \frac{\eta_{\text{max}}^2 m \Omega^2 x_0^2 \left(\tanh \frac{z_0}{2x_0} \right)^2}{16} \quad (3.16)$$

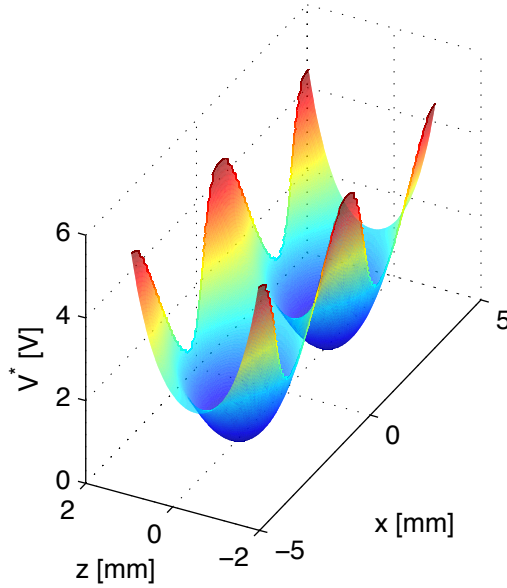
is reached at a RF amplitude of U_0^{max} with

$$\frac{8\sqrt{2}}{\pi^2} U_0^{\text{max}} = \frac{\eta_{\text{max}} m \Omega^2 x_0^2 \tanh \frac{z_0}{2x_0}}{2q}. \quad (3.17)$$

The linear multipoles and planar traps have similar trap depths for comparable geometric parameters. Also, the decrease in trap depth upon doubling the number of poles is comparable. However, for the planar traps, the trap depth decreases more slowly with increasing RF amplitude once the adiabatic trapping volume becomes smaller than the physical volume of the trap.

A higher trap depth is desirable because it increases the storage time and the efficiency with which ions can be injected. However, increasing the width of the RF electrodes reduces the field-free region in the center of the trap as in the case of linear multipoles (see Fig. 2.10). This is evident in Fig. 3.8, which displays the effective potential V^* (Eqn. 3.13) for a 93 amu ion in a planar trap with 5 mm distance of the RF electrode arrays, 2 mm electrode width, and a 3.2 MHz RF of 200 V amplitude; only the regions with $\eta < 0.3$ are shown. Furthermore, a series of local minima in the center of the trap is visible. Under these conditions, RF heating of the ions can be expected.

Figure 3.8: Simulation of the effective potential V^* of a planar multipole trap showing a series of local minima in its center. The simulation assumes a 93 amu ion in a planar trap with 5 mm distance of the RF electrode arrays, 2 mm electrode width, and a 3.2 MHz RF of 200 V amplitude. Only the regions with $\eta < 0.3$ are shown.



It is also apparent from Fig. 3.8 that the trap depth is limited by the minima of the effective potential that occur on the border of the adiabatic region in between two electrodes. These minima become more pronounced with wider electrodes and reduces the trap depth for higher RF amplitudes (Eqn. 3.15 and Fig. 3.7).

Taking the above considerations into account, an electrode width of 1 mm was chosen as a compromise, which, at the same time, did not render the manual assembly of the trap too difficult. As will be shown in section 3.7.4, the local minima of the effective potential are actually beneficial, as they can be used to increase the extraction efficiency. For the purpose of buffer gas cooling, however, a smaller electrode width would have to be used in future versions of the trap. This could be realized in a chip-based design, where a better alignment could be achieved for an even smaller geometry.

The spacing of the two opposite layers of RF and DC electrodes of 5 mm was likewise chosen as a compromise between different requirements. A smaller spacing will help to focus the ions in the central plane of the trap, which improves the resolution of the TOF mass spectra. However, it will become increasingly difficult to inject an ion beam into the smaller volume in between the electrodes.

The extraction plates (“repeller” and “extractor”, see Fig. 3.5) that surround the trap were added in order to achieve more homogeneous extraction fields. They are placed at a convenient distance of 2 mm from the trap electrodes. Figure 3.9 shows a simulation of the potential Φ in a two-dimensional trap with typical extraction voltages applied to the electrodes (see figure caption). The cut along the x coordinate at a distance of 1 mm from the lower layer of trap electrodes (left) shows a periodic variation of the potential in the center of the trap of about 14 V if the extraction plates are grounded (lower curve), while the potential is homogeneous when suitable voltages are applied to the extraction electrodes. Similarly, a cut along the z dimension through the center of the trap (right) demonstrates how the extraction electrodes improve the homogeneity of the extraction field.

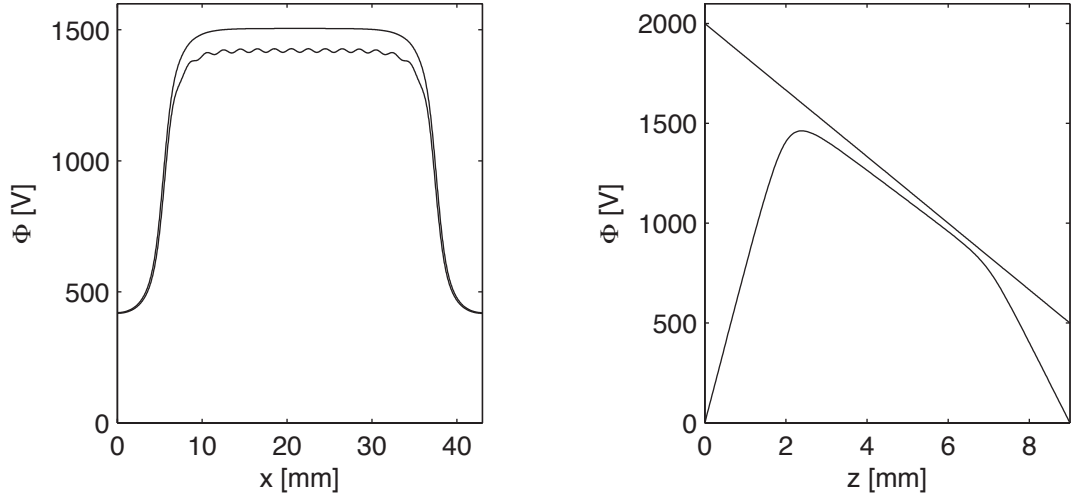


Figure 3.9: The effect of the extraction plates on the extraction fields. Simulation of the electric potential in a two-dimensional trap with different extraction voltages applied to the electrodes. Cross sections along the x coordinate at a distance of 1 mm from the lower comb (left) and along the z coordinate in the center of the trap (right) are shown. Potentials: “Repeller” 2000 V or 0 V (upper and lower curves, respectively), lower RF electrodes 1667 V, upper RF electrodes 833 V, “extractor” 500 V or 0 V (upper and lower curves, respectively), trapping DC electrodes 400 V.

The effect of any grounded surfaces would, of course, be smaller if they were separated from the trap by more than 2 mm. Nevertheless, the extraction plates help to create well-defined extraction fields. Moreover, they can be used to modify the trapping potentials during ion storage. They also reduce the conductance of the trap, which is beneficial if gas is pulsed into the trap in order to decelerated ions that are injected from the outside.

Figure 3.9 also illustrates the effect of the trapping DC electrodes, which are kept at 400 V in the simulation. Within a distance of 10 mm from the center of the trap, their contribution to the extraction potential is negligible. However, even with a potential of only 10 V on the DC electrodes, the ion cloud is confined to a far smaller region (see below). For this reason, it is not necessary to apply high voltage pulses to the DC electrodes during extraction as well, which simplifies the electronics of the traps.

Apart from instrument parameters (*e.g.* the transmission of various grids or the homogeneity

of the extraction fields), the fraction of ions that reaches the detector (*i.e.* the duty cycle) and the resolution of the TOF spectrum largely depend on the spatial and velocity spread of the ion cloud at the moment of extraction. In order to determine the phase space distribution of the ion cloud in the planar trap, ion trajectories were simulated for the actual three-dimensional electrode geometry and typical operation conditions (Fig. 3.10). The hard sphere collision model implemented in SIMION was used to simulate the effect of the background gas, with ^4He as collision gas at a pressure of 1e-4 mbar and a temperature of 298 K. Ion trajectories were started in the center of the trap, and the position and velocities were recorded every μs . The simulations were stopped once the extracted distributions were stable within reasonable limits. The actual experimental pressures were one to three orders of magnitude lower (see section 3.7). However, in order to achieve fast equilibration and have the ion explore the accessible phase space in a reasonable amount of time, a higher pressure was simulated. It should be noted that these simulations neglect the effect of space charge.

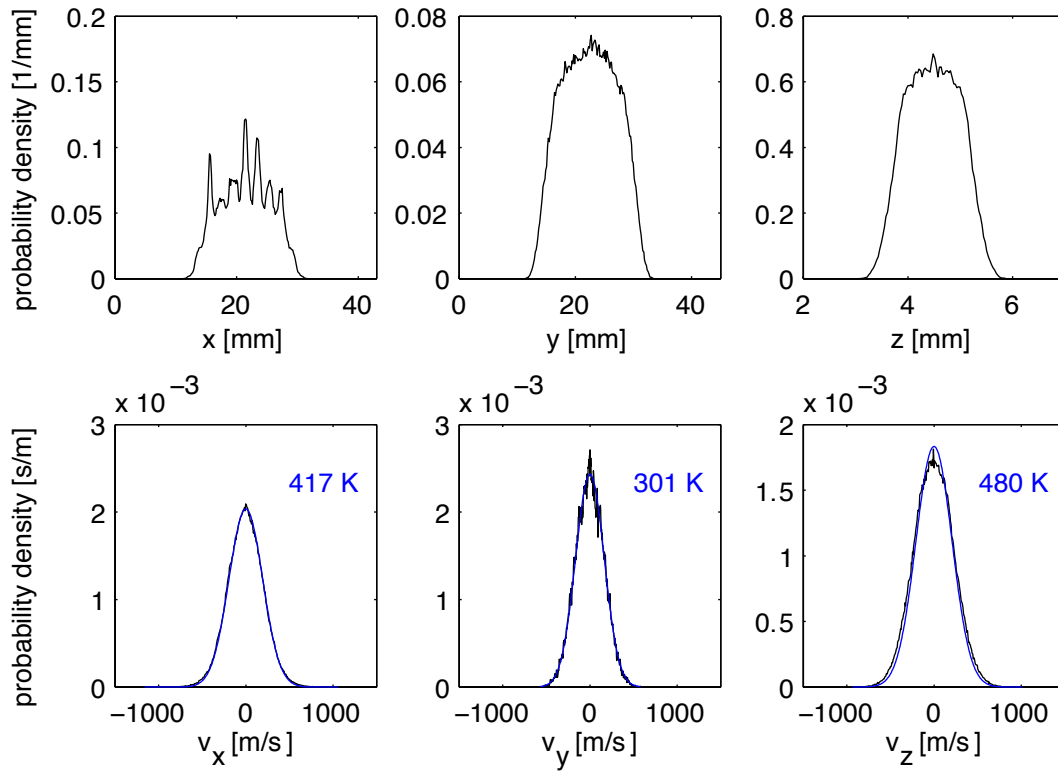


Figure 3.10: Simulation of the phase space distribution of a 93 amu ion in the three-dimensional planar trap at 298 K with a helium pressure of 1e-4 mbar. The extraction plates are grounded, 10 V are applied to the trapping DC electrodes, and a 3.2 MHz RF with 60 V amplitude and 0 V pole bias is simulated. The three velocity components are fitted with a one-dimensional Maxwell-Boltzmann distribution (blue) in order to obtain the translational temperatures.

With a potential of 10 V on the trapping DC electrodes, the ion cloud spans about 15 mm in the x and y dimensions (designations see Fig. 3.5). It is therefore smaller than the 25 mm aperture of the Einzel lens that is used in the TOF mass spectrometer. The distribution in x is modulated with the period of the electrode distance, since ions preferentially accumulate in the

local traps in between two neighboring electrodes (see Fig. 3.8). These local minima reduce the mobility of the ion in the x direction. Because of the limited amount of time available for the simulation, the obtained distribution is therefore not symmetric. With the spatial spread of the ions in the extraction direction of ~ 1.6 mm (comparable dimensions are found in quadrupole ion trap/TOF instruments), the ion cloud resembles a thin, square slice.

Fitting the three velocity distributions with a one-dimensional Maxwell-Boltzmann law (Fig. 3.10) yields three different translational temperatures $T_x = 417$ K, $T_y = 301$ K, and $T_z = 480$ K. Whereas T_y is close to the buffer gas temperature, T_x and T_z are ~ 120 and ~ 180 K higher, which points to considerable RF heating. It is instructive to analyze the mean absolute velocity components $\langle |v_x| \rangle$, $\langle |v_y| \rangle$, and $\langle |v_z| \rangle$ as a function of the spatial coordinates, as shown in Fig. 3.11.

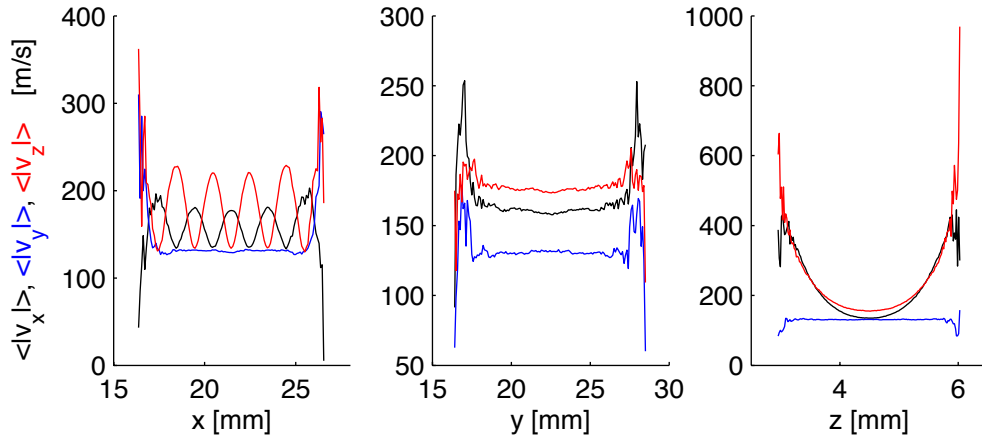


Figure 3.11: The simulated mean absolute velocity components of an ion in the three-dimensional planar trap as a function of the spatial coordinates. Here, a 93 amu ion, a temperature of 298 K, and a helium pressure of $1e-4$ mbar are assumed. The extraction plates are grounded, the trapping DC electrodes are set to 400 V, and a 3.2 MHz RF with 60 V amplitude and 0 V pole bias is simulated.

In this simulation, the trapping DC electrodes were set to 400 V; nevertheless, similar translational temperatures are obtained. The dependence of the three velocity components on the x coordinate of the ion shows that $\langle |v_x| \rangle$ and $\langle |v_z| \rangle$ are periodically modulated, with their minima approaching the nearly constant value of $\langle |v_y| \rangle$. This behavior is obviously connected to the modulation of the RF electrode potential in the x direction and the local minima of the effective potential of the trap. In between two opposite electrodes, the ions experience an oscillating electric field that has its largest component in the z direction, while in between two neighboring electrodes, it points in the x direction. This explains why $\langle |v_z| \rangle$ has maxima at the position of the electrodes, whereas $\langle |v_x| \rangle$ goes through a minimum. $\langle |v_y| \rangle$ is constant over a wide range, since the electric field has no y component.

The three mean absolute velocity components are largely independent of the y position of the ion. However, they peak close to the edge of the ion cloud (as most curves in Fig. 3.11 do), which is probably due to the fact that only the fast ions can reach this region at all. $\langle |v_y| \rangle$ is also independent of the z coordinate, while $\langle |v_x| \rangle$ and $\langle |v_z| \rangle$ increase when the ion

approaches the RF electrodes. In the center of the trap, they are close the nearly constant value of $\langle |v_y| \rangle$. In summary, this analysis shows that RF heating occurs in the present geometry of the trap, which originates from oscillations of the ions in the x and z direction. The specific electrode geometry of the planar trap leads to three different translational temperatures for the three space coordinates.

Figure 3.12 shows the simulated phase space distribution for a buffer gas temperature of 6 K with 10 V RF amplitude, 10 V applied to the DC electrodes, and otherwise identical conditions. The spatial spread of the ions in the x and y direction shrinks to 4 and 5 mm, respectively, while

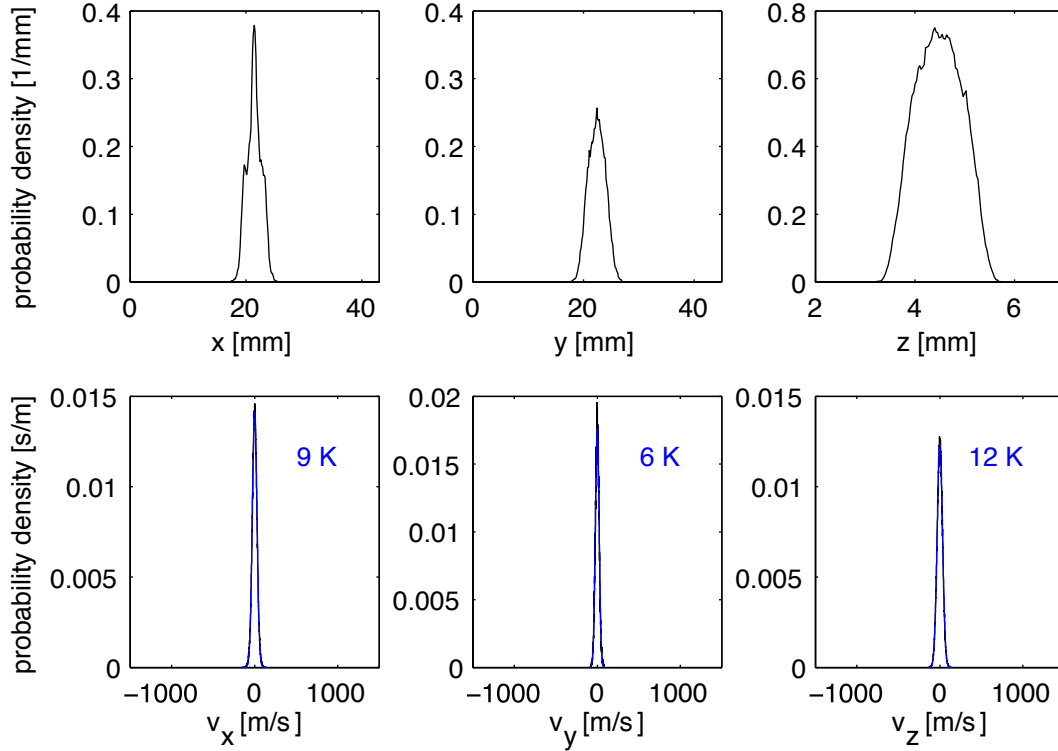


Figure 3.12: Simulation of the phase space distribution of a 93 amu ion in the three-dimensional planar trap at 6 K with a helium pressure of $1e-4$ mbar. The extraction plates are grounded, 10 V are applied to the trapping DC electrodes, and a 3.2 MHz RF with 60 V amplitude and 0 V pole bias is simulated. The three velocity components are fitted with a one-dimensional Maxwell-Boltzmann distribution (blue) in order to obtain the translational temperatures.

the thickness of the ion cloud only slightly decreases to ~ 1.5 mm (the lower temperature and the lower RF amplitude compensate each other). From the velocity distributions, translational temperatures of $T_x = 9$ K, $T_y = 6$ K, and $T_z = 12$ K are obtained, close to the temperature of the bath gas. This suggests that buffer gas cooling would still be feasible with this geometry of the trap, at least for heavy ions.¹⁴⁹

3.6 Realization

The development of the planar multipole ion trap time-of-flight mass spectrometer proceeded in several stages. The proof of principle was established with a first prototype. An improved

second version was subsequently used for characterization experiments and, finally, coupled to the tandem quadrupole mass spectrometer described in chapter 2.

3.6.1 Construction of the Prototype

This section briefly describes the design of the first prototype of the trap, which is shown in Fig. 3.13, and discusses flaws of the construction that were identified. The electrodes were mounted

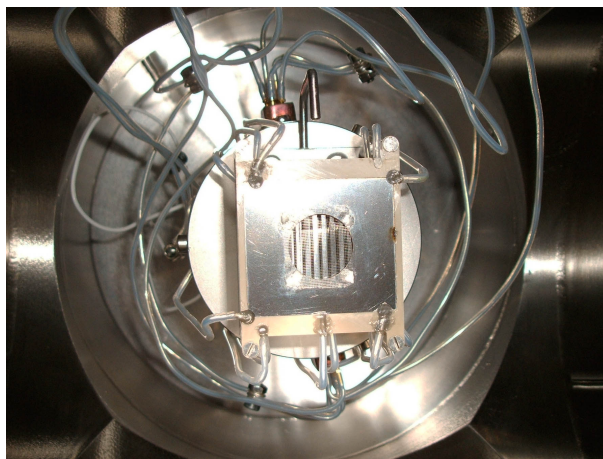


Figure 3.13: Photograph of the prototype of the trap.

onto PEEK supports by simply pressing them into grooves on their surface. While this method would in principle allow one to dispense with adhesives, the construction became very delicate, so that some electrodes had to be fixed with Araldite epoxy. Electrical contact was made by tin-soldering silver-coated copper wires to the electrodes. The assembled trap was then mounted onto a cylinder that was attached the flange. The photograph also shows the bent gas inlet tube that was used to leak the sample into the trap.

Some of the employed materials had limited vacuum compatibility, so that the pressure in the trap chamber did not fall below $1\text{e-}7$ mbar even after prolonged heating. The stainless-steel electrodes constituted another problem, as the vacuum cleaning procedure left stains on their edges and surface that indicated oxidation. After prolonged operation in vacuum, black marks appeared on the electrodes and the supports (see the photograph), which seems to suggest that arcing had occurred.

After initial successful testing of the device, the ion signal became unstable and potentials had to be adjusted frequently. Most notably, the signal would decrease during operation over a period of several hours and finally vanish. This behavior indicated that non-conductive surfaces were charging up and disturbing the trapping and extraction fields.

3.6.2 Construction of an Improved Version

The second version of the trap was designed with the goal to avoid all the drawbacks of the prototype. At the same time, features were incorporated that would make it possible to couple

the device to the tandem quadrupole mass spectrometer in a second step. Figure 3.5 depicts an exploded view of the trap itself, while Fig. 3.14 shows how the assembled trap is mounted.

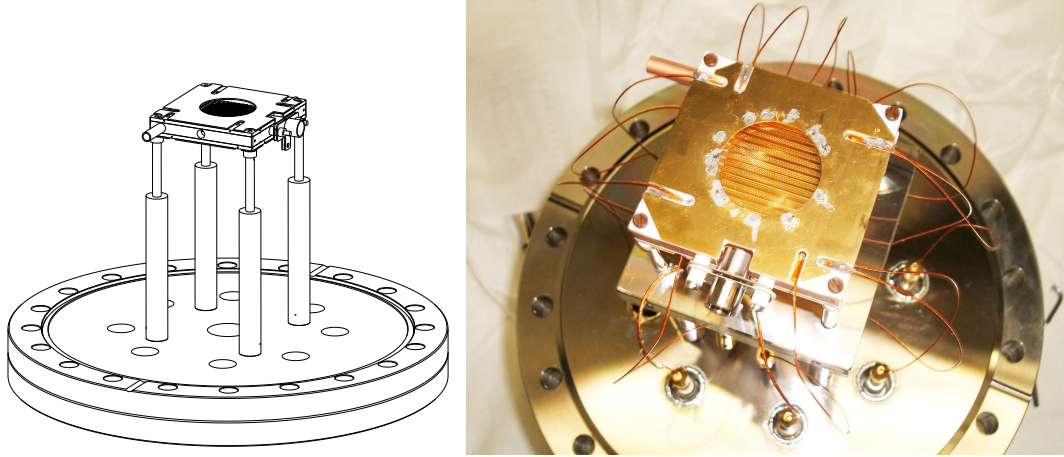


Figure 3.14: The second version of the trap, assembled and mounted onto a flange.

The RF and DC electrodes of the trap were laser cut out of 0.3 mm thick stainless-steel sheets, while 0.5 mm thick sheets were used for the extraction plates. A circular pattern of holes was cut into the RF combs in order to increase ion transmission upon ejection. The upper extraction plate (53×55 mm) features a 25 mm diameter hole, which was covered with a 70 lines per inch, 90% transmission nickel mesh (Precision Eforming, MN17) that was soldered to the upper surface after all electrodes had been coated with a $1 \mu\text{m}$ layer of gold (Estoppey-Addor).

The electrodes were glued onto Macor supports ($53 \times 55 \times 1.75$ mm) with a vacuum-compatible epoxy (EPO-TEK 353 ND). These supports feature a 31×27 mm hole that leaves the RF electrodes free standing in the center. The alignment of the RF and DC electrodes was assured by 0.25 mm deep grooves on the surface of one side of the Macor frame, which positions them at a center distance of ~ 2 mm from the extraction plate.

The application of the epoxy proved challenging, since it becomes very mobile during the curing process and, by capillary action, tends to cover all adjacent surfaces including the electrodes. Moreover, heating the entire support to $\geq 80^\circ\text{C}$ for curing would sometimes break existing glue points because of the difference in dilation of the Macor and the stainless-steel electrodes. The technique that we developed, especially for gluing the tips of the comb shaped electrodes to the support, consists in applying minute amounts of glue with the tip of a fine syringe under the microscope and then locally heating the electrode with a solder iron whose tip presses down on the structure.

The ends of silver-coated copper wires (0.25 mm diameter) with Kapton insulation (Kurt J. Lesker) were soldered onto the trap and extraction electrodes in order to establish the electrical contact. The solder points are situated on the side of the electrodes that faces the Macor support and the wires are guided by means of grooves in the frame.

A copper frame spaces the upper and lower half of the trap such that the trap electrodes are

~ 5 mm apart in the z direction. It is electrically contacted with a wire that is attached on one side with an M2 screw and features a tube that can serve as a gas inlet, a pair of opposite holes for laser access, and an opening into which the assembly of a pair of electrostatic lenses inserts that are used for the purpose of ion injection. In the initial characterization experiments, the lens assembly was not mounted and no gas was injected through the tube, since ions were created inside the trap by REMPI of gaseous neutrals. The sample was leaked into the chamber such that no direct flow could strike the electrodes in order to avoid contamination of the surfaces.

Figure 3.14 shows the assembled trap. Vespel screws are used to mount the trap onto four stainless-steel rods that are bolted into a rotatable flange. Ceramic spacers prevent electrical contact between the “repeller” electrode and the poles. MHV feedthroughs on the flange are used for connections to the extraction plates and RF electrodes, while a 10-pin connector in the center of the flange is used for the remaining potentials.

The assembly of the trap with the new design proved overall simpler and more reliable. After only three days of heating, a pressure of 2×10^{-8} mbar was reached in the vacuum chamber housing the trap, which demonstrates the better vacuum compatibility of the design. No sign of arcing could be detected, and a stable signal was observed over prolonged periods of operation.

3.6.3 The Test Setup

For the initial testing and characterization of the trap, a test setup was used (see Fig. 3.15), in which the trap replaces the repeller and extractor of a commercial reflectron (Jordan TOF Products, Inc., D-850). It is mounted in the center of a six-way cross chamber, which is connected to the 81 cm long flight tube. Aniline vapor seeded in helium is continuously leaked into the chamber, and ions are created inside the trap by laser ionization. After ejection, the ions pass a 25.4 mm inner diameter Einzel lens, the first element of which is covered with a grid to serve as the third electrode in a Wiley-McLaren type electrode arrangement. The 15 mm inner diameter conductance limit separating the trap chamber and the flight tube and two sets of deflection plates follow. When the instrument is operated in linear mode the ions strike an 18 mm micro channel plate (MCP) detector. In reflectron mode, suitable voltages are applied to the reflectron assembly, so that the ions are reflected and focused onto a second 40 mm MCP detector.

The trap chamber and flight tube are pumped by a 400 l/s turbomolecular pump (Leybold Vakuum GmbH, Turbovac 361) and a 170 l/s turbomolecular pump (Pfeiffer, TPU 170), respectively, that are both backed by a $5 \text{ m}^3/\text{h}$ rotary vane pump (Pfeiffer, DUO 5). Pressures in the trap chamber are adjusted with a leak valve, while the pressure in the flight tube is usually one order of magnitude lower, reaching $< 2 \times 10^{-9}$ mbar without gas load.

3.6.4 Coupling to the Tandem Quadrupole Mass Spectrometer

In a second step, the trap and reflectron were coupled to the tandem quadrupole mass spectrometer described in chapter 2, so that the injection of externally generated ions could be

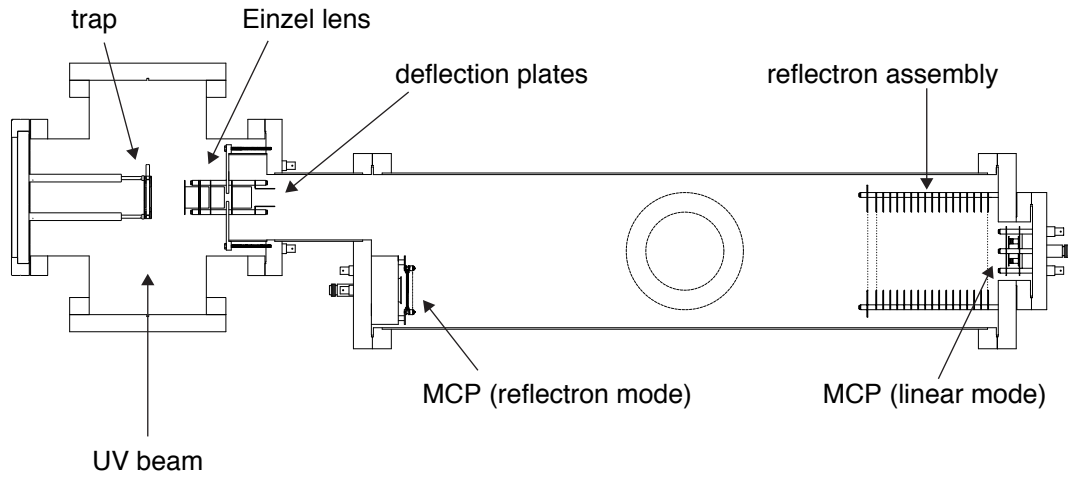


Figure 3.15: Schematic representation of the test setup. (Adapted from a drawing provided by the manufacturer under <http://www.rmjordan.com>.)

investigated. To this end, a 19 cm long octopole (3 mm rods on a 9 mm inscribed diameter, with entrance and exit lens) was added to the second bender (see Fig. 3.16) to guide ions into the trap, which is mounted in the center of a CF 160 cube.

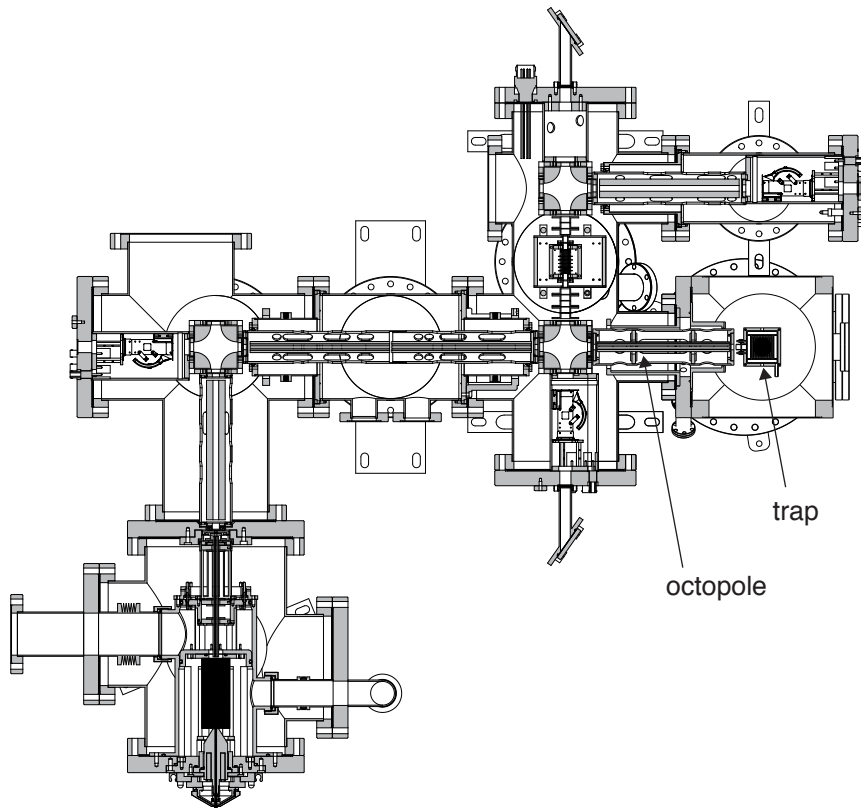


Figure 3.16: Cross section of the tandem quadrupole mass spectrometer with the trap coupled to the second bender.

The reflectron is placed below the cube with a slightly shorter flight tube of 70 cm length, which rests upon three feet attached to its bottom flange. The photograph in Fig. 3.17 shows the

trap hanging from the upper flange of the cube, with the octopole approaching it from the left. The Teflon gas inlet tube is attached to the copper frame of the trap on the right and connects to a solenoid valve (Parker Hannifin, General Valve) on the outside of the chamber. The third Wiley-McLaren electrode (the front plate of the first element of the Einzel lens) is placed at a distance of about 1 cm from the extractor electrode of the trap. The trap chamber and flight tube are pumped by a 685 l/s and a 260 l/s turbomolecular pump, respectively (Pfeiffer, HiPace 700 and HiPace 300), that are both backed by a 5 m³/h rotary vane pump (Pfeiffer, DUO 5).

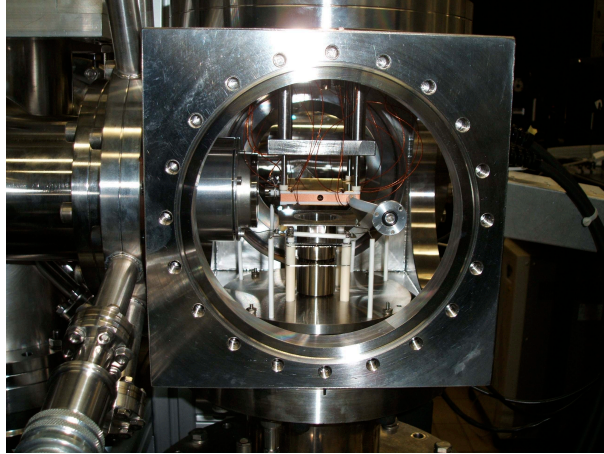


Figure 3.17: Photograph of the trap coupled to the tandem quadrupole mass spectrometer, showing the trap in the middle with the gas inlet tube on the right, the octopole pointing into the trap chamber from the left, and the Einzel lens of the reflectron below the trap.

3.6.5 Electronics

Various RF generators have been developed to drive multipoles^{148,238–241} (and a model corresponding to each of the cited designs has been employed in this thesis). They are based on push-pull oscillators that either directly drive an LC-circuit consisting of an air coil and the capacitance of the multipole or use a step-up transformer, so that the resonant circuit is composed of the secondary coil and the capacitance of the multipole.

For the operation of quadrupole ion trap TOF mass spectrometers, it is necessary to rapidly switch off the RF, which is normally applied to the ring electrode, before the end caps are pulsed to high voltage in order to extract the ions. This is usually achieved by stopping the oscillator and shorting the ring electrode to ground.^{200,242,243} For the purpose of developing a planar ion trap TOF mass spectrometer, a further complication arises since high voltage pulses have to be applied to the same electrodes that carry the RF.¹⁵⁷ A similar problem had to be solved for a cylindrical ion trap TOF mass spectrometer with two separate ring electrodes that simultaneously serve as RF and extraction electrodes²⁰⁸ and for the C-trap,²²⁰ a c-shaped quadrupole trap used to accumulate ions and then eject them in the radial direction so that they can be focused into an orbitrap.

Our solution for a viable circuit is schematically depicted in Fig. 3.18. The entire sequence

of events is controlled with an external TTL pulse (“RF start and stop”), whose rising edge starts the trapping cycle, while its falling edge triggers the ejection of the ions. Upon arrival of the control TTL, the timing unit of the instrument (“synchronization and delays”) enables an oscillator (“osc”), whose frequency can be fine-tuned to the resonance frequency of the circuit of about 3.2 MHz. This oscillator drives a variable current into a resonant circuit consisting of the primary coil of an air transformer as well as an additional capacitance and inductance. A RF waveform of variable amplitude is thereby generated in the two secondary coils, which are connected to the two pairs of comb electrodes. Each pair of combs is equivalent to a capacitance between the ends of the coil.

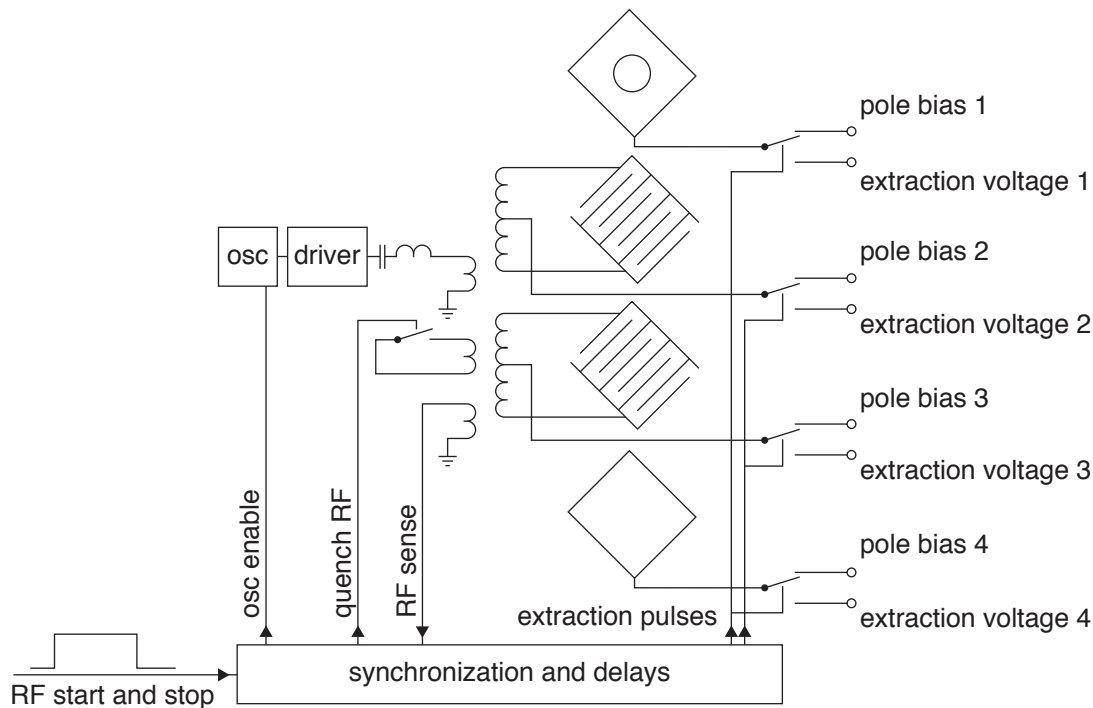


Figure 3.18: Schematic circuit of the RF/high voltage pulse generator used to generate the waveforms on the trap electrodes.

While ions are trapped, two separate pole biases (“pole bias 2” and “pole bias 3”) are applied to the RF electrodes via the center taps of the secondary coils. The extraction electrodes surrounding the trap are kept at a DC voltage labeled “pole bias 1” and “pole bias 4”, respectively. At the falling edge of the TTL, the timing unit synchronizes the following series of events. The oscillator is immediately disabled, and the first zero passage of the RF that is detected (“RF sense”) triggers the “RF quench” and the two separate “extraction pulses” on the RF electrodes and extraction plates, which occur after independently adjustable delays.

In order to rapidly shut down the RF, a separate secondary coil is short-circuited. The RF electrodes and extraction plates are pulsed to high voltage by means of MOSFET switches in push-pull configuration. The “extraction voltage 1” and “extraction voltage 4” are directly applied to the extraction plates, while the voltages on the RF combs are switched via their

center taps (“extraction voltage 2” and “extraction voltage 3”).

The RF generator was mounted as close as possible to the electrical feedthroughs, so that coaxial cables of only 20 cm length could be used and the total capacitance of the trap and cables could be kept as small as possible. In order to generate four symmetric RF outputs and to achieve a rapid quenching of the RF, a good coupling between the various coils is necessary, which would have been difficult with the coils wound onto the usual tube shaped coil forms. The individual coils were therefore wound onto discs, which could be closely stacked, so that a good coupling could be achieved. With this design, a 10% to 90% rise time of the extraction pulses on the RF combs of about 80 ns could be realized. After the short circuit, the RF amplitude decreases to about 43%, 16%, and 8% in one, two, and three RF periods, respectively, while smaller oscillations persist for about another 10 periods (see also Fig. 3.23 and section 3.7.5, where the influence of those residual oscillations on the signal and resolution are studied).

The following DC voltages are necessary to operate the trap. High voltages are generated with the power supply provided by the manufacturer of the reflectron (Jordan TOF Products, Inc., D-603) and several other high voltage power supplies (Bertran, 205 B-05R and EMCO High Voltage Corporation, Octo-Channel High Voltage System). Voltages on other electrostatic elements as well as the pole bias of the home-built octopole are provided from a Spectrum Solutions TD 1400 and two Dr. K. Witmer TF 300/0.25 power supplies. The octopole RF is generated by a MassTech RF Quad Generator. An Iota One pulse driver (Parker Hannifin) is used to pulse the solenoid valve.

3.7 Characterization

A proof of principle demonstration of a novel scientific instrument and the successful testing of a prototype are by themselves of only limited use. Only careful characterization can help to unveil limitations and establish improvements of the design, increase the theoretical understanding of the technique, and maybe lead to new developments. The characterization essentially consists of varying instrumental parameters and analyzing the effect with respect to different figures of merit, which could include *e.g.* the ion yield or signal intensity, the resolution of the TOF mass spectrum, and the storage time of the trap. Since these figures of merit are a function of a large number of variables, experiments should be carried out that yield useful cuts through this multidimensional surface that capture the essential characteristics. This is the goal of this section.

3.7.1 Experiments with the Test Setup

In the experiments using the test setup ions are directly created inside the trap. To this end gaseous aniline entrained in helium is leaked into the trap chamber, which is usually kept at pressures between $1\text{e-}7$ and $1\text{e-}5$ mbar. Aniline is ionized with the frequency doubled output of a Nd:YAG pumped dye laser at 281.5 nm with pulse energies of ~ 1 mJ/pulse, which is focused

parameter	value during trapping	value during extraction
“repeller”	0 V	2000 V
first RF combs	0 V pole bias	1768 V
second RF combs	0 V pole bias	686 V
“extractor”	0 V	326 V
DC electrodes	400 V	400 V
Einzel lens		0 V
deflector plates x		89 V
deflector plates y		0 V
first reflector voltage		816 V
second reflector voltage		1300 V
MCP detector		1700 V
RF amplitude	60 V	0 V
trapping time	variable, mostly 30 ms	
delay between the high voltage pulses of combs and plates	0 ns	
delay between short circuit and high voltage pulses	~500 ns	
number of averages	400	

Table 3.1: Typical voltages and timing parameters for the operation of the planar trap/TOF mass spectrometer in the test setup.

with a 50 cm lens into the center of the trap. The laser is operated at a frequency of 20 Hz. For experiments requiring a longer experimental cycle, a mechanical shutter is employed to reduce the number of laser pulses. Depending on the nature of the experiment, ions are stored for a variable amount of time and ejected in order to obtain a TOF spectrum. Table 3.1 lists typical values for the various voltages and timing parameters of the trap.

The experiments are timed with a Berkeley Nucleonics model 555 and a Stanford Research Systems DG 535 delay generator. TOF mass spectra are recorded with a 200 MHz, 2.5 GS/s oscilloscope (LeCroy WaveSurfer 24Xs-A), and a simple Visual Basic script is used to acquire, average, and store the data. A TTL output of the RF generator corresponding to the high voltage pulse on the RF combs is used to trigger the acquisition of a TOF spectrum.

3.7.2 TOF Mass Spectra with and without Trapping

Figure 3.19 compares mass spectra of aniline and its fragment ions that were obtained with static extraction voltages applied to the trap electrodes (top), so that the ions are immediately extracted after creation, and after 30 ms of trapping (bottom). For both measurements, the parameters were separately optimized; the settings for the trap mode spectrum are given in table 3.1. A voltage of 400 V was kept on the DC electrodes even when ions were extracted promptly, since it was found that applying the extraction voltages to the corresponding DC electrodes did not have any perceivable influence. The measurements were carried out at a pressure of

$\sim 8 \times 10^{-6}$ mbar and a RF amplitude of 60 V. The spectrum with static voltages is dominated by

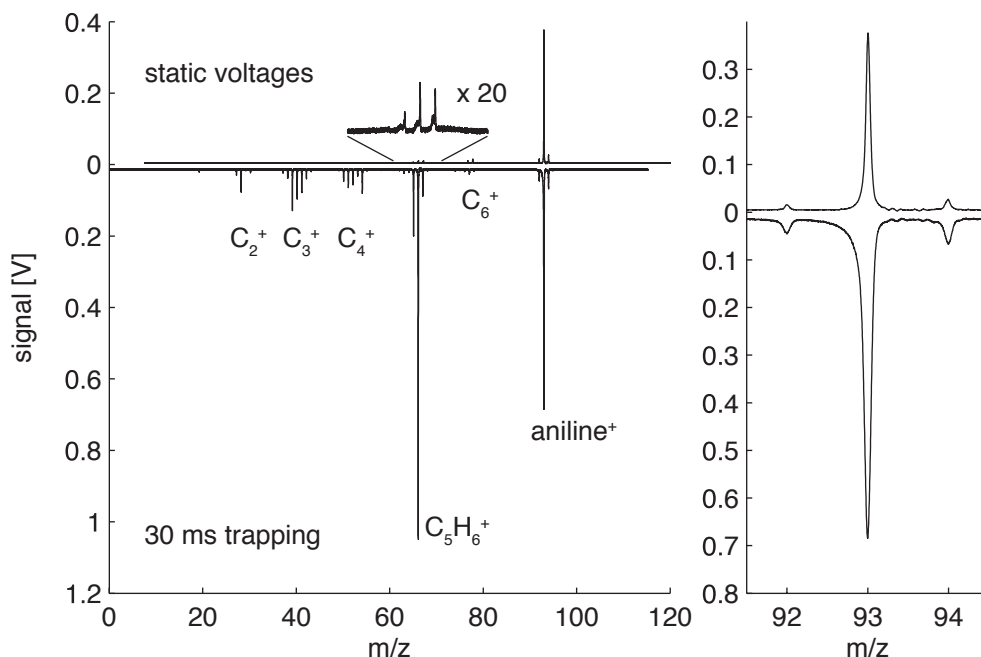


Figure 3.19: Comparison of mass spectra of aniline and its fragment ions obtained with static extraction voltages applied to the trap electrodes and after 30 ms of trapping.

the aniline parent ion at $m/z = 93$. At the employed laser power, some fragment ions are created, although they appear with much lower intensity. In the spectrum obtained after 30 ms of trapping, the parent ion peak appears with about 2.5 times the integrated intensity, while a range of fragments is visible, with the peak at $m/z = 66$ now dominating the spectrum.

The fragmentation behavior of aniline following REMPI is well-documented.^{244–246} For higher laser pulse energies, the absorption of further photons leads to the creation of a range of C_2^+ to C_6^+ fragments, with $C_5H_6^+$ (loss of HCN) as the most intense channel. The fact that strong fragmentation is observed upon trapping while fragments are nearly absent when the ions are extracted promptly may have two reasons. Because of the high trapping voltages applied to the DC electrodes, the ions are accelerated towards the center of the trap after creation and may be collisionally activated in this process, which could lead to an enhancement of the fragmentation efficiency (see also section 3.7.8, where the motion of the ions in the trap is analyzed in more detail). Moreover, it appears that at least the C_5^+ fragments are not formed promptly and may therefore be suppressed when the ions are extracted immediately. This is supported by the asymmetric peak shape in the spectrum with static voltages (see the inset of Fig. 3.19), which points to delayed fragmentation of metastable aniline ions.²²²

The observed increase in parent ion signal when ions are trapped before extraction can be understood on the basis of the results of sections 3.7.8 and 3.7.10. Briefly, the conclusion drawn there is that a redistribution of the ions in the trap occurs. The ion cloud is initially created along the entire laser beam path. However, only the ions in the center of the trap can be

efficiently extracted and reach the detector, so that prompt extraction is accompanied by ion losses. If the ions are stored before they are extracted, the ion cloud is focused to the center of the trap, which leads to the observed increase in signal intensity.

From the aniline parent ion peak (see Fig. 3.19, right), a mass resolution of $m/\Delta m = 1650$ for the spectrum with static voltages can be calculated. In trap mode, a lower resolution of only 890 is obtained. The comparison of both values allows one to disentangle different contribution to the peak width. The peak width with static voltages can be considered a measure of the quality of the alignment of the trap and the inherent performance of the reflectron itself. The increase in peak width observed when ions are trapped before extraction originates from the principle of operation of the trap. (It should, however, be noted that for trapped ions, a resolution of more than 1300 could be achieved when higher RF amplitudes were used, see section 3.7.15.)

It appears that one of the major contributions to the decrease in resolution should be the different spatial distribution of the ions when trapped. The focused laser beam initially creates an ion cloud with a very low spatial spread in the extraction direction, so that a high mass resolution is obtained if the extraction occurs promptly. The ion cloud subsequently expands to fill the trap volume, so that its larger spatial distribution leads to a reduction in resolving power (see section 3.7.8). This interpretation is supported by the observation that focusing the ion cloud more strongly by using higher RF amplitudes improves the resolution (see section 3.7.9). Further contributions to the peak width can originate from imperfections in the waveforms on the electrodes, such as residual RF oscillations on the combs (see section 3.7.5) and the finite rise times of the high voltage pulses. The aniline parent ion peak in the trap mode spectrum shows a slight shoulder on the lower-mass side. This asymmetry is not observed for most of the other masses like *e.g.* the C_2^+ to C_6^+ fragments and can be eliminated with a different choice of parameters.

3.7.3 Background Signal

Figure 3.20 shows a spectrum recorded after 10 s of trapping. As will be discussed below, the ions created by the laser pulse have largely escaped from the trap at this point in time. However, a large signal of aniline parent remains. A similar spectrum, though much lower in intensity, can be recorded if the laser is not fired at all. This suggests that gaseous aniline is ionized inside the trap, which could be due to plasma processes, which become even more likely once free electrons are created during the laser pulse. The increased intensity of the peak at $m/z = 94$ compared to the aniline parent ion peak points to processes in which aniline ions abstract an H atom from background gas. Weak fragment ion signals at $m/z = 39, 54$ and 65 are also observed.

For a short trapping time of *e.g.* 30 ms (as in Fig. 3.19) these processes do not play any role, which is, for example, evident from the isotope pattern of the parent ion peak. In order to derive trap characteristics from TOF mass spectra measured at long trapping times, however, one cannot rely on mass peaks which appear as background signal as well. Fortunately, laser

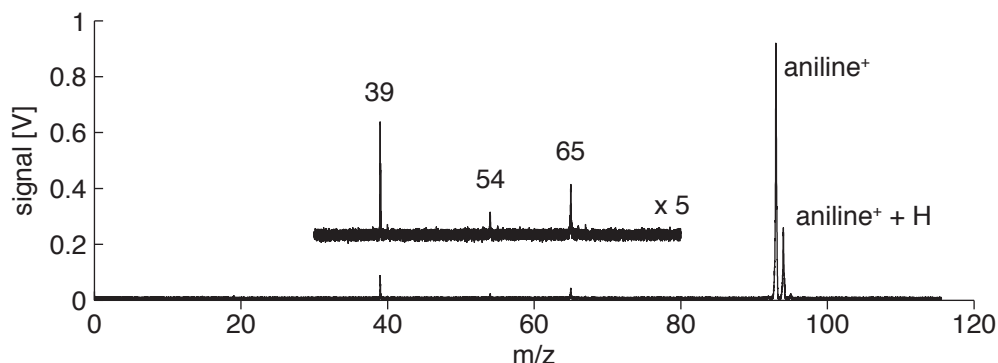


Figure 3.20: Spectrum recorded after 10 s of trapping showing background signal of aniline and some fragments.

ionization with a focused beam creates a range of fragments that do not coincide with fragments arising from background ionization.

3.7.4 Local Minima of the Effective Potential

As discussed in section 3.5, the chosen electrode geometry (1 mm wide RF electrodes, 1 mm apart) represents a compromise between the conflicting goals of achieving a high trap depth and a large field-free region in the center of the trap. The calculations predict local minima of the effective potential in the center of the trap, which are also reflected in simulated ion distributions (see Fig. 3.10). However, these simulations do not include space charge effects, and one might wonder if those local traps have any effect on the performance of the instrument.

The upper half of Fig. 3.21 shows the simulated effective potential in the center of a two-dimensional trap. The phases are applied as has been assumed so far, *i.e.* with the opposite phases applied to opposite electrodes. 15 local minima are visible, which are located in between neighboring electrodes, with the central minimum exactly in the center of the trap. (The potential for twice the number of electrodes with 0.5 mm width is drawn in blue and shows no local minima.)

If the RF phases on the upper combs are swapped as schematically indicated in the lower part of Fig. 3.21, the trap depth is essentially unchanged. This is the case because the field that an ion experiences is largely dominated by the closest RF comb due to the exponential dependence of the potential on the z coordinate (see Eqn. 3.13). However, the simulated effective potential now features 14 minima that are situated in between two opposite electrodes. This behavior can easily be rationalized, since minima of the effective potential correspond to saddle points of the potential, which obviously change their position in the described manner if the phases on one comb are swapped.

If ions are preferentially located in these minima, their extraction efficiency would consequently depend on the way the phases are applied, since the transmission is higher for ions passing in between the electrodes. Figure 3.22 shows mass spectra recorded with different RF

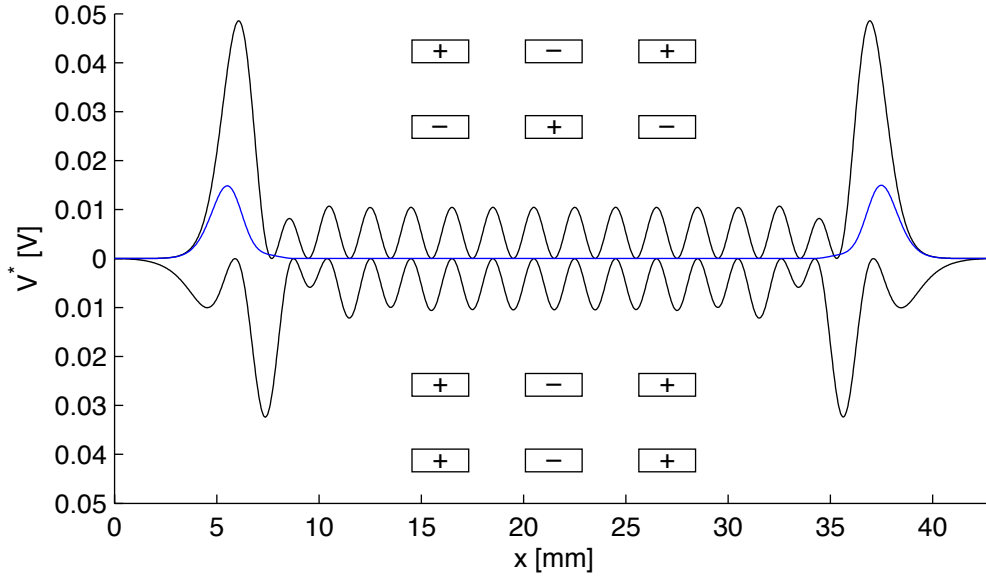


Figure 3.21: Simulation of the effective potential V^* in the center of a two-dimensional planar trap. Different positions of the local minima result when the same or the opposite RF phase are applied to opposite electrodes. Simulations for a trap with 1 mm (black) and 0.5 mm wide electrodes (blue) are shown for a 93 amu ion and a 3.2 MHz RF with 60 V amplitude. The RF phases are applied as indicated in the insets.

phases (top) and the same RF phase (bottom) connected to opposite electrodes (see the insets). A large RF amplitude of 213 V was used, which increases the depth of the local traps. With 400 V applied to the trapping DC electrodes, the ions are focused to the center of the trap, however, it can be assumed that after 30 ms of trapping and at a pressure of $3\text{e-}7$ mbar the ion cloud has not yet fully collapsed to its equilibrium size (see sections 3.7.6 and 3.7.10). Both mass spectra were recorded with otherwise identical parameters, and it was verified independently that these represent optimum conditions for both configurations.

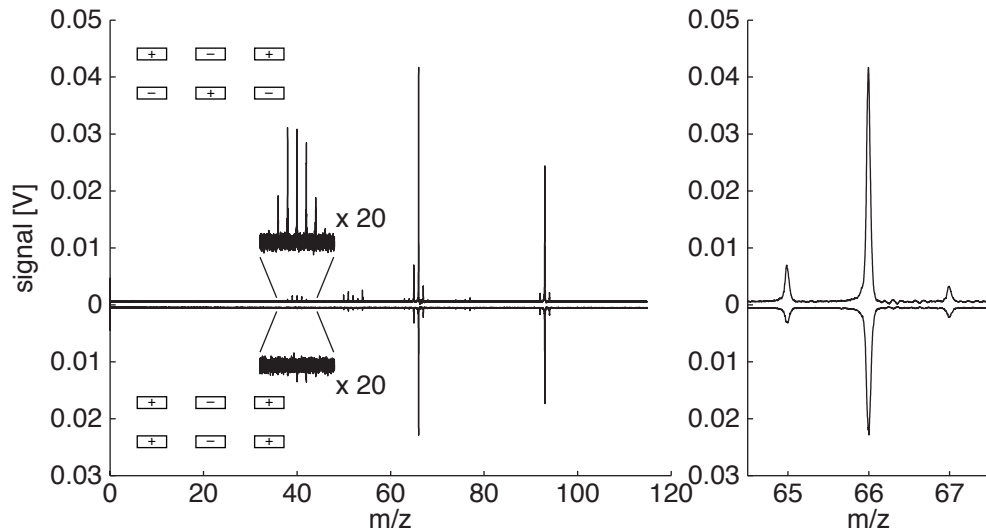


Figure 3.22: Mass spectra recorded with the same or the opposite RF phase applied to opposite electrodes, as indicated in the insets, but otherwise identical conditions: pressure $3\text{e-}7$ mbar, trapping DC 400 V, RF amplitude 213 V, 30 ms trapping, 400 averages.

As predicted, the top spectrum with different RF phases on opposite electrodes shows higher signal intensities. For the C_5H_6^+ fragment at $m/z = 66$, for example, the integrated intensity is 56% higher, while the C_2^+ ions are almost absent in the lower spectrum (see the insets of Fig. 3.22). In general, the increase in signal is larger for the lower masses, which is consistent with the hypothesis that local traps are the origin of the observed behavior, since their depth is inversely proportional to the ion mass (Eqn. 3.14). Since the effective potential is proportional to the square of the RF amplitude, the observed effect should be less pronounced for a lower RF amplitude. Indeed, at 60 V amplitude, the differences in integrated peak intensity are smaller, *e.g.* only 16% for the C_5H_6^+ fragment.

At the same time, a change of resolution can be observed. For the $m/z = 66$ peak, for example, resolutions of 1180 and 1010 are measured in the top and bottom spectrum of Fig. 3.22. Again, the effect is less pronounced for a lower RF amplitude. It appears that ions that are extracted through the holes in the RF combs have a higher probability of colliding with the electrodes, so that a lower mass resolution results.

The above experiments strongly suggest that local minima of the effective potential are indeed present as predicted from calculations and do have an effect on the ion distribution. Whereas they might prove disadvantageous if ions are to be cooled due to increased RF heating, they can be used to accumulate ions in between the RF combs, where higher ion transmission and resolution can be achieved. All following experiments were carried out with opposite RF phases connected to opposite electrodes.

Simulations show that the effect of the local traps on the ion distribution can be strongly reduced if desired. A potential applied to the extraction plates will leak into the trapping volume. This effect is obviously stronger in between the RF electrodes, so that a suitable repulsive voltage on the extraction plates can be used to compensate for local minima that are situated there. At 6 K buffer gas temperature and a RF of 60 V amplitude, a 93 amu ion will get trapped in a local minimum and will not be able to leave it. With a suitable repulsive voltage on the extraction plates, its distribution along x becomes homogeneous. However, increased RF heating results, since the field of the extraction plates pushes the ion into regions of higher RF fields.

3.7.5 Extraction Phase

As outlined in section 3.6.5, three different events determine the extraction conditions. After a zero passage of the RF has been detected, the RF is short-circuited, and high voltage pulses are applied to the RF combs and the extraction plates. The three corresponding delays can be adjusted separately. Figure 3.23 shows two waveforms (black) that were recorded on one of the RF combs with a RF amplitude of ~ 50 V and a high voltage pulse of 1.5 kV. The short circuit and the high voltage pulse were timed to occur simultaneously. The two waveforms differ in the phase of the RF at which the ions are extracted. The phases were adjusted to ~ 0 (maximum

voltage on the comb) and $\sim \pi$ (minimum voltage on the comb).

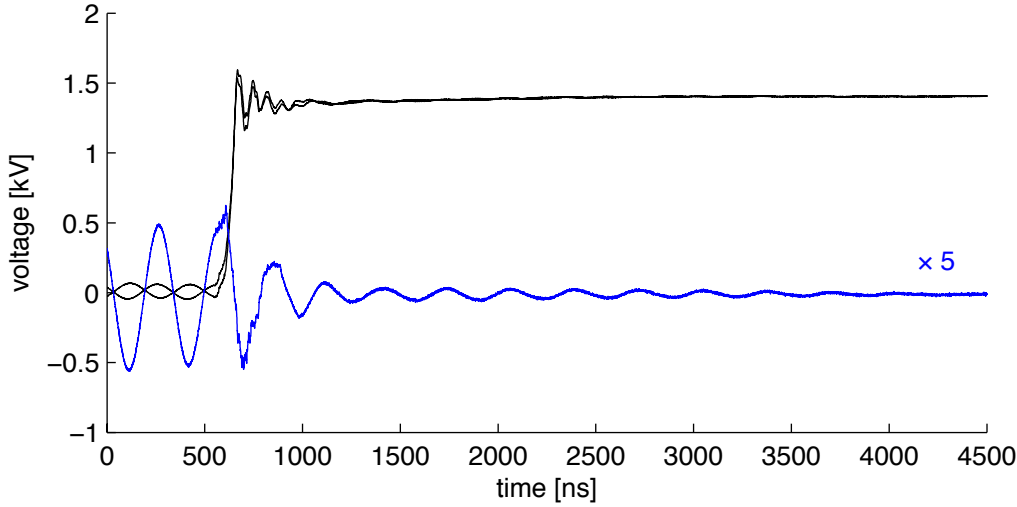


Figure 3.23: Waveforms on one of the RF electrodes for two different extraction phases (black) as well as their difference (blue). Short circuit and extraction pulse are simultaneous.

The difference of both waveforms (blue) reveals that residual RF oscillations are still present after the short circuit. They show an initial fast decay to an amplitude of below 2 V within three oscillations and are subsequently damped more slowly, persisting for about another ten periods. In the case of Paul trap/TOF instruments, (residual) RF oscillations during extraction were found to be detrimental to the mass spectral resolution.^{197,200,207} In order to study the effect of these residual oscillations in the current setup, mass spectra were recorded for different extraction phases after 30 ms of trapping. The short circuit of the coils and the high voltage pulse were timed to occur simultaneously. The waveform on one of the combs was simultaneously recorded, so that the extraction phase could be determined by fitting a cosine to the RF part of the waveform and a third-order polynomial to the initial rise of the high voltage pulse and calculating their intersection. The integrated peak intensity and mass spectral resolution were extracted from a gaussian fit to several of the mass peaks.

The relative peak intensities as a function of the extraction phase are shown in Fig. 3.24 for the ions with $m/z = 28, 66$, and 93 . The data are corrected for a drop in pressure from $2.4\text{e-}6$ to $9.4\text{e-}7$ mbar in the chamber (and a corresponding drop in sample concentration) that occurred during the course of the experiment.

A periodic modulation of the ion signal with the RF phase is apparent, with the variation amounting to 70-80% of the maximum signal. The curves are shifted to later phases for lower masses. This observation can be explained if one considers that ions passing between the RF electrodes will be deviated if residual RF oscillations are present, so that the divergence of the beam in the y dimension is increased and fewer ions reach the detector. The amount of deviation obviously depends on the RF phase at which the ions pass the combs which leads to the observed phase dependence. Optimum transmission will occur if the ions pass the electrodes during a

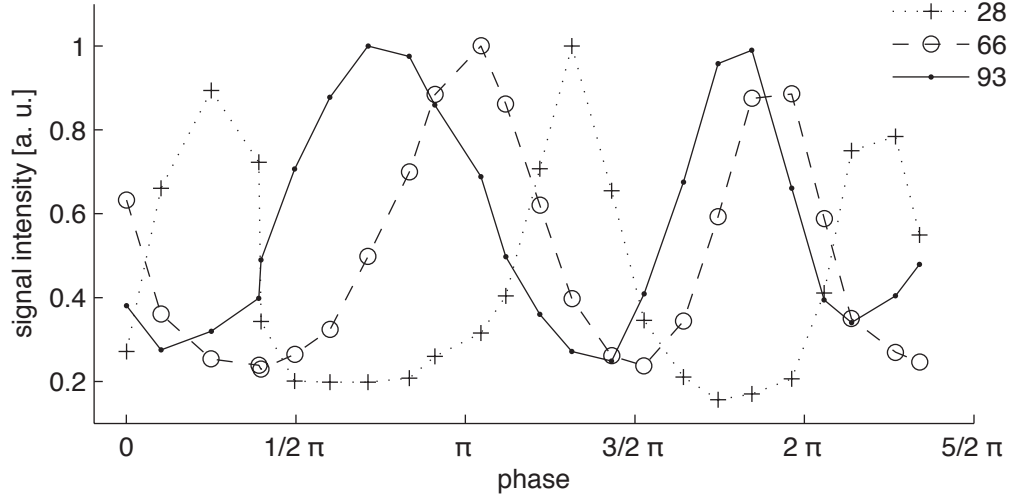


Figure 3.24: Dependence of the ion signal on the extraction phase. The integrated signal intensities for the species with $m/z = 28$, 66, and 93 are shown as a function of the extraction phase for simultaneous short circuit and high voltage pulses.

zero passage of the residual RF. Since lighter ions reach the combs faster, their transmission maximum occurs for later extraction phases. The mass resolution is likewise modulated with the RF phase, and the curves for different masses are shifted relative to each, comparable to the curves for the signal intensity. However, these data show a poor signal to noise ratio and are therefore not discussed in more detail here.

Extraction efficiency and resolution should increase if the extraction is delayed with respect to the clamping of the RF, so that much lower RF amplitudes are present at the moment of extraction. This is evident from the experimental results shown in Fig. 3.25. Here, the simultaneous extraction pulses were fixed to a specific delay and RF phase, while the timing of the short circuit was varied. Figure 3.25 shows the integrated signal intensity as well as the resolution of the aniline cation peak as a function of the delay of the short circuit relative to the extraction pulses.

At positive delays, the short circuit follows the extraction pulse so that the ions are extracted while the RF is still applied to the combs. Upon moving to negative delays, the signal rises sharply, reaching twice the level when the short circuit precedes the extraction pulses by ~ 100 ns. The resolution shows a similar behavior. In between a delay of -100 ns and 0 ns, it suddenly drops from a level of about 1000 to a level of about 850. This means that if the RF is short-circuited at least 100 ns before the extraction of the ions, the residual oscillations are sufficiently reduced, so that a detrimental effect on the signal and resolution can be avoided.

Figure 3.26 shows another experiment, in which the short circuit was fixed to a specific timing and RF phase while the simultaneous extraction pulses were delayed by 600 to 1000 ns, *i.e.* about two to three RF periods. The signal and resolution of the ions with masses 28, 66, and 93 are shown.

While signal and resolution are not constant, the fluctuations are not correlated with the

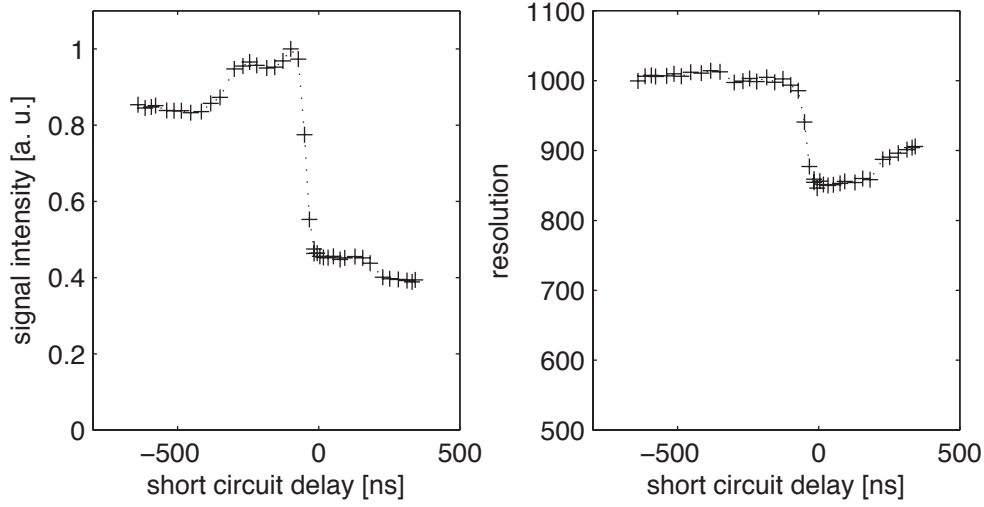


Figure 3.25: Dependence of the ion signal and resolution on the delay between the short circuit and the extraction pulses. The relative integrated signal intensity and resolution of the aniline ion peak are shown as a function of the delay of the short circuit relative to the extraction pulses, which are kept fixed in time and occur at a fixed phase of the RF. For negative delays, the short circuit precedes the extraction.

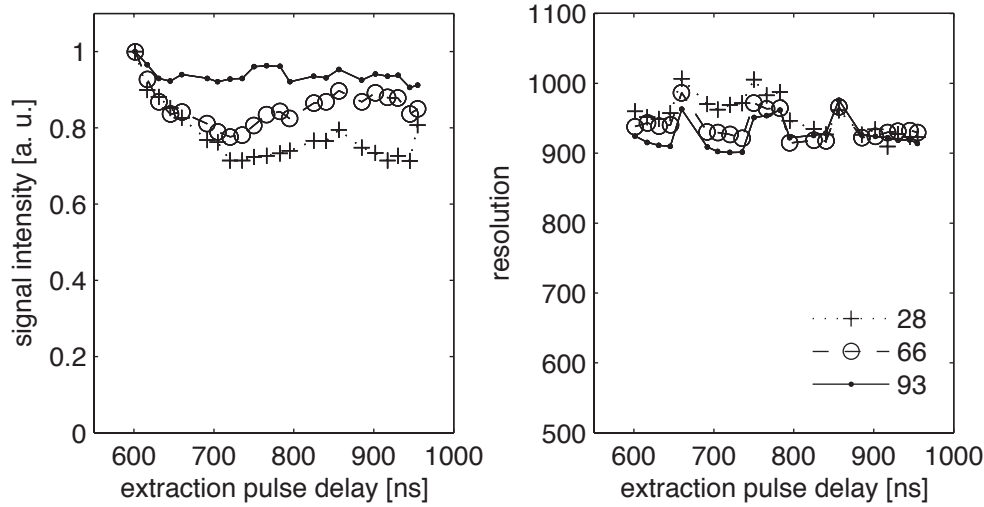


Figure 3.26: Dependence of the ion signal and resolution on the delay between the short circuit and the extraction pulses at long delays. The relative integrated signal intensity and resolution for the ions with $m/z = 28$, 66, and 93 are shown as a function of the delay between the short circuit and the extraction pulses. The extraction pulses follow the short circuit, which is kept fixed in time and occurs at a fixed phase of the RF.

RF half-period of ~ 150 ns. Most notably, no mass-dependent phase shift for different species is observed, which makes it likely that the variations originate from systematic errors. It can be concluded that at these long delays between short circuit and ion extraction, no influence of residual RF oscillations on the signal and resolution can be detected within the accuracy of the measurement. For this reason, all following measurements were carried out with the extraction pulses delayed by ~ 500 ns with respect to the short circuit.

3.7.6 Trapping DC Voltage

Figure 3.27 displays the dependence of the integrated intensity and resolution of the aniline cation peak as a function of the voltage that is applied to the trapping DC electrodes. The experiments were carried out at a pressure of 2.5×10^{-8} mbar and with an ion storage time of 40 ms. The observed trend is practically identical for ions of different mass. No signal is

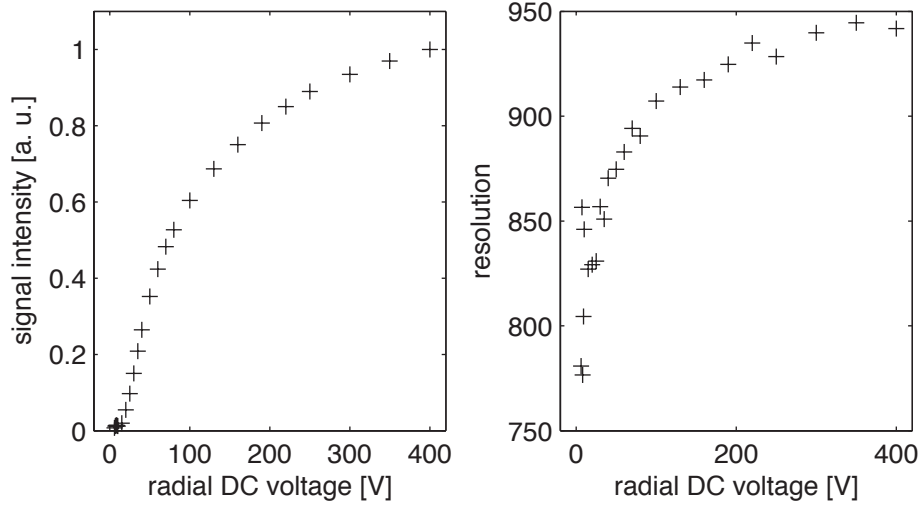


Figure 3.27: Signal intensity and resolution of the aniline cation mass peak as a function of the voltage applied to the trapping DC electrodes.

measured without voltage applied to the trapping DC electrodes. It rises steeply up to a voltage of 100 V and then starts to level off at 400 V, the highest voltage measured. The resolution shows a similar trend, rising from about 780 at 6 V to about 940 at 400 V.

A simulation of the different ion distributions in the trap that result when either 10 V or 400 V are applied to the trapping DC electrodes seems to offer an explanation (Fig. 3.28, black and blue curves, respectively). Although the fields from the DC electrodes do not penetrate deeply into the trapping volume, higher potentials on the trapping electrodes strongly reduce the spatial extent of the ion cloud in the x and y directions (while the distribution in the z dimension is almost unchanged). At 400 V, the shape of the x distribution indicates that the ions are now mostly confined to only three local minima that occur in the effective potential, compared with nine at 10 V. The half width of the ion cloud in the y dimension similarly shrinks from 15 mm to 5 mm.

A smaller ion cloud can explain a better mass resolution of the TOF mass spectra. Also, if the extraction efficiency is higher for ions located in the center of the trap, the gain in signal for higher trapping DC voltages could be accounted for. However, the analogous experiments described in section 3.7.17, where externally generated ions are injected into the trap, do not show the same behavior. It appears more likely that the high trapping voltages necessary to maximize signal and resolution rather indicate flaws in the operation of the trap. The observation of ion signal without ionizing laser (see section 3.7.3) already indicates that plasma processes

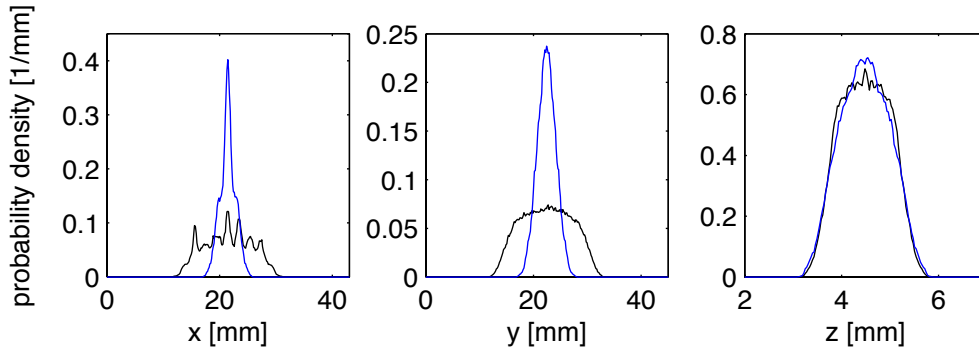


Figure 3.28: Simulation of the ion distribution in the three-dimensional trap at 298 K and $1\text{e-}4$ mbar helium pressure, with 10 V (black) and 400 V (blue) applied to the trapping DC electrodes.

might be occurring inside the trap. Since the largest RF fields occur at the edges of the electrode array (see Figs. 3.21 and 3.42), confining the ions closer to the center of the trap could possibly prevent them from being neutralized with free electrons.

Another possible explanation could be the charging up of nonconducting surfaces through ions created directly by laser ionization or in plasma processes, which could lead to ion losses and a reduction of the resolution. Since the Macor supports are the most likely candidates to carry patch potentials, removing the ions from their vicinity could lead to the improvements in resolution and ion signal that are observed at higher DC voltages. Section 3.7.17 will shed some more light on this issue and show that the observed behavior must be linked to the method of ion creation and not to the inherent properties of the trap.

3.7.7 Pressure

Investigations on the properties of quadrupole ion trap/TOF mass spectrometers identified the following dilemma, which all ion trap/TOF devices face. While the injection efficiency of externally generated ions increases with the helium pressure inside the trap, the mass spectral resolution decreases due to a larger number of collisions during extraction.^{214, 247} In order to analyze the effect of the pressure in the current setup, mass spectra were recorded for different pressures under otherwise identical conditions. Figure 3.29 displays the mass resolution of the aniline ion peak as a function of the pressure in the trap chamber (which was one order of magnitude higher than the pressure in the flight tube). The behavior is similar for different masses, although different resolutions for different masses are observed at the same pressure.

A resolution of about 810 is measured at a pressure of $2.8\text{e-}7$ mbar. It increases to its maximum of about 870 at $1\text{e-}5$ mbar and subsequently falls to a value of about 720 at $7.5\text{e-}5$ mbar. This agrees qualitatively with the findings of a study on a quadrupole ion trap/TOF instrument,²⁴⁷ which argued that collisions during extraction lead to a lower resolution at higher pressures. The observed decrease in resolution at low pressures was ascribed to insufficient collisional cooling of the ions after they had been injected into the trap.

In the present experiment, ions are generated inside the trap along the laser beam path,

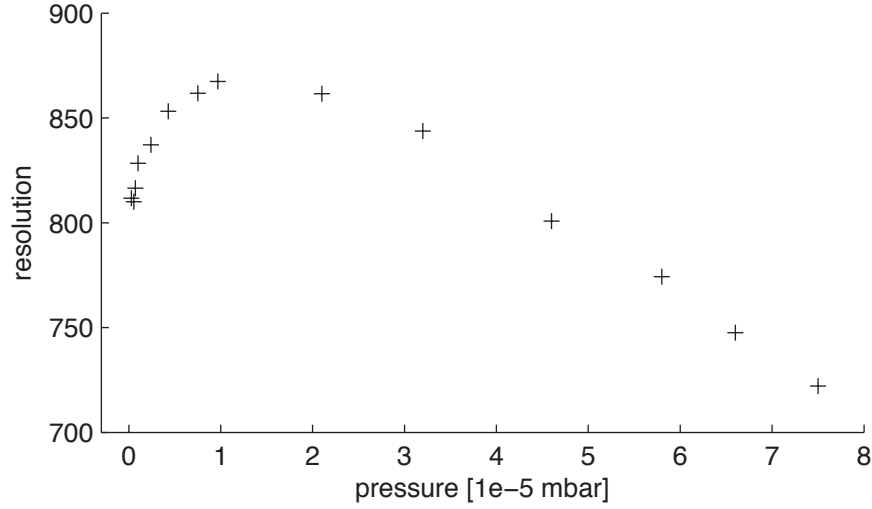


Figure 3.29: Mass resolution of the aniline ion peak as a function of the pressure in the trap chamber.

starting from a thermal speed distribution of the neutrals, so that it seems, at first sight, that no collisional cooling should be necessary. However, as will be detailed in the following section, the high trapping potential of 400 V applied to the DC electrodes accelerates the ions towards the center of the trap after they have been created. Thus, ions created far from the trap center initially acquire high translational energies. At low pressures, the trapping time is insufficient to cool the ions, so that a lower mass resolution results.

3.7.8 Ion Motion

Figure 3.30 displays the integrated signal intensity and resolution of the aniline peak as a function of trapping time, recorded with 60 V RF amplitude and at a pressure of 4.6×10^{-7} mbar. The signal initially falls steeply and reaches a minimum at about 40 ms, before it recovers within the following 2 s. The resolution drops from an initial value of almost 1200 to a minimum of about 840 on the same time scale of 40 ms and then rises again to asymptotically approach a value of about 900. The signal and resolution of other mass species show a qualitatively similar behavior.

These observations support the above interpretation of the results on the low pressure dependence of the mass resolution, since they suggest that at low pressure, the ion cloud equilibrates only on the time scale of several seconds. The ions are initially created with thermal velocities, but immediately accelerated by the DC trapping fields. A larger velocity spread decreases the extraction efficiency as well as the resolution. Some of the fast ions cannot be trapped and escape from the extraction volume, leading to further signal losses. As the ion cloud is recooled and focused to the center of the trap, signal and resolution increase again. It should be noted that at a pressure of 1×10^{-5} mbar or above, the initial drop in ion signal can no longer be observed (see Fig. 3.34). Instead, the signal rises immediately and peaks within several ms. It appears that at higher helium densities, the time scale for the initial drop is so short that it is not

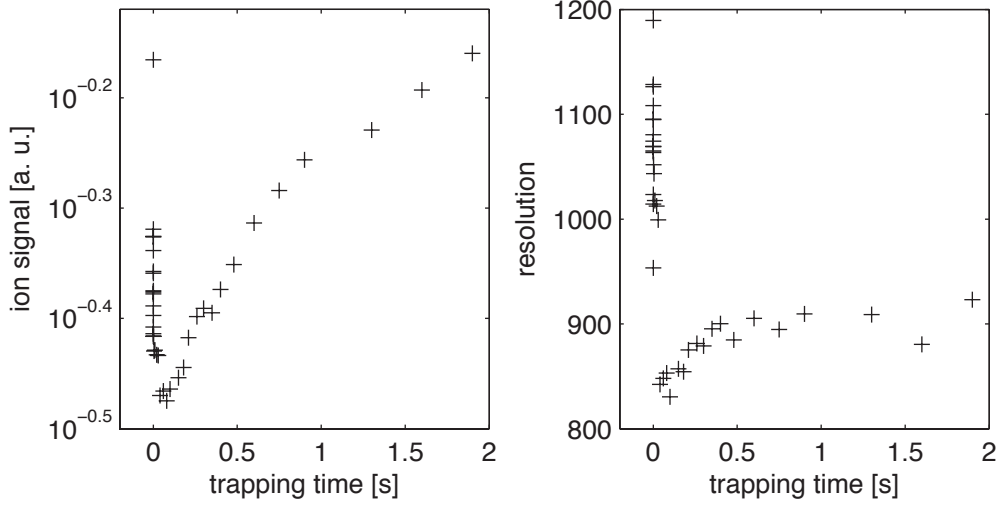


Figure 3.30: Integrated signal and resolution of the aniline cation peak as a function of the trapping time. Mass spectra were recorded with 60 V RF amplitude and at a pressure of 4.6×10^{-7} mbar.

captured any longer.

This interpretation is also qualitatively confirmed by a SIMION simulation of 595 ion trajectories starting from a thermal distribution (298 K) of 93 amu ions along a line through the center of the three-dimensional trap (60 V RF amplitude, 400 V applied to the DC electrodes). A helium pressure of 1×10^{-4} mbar was simulated in order to save computing time, and the buffer gas temperature was set to 298 K. Figure 3.31 shows the standard deviations of the ion coordinates σ_i and velocity components σ_{v_i} as a function of time, which can be considered a measure of the spatial extent of the ion cloud and the translational temperature of the ions.

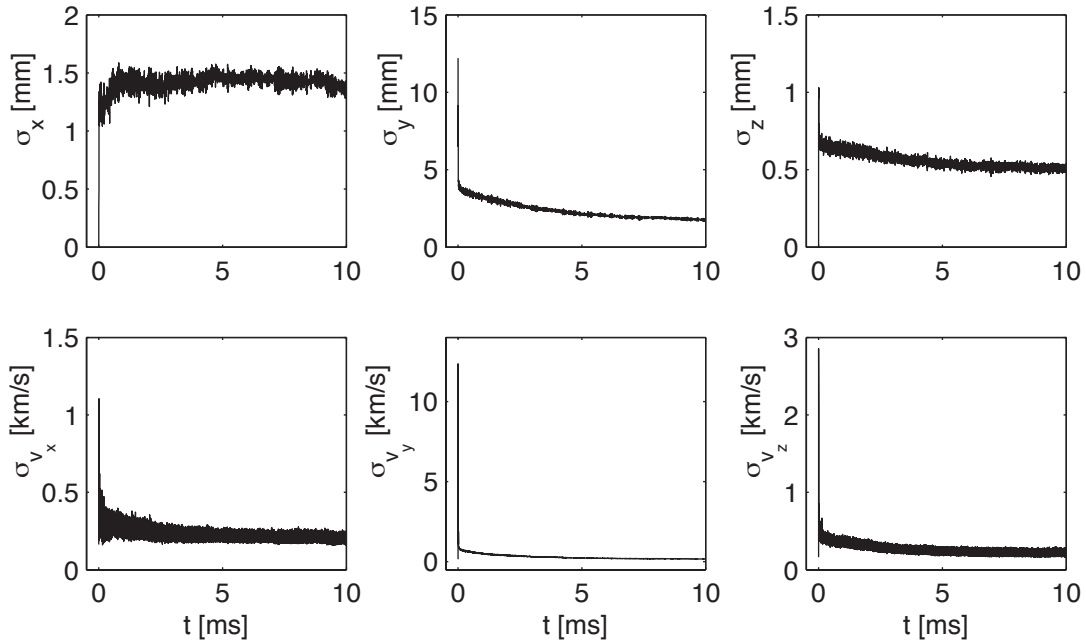


Figure 3.31: Simulation of the trajectories of ions created by laser ionization in the three-dimensional trap. The standard deviations of the ion coordinates and velocity components as a function of time demonstrate the relaxation of the ion cloud.

Since in the simulation, the ions are initially distributed along a line in the y direction, the ion cloud has a large initial spread in this dimension. Within the first $10 \mu\text{s}$, σ_y drops sharply, as the ions are accelerated towards the center of the trap and some of the ions with high kinetic energies are lost. Subsequently, the ion cloud is slowly cooled to its equilibrium width. In the x and z dimensions, the ions start from a point and then fill the trap volume. σ_z first overshoots its equilibrium value and then approaches it from above.

This behavior can be understood when considering the standard deviations of the components of the ion velocity. All three components start at the value corresponding to a thermal distribution. As the ions are accelerated in the y direction, σ_{v_y} rises sharply. In collisions, kinetic energy is transferred into the x and z dimensions, so that σ_{v_x} and σ_{v_z} peak at the same time as σ_{v_y} . At the simulated pressure of $1\text{e-}4$ mbar (which is larger than the experimental pressures), the velocities then recool to their equilibrium values on a time scale of several ms. It is thus conceivable how at low pressures, collisional cooling could be insufficient, so that the ions initially have a larger spatial spread and a wider velocity distribution, which leads to the observed decrease in resolution at low pressures and short trapping times. This investigation lays the basis for section 3.7.15, which studies the injection of externally generated ions into the trap. While a gas pulse is necessary to decelerate the arriving ions, residual gas at the moment of extraction is detrimental to the resolution.

3.7.9 RF Amplitude, Studied in the Test Setup

While the voltage on the DC electrodes determines the width of the ion package in the x and y dimensions (see section 3.7.6), the RF amplitude controls the spread of the ion cloud in z direction. Figure 3.32 displays the dependence of the ion signal and mass spectral resolution on the RF amplitude.

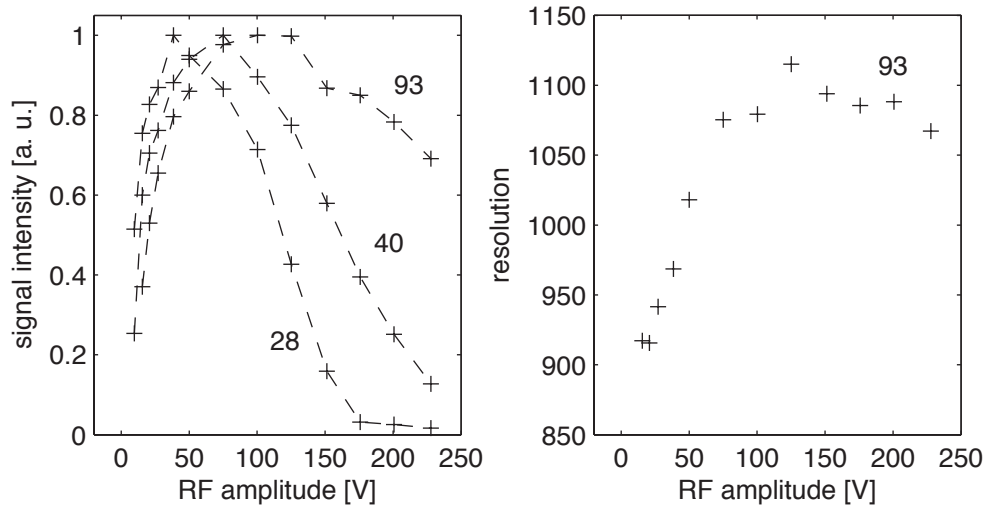


Figure 3.32: Dependence of the ion signal and resolution on the RF amplitude. The relative integrated signal of the 93, 40, and 28 amu mass peaks and the resolution of the 93 amu mass peak are shown as function of the RF amplitude.

For the three masses shown ($m/z = 93$, 40, and 28), the signal intensity initially increases steeply with the RF amplitude and then goes through a maximum, before it falls again. The maximum, however, is mass-dependent and shifts to higher amplitudes for higher masses, which is in line with the mass-dependent storage and transmission properties of linear multipoles. It also qualitatively agrees with Eqn. 3.17, which shows that the amplitude corresponding to the maximum achievable trap depth is proportional to the ion mass. However, the maximum trap depths are predicted to occur at lower amplitudes than the maxima of the curves recorded in Fig. 3.32, *e.g.* the maximum trap depths for 28 and 93 amu ions are already reached at ~ 7 and ~ 24 V, respectively.

Besides the trap depth, the measured signal intensities also depend on the efficiencies of ion deceleration and extraction, which both increase with the RF amplitude. As described in section 3.7.7, ions that are created far from the center of the trap initially acquire high kinetic energies. At higher RF amplitudes, the probability increases that these fast ions can be successfully decelerated and trapped. The effect of the RF amplitude on the extraction efficiency is analyzed in Fig. 3.33, which displays simulated ion distributions at 60 V (black) and 200 V RF amplitude (blue). The distribution in the x direction shows that at higher RF amplitudes, the ion population is more strongly confined to the local minima occurring in between neighboring electrodes, so that fewer ions will collide with the electrodes during extraction. Finally, higher RF amplitudes could also compensate any misalignment of the electrodes by pushing the ions to the center of the trap and further away from the combs, so that the effect of any field distortions is mitigated.

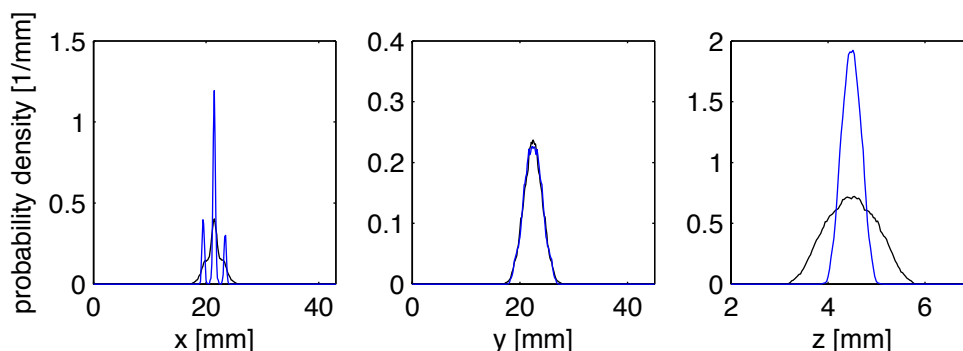


Figure 3.33: Simulated spatial distribution of the aniline cation ($m/z = 93$) for a RF amplitude of 60 V (black) and 200 V (blue) with 400 V applied to the trapping DC electrodes.

A mass-dependent storage efficiency is undesirable for analytical purposes or *e.g.* in laser experiments where fragments have to be stored along with the parent ions. By reducing the width and distance of the RF electrodes, the mass-dependence of the maximum trap depth can be reduced (see Eqns. 3.15–3.17 and Fig. 3.7).

The dependence of the resolution on the RF amplitude is similar for different mass peaks, although a lower resolution is observed for the lower masses. As shown for the aniline cation (Fig. 3.32, right), the resolution increases with the amplitude, here from about 920 at 20 V

to about 1075 at 100 V before it levels off. This effect can be understood if one considers the effect of the RF amplitude on the ion distribution in the extraction direction (see Fig. 3.33). While the distribution in the y dimension is practically unchanged when the RF amplitude is increased from 60 V (black) to 200 V (blue), the ion cloud is focused in the z dimension, so that its width is reduced from about 1.5 to 0.5 mm. This explains why the resolution initially increases with the RF amplitude, as a smaller spatial spread in the extraction direction will improve the resolution.

The fact that the resolution does not increase any further once the amplitude surpasses ~ 125 V could point to the occurrence of space charge effects, which are not included in the simulation and which would not allow the ion cloud to be focused any further. However, under different experimental conditions and with a larger number of ions, the resolution was found to increase up to an amplitude of 200 V, which makes it more likely that different factors limit the resolution in the test setup (see the discussion in section 3.7.14).

3.7.10 Trapping Time in the Test Setup

In order to determine the trapping time of the planar trap, one cannot rely on the signal of the aniline cation or any other species that is continuously being generated inside the trap even without interaction with the ionizing laser (see section 3.7.3). In Fig. 3.34, the intensity of the C_5H_6^+ ion ($m/z = 66$) is therefore monitored as a function of the trapping time, since this laser induced fragment is largely absent from the background spectrum in Fig. 3.20. In this experiment, the trap was operated with a RF amplitude of 60 V.

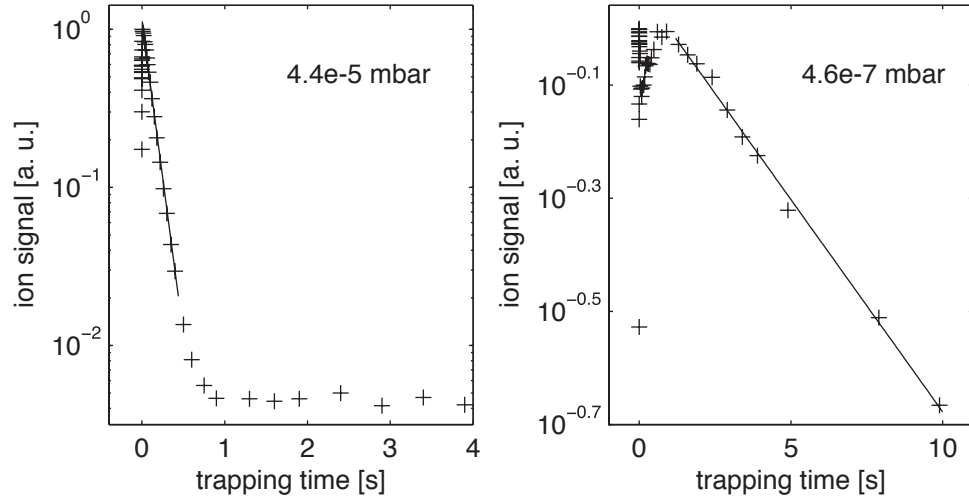


Figure 3.34: Determination of the trapping time of the test setup for different pressures. The signal of the $m/z = 66$ fragment ion is shown as a function of the trapping time at a pressure of $4.4\text{e-}5$ mbar (left) and $4.6\text{e-}7$ mbar (right). A $1/e$ time of 110 ± 1 ms and 5.8 ± 0.1 s, respectively, is determined from the fit.

The time dependence of the ion signal shows marked differences when recorded at $4.4\text{e-}5$ mbar (left) and $4.6\text{e-}7$ mbar (right). At high pressure, the signal peaks after 5 ms and then decreases

with a $1/e$ time constant of 110 ± 1 ms, as determined from the fit shown in Fig. 3.34. A small, constant background signal can still be observed after several seconds. At low pressures, the ion signal shows a time dependence similar to the one described in section 3.7.8, which was explained with the motion of the ions in the trap. However, since the C_5H_6^+ fragment is not being created promptly, the ion signal first rises sharply within the first 100 μs (which is not the case for the other masses). As noted before, the signal then drops, reaches a minimum at about 60 ms, rises again as the ion motion is being cooled, and then decreases exponentially after a second maximum at 900 ms. From a fit to the exponential decay, a trapping time of 5.8 ± 0.1 s can be determined.

By lowering the pressure by two orders of magnitude, the achievable storage time of the trap increases by a factor of 50. Together with the indications noted above that plasma processes might be occurring inside the trap (see section 3.7.3), this observation suggests that a higher number density of the neutral sample leads to a deterioration of the properties of the trap. The observed loss rates would then not be inherent to the trap, but could originate from the operating conditions. This question will be discussed again in section 3.7.16, where the trapping time of the very same trap is determined in the absence of any background gas except helium (which is necessary in order to trap the externally generated ions). Another increase of the storage time of almost two orders of magnitude is observed under these conditions, which supports the above interpretation of the results with the test setup.

3.7.11 Experiments with the Trap Coupled to the Tandem Quadrupole Mass Spectrometer

As a step towards the goal of using the trap for the buffer gas cooling of externally generated ions, the trap was coupled to the tandem quadrupole mass spectrometer described in section 2, so that the injection of ions could be studied (see section 3.6.4). In these experiments, ions are generated by nano-ESI of a 10 μM /1 μM solution of the amino acids serine and phenylalanine in methanol/water (50:50) to yield a range of different molecular ions, clusters, and fragments. They are stored in the octopole between the first two benders at a helium pressure of $1\text{e-}4$ mbar and periodically ejected at a frequency of 10 Hz. Passing straight through the second bender and the second octopole, they enter the trap. They are decelerated in collisions with helium, which has been pulsed into the trap prior to their arrival, stored for 90 ms, and ejected in order to obtain a TOF spectrum. In another type of experiment, the ions are first injected into the 22-pole and stored for about 50 ms. The voltages on the second bender and the lenses before the 22-pole are subsequently switched, so that the ions can be ejected from the 22-pole and transferred into the trap, where they are stored for about 35 ms, before a TOF spectrum is acquired.

Table 3.2 lists typical values for the various voltages and timing parameters of the trap used in these experiments. The extraction voltages are different from the ones given in table 3.1, since

parameter	value during trapping	value during extraction
“repeller”	0 V	2000 V
first RF combs	-30 V pole bias	1629 V
second RF combs	-30 V pole bias	864 V
“extractor”	0 V	718 V
entrance DC electrodes	-17 V	-17 V
other DC electrodes	30 V	30 V
trap frame	-120 V	-120 V
Einzel lens		0 V
deflector plates x		135 V
deflector plates y		0 V
first reflector voltage		867 V
second reflector voltage		1500 V
MCP detector		1450 V
RF amplitude	200 V	0 V
trapping time	variable, mostly 90 ms	
delay between the high voltage pulses of combs and plates	0 ns	
delay between short circuit and high voltage pulses	~500 ns	
number of averages	400	

Table 3.2: Typical voltages and timing parameters for the operation of the planar trap/TOF mass spectrometer when coupled to the tandem mass spectrometer described in chapter 2.

the distance of the third Wiley-McLaren electrode from the trap is now shorter. Moreover, the voltage applied to the two trapping DC electrodes that the ions pass upon injection is different from the potential on the remaining DC electrodes, which greatly enhances the injection efficiency. With a voltage of -120 V applied to the frame of the trap, a further increase in ion signal can be achieved. Since the potential of the frame does not influence the storage time of the trap, this observation suggests that the signal enhancement is due to an improved injection efficiency. Finally, a lower voltage on the MCP detector is used to avoid saturation due to the much larger ion signals.

The experiments are timed with a Berkeley Nucleonics model 565 delay generator and National instruments timers as described in section 2. As before, TOF mass spectra are recorded with a 200 MHz, 2.5 GS/s oscilloscope (LeCroy WaveSurfer 24Xs-A), which runs a Visual Basic script for the purpose of data acquisition. A TTL output of the RF generator corresponding to the high voltage pulse on the RF combs is used to trigger the acquisition of a TOF spectrum.

3.7.12 Comparison of Quadrupole and TOF Mass Spectra

Figure 3.35 compares a TOF mass spectrum of a serine/phenylalanine mixture (A, bottom) using the planar trap with a mass spectrum obtained by scanning the first linear quadrupole

analyzer of the instrument and recording the continuous ion signal as a function of the selected mass (A, top). The TOF spectrum was obtained by first accumulating the ions in the octopole, injecting them into the 22-pole and then transferring them into the trap. The trapping and extraction parameters are listed in table 3.2. The region of the protonated phenylalanine peak in the TOF spectrum is shown in (B).

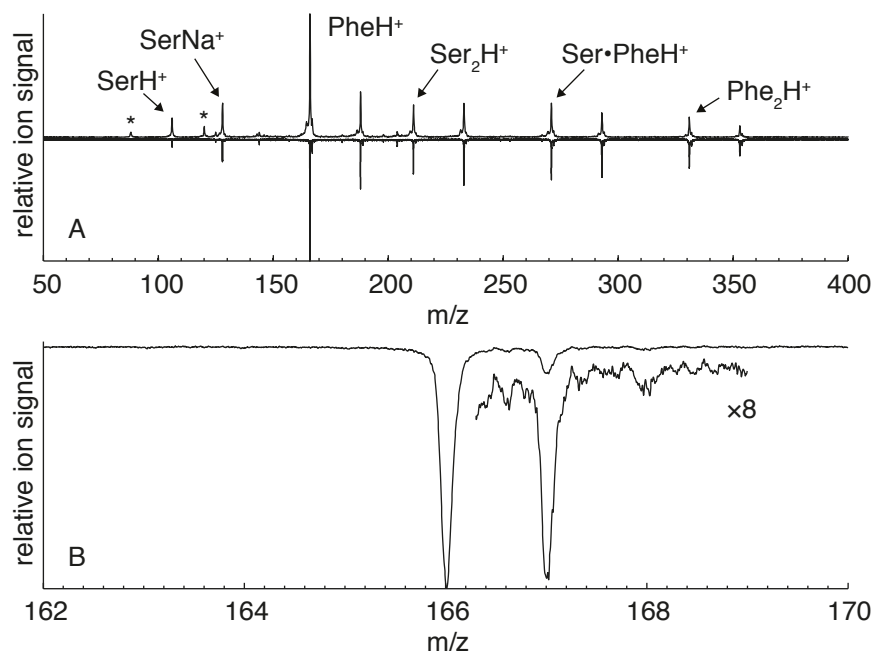


Figure 3.35: (A) Mass spectra recorded with the first quadrupole analyzer (top) and with the planar trap/TOF mass spectrometer (bottom) of an electrosprayed mixture of serine and phenylalanine. (B) The region of the protonated phenylalanine peak in the TOF spectrum.

The protonated amino acids, their singly-protonated 1:1 clusters, as well as the corresponding sodiated species can be identified in (A). The two spectra are largely similar, however, a slight discrimination of the lower masses in the TOF spectrum is apparent. In section 3.7.14, it was shown how at high RF amplitudes on the trap combs, lower masses are slightly suppressed. Since the above spectrum was recorded with a RF amplitude of 200 V, this could explain the observed difference. However, the mass discrimination could also be a consequence of the chosen RF amplitudes of the octopole and 22-pole or the settings of the quadrupole benders. The mass peaks at 88 and 120 amu (marked with asterisks) are absent in the TOF spectrum, which makes it likely that they belong to clusters that dissociate upon trapping.

As most other species in the quadrupole mass spectrum, the protonated phenylalanine peak at 166 amu (Fig. 3.35, right) is accompanied by a number of smaller peaks at lower masses which are absent in the TOF spectrum. This could also point to larger multiply charged clusters which dissociate upon trapping. More likely, they are an artifact which we frequently observe for some combinations of the quadrupole resolution and the ion velocity in the quadrupole.

3.7.13 TOF Mass Spectra of Laser Induced Fragment Ions

The development of the instrument described in this chapter was originally motivated by the goal to obtain a TOF spectrum of the ions stored in the 22-pole with good sensitivity and resolution. Figure 3.36 presents a proof of principle experiment, in which mass selected protonated phenylalanine ions were cooled in the 22-pole (trap temperature of 4 K) and then injected into the planar trap to obtain a TOF mass spectrum. The spectrum in the bottom part of Fig. 3.36 (“laser off”) shows the intense peak of protonated phenylalanine at $m/z = 166$ (cut off at 15 mV) as well as a CID fragment at $m/z = 120$ (loss of H_2O and CO).²⁴⁸ Moreover, metastable fragmentation due to collisional activation during extraction is evident from the broad features at $m/z = 90 - 120$.

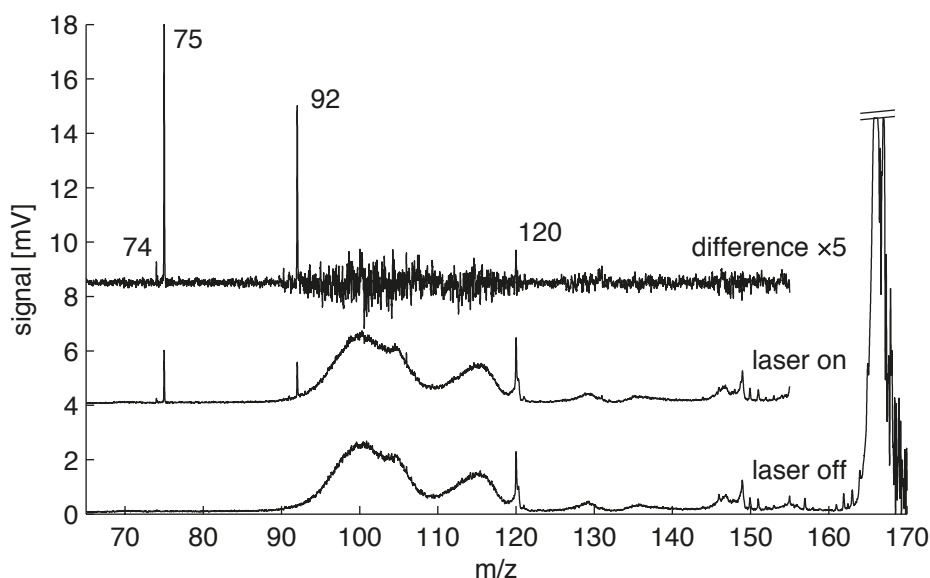


Figure 3.36: TOF mass spectrum of photofragments of protonated phenylalanine (mass selected in the first quadrupole). The difference of the spectra recorded with and without laser irradiation reveals the creation of fragments at 75, 92, 120, and 74 amu. The spectra were recorded with 1200 averages.

When the ions stored in the 22-pole are irradiated at 37529.6 cm^{-1} (which corresponds to the band origin of conformer B in the terminology of reference ¹¹³), photofragments are created, which can successfully be detected in the TOF spectrum (Fig. 3.36, “laser on”). In a previous study employing a quadrupole for mass selection, their masses were assigned as $m/z = 74$ and $m/z = 91 - 93$.¹¹³ The higher resolution that is available with the current setup, however, allows for an unambiguous assignment. As the difference of both mass spectra shows, the most intense fragmentation channel actually corresponds to the loss of the phenylalanine side chain at $m/z = 75$ ($-\text{C}_7\text{H}_7$) and is accompanied by a much weaker channel at $m/z = 74$, where the additional loss of an H atom is observed ($-\text{C}_7\text{H}_7 - \text{H}$). The second most intense fragment actually appears at $m/z = 92$ ($-\text{H}_2\text{O} - \text{CO} - \text{HCN} - \text{H}$), which corresponds to none of the channels observed in CID experiments. Furthermore, an enhancement of the fragment at 120 amu can be detected.

The observed metastable fragmentation contributes to a background signal that interferes with the fragment ion signal. It could be eliminated if a mass gate was used to suppress the parent ion signal. In order to implement a TOF detection scheme for photofragments generated in the 22-pole as outlined above, it would, furthermore, be necessary to develop suitable data acquisition software, improve the transfer of the ions into the trap, and, probably, deal with sources of analog noise, which was beyond the scope of this work.

3.7.14 RF Amplitude, Studied with the Trap Coupled to the Tandem Quadrupole Mass Spectrometer

Figure 3.37 displays the signal intensity and resolution of the protonated phenylalanine peak ($m/z = 166$) as a function of the RF amplitude. Ions were collected in the first octopole (0 V pole bias) and injected straight into the trap (-30 V pole bias), where they were stored for 90 ms before a TOF spectrum was recorded. The observed dependence is comparable for ions of different mass.

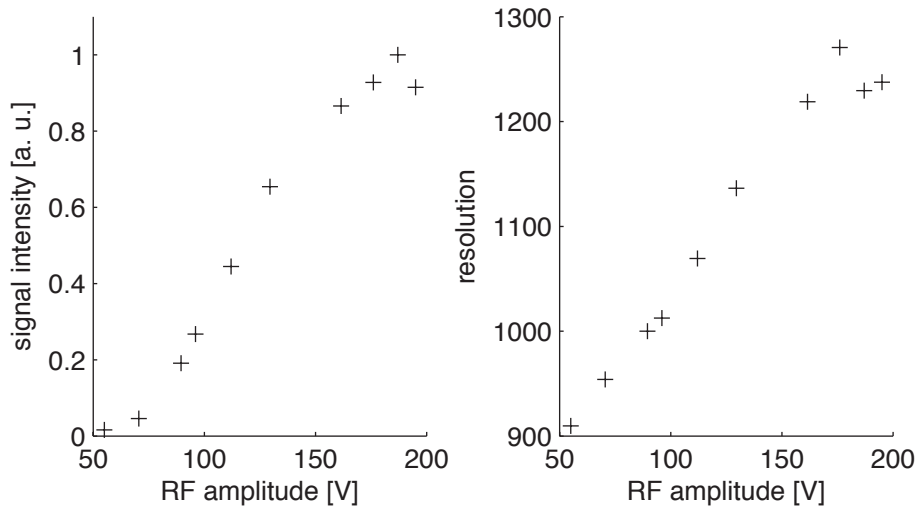


Figure 3.37: Dependence of the signal intensity and resolution of the protonated phenylalanine peak ($m/z = 166$) on the RF amplitude.

The ion signal increases steadily with the RF amplitude (in the measured range up to 200 V), which is ascribed to an increased ion injection efficiency at higher RF amplitudes. As discussed in section 3.5, the trap depth initially rises with the square of the RF amplitude, but goes through a maximum once the volume in which adiabatic ion motion is possible becomes smaller than the physical volume of the trap (see Fig. 3.7). Under the present conditions, the maximum trap depth is reached at a RF amplitude $U_0^{max} = 37$ V (Eqn. 3.17). It is therefore clear that the observed increase in ion signal is not due to a higher trap depth, but to an increasing injection efficiency. Under the present experimental conditions, ions are essentially unguided inside the bender, which seems to result in a divergent ion beam that requires higher injection energies (30 V) for efficient trapping. It appears that higher RF amplitudes increase the probability of a successful reflection of a fast ion at the RF combs shortly after injection and that the higher

injection efficiency more than compensates the lower trap depth.

Figure 3.37 also shows that the resolution of the TOF mass spectra continuously increases with the RF amplitude, which resembles the behavior that was found in experiments with the test setup (section 3.7.9). There, however, no further increase of the resolution was found beyond an amplitude of ~ 125 V. Two explanations for this discrepancy seem probable. In experiments with the test setup, evidence was found that plasma processes take place within the volume of the trap, which are fueled by the presence of neutral sample. These processes could lead to a charging up of non-conductive surfaces like the Macor frame, which could either prevent the ion cloud from being focused any tighter with increasing RF amplitude or simply limit the achievable resolution due to the resulting inhomogeneous extraction fields.

The following sections contain further examples of how superior results could be obtained with the present setup as compared to the test setup. Since the very same trap was used in both instances, this strongly suggests that the different method of ion generation is at the origin of the observed differences.

3.7.15 Gas Pulse

When ions are injected into the trap, a high gas density is desirable for optimum trapping efficiency, while a low pressure at the moment of ion extraction will lead to a higher resolution. In order to reach higher peak pressures inside the trapping volume during the helium pulse while reducing the overall gas load on the system, a copper frame was inserted in between the upper and lower half of the trap, which reduces the conductance of the otherwise open structure (see Fig. 3.5). Gas is injected through a tube attached to the frame.

The following experiment was carried out in order to determine the temporal profile of the gas pulse and the injection efficiency as a function of time. Different ions produced from nano-ESI of a serine/phenylalanine solution were stored in the first octopole. A $80\ \mu\text{s}$ long ion package was periodically injected into the trap and stored for about 90 ms, before a TOF spectrum was acquired. The length of the helium pulse that was injected prior to the arrival of the ions was adjusted for maximum ion signal. Figure 3.38 displays the total ion signal of some of the most intense mass peaks as a function of the delay between the arrival of the ions and the gas pulse.

The injection efficiency rises steeply and peaks after the first $400\ \mu\text{s}$, drops to 80% of its maximum after another $500\ \mu\text{s}$, and then decreases exponentially with a $1/e$ time of about 1.75 ms. Efficient ion injection occurs over a period of about 1 ms. Because several collisions with helium atoms are necessary to decelerate an ion, the injection efficiency will depend more than linearly on the gas density. The ion signal therefore drops rapidly as the pressure in the trap decreases, so that ~ 3 ms after its maximum, the injection efficiency already becomes vanishingly small. For longer time scales, information about the pressure inside the trap can be obtained from the extraction efficiency and resolution of the TOF mass spectra. With the ion package and the gas pulse synchronized for maximum signal, the intensity and resolution of the

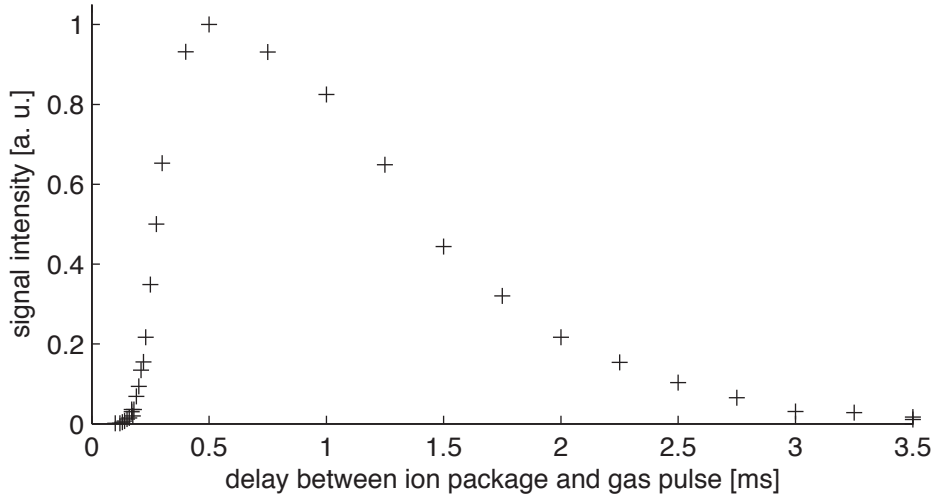


Figure 3.38: Characterization of the injection efficiency as a function of the delay between the helium pulse and the moment of ion injection.

protonated phenylalanine peak ($m/z = 166$) were monitored as a function of the trapping time (Fig. 3.39).

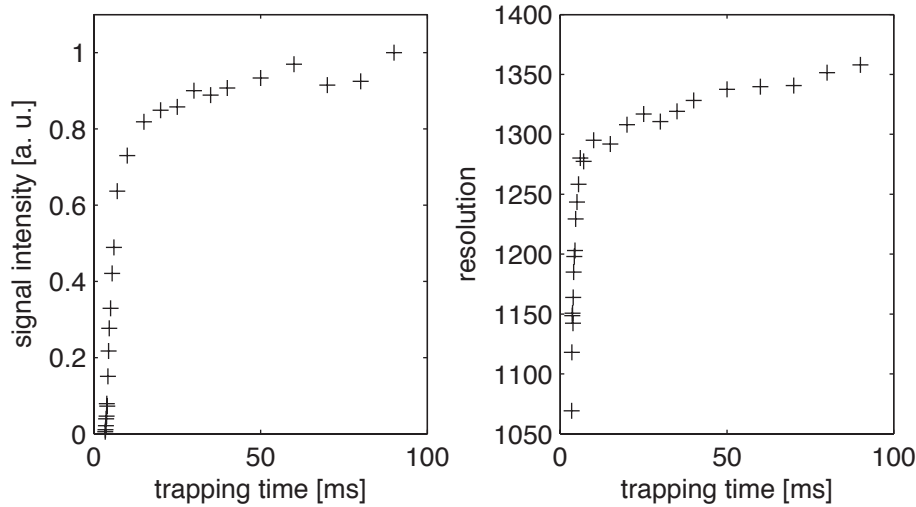


Figure 3.39: Dependence of the signal intensity and resolution of the protonated phenylalanine peak ($m/z = 166$) on the trapping time.

No TOF spectrum can be recorded within the first ~ 3.5 ms because of the high gas density inside the trap. The signal intensity rises steeply up to 15 ms after ion injection and then continues to increase steadily, although at a lower rate. The resolution shows a similar behavior, rising from below 1100 to about 1300 within the first 10 ms and then increasing more slowly to about 1350 after 90 ms of trapping.

This section highlights how a subtle balance has to be struck between the conflicting requirements of generating high pressures inside the trap during ion injection and low pressures during extraction, while keeping the overall gas load sufficiently small. The instrument presented here faces essentially the same dilemma as the Paul trap/TOF devices with respect to the pressure.

However, the problem should be less severe, since considerably higher injection efficiencies can already be expected at lower pressures. With a higher pumping speed in the trap chamber, one could omit the frame that was placed in between the two halves of the trap, so that a faster pump-out time could be realized, leading to a higher resolution at earlier extraction times. Injecting compressed ion packages would also facilitate the task, since the high pressure necessary for efficient injection would not have to be maintained for a long time, so that shorter helium pulses could be used. Finally, the picture will change at cryogenic temperatures, where the pump-out times will be longer.

3.7.16 Trapping Time of the Trap Coupled to the Tandem Quadrupole Mass Spectrometer

Figure 3.40 shows the ion signal of protonated phenylalanine and its CID fragment ($m/z = 166$ and 120) as a function of time between ion injection and acquisition of a TOF spectrum. Mass selected protonated phenylalanine was stored in the octopole and directly injected into the trap, which was operated at an amplitude of 200 V. The data points up to 100 ms, 60 s, and 300 s were recorded with 400, 10, and 4 averages, respectively.

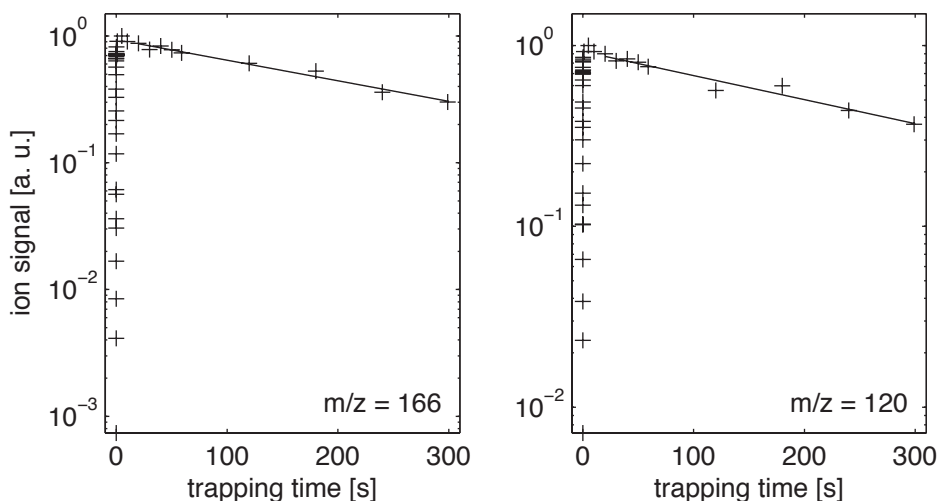


Figure 3.40: Determination of the trapping time for protonated phenylalanine and its CID fragment ($m/z = 166$ and 120, respectively). A $1/e$ time of 268 ± 14 s and 327 ± 28 s, respectively, is determined from a fit for trapping times ≥ 20 s.

The ion signals peak at about 5 s trapping time and then gradually decrease to about 30% and 37% of their maximum over a time of 300 s. A $1/e$ time of 268 ± 14 s and 327 ± 28 s, respectively, is determined from a fit for trapping times ≥ 20 s. Surprisingly, the achievable trapping times are almost two orders of magnitude longer than the ones determined with the test setup (section 3.7.10). However, it is hard to imagine how this result could be due to an artifact. Unlike in the test setup, no neutral sample is present that could fuel the continuous regeneration of the ionic species. Furthermore, similar trapping times are observed for very different masses, while species other than the ones injected into the trap do not appear in the mass spectrum.

Finally, the fact that the ion signal decreases exponentially after a trapping time of 5 s and does not continue to grow indicates that the ions are not continuously regenerated.

If plasma processes are the origin of the ionization of neutral sample in the test setup, it is conceivable that free electrons involved in the same processes could lead to a fast neutralization of the ions. Neutralization, rather than escape of the ions from the trapping volume, would then be at the origin of the observed loss rates. Free electrons could also originate from the laser pulse in the first place and speed up the creation of a plasma. Another possible explanation for the inferior trapping times in the test setup could also be the contamination of the electrode surfaces with neutral sample, which is excluded under the much better vacuum conditions of the present setup.

3.7.17 Trapping DC Voltage

Another surprising result was found when the signal of protonated phenylalanine was monitored as a function of the voltage on the six DC electrodes surrounding the trap that do not function as entrance electrodes (Fig. 3.41). Mass selected ions were stored in the first octopole and injected into the trap, which was operated with a pole bias of -30 V, a RF amplitude of 143 V, and -17.3 V applied to the entrance DC electrodes. After 90 ms of storage, a TOF spectrum was acquired.

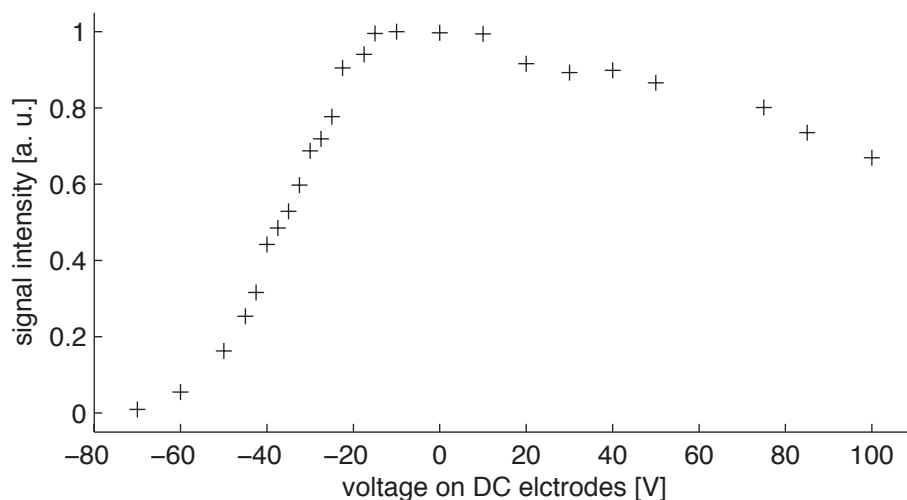


Figure 3.41: Dependence of the ion signal on the voltage applied to the trapping DC electrodes. The signal of protonated phenylalanine ($m/z = 166$) is displayed as a function of the voltage applied to the six DC electrodes that do not serve as entrance electrodes (labeled as “other DC electrodes” in table 3.2).

Marked differences are observed compared to the analogous experiment with test setup, where the signal dropped with decreasing trapping DC, reaching zero when the pole bias voltage was applied to the DC electrodes (see section 3.7.6). Here, the ion signal has a maximum when the voltage applied to the DC electrodes lies about 30 V above the pole bias and steadily decreases for higher voltages. Most strikingly, however, the signal is still at 60% of its maximum

with the DC electrodes held at the pole bias potential (-30 V) and falls only slowly when the trapping potential is lowered further. It drops to 50% when the DC electrodes are held at ~ 10 V below the pole bias and only approaches zero at ~ 40 V below the pole bias. This finding essentially means that the DC electrodes are not necessary to confine the ion cloud to the trapping volume, which seems at odds with the way multipole traps are usually operated.

Simulations of ion trajectories including collisions with helium at 298 K show that ions can be trapped over long periods of time even if the DC electrodes are kept at the pole bias potential. In order to understand this phenomenon, it is helpful to consider the simulated effective potential V^* of the RF field in the center plane of the trap (Fig. 3.42).

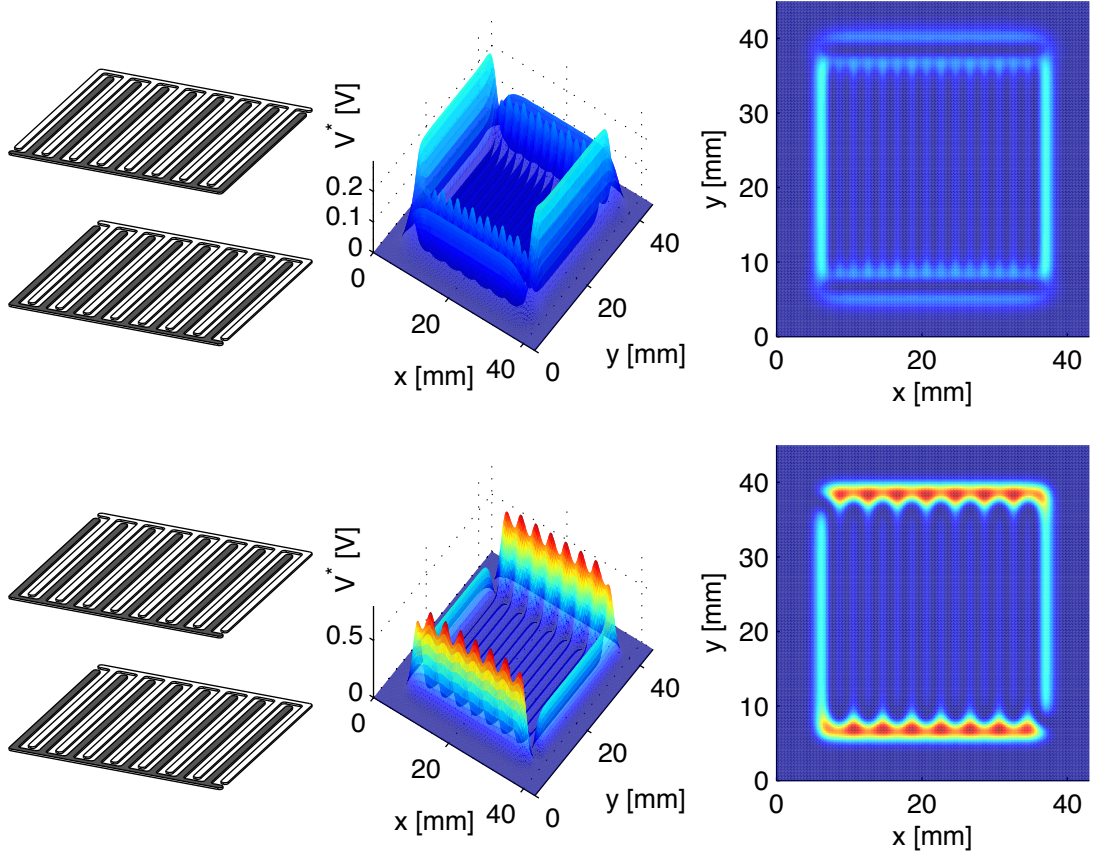


Figure 3.42: Simulation of the effective potential V^* for a 166 amu ion in the center plane of the trap (3.2 MHz RF, 200 V amplitude). Opposite RF phases are applied to opposite electrodes. Fringe fields lead to effective potential walls surrounding the RF electrode array in the current electrode arrangement (top row). In an alternative geometry (bottom row), gaps are visible at the upper left and lower right corners of these walls.

In the electrode arrangement of the current setup (top row), small effective potential walls surround the RF electrodes. They originate from fringe fields at the edges of the electrode arrays and are sufficiently high to confine the ion cloud in the x and y directions. The walls stretching in the y dimension are also visible in the two-dimensional simulation of Fig. 3.21. They arise because the outermost electrodes of the comb structure only have one neighboring electrode of opposite phase, so that the field in their vicinity is no longer multipolar. For a 166 amu ion

(3.2 MHz RF, 200 V amplitude, opposite RF phases applied to opposite electrodes), these walls have a height of about 0.3 V. The jagged effective potential barriers stretching in the x direction have a height of about 0.16 V and originate from the oscillating fields between the electrode tips and the handle of the opposite comb. Where both RF walls join, they form a saddle point, which creates a barrier of 0.14 V.

The simulations thus demonstrate that ions can be stored in an “RF only” trap, in which fringe fields prevent the ions from escaping in the x and y directions. However, if the DC electrodes are set to a potential of only 1 V below the pole bias, the ions escape as soon as they approach the DC electrodes. Fringe fields therefore cannot be the only explanation for the observed effect. It seems possible that a slight misalignment of the delicate RF electrodes could create local minima of the effective potential close to the center of the trap. They could be deep enough to locally confine ions despite an attractive potential on the DC electrodes, whose fields do not penetrate deeply into the trap. Another explanation for the observation could be that the Macor supports surrounding the free-standing electrode structure charge up and create trapping fields of their own.

In the experiments with the test setup, a trapping voltage of 400 V maximized the ion signal and resolution. With the setup described here, however, the resolution showed only a slight variation with the trapping voltage. Since the exact same ion trap was used for both experiments, this strongly suggests that the different observations are linked to the method of ion generation and not to inherent properties of the trap. If in the test setup, ions are, indeed, destroyed in plasma processes or patch potentials lead to ion losses and shorter storage times, as discussed above, this could simply mask the more subtle effects that could be studied here.

The arrangement of the RF combs (Fig. 3.42, top left) has D_2 symmetry if one also considers the handles of the combs. However, an alternative structure with D_{2h} symmetry is also conceivable (Fig. 3.42, bottom). Interestingly, the RF walls created by the fringe fields in such a configuration leave two gaps (upper left and lower right corner). In simulations, ions are found to escape from the trapping volume through these openings if no trapping potential is applied to the DC electrodes.

3.8 Conclusions and Outlook

In this chapter, the design, development, and characterization of a planar multipole ion trap TOF mass spectrometer was described. The process involved the construction of two generations of the trap, which were coupled to an existing reflectron time-of-flight mass spectrometer. The final design employed laser cut gold coated electrodes on Macor supports. Suitable electronics were developed to supply the complex waveforms to the trap electrodes. A trapping time of 268 s for $m/z = 166$ ions and resolutions above 1300 could be achieved. Ion generation inside the trap by laser ionization as well as the injection of externally generated ions were demonstrated. For the latter experiments, the trap was coupled to a tandem quadrupole mass spectrometer with

a cryogenic 22-pole ion trap, which involved equipping the planar trap with a short octopole guide and ion optics, so that ions could be injected. With this setup, sufficient sensitivity was demonstrated to detect laser fragments that had been generated in the 22-pole.

Despite these encouraging results, the present instrument is obviously still at the level of a prototype, and the principle advantages of the design that theory and calculations predict have not been fully realized or even explored. In the following, different aspects of the instrument performance are discussed and suggestions are presented for future improvements and possible applications.

Background signal In experiments with the test setup, it became obvious that the gaseous neutral sample present in the trap volume was continuously being ionized and fragmented, probably through plasma processes occurring inside the trap. Evidence was found that these undesirable processes reduced the achievable storage time and mass resolution. The trap electrodes had been designed with rounded tips so as to avoid these complications. When viewed under a microscope, however, the electrodes show sharp edges which result from their fabrication by laser cutting. Moreover, little spikes of molten material protrude from their surface near the cut. In a future design, a fabrication method that eliminates these defects and produces rounded edges might considerably improve the performance of the instrument. However, with helium as the only background gas, evidence for these processes could no longer be found.

Injection efficiency Theoretical considerations suggest that injecting ions into a planar ion trap should be possible with near 100% efficiency, comparable to linear multipoles and in strong contrast to Paul traps. However, absolute injection efficiencies are notoriously difficult to measure, and no rigorous study could be undertaken with the setup in its current configuration. Sufficient sensitivity could be demonstrated to detect the small number of laser fragments that had been generated in the 22-pole. A slight mass discrimination was observed, which originates from the mass-dependence of the RF amplitude corresponding to optimum trapping conditions.

The experiments also suggest that a good collimation of the ion beam improves the injection efficiency, which is understandable given the small separation of the trap electrodes of only 5 mm. A more careful design of the ion optics preceding the trap and the addition of several planar DC electrodes to the entrance side of the trap to better steer the incoming beam might improve the trapping efficiency.

Pressure The instrument faces the same dilemma as quadrupole ion trap/TOF devices. While a collision gas is necessary to efficiently inject and cool ions, high pressures deteriorate the achievable mass resolution. Increasing the conductance of the trap while providing enough pumping speed would decrease the pump-out time and thereby the pressure at the moment of extraction. Ideally, ions could be injected in a short bunch and decelerated in a pulse of collision gas passing straight through the trap. Lowering the energy of the arriving ions could also

reduce the pressure that is necessary for efficient injection. In the end, however, the conflicting requirements of efficient ion injection and high mass resolution cannot be fully reconciled and represent a fundamental drawback of the approach.

Resolution With static voltages applied to the trap electrodes, so that ions created by laser ionization inside the trap were promptly ejected, a mass resolution of 1650 was obtained. For a given laser pulse length and diameter of the focus, this resolution is limited by properties of the reflectron (reflector with grids, stability of the electronics, detector rise time, etc.) as well as by the homogeneity of the extraction fields inside the trap. In the current design of the trap, the latter is limited by the finite width and the imperfect alignment of the free-standing RF electrodes, which can be recognized upon close inspection. These defects could be eliminated and the resolution could be improved if one were able to produce thin, free-standing structures with high precision. While this would be difficult in a manually assembled trap, the use of microfabrication techniques could offer a solution.

When ions were trapped prior to extraction a decrease in mass resolution was observed. The larger spatial spread of the ions in the trap was identified as one of its major causes, and it was demonstrated how it can be reduced with higher RF amplitudes. Other contributions to the peak width were found to arise from limitations of the electronics. Ions passing in between the RF electrodes are deflected by the residual RF oscillations, so that different flight paths and a loss of resolution result.

While eliminating residual oscillations entirely by improving the electronics might prove challenging, another approach could be to operate the trap differently. After ion injection, one could stop the RF on the upper combs (the ones that the ions pass upon extraction) and at the same time apply a repulsive potential to them. In this configuration, ions would be trapped by the DC potentials on the trapping electrodes and the upper combs as well as the RF on the lower combs. During ejection no residual RF would then be present on the upper RF electrodes. It is also conceivable to replace the upper combs by a DC electrode entirely. However, a trap with this electrode configuration would no longer possess a field-free region and show several of the associated drawbacks.

A further improvement of the resolution could be obtained by optimizing the electronics to reduce the jitter of the RF clamping and extraction pulses and to shorten the rise time of the extraction pulses.

Trap design and fabrication method The assembly of the trap in its current design presents a considerable challenge. The RF electrodes are so delicate that they will almost inevitably be deformed in the process. Any misalignment of the RF electrodes, however, leads to distortions of the trapping and extraction fields. For the purpose of buffer gas cooling, it would be necessary to reduce the RF electrode width and spacing even further, in order to elim-

inate the local minima of the effective potential in the center of the trap. Moreover, in order to increase ion transmission, the RF electrodes would ideally have to be constructed from thin wires — as if one were to apply the trapping RF to a Bradbury–Nielsen gate²⁴⁹ surrounded by the DC electrodes.

It appears close to impossible to realize such a design with the current fabrication method. Future versions of the trap should therefore be manufactured using MEMS technology, which allows for the construction of miniaturized structures with high precision. The fabrication of a Bradbury–Nielsen gate with 10 μm thick wires and 80% transmission, for example, has been demonstrated²⁵⁰ (although with much smaller dimensions).

Next steps Using the planar trap routinely to obtain TOF mass spectra of laser fragments created in the 22-pole mainly involves programming suitable data acquisition software and integrating it into the program that controls the tandem quadrupole mass spectrometer and the acquisition of laser spectra (see section 2.9). It might, however, also be necessary to solve a number smaller problems in order to achieve the desired sensitivity. Fine tuning of the ion optics might improve the transfer of ions from the 22-pole into the planar trap. Due to the limited dynamic range of the detector, it is difficult to detect a small number of fragment ions simultaneously with a the large number of parent ions. Adding a mass gate to the reflectron could help to reduce or cut out the parent ion signal. A mass gate could also be used to eliminate the signal from metastable fragmentation. It should, however, also be possible to find extraction conditions under which metastable fragmentation is strongly reduced.

In order to use the planar trap for buffer gas cooling, it would be necessary to attach the trap to a cold head. While allowing for good heat conductivity, the construction should not transfer mechanical vibrations to the trap. As mentioned above, the trap should be redesigned with a larger number of poles and manufactured with MEMS technology in order to avoid local traps, which might lead to RF heating. Tomography experiments would be useful to characterize the ion distribution and the quality of the alignment, as has previously been suggested.²³⁴

Possible applications It is my hope that the instrument presented in this chapter will prove a useful scientific tool beyond the context of this work. A few ideas are suggested in the following.

Quadrupole ion trap/TOF instruments have found widespread use because of their ability to combine the storage capabilities of an ion trap with the speed and resolution of TOF mass spectrometry.²⁵¹ The instrument presented here has a similar principle of operation. However, its particular electrode geometry should also allow one to realize better extraction fields and an ion injection efficiency approaching 100%. It therefore appears that a planar trap/TOF mass spectrometer could offer advantages over the quadrupole ion trap instruments, especially for applications involving externally generated ions.

For example, a quadrupole ion trap has been used to accumulate analyte ions and inject

them as a narrow package into an ion mobility drift tube.²⁵² More recent designs frequently employ the end section of an hour glass-shaped ion funnel for this purpose.⁴³ Using a planar trap instead might offer the advantage of combining a high injection efficiency with good storage properties and the ability to extract a narrow ion package.

The accumulation of ions and subsequent ejection in a narrow package is also the purpose of the C-trap,²²⁰ which can be used to couple various ion sources to an orbitrap mass analyzer.²⁵³ In order to achieve coherent ion motion in the orbitrap and obtain a high mass resolution, the ion bunch should be short and have a low spread of kinetic energies and transverse velocities.²²⁰ A planar trap should be able to accumulate ions with a similar efficiency as a C-trap. However, with the entrance of the orbitrap placed at the space focus of a planar trap/Wiley-McLaren setup much shorter ion packages could probably be injected while energy and velocity spreads would be comparable.

Reflectron TOF mass spectrometers have been used with great success for the spectroscopic investigation of ionic clusters.^{125–127} In these experiments, the reflectron is operated as a tandem mass spectrometer, and mass selection of parent and fragment ions is achieved in the drift region before and after the ion mirror, respectively. Ions are generated in a molecular beam and extracted into the flight tube. On their way to the ion mirror they separate according to their mass. The parent ion package is irradiated with a laser pulse, which induces fragmentation. Parent and fragment ions arrive at the detector at different times so that a laser spectrum can be recorded by monitoring the fragment signal as a function of wavelength. A planar trap/TOF instrument could easily serve to extend this technique to the study of buffer gas cooled ions. Moreover, when a cold trap is used to grow clusters with a background gas, a range of different cluster sizes usually results. Similarly, when mass selected clusters are injected into a cold trap, CID can occur, so that several cluster sizes are present at the same time. Operating the reflectron in tandem mass spectrometry mode as described above could add another mass selection step, so that the spectrum of a single species could be obtained.

Velocity map ion imaging is an important technique in the field of molecular dynamics, since it allows one to probe the three-dimensional velocity distribution of scattered particles or the products of unimolecular reactions.²⁵⁴ Imaging studies are frequently performed using molecular beams. However, if one could incorporate a modified planar trap into an imaging setup, this could open up the possibility to study reactions of trapped, buffer gas or even laser cooled²⁵⁵ ions.

Chapter 4

Spectroscopy of a Protonated Amino Acid Dimer

4.1 Motivation

A protonated dipeptide in the gas phase is possibly the simplest conceivable system that could be studied to gain insight into the intramolecular interactions governing the structure and function of proteins.^{95, 114, 256} While reduced to its very essentials, such a model still features the fundamental interactions that in a large number, give rise to the complexity of big, solvated proteins.

By analogy, a protonated cluster of two amino acids can be considered an essential model of the interaction of two separate proteins. The object of study that was chosen here is a protonated complex of L-phenylalanine and L-serine (Fig. 4.1) — phenylalanine because it usually gives rise to well-resolved UV spectra⁵⁰ and serine as one of the smaller amino acids which possesses an additional OH oscillator.

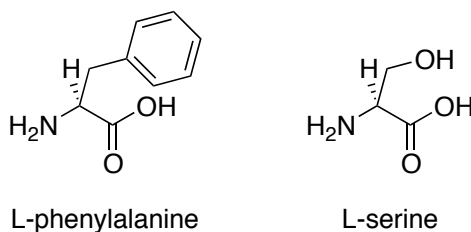


Figure 4.1: Chemical structures of the amino acids L-phenylalanine and L-serine.

At first sight, this system might appear rather simple, and it might seem that it would be similar to a dipeptide. However, since the amino acids are not covalently linked, a much larger degree of conformational flexibility can be expected. Furthermore, it is not obvious which of the amino acids carries the proton and if the other amino acid is in its neutral or zwitterionic state. Finally, the cluster features seven hetero atoms and eight N- or O-bound hydrogens, which gives rise to a plethora of possibilities for different intra- and intermolecular hydrogen bonding networks.

Single, protonated amino acids in the gas phase have been investigated with several spectroscopic techniques. The electronic spectra of protonated tryptophan and tyrosine^{106, 110, 257–259} as well as of deprotonated tryptophan²⁶⁰ have been reported. Vibrationally resolved spectra could be obtained for buffer gas-cooled protonated tyrosine and phenylalanine at ~ 12 K, while protonated tryptophan has an intrinsically broad spectrum, due to its ultrafast excited state dynamics.^{106, 113} The effect of microsolvation on the excited state lifetime of protonated tryptophan has also been investigated.¹¹¹

A number of IR spectroscopic studies, mostly using the IRMPD approach, have addressed the question whether cationized amino acids adopt a zwitterionic structure in the gas phase. Whereas protonated amino acids were found to be non-zwitterionic,^{29, 87} metal cations can stabilize the zwitterionic structure.^{87, 104, 261} IRMPD spectra have also been recorded of protonated lysine (produced by a photochemical method in a molecular beam)²⁶² and a protonated synthetic amino acid.²⁶³

The only conformer specific IR spectra of protonated amino acids have been reported for phenylalanine and tyrosine in a 22-pole ion trap at ~ 12 K.¹¹³ Under these conditions, only two conformers of protonated phenylalanine were found, which differ only in a rotation around the C_α - C_β bond. For protonated tyrosine, the same conformational preferences for the orientation of the side chain were observed. However, with two possible orientations of the tyrosine OH group, a total of four conformers were found.

Spectroscopic investigations of protonated amino acid dimers have, so far, been limited to IRMPD studies at room temperature. Glycine dimer, the simplest protonated dimer, has been the subject of several studies, which, however, disagree on the structure that they assign to the observed spectra. Based on a spectrum in the hydrogen stretch region, a non-zwitterionic structure was proposed in which the ammonium group is solvated by the carbonyl oxygen of the same amino acid as well as the nitrogen and carbonyl oxygen of the second amino acid.⁹⁸ A closely related structure had previously also been suggested in the context of BIRD experiments.²⁷ A different conformation was subsequently calculated to be lower in energy, and agreement of the corresponding spectrum with experimental spectra in both the fingerprint and N-H/O-H stretch region was reported.^{102, 264–266} Here, the ammonium group is likewise complexed by both carbonyl oxygens. However, the amino group of the neutral glycine engages in an intramolecular hydrogen bond with the carboxylic acid hydrogen. (It should be noted that, actually, two different structures with the same hydrogen bonding pattern are reported that differ in a 180° rotation around the intermolecular hydrogen bond.)

The spectra of the alanine and valine dimers and the mixed alanine/glycine dimer were found to strongly resemble that of the glycine dimer in the fingerprint range. It was concluded that similar structures should be at the origin of this observation, and conformations with an identical hydrogen bonding pattern were assigned.²⁶⁵ Similarly, the spectra of the serine and threonine dimers and the mixed serine/threonine dimer were found to be very similar in the

OH and NH stretch region.^{98,267} For the serine dimer, several non-zwitterionic structures were suggested in which the ammonium group engages in several intermolecular hydrogen bonds.²⁶⁷ Zwitterionic structures were only assigned to the proline dimer¹⁰² and the mixed glycine/lysine dimer, while the spectrum of the lysine dimer seemed to indicate a zwitterionic structure but could not provide conclusive evidence.⁹⁸

It has been noted that it “is still a matter of debate how much detailed information IR spectroscopy can yield on room-temperature ions. For these proton-bound complexes many conformations are possible and multiple structures may be populated at room temperature.”⁸⁷ Another point of concern may be the calculations. Structures are frequently assigned based on a good match with the calculated spectrum of one of the lowest-energy conformers. However, in most cases no stringent test is used if the PES has been exhaustively sampled, so that it can be assumed that all relevant conformations have actually been included in the calculation. The large conformational space of the dimers may even render it impossible “to search for all possible conformational minima, because that would be computationally prohibitive.”⁹⁸ Moreover, even a good visual agreement between the experimental spectrum and a calculated spectrum may be deceptive, since different species may possess similar spectra. However, in some cases, the bands of two different species that appear at a similar spectral position and with a similar intensity might be due to different vibrations. Isotopic substitution experiments offer the possibility to verify the correct assignment of the IR bands and can therefore deliver more stringent criteria for the structural assignment.

Several complexes of a metal ion with two amino acids have also been investigated, including the sodium bound glycine dimer,²⁶⁶ the tryptophan dimer with several divalent metal cations,^{104,268} and the deprotonated phenylalanine dimer with a divalent zinc ion.⁸⁹ The proposed structures show marked differences to the proton bound species, which are characterized by their hydrogen bond networks. Here, the solvation of the metal by the Lewis basic groups of the amino acids largely dominates the structure.

The proton affinities of serine and phenylalanine have been tabulated as 914.6 kJ/mol and 922.9 kJ/mol, respectively.²⁶⁹ Most investigations, including more recent studies, agree that phenylalanine possesses the higher proton affinity by up to 20 kJ/mol.^{270–274} It should therefore be expected that phenylalanine carries the proton in the complex with serine.

Only limited data are available for the dissociation energies of protonated amino acid dimers. For the glycine, alanine, and lysine homodimers as well as the mixed glycine/alanine dimer, the same binding energy of 111 ± 5 kJ/mol was determined from BIRD measurements,²⁷ in close agreement with the dissociation enthalpies for the glycine dimer of 114 ± 7 kJ/mol²⁶⁴ and 130 ± 8 kJ/mol²⁷⁵ obtained from pulsed-ionization high-pressure mass spectrometry experiments.

By comparison, a UV photon at $37\,520.9\text{ cm}^{-1}$ (the band origin of conformer A of protonated phenylalanine in the terminology of reference¹¹³) corresponds to ~ 449 kJ/mol, more than four times the dissociation energy, while the absorption of one IR photon at 3000 cm^{-1} (~ 36 kJ/mol)

is insufficient to dissociate the cluster.

In the following, the UV spectrum as well as the isomer-specific IR spectra of the protonated dimer in the electronic ground state are presented. The interpretation of the IR spectra provides structural information about the dimers. In particular, evidence is obtained that the dimers adopt a non-zwitterionic structure, *i.e.* both carboxylic acid groups are protonated and one of the amino groups carries the excess proton. Such structures should exhibit two carboxylic acid OH stretch vibrations as well as a group of three ammonium NH stretches and a group of two amino NH stretches. These two groups of NH stretches can be identified based on their different spectral positions, line widths, and intensities. When phenylalanine is ^{15}N labeled, isotope shifts of either the ammonium or amino NH stretches are observed, which is used to corroborate the assignment of the two groups of NH stretch vibrations. Moreover, from these isotope shifts, the protonation site can be determined.

4.2 Experimental Approach

Experiments were carried out with the setup described in chapter 2 and the experimental sequence detailed in section 2.2 therein. The protonated 1:1 clusters of L-phenylalanine and L-serine (both Sigma Aldrich) are generated by nano-ESI of a methanol/water solution (1:1) that is 100 μM and 1 mM in the two amino acids, respectively. The experiment is operated at 10 Hz. Ions are accumulated in the hexapole and periodically released, mass selected in the first quadrupole and injected into the 22-pole. After allowing sufficient time for cooling, the ions are irradiated with IR and UV pulses. After subsequent ejection from the 22-pole, parent or fragment ions are mass selected in the second quadrupole and detected.

Ultraviolet laser radiation (0.5-1.5 mJ/pulse) is generated by doubling the output of a Nd:YAG pumped dye laser (Lambda Physik). A slightly convergent UV beam is used, with a diameter of about 1 mm at the position of the trap, where it is overlapped with an IR beam for the double-resonance experiments. Infrared radiation is produced with an IR optical parametric oscillator/amplifier (LaserVision OPO/OPA, 3-10 mJ/pulse). Its output is focussed with a 60 cm lens such that the IR beam is slightly larger than the UV beam inside the entire trap volume. The spectra are normalized on the parent ion intensity and the simultaneously recorded laser power. The different spectroscopic techniques that are used in this work are described in section 4.3.

4.3 Spectroscopic Techniques

Different spectroscopic schemes are employed to obtain different kinds of information. In order to record a UV spectrum (Fig. 4.2), the photofragment intensity is monitored as a function of the UV laser wavelength. The fragmentation results either from processes on an excited state surface or in S_0 after internal conversion (IC).

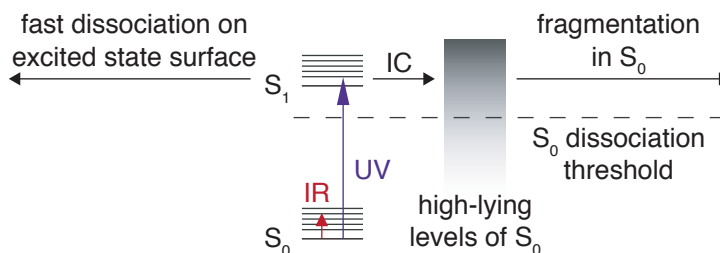


Figure 4.2: Spectroscopic schemes used to obtain a UV spectrum (UV laser only), an IR/UV hole burning spectrum (IR laser fixed to a specific transition and preceding the UV laser, which is being scanned), and an IR depletion spectrum (the IR laser is being scanned and precedes the UV pulse, which is fixed to a specific transition).

In order to assign different transitions in the UV spectrum to different isomers, an IR laser pulse, tuned to an infrared transition of one of the isomers, is fired ~ 50 ns prior to the UV laser. After the absorption of an IR photon, intramolecular vibrational energy redistribution (IVR) occurs, which leads to a statistically broadened UV spectrum, so that a decreased UV fragmentation signal is observed on UV bands corresponding to the same isomer. The difference of the fragmentation signal recorded with and without the IR laser yields an IR/UV hole burning spectrum, which corresponds to the UV spectrum of a single isomer. When, instead, the UV laser is fixed to the transition of one isomer and the IR laser is scanned, an IR/UV depletion spectrum is obtained, which reflects the IR spectrum of a single isomer.

The IR spectrum of an excited state species can be obtained if the order of the IR and UV pulses is inverted, as illustrated in Fig. 4.3, and the IR pulse is fired before the excited state has decayed. The absorption of one IR photon can change the fragmentation pattern in the excited state if different fragmentation or deactivation pathways exist that are close in energy, so that a modified branching ratio can be observed. Monitoring the depletion or appearance of one fragment will then yield the IR spectrum of a single isomer in the excited state. At the same time, this technique does not probe species that have undergone internal conversion to the S_0 surface, since the additional energy of one IR photon does not significantly alter the fragmentation behavior of a hot ground state species for which different fragmentation channels involving different electronic surfaces are not accessible.

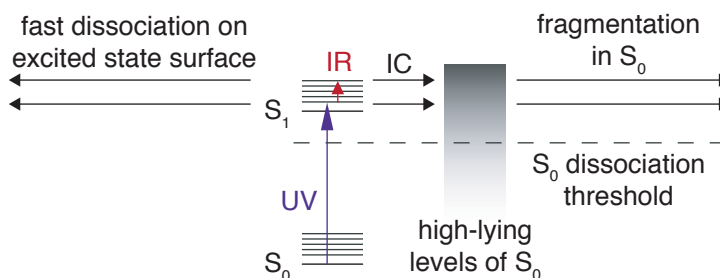


Figure 4.3: Spectroscopic scheme to obtain the IR spectrum of a single isomer in the excited state. The IR laser follows the UV laser and induces a change in the observed fragmentation pattern if in resonance with a transition of an excited state species.

This technique is analogous to a spectroscopic scheme that has previously been employed to record the excited state IR spectra of neutrals, which is possible if the absorption of an IR photon changes the fluorescence quantum yield of the excited state species.⁷⁵

4.4 Ground State Spectra

Figure 4.4 shows the mass spectrum that is obtained when protonated phenylalanine/serine dimer ions ($m/z = 271$) are stored in the 22-pole (bottom). Apart from the protonated amino acid dimer (271 amu), a CID fragment at 166 amu is visible, which corresponds to protonated phenylalanine, while protonated serine (106 amu) is hardly visible, in agreement with the relative proton affinities of the two amino acids. Upon irradiation of the ions at 38432.8 cm^{-1} (Fig. 4.4,

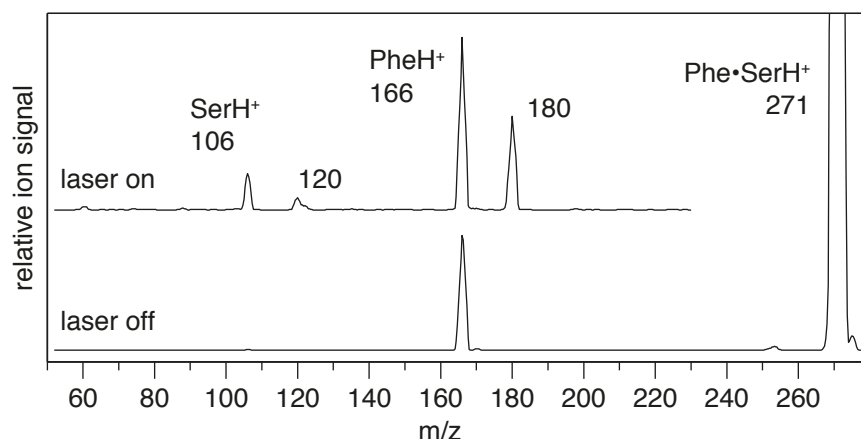


Figure 4.4: Mass spectrum obtained when protonated phenylalanine/serine dimer ions ($m/z = 271$) are stored in the 22-pole (bottom) and irradiated at 38432.8 cm^{-1} (top).

top), the channels with $m/z = 166$ and 106 are enhanced. Further laser fragments appear at $m/z = 180$ (loss of the phenylalanine side chain) and $m/z = 120$ (loss of H_2O and CO from protonated phenylalanine), in analogy to the fragmentation pattern in bare protonated phenylalanine (see section 3.7.13). However, the fragment at 120 amu is now also accompanied by a less intense mass peak at 122 amu (loss of CO_2 from protonated phenylalanine). The same fragmentation pattern is observed on different UV transitions. Unless otherwise noted, laser spectra were recorded while monitoring the 180 amu channel, which is the most intense, background-free channel.

Figure 4.5 shows the UV spectrum of the dimer recorded in the 180 amu channel. The first transition occurs at 37596.1 cm^{-1} , about 75 cm^{-1} blue-shifted from the first band in the spectrum of bare protonated phenylalanine.¹¹³ Infrared depletion spectra were recorded for a number of transitions in order to identify different isomers contributing to the spectrum. With the UV laser fixed to the bands marked with arrows at 37596.1 (A), 37613.7 (B), 37664.4 (C), 37866.6 (D), and 38432.8 cm^{-1} (E), isomer specific IR spectra were obtained, which are shown in Fig. 4.6. To facilitate the discussion, shading indicates the spectral ranges of different

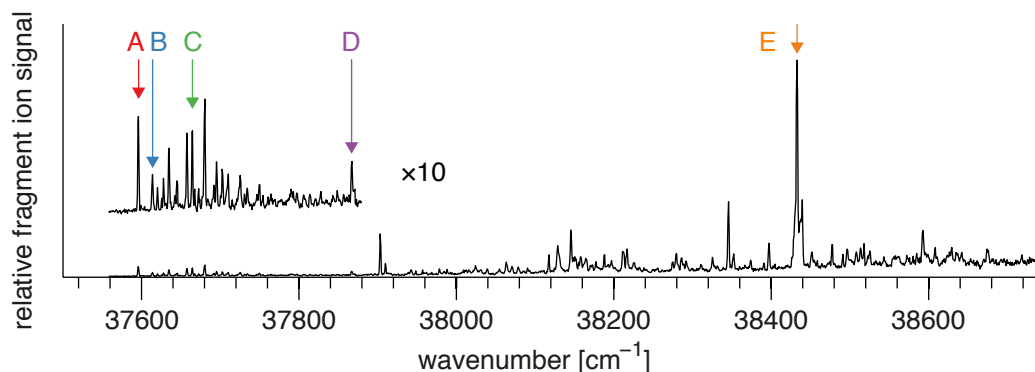


Figure 4.5: The UV spectrum of the protonated phenylalanine/serine dimer, recorded in the 180 amu channel.

hydride stretch vibrations. The IR spectra are well-resolved, and clearly belong to different conformations. A number of weaker transitions in the range below 3100 cm^{-1} are assigned to the six aliphatic and five aromatic CH stretches. At least in the case of isomer E, where the best signal to noise ratio could be achieved, all eleven transitions can clearly be accounted for. The NH stretch vibrations and, possibly, any red-shifted hydrogen-bonded OH stretches, appear between 3100 and 3500 cm^{-1} . The free carboxylic acid OH stretches are observed in a narrow window between 3560 and 3575 cm^{-1} , while the vibrations above 3600 cm^{-1} are assigned to the OH stretch of the serine side chain.

In all of the probed conformations, the serine side chain OH stretch vibration is found to be almost unperturbed and appears between 3660 and 3680 cm^{-1} , with the exception of isomer A, where the vibration is red-shifted to 3604 cm^{-1} . This shift is indicative of a weak hydrogen bond, whose nature is further discussed in section 4.6, where evidence is provided that it is likely a π -hydrogen bond with the aromatic ring. The spectrum of isomer C exhibits an additional peak at 3604 cm^{-1} , which is most likely an artifact, since it is too weak for an OH stretch vibration and, furthermore, coincides exactly with the alcohol OH stretch of isomer A. A weak electronic transition of isomer A probably coincides with the UV transition of isomer C that was probed here, so that a minor contribution to the IR spectrum from isomer A can be observed.

Isomers A, C, and D clearly show two free carboxylic acid OH stretches, which directly excludes that these conformations could be zwitterionic. Spectra B and E exhibit only a single, narrow peak in this region, which seems to be due to a single OH stretch vibration. However, it cannot be excluded that two free carboxylic acid OH stretches are actually present which simply cannot be resolved.

For several gas-phase conformers of neutral phenylalanine^{63,276} as well as tryptophan⁶⁴ and tyrosine,²⁷⁷ an intramolecular hydrogen bond between the acid proton and the amino nitrogen was observed. The same intramolecular hydrogen bonding motif is adopted by the neutral glycine moiety of the protonated glycine dimer.^{102,264–266} Moreover, it was suggested that the alanine and valine dimers as well as the mixed alanine/glycine dimer should have analogous

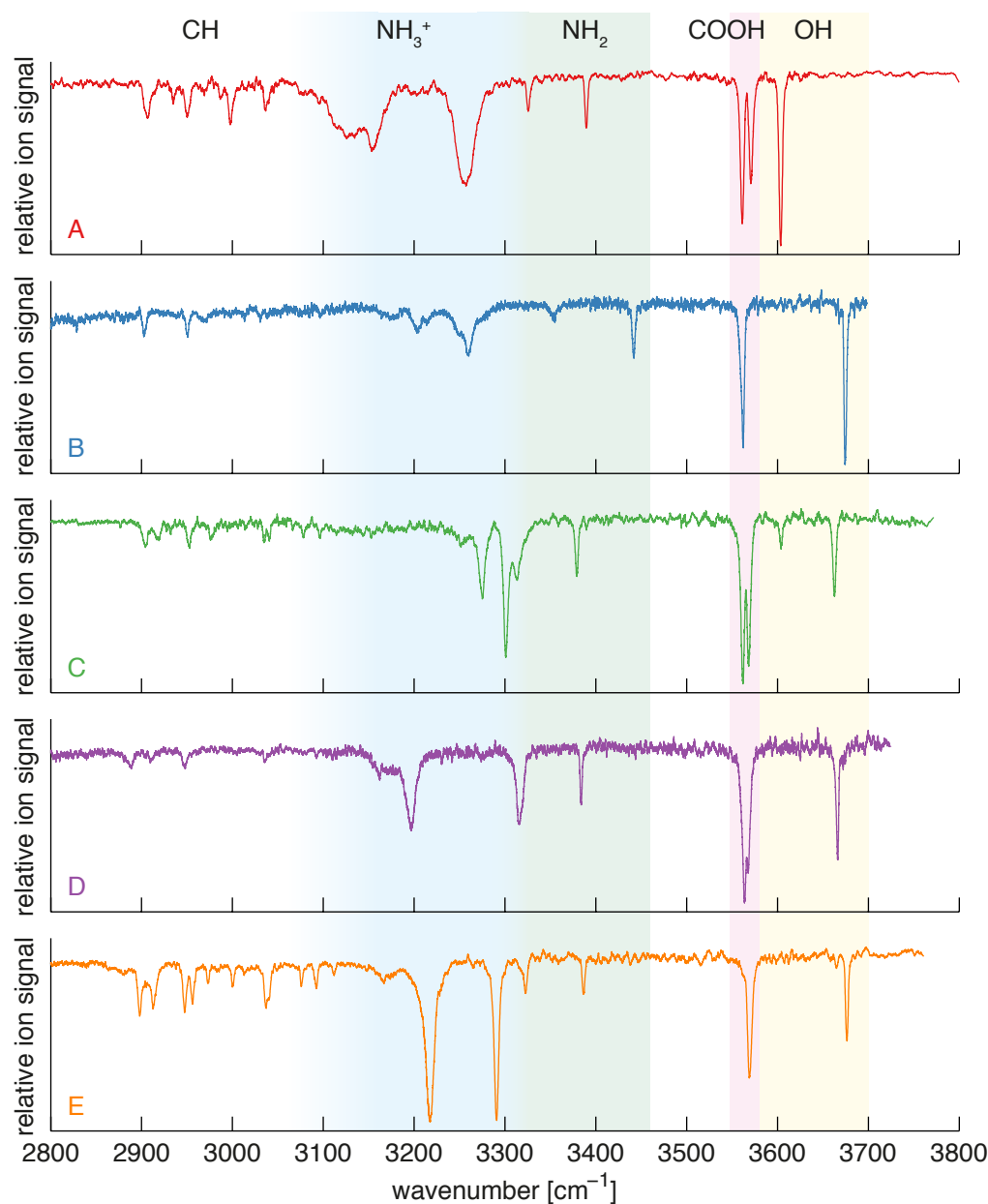


Figure 4.6: IR depletion spectra recorded on the different UV transitions indicated with arrows in Fig. 4.5: 37596.1 (A), 37613.7 (B), 37664.4 (C), 37866.6 (D), and 38432.8 cm^{-1} (E). Shading indicates the spectral ranges of different hydride stretch vibrations.

structures.²⁶⁵ Such an intramolecular hydrogen bond involving the neutral amino acid can be excluded for the structures with two free carboxylic acid OH stretches.

It is reasonable to assume that the dimer would stabilize itself by maximizing the number of hydrogen bonds. As potential hydrogen bond donors, the NH_2 , NH_3^+ , and OH protons are available. The latter, however, are mostly bystanders of the hydrogen bond network, as can be concluded from the observation of two or three free OH stretch vibrations for any of the isomers. Only isomers B and E could possibly possess a single strong OH hydrogen bond involving the carboxylic acid proton. The clusters should therefore be largely dominated by hydrogen bonds

with the ammonium protons, which can be expected to be stronger donors than the amino group protons due to the presence of the charge. Structures that are characterized by several intermolecular hydrogen bonds with the ammonium group have also been suggested for the protonated serine dimer.²⁶⁷

The IR spectra show pronounced differences in the range between 3100 and 3500 cm^{-1} . In the case of isomer A, five transitions are observed, which are readily assigned to the three ammonium NH stretches (3128, 3155, and 3256 cm^{-1}) and the two amino NH stretches (3326 and 3389 cm^{-1}), as expected for a non-zwitterionic structure. The assignment of the amino NH stretch vibrations is supported by the gas phase spectra of the neutral aromatic amino acids. There, the symmetric and antisymmetric NH stretch vibrations appear as sharp transitions in the range of 3330–3370 cm^{-1} and 3390–3440 cm^{-1} , respectively, with the antisymmetric stretch being more intense.^{63,64,277} These observations agree closely with the frequencies, intensity ratio, and line widths found here. The ammonium NH stretches are expected to be red-shifted with respect to those of the amino group, in agreement with the above assignment. This is, for example, the case in the matrix spectrum of zwitterionic tryptophan, where they appear between 3130 and 3340 cm^{-1} .²⁷⁸ In the spectra of cold, protonated dipeptides on the other hand, a single ammonium NH stretch appears between 3350 and 3375 cm^{-1} , which was rationalized with a specific hydrogen bonding pattern.¹¹⁴ The assignment of the ammonium NH bands solely on the basis of their frequencies might therefore not be definitive. However, the NH stretch vibrations of isomer A below 3300 cm^{-1} show a considerable broadening, which is characteristic for hydrogen-bonded ammonium NH vibrations^{113,114} and thus confirms their assignment.

Further evidence is provided by the IR spectrum of isomer A with ^{15}N labeled phenylalanine (Fig. 4.7). ^{15}N substitution had previously been employed to identify the different NH stretches of a polypeptide and to verify the correct sequence of peaks in the calculated spectrum. A redshift of about 8 cm^{-1} was typically observed for the labeled amide NH vibrations.¹¹⁶ Figure 4.7 compares the spectra of the labeled clusters (bottom traces) with the spectra of their ^{14}N counterparts (top traces). For isomer A, the three broad bands between 3100 and 3300 cm^{-1} are found to red-shift by an average 7 cm^{-1} , which confirms their assignment as ammonium NH stretch vibrations. The symmetric NH_2 vibration of the amino group at 3326 cm^{-1} is also slightly red-shifted by $\sim 2 \text{ cm}^{-1}$, probably due to coupling with the ammonium vibrations, while the asymmetric stretch appears unchanged. It can be concluded that the excess proton is located on phenylalanine, as expected from the difference in proton affinities of the two amino acids.

The protonated glycine dimer features a vibration at 2440 cm^{-1} , which was assigned to the strongly red-shifted vibration of the ammonium hydrogen involved in the only intermolecular hydrogen bond.²⁶⁶ The fact that all three ammonium vibrations of isomer A can be observed in the range between 3100 and 3300 cm^{-1} is therefore remarkable. This observation may suggest that the ammonium group is involved in several weaker hydrogen bonds of similar strength.

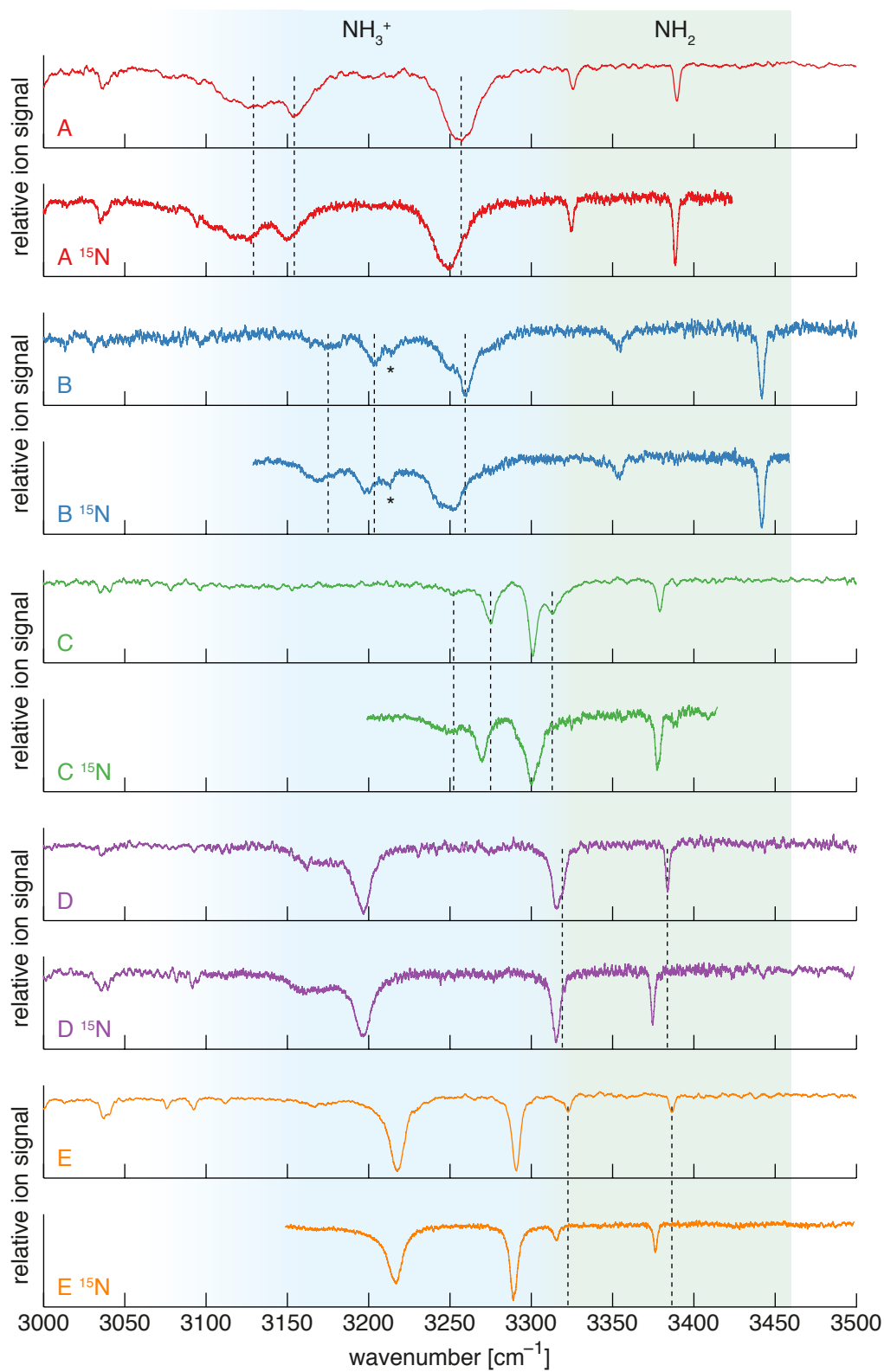


Figure 4.7: Spectra of the various isomers in the NH stretch region with ^{15}N labeled phenylalanine (bottom traces) and natural isotope abundance (top traces).

This is in agreement with the conclusion drawn above that the hydrogen bond network should be dominated by several hydrogen bonds with the ammonium group.

As in the case of isomer A, ^{15}N labeling of phenylalanine in B and C reveals two different groups of vibrations (Fig. 4.7). Three bands in the NH_3^+ range undergo a red-shift, while two bands in the NH_2 range remain essentially unchanged. In analogy to A, they are therefore assigned to the NH_3^+ and NH_2 vibrations, respectively, and it can be concluded that B and C are both non-zwitterionic, protonated on the phenylalanine amino group, and structurally related to A. In the spectrum of B, the amino NH stretches appear blue-shifted to 3353 and 3442 cm^{-1} , which is, however, still within the range that can be expected from the spectra of neutral amino acids (see above). The three bands at 3175, 3203, and 3260 cm^{-1} shift upon isotopic substitution and are therefore assigned to the ammonium NH stretches. The band at 3260 cm^{-1} is accompanied by a shoulder at 3249 cm^{-1} , which appears shifted in the ^{15}N labeled compound. This shoulder is also observed when the IR spectrum is recorded with the UV laser fixed to a different transition of isomer B. It is therefore unlikely that it should be due to an artifact, although no ready explanation for this shoulder is available. Also, the spectrum does not show any indication in any other spectral range for contributions from another isomer. An additional band appears at 3214 cm^{-1} , which does not shift upon ^{15}N substitution (marked with an asterisk in Fig. 4.7). It is tentatively assigned to the remaining carboxylic acid OH stretch vibration, which is red-shifted due to a strong hydrogen bond. This assignment is supported by the observation of hydrogen bonded carboxylic acid OH stretches in the range of 3200–3300 cm^{-1} for a coiled dodecapeptide¹¹⁶ and some conformations of the neutral aromatic amino acids featuring an intramolecular hydrogen bond.^{63,64,277} Labeling of the phenylalanine nitrogen of isomer C leads to a redshift of the bands at 3252, 3275, and 3314 cm^{-1} , which are therefore assigned to the phenylalanine ammonium vibrations. Compared with the other isomers, these vibrations appear at higher wavenumbers, so that the two groups of NH stretch bands overlap. The peaks at 3301 cm^{-1} and 3379 cm^{-1} are assigned to the symmetric and antisymmetric stretch of the serine amino group, respectively.

The spectra D and E show the opposite pattern of isotope shifts. A redshift is observed for the two NH vibrations with the highest wavenumbers, while the remaining transitions are unchanged. This is most easily recognized for E, where the bands at 3323 and 3387 cm^{-1} clearly undergo an isotope shift. They are assigned to the NH_2 vibrations, which is furthermore supported by their positions, line widths, and intensities. The three ammonium stretches and the second carboxylic acid OH stretch are left to be assigned, which renders the interpretation of the only three remaining bands at 3167, 3218, and 3291 cm^{-1} less straight forward. If one of the carboxylic OH groups should be hydrogen bonded, it would be expected to appear red-shifted. This could lead one to speculate that in the NH_3^+ range, two bands might overlap. Alternatively, one of the ammonium stretches could be strongly red-shifted and not appear in the spectral range investigated here. In isomer D, the shift of the asymmetric NH_2 stretch at

3384 cm^{-1} can clearly be observed, whereas that of the symmetric stretch is only indirectly evident from the peak at 3316 cm^{-1} . While the position of this peak is unchanged, its blue shoulder at 3319 cm^{-1} disappears and its width decreases from about 9 to 6 cm^{-1} , which is significant given the IR resolution of about 1 cm^{-1} . This suggests the assignment of the shoulder at 3319 cm^{-1} to the symmetric stretch. The bands at 3316 , 3163 , and 3197 cm^{-1} are assigned to the ammonium stretch vibrations. In conclusion, isomers D and E are both non-zwitterionic and protonated at the amino group of the less basic amino acid, serine. They are structural isomers of the other three clusters and possess a different bond connectivity. It thus appears that structural effects override the inherent basicities of the two amino acids or, in other words, that more favorable intra- and intermolecular interactions compensate for the energy cost of transferring the proton from phenylalanine to serine.

In previous studies of protonated amino acid dimers using IRMPD spectroscopy, the experimental spectrum has mostly been attributed to the presence of a single isomer. The isomer specific depletion spectra presented here paint a more complex picture for the protonated phenylalanine/serine dimer. However, the question has not been addressed, so far, how many isomers are present. To this end, IR/UV hole burning spectra were recorded. When the serine side chain OH stretches of isomers A, C, and E at 3604 , 3663 , and 3677 cm^{-1} , respectively, were pumped, the corresponding hole burning spectra A, C, and E were obtained (Fig. 4.8). Close inspection reveals that these three hole burning spectra alone can account for every single peak of the UV spectrum within the limits of the experimental signal to noise level, while the isomer specific IR spectra demonstrate the presence of at least five different species. This means that some hole burning spectra must contain contributions from several isomers. Indeed, pumping the NH stretch vibration of isomer B at 3442 cm^{-1} results in the hole burning spectrum B, which shows a subset of the bands in spectrum E. The latter must therefore have contributions from isomers B and E, although their serine side chain OH stretch vibrations are separated by 3 cm^{-1} . Obviously, at the IR laser power of about 10 mJ/pulse that was used in these experiments, the transitions of the two isomers are sufficiently broadened and deplete so readily that they cannot be distinguished. While experiments with attenuated IR power could circumvent this difficulty, isomer D does not even possess a transition that does not overlap with any of the other isomers. It is evident that the IR/UV hole burning technique is not suitable to settle the question how many isomers are present and that UV/UV hole burning spectra might be a better tool for this purpose. Since IR depletion spectra could not be recorded for all the UV transitions observed in Fig. 4.5, it has to be concluded that the protonated phenylalanine/serine dimer possesses at least five different isomers.

Figure 4.9 compares UV spectra of the dimer that were recorded in the 180 amu channel (top) and the 120 amu channel (bottom). The two spectra are largely similar. However, a broad background signal appears in the 120 amu channel, which extends down to below 36500 cm^{-1} , as well as two sharp transitions at 37512.1 and 37521.9 cm^{-1} . This observation points to the

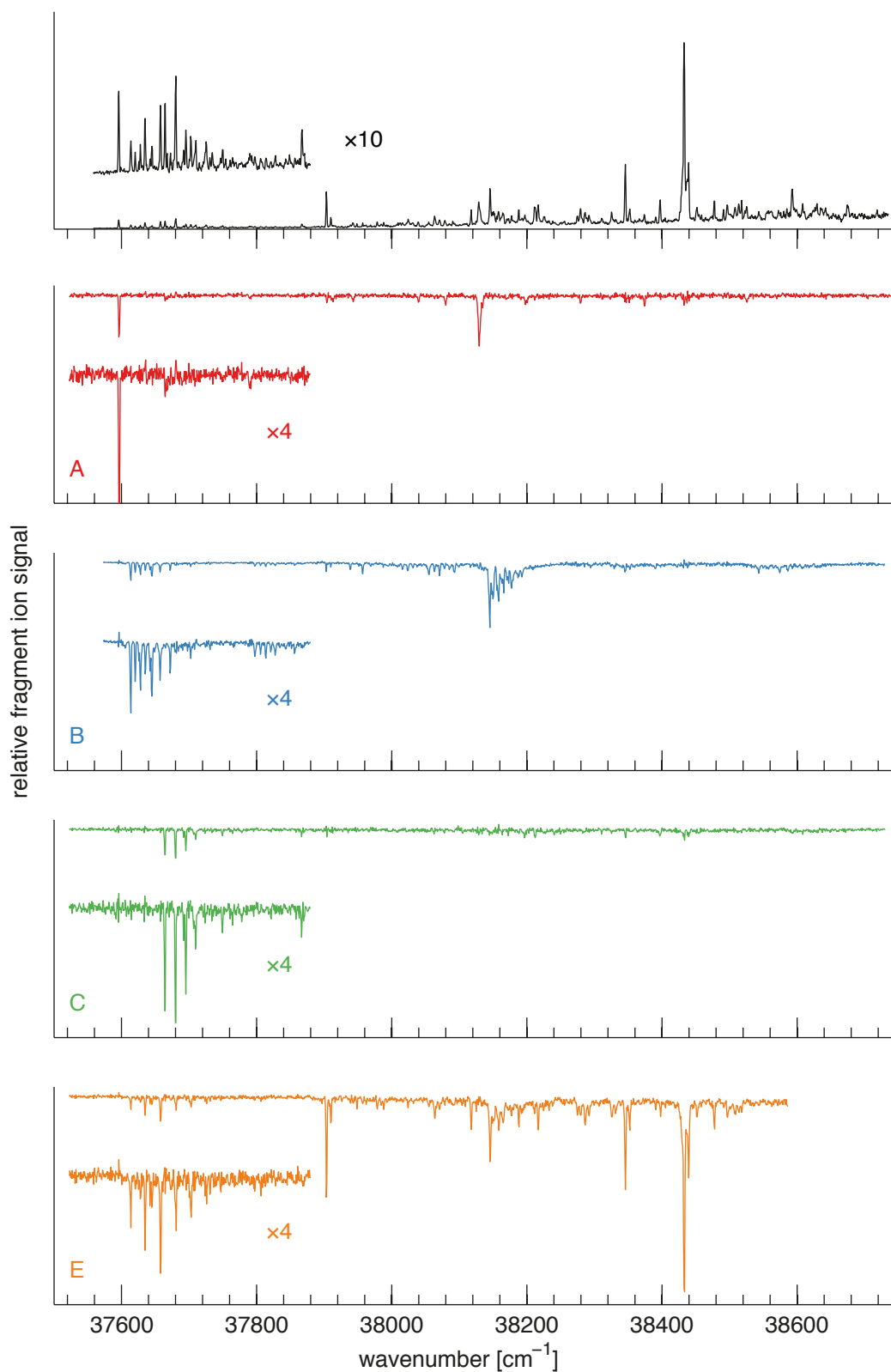


Figure 4.8: The UV spectrum of the protonated phenylalanine/serine dimer, recorded in the 180 amu channel (top) together with IR/UV hole burning spectra. The hole burning spectra A, C, and E are obtained by pumping the serine alcohol OH stretches of isomers A, C, and E (see Fig. 4.6) at 3604, 3663, and 3677 cm^{-1} , respectively. Pumping the NH stretch vibration of isomer B at 3442 cm^{-1} results in the hole burning spectrum labeled B.

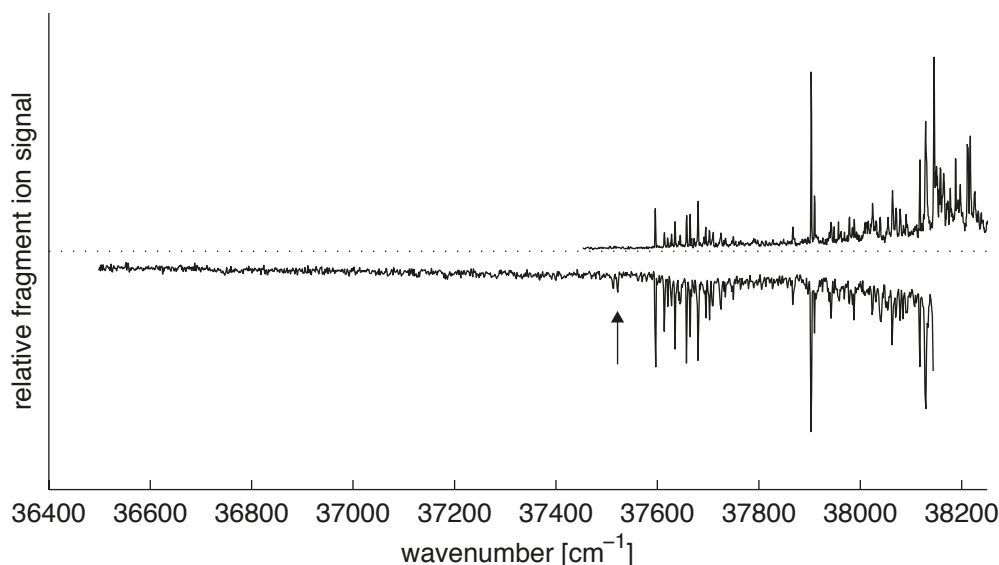


Figure 4.9: Comparison of the UV spectra of the protonated dimer in the 180 amu channel (top) and in the 120 amu channel (bottom).

existence of at least one further species, which possesses a different fragmentation pattern and a (mostly) broad UV spectrum. Again, it would be useful to carry out UV/UV hole burning experiments, in order to selectively obtain the UV spectrum of this species. Similar cases have previously been reported for neutrals, where different conformers of the same species showed either a well-resolved or a broad UV spectrum. These findings were explained with a conformer dependent energy ordering of several close-lying electronic states and the existence of a fast deactivation pathway through several conical intersections for some of the conformations.^{61, 74, 279}

Figure 4.10 shows the IR gain spectrum in the 120 amu channel that is obtained with the UV laser fixed to the transition at 37521.9 cm⁻¹ (marked with an arrow in Fig. 4.9). With the UV laser in resonance with the band at 37512.1 cm⁻¹ or tuned further to the red, to 37451.9 cm⁻¹, the same spectrum is obtained. The spectrum appears largely like a weighted sum of the different

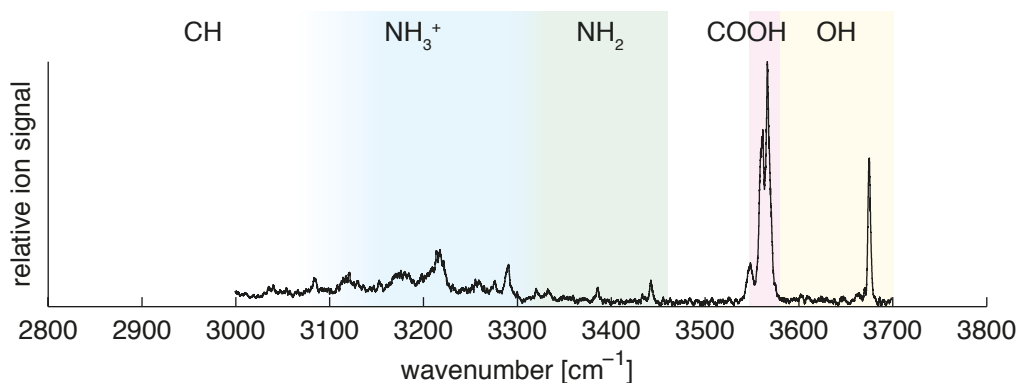


Figure 4.10: IR gain spectrum in the 120 amu channel obtained with the UV laser at 37521.9 cm⁻¹ (marked with an arrow in Fig. 4.9).

IR spectra of Fig. 4.6 and obviously contains important contributions from gains of the different

isomers identified above.²⁸⁰ Only the peak at 3548 cm^{-1} cannot be explained by any of the spectra in Fig. 4.6. It corresponds to a slightly red-shifted carboxylic acid OH stretch band and points to a new isomer. It is not clear whether this peak belongs to a species with a broad UV spectrum or whether it is actually due to another, yet unidentified isomer with a sharp spectrum. Further experiments will be necessary to settle this question. In conclusion, the observation of broad features in the UV spectrum of Fig. 4.9 and of new IR features in the gain spectrum of Fig. 4.10 provides evidence that the number of isomers is greater than five under the present experimental conditions.

4.5 Quantum Chemical Calculations

Since there is no direct way to obtain the complete structure of a molecular species from its gas phase IR spectrum, quantum chemical calculations are frequently carried out to aid the analysis of the spectra. In flexible molecules, this approach usually involves guessing the structures of possible conformers and optimizing them with an *ab initio* method that is assumed to describe the system with sufficient accuracy. Structures can then be assigned based on a convincing match between the calculated (harmonic) and the experimental spectra. Under the assumption that the species can efficiently reach the lowest lying minima of the PES under the experimental conditions, the search for a matching spectrum is frequently restricted to a limited number of structures of lowest energy. A small energy range is usually considered, which is determined by the assumed error of the calculated energies.

For systems with a large conformational space, it becomes virtually impossible to guess *all* the relevant minima of the PES. For peptides, a conformational search on the force field level is therefore frequently used to generate suitable starting structures for the geometry optimization. This approach assumes that the employed force field is similar to the *ab initio* PES (*i.e.* it features the same minima) and that the search samples the PES sufficiently, so that no relevant structure is omitted. Again, only the lowest-energy structures determined with the force field are used for the geometry optimization, and the chosen energy range essentially reflects the assumed error of the force field energy. The power of this approach has been demonstrated, for example, in the analysis of the spectra of cold protonated amino acids and short peptides,⁵⁰ while it did not lead to success for some larger peptides.⁹ However, one would expect that a protonated amino acid dimer should still be sufficiently small and simple.

Following the reported procedure,⁵⁰ a Monte Carlo conformational search was performed with the AMBER* force field as implemented in the MacroModel package.²⁸¹ Zwitterionic structures had previously only been reported for basic amino acids and dimers containing either proline or lysine.⁸⁷ Furthermore, the above analysis of the IR spectra does not support the formation of a zwitterion, so that only non-zwitterionic structures with the excess proton either bound to the phenylalanine or serine amino group were considered. Within a range of 50 kJ/mol, 1480 and 462 conformers were found, respectively. A large number of search iterations was chosen

to ensure complete sampling of the PES. If additional iterations do not yield any new structures, the search can reasonably be considered exhaustive. The 100 lowest energy structures with the proton located on phenylalanine or serine were found 67 and 174 times on average, respectively, although 3 and 11 structures were only generated a single time.

Of each group, 120 structures were optimized on the M06/6-31G* level,²⁸² and frequency calculations were used to verify that the calculations had converged to a minimum. Fig. 4.11 displays the relative (zero point-corrected) M06 energies as a function of the relative force field energies. The structural families with the proton located on serine and phenylalanine are represented with open and filled circles, respectively. Fits of the data points with straight lines

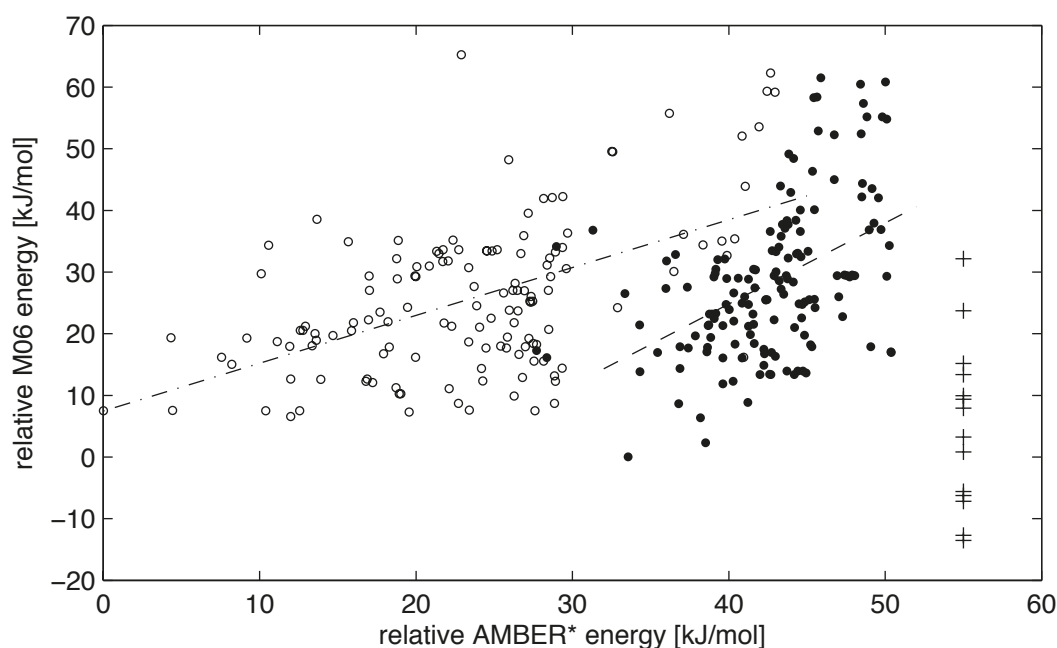


Figure 4.11: Relative (zero point corrected) DFT energy versus relative force field energy for the lowest energy structures obtained in the conformational search. Isomers in which either serine or phenylalanine carries the proton (120 each) are marked with open and filled circles, respectively. Calculations for several additional structures featuring two free carboxylic acid OH groups are also included. A fit of a straight line to the data is indicated with a dash-dotted (protonated serine) and dashed (protonated phenylalanine) line. The DFT energies obtained after optimizing several guessed structures are marked with crosses.

yield slopes of 0.78 (protonated serine, dash-dotted line) and 1.31 (protonated phenylalanine, dashed line) with r^2 values of 0.28 and 0.22, respectively. The lower slope for the isomer family with protonated serine is in part due to the fact that upon M06 optimization, starting structures with higher AMBER* energies converged frequently to lower-energy conformations. The root mean squared errors of the relative AMBER* energies are determined to be 10.52 kJ/mol and 10.95 kJ/mol.

The positive slopes seem to indicate that the AMBER* and M06 PES are similar enough for the structures considered here so that a correlation of their corresponding energies can be observed. Structures have been tested within an energy window of about 30 kJ/mol and

20 kJ/mol, corresponding to about three and two times the error of the force field energies of about 11 kJ/mol. It would therefore seem reasonable to assume that the optimization of further force field conformations of even higher energy would yield DFT energies lying considerably above the global minimum. However, a comparison of the experimental and calculated IR spectra revealed marked differences. Most notably, several experimental spectra feature three free OH oscillators, whereas in the vast majority of the 240 structures considered thus far, at least one of the OH groups is a hydrogen bond donor. This is illustrated in Fig. 4.12, which shows the three lowest-energy DFT conformers of the protonated phenylalanine family (a–c) and the protonated serine family (d–f); the energy increases from left to right. Intramolecular hydrogen bonds are indicated in blue, while intermolecular hydrogen bonds involving the ammonium group or an OH group are shown in green and red, respectively. In each of the conformations, two OH donor hydrogen bonds can be found. (In structure d, an additional interaction of one of the serine carboxylic acid OH groups with the aromatic ring can be observed.)

It might therefore appear that the AMBER* force field disfavors hydrogen bonding patterns in which several OH groups are free. Additional calculations were therefore performed of structures outside of the energy window considered so far that feature at least two free carboxylic acid OH groups. These data points are also included in Fig. 4.11 and appear at higher AMBER* energies. They extend the considered energy window by another ~ 20 kJ/mol and ~ 10 kJ/mol for the families with protonated serine and phenylalanine, respectively. The corresponding DFT energies, however, were found to lie at least 10 kJ/mol higher than the lowest energies determined initially.

The structures a–f are characterized by a maximum number of hydrogen bonds, four in each isomer. However, the pattern of intra- and intermolecular hydrogen bonds almost inevitably involves the OH groups. In an attempt to construct conformations with a larger number of free OH oscillators, a different hydrogen bonding network was therefore adapted. Several structures were guessed in which the ammonium group of protonated phenylalanine forms three intermolecular hydrogen bonds with the serine hetero atoms. Such a configuration, which is driven by intermolecular charge solvation, leaves at least two of the three OH hydrogens free. The optimized DFT energies of 14 such structures are marked with crosses in Fig. 4.11. Five of them possess a lower energy than the best structure obtained with the conformational search, the lowest being favored by 13.5 kJ/mol.

The three lowest-energy structures are illustrated in the bottom row of Fig. 4.12 (g–i), each of them featuring three intermolecular hydrogen bonds (green) involving the ammonium hydrogens. The two structures of lowest energy (g and h) also show an intermolecular hydrogen bond between the phenylalanine carbonyl oxygen and the serine alcohol hydrogen. In structure (i), even all three OH groups are free, as experimentally observed for some of the isomers. Here, all four hydrogen bonds are formed with the ammonium group. The serine carbonyl oxygen, which forms one of them, points in between the three ammonium hydrogens.

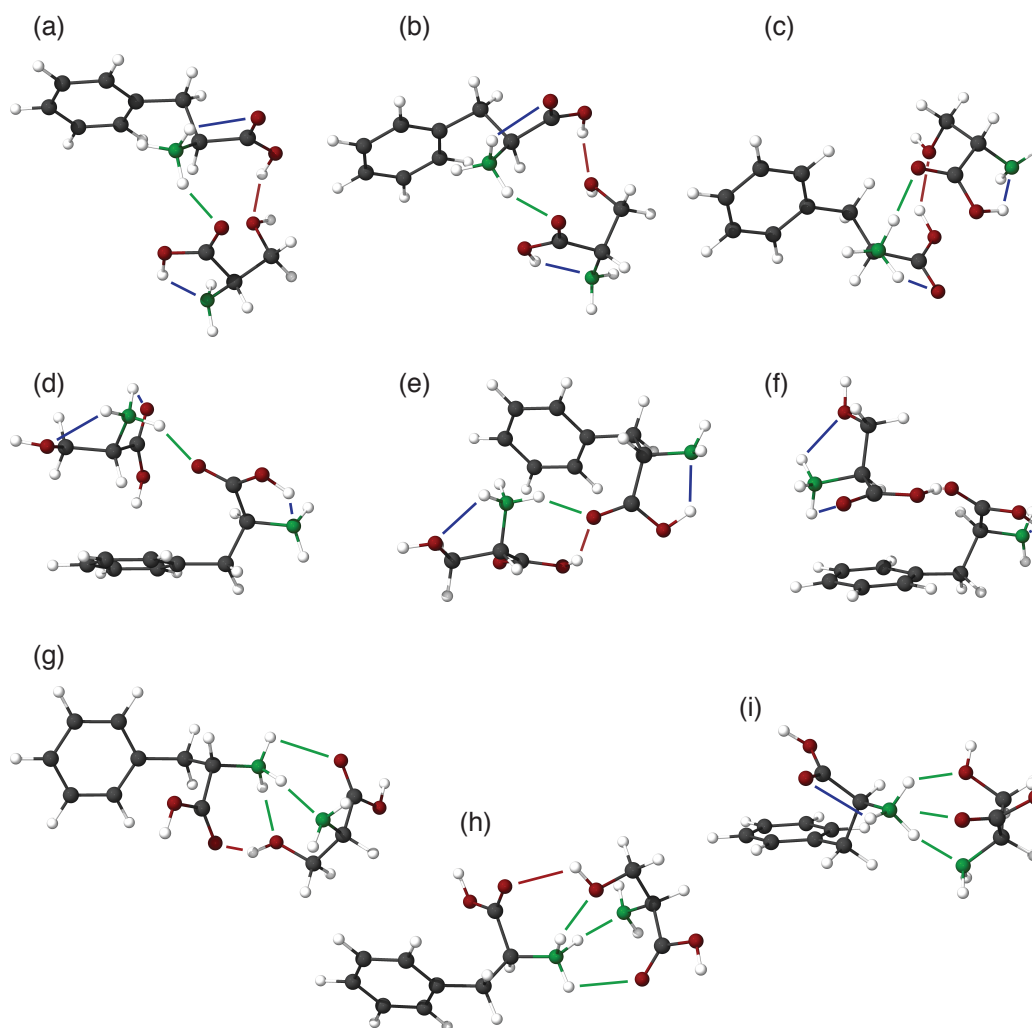


Figure 4.12: DFT optimized structures of different isomers of the protonated amino acid dimer. Lowest energy structures obtained from the force field conformational search with the excess proton located on phenylalanine (a–c) and serine (d–f) are shown together with the best structures obtained by guessing (g–i).

When isomer (g) was used as the starting point of a conformational search, a new set of conformations was generated that are structurally related to (g) and the other guessed structures. Most of them feature several hydrogen bonds with the ammonium group and two or three free OH groups. The 50 most stable structures were optimized on the DFT level and are included in Fig. 4.13, which displays their relative MO6 energies as a function of the relative AMBER* energies together with those of the structures already considered in Fig. 4.11. They can be distinguished by their force field and DFT energies that are up to ~ 40 kJ/mol lower than those of the lowest energy isomers found before. As in Fig. 4.11, open and filled circles represent isomers that are protonated on the phenylalanine and serine amino group, respectively.

These findings suggest that the Monte Carlo search algorithm does not sample the PES efficiently. Depending on the starting structure, only certain structural families are explored and the algorithm is obviously not able to jump from one basin of the PES to another. It

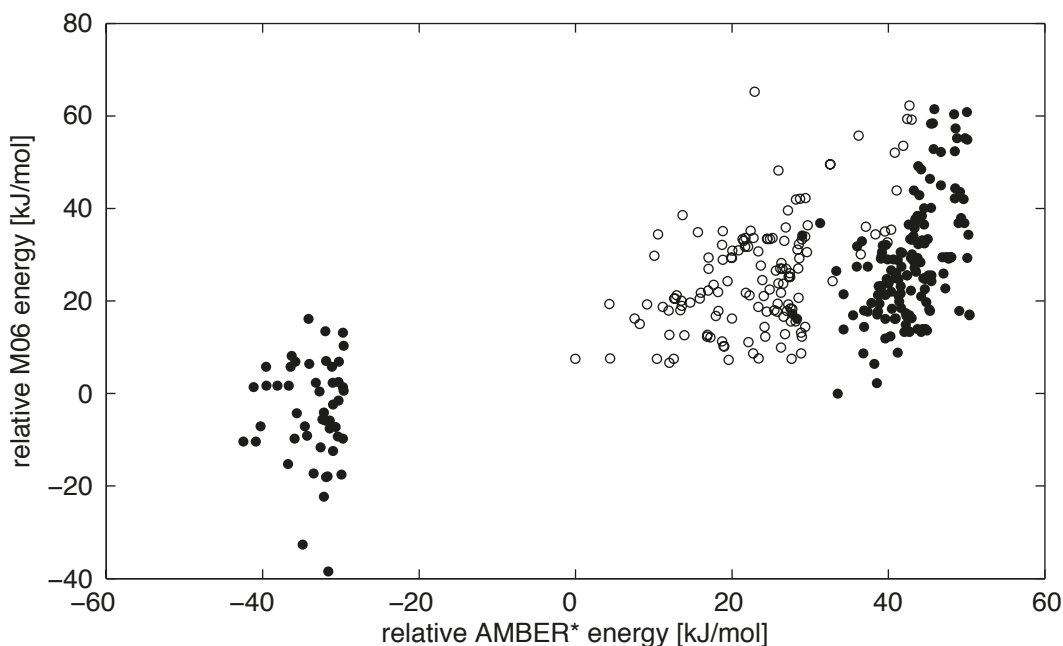


Figure 4.13: Relative (zero point corrected) DFT energy versus relative force field energy for the lowest energy structures obtained in the conformational search. Isomers in which either serine or phenylalanine carries the proton are marked with open and filled circles, respectively. For the family with protonated phenylalanine, the conformational search generates conformers of different structural families depending on the starting structure that is used.

may seem surprising that the conformational search should be inefficient for such a small and flexible system, particularly, since some dipeptides had previously been found to be perfectly tractable.¹¹⁴ In order to convert between the different types of structures, the breaking of several hydrogen bonds and the rearrangement of the entire hydrogen bond network is necessary. The associated energy cost obviously hinders the search algorithm to leave one valley and enter a different one. More sophisticated (and more expensive) algorithms might be better suited for the exploration of the PES, which was, however, beyond the scope of this work.

It has to be concluded that with the simple methodology employed here, it is impossible to exhaustively explore the protonated phenylalanine/serine PES and assign calculated structures to the experimental spectra in a deterministic and reliable procedure. However, the computational results may still serve to elucidate some of the structural features of the dimer.

Figure 4.14 compares the experimental spectra of isomers A and B with calculated (harmonic) spectra. To account for anharmonicity and for ease of comparison, they have been scaled with a factor of 0.955. The spectra labeled a–i correspond to the structures shown in Fig. 4.12. The serine side chain OH stretch is indicated in violet, the carboxylic acid OH stretches in red, and the ammonium NH stretches in green. The weak NH stretch vibrations of the amino group (blue) are marked with arrows to increase their visibility. The transitions at 3210 and 3215 cm^{-1} in spectrum (d) correspond to strongly mixed NH/carboxylic OH stretches and are therefore neither colored green nor red.

All calculated spectra in Fig. 4.14 feature a free alcohol OH stretch vibration in agreement

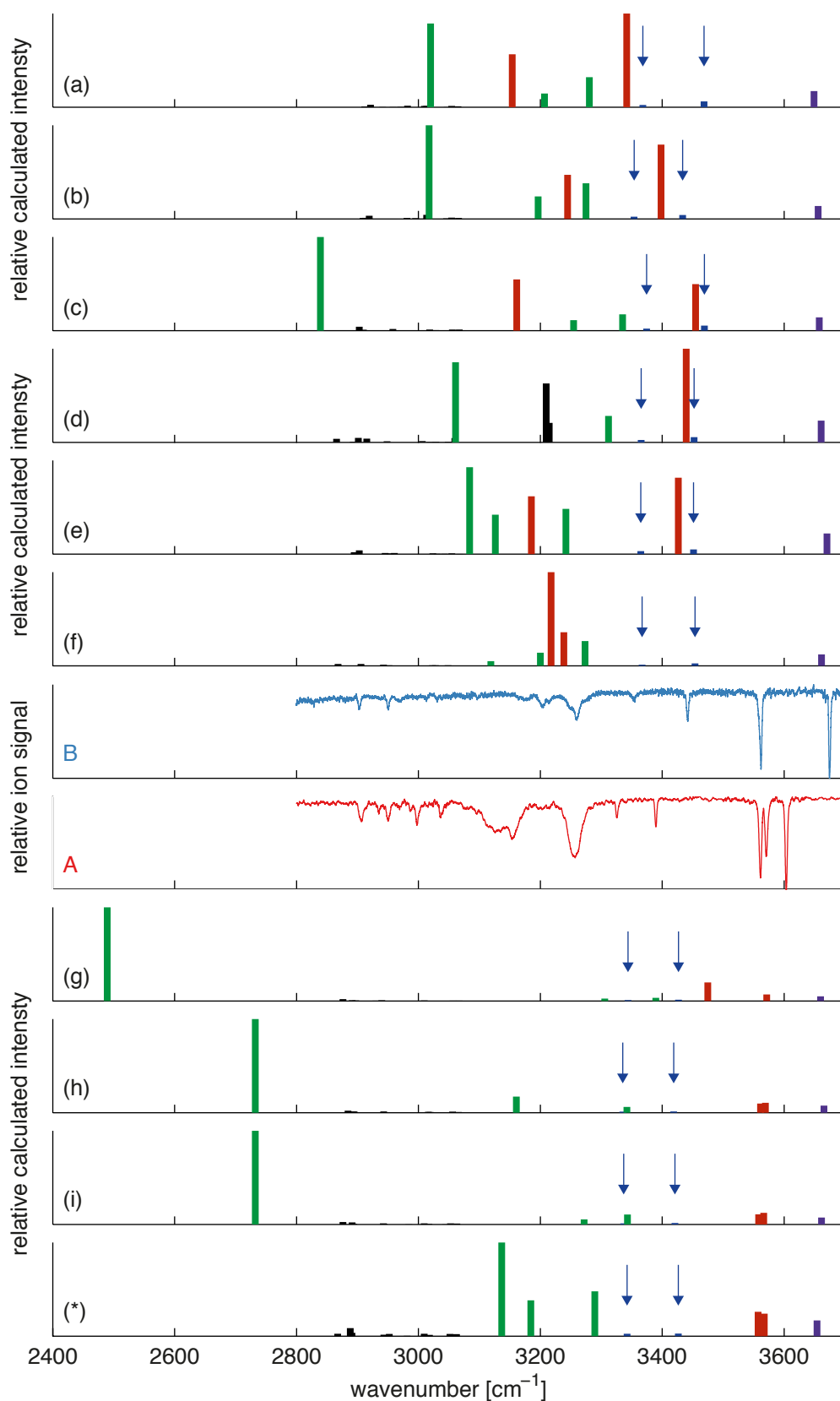


Figure 4.14: Comparison of two experimental IR spectra (middle) with calculated spectra of structures obtained from the conformational search (top) and guessed structures (bottom). The labels of the spectra refer to the structures displayed in Figs. 4.12 and 4.16. The calculated spectra are scaled with a factor of 0.955. The serine side chain OH stretch is indicated in violet, the carboxylic acid OH stretches in red, and the ammonium NH stretches in green. The weak NH stretch vibrations of the amino group (blue) are marked with arrows to increase their visibility.

with the majority of the experimental IR spectra. As mentioned above, the spectra a–f, which correspond to the lowest energy structures obtained from the initial conformational search, provide a poor match for the experimental spectra, since they do not show any free carboxylic acid OH stretches. In all of these structures, the neutral amino acid features an intramolecular hydrogen bond between the nitrogen and the carboxylic acid proton. The corresponding OH stretch vibration is calculated to shift to the range between 3150 and 3250 cm^{-1} , in good agreement with experimental observations for the neutral aromatic amino acids.^{63,64,277} The remaining carboxylic acid group mostly functions as a hydrogen bond donor in an intermolecular hydrogen bond with an oxygen atom. (The only exception is structure d, in which the hydrogen interacts with the aromatic ring.) A smaller redshift is associated with these hydrogen bonds, and the corresponding OH stretch vibrations are calculated to appear between 3340 and 3460 cm^{-1} . Only in structure f, where this interaction is the only intermolecular hydrogen bond, a larger shift is observed.

A weakly hydrogen bonded carboxylic OH stretch band could in principle explain the transition of isomer B at 3442 cm^{-1} . It would then, however, be difficult to assign the two stretches of the NH_2 group, and one would have to assume a zwitterionic structure. Moreover, the calculations suggest that such a red-shifted OH stretch vibration should be more intense than the free alcohol OH band, in contrast to the experimental findings. An alternative explanation is offered by the spectra of structures a–f, which feature an intramolecular hydrogen bond between the carboxylic acid OH proton and the amino group of the neutral amino acid. The symmetric and antisymmetric NH stretch vibrations of these isomers appear blue-shifted (as compared, for example, to the spectra of structures g–i, where such a hydrogen bond is absent). One could therefore speculate that isomer B possesses this type of intramolecular hydrogen bond, which would at the same time explain the absence of the second free carboxylic OH stretch and the blueshift of the NH bands of the amino group. Further experiments will be necessary to verify this hypothesis.

The different hydrogen bond topology of the structures g–i manifests itself in their calculated IR spectra (Fig. 4.15). Isomer g features one free carboxylic OH stretch, while h and i possess even two. The strong $\text{NH}\cdots\text{N}$ hydrogen bond that all three structures have in common leads to a strong redshift of the corresponding ammonium NH stretch band, which is predicted to appear below 2800 cm^{-1} . This, however, is at odds with the experimental spectra which clearly show three ammonium bands for several of the observed isomers. With the goal of finding an isomer that features the same hydrogen bonding pattern as the structures g–i, but shows better agreement with the experimental spectra, the structure displayed in Fig. 4.16 was constructed by simply rotating the serine moiety in structure i.

Here, the amino group nitrogen points in between the ammonium hydrogens, which are all complexed by an oxygen atom. The calculated spectrum (marked with an asterisk in Fig. 4.14) reveals that, indeed, all hydrogen bonds are of similar strength, so that none of the ammonium

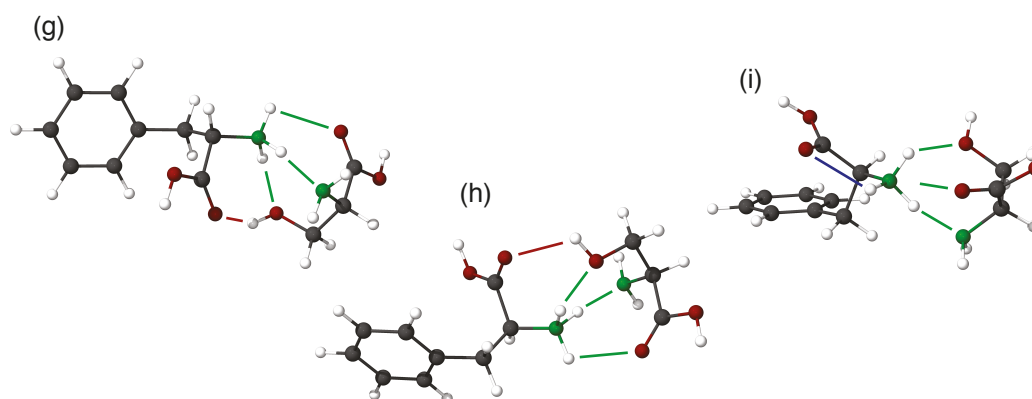
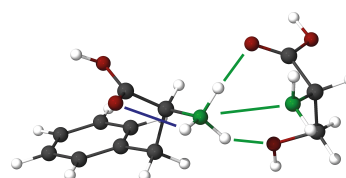


Figure 4.15: DFT optimized structures of the best isomers of the protonated dimer that were obtained by guessing.

Figure 4.16: Structure of the dimer corresponding to the spectrum marked with an asterisk in Fig. 4.14.



stretches experiences a strong redshift. The energy of this isomer lies 8.0 kJ/mol above the energy of structure g, but still 5.6 kJ/mol below the energy of the best force field isomer (a). The calculated spectrum of this isomer provides the best agreement with the general features of the IR depletion spectra. However, it is unlikely that it should accidentally correspond to the true structure of any of the isomers that were identified experimentally. The vast majority of the calculated spectra of the isomers that were obtained when the conformational search was started with structure (d) are similar to the spectra (g–i) and show the characteristic red-shifted ammonium NH stretch that arises from a hydrogen bond with the amino group nitrogen of the neutral amino acid.

In summary, this section documents the failure of a frequently used approach for analyzing the gas phase spectra of peptides by means of quantum chemical calculations. It was shown, specifically, that the initial exploration of the PES of the protonated phenylalanine/serine dimer on the force field level fails, due to an inefficient sampling with the Monte Carlo search algorithm that was employed here. However, in the absence of a tool for sampling the entire conformational space in a reliable fashion, quantum chemical calculations can only yield qualitative information. They suggest that the structures of the protonated dimer should be dominated by hydrogen bonds with the ammonium group. Maybe most importantly, these investigations underline the complexity of the protonated dimer from the perspective of the computational tractability of the problem.

4.6 Excited State Spectra

This section about the spectroscopic properties and dynamics of the UV excited dimers should be considered as work in progress. While several new insights could be gained and corroborated, even more open questions remain, some of which could easily be answered with the methods established in this section. For example, the limited time available did not permit to investigate all the isomers of the protonated dimer.

As illustrated in Fig. 4.3, the IR spectrum of the excited state of an ion can be obtained if the absorption of an IR photon changes the fragmentation pattern of this species. Figure 4.17 presents difference mass spectra obtained by subtracting the mass spectrum recorded after UV (only) excitation from the mass spectrum corresponding to UV excitation followed by IR irradiation. In each of these spectra, the OPO was tuned to the OH stretch transition of one of the carboxylic acid groups. The change of the fragmentation pattern upon IR absorption is evident from positive peaks (enhancement of a mass channel) and negative peaks (depletion). It should be noted that the parent ion signal at $m/z = 271$ does not entirely disappear due to shot-to-shot signal fluctuations.

The spectra a–d were recorded with a delay of approximately 10 ns between the UV and the IR laser pulses. Spectra a and b correspond to UV excitation of isomer A at 37596.1 cm^{-1} and 38129.4 cm^{-1} , respectively, while c and d were obtained when exciting isomers B and E on the usual transitions as marked in Fig. 4.5. The four spectra show depletion of the 180 amu channel (loss of the phenylalanine side chain), while the 120 amu fragment (dissociation of the cluster and H_2O and CO loss from protonated phenylalanine) as well as the 106 and 166 amu channels (corresponding to the intermolecular dissociation of the cluster with the proton remaining either on serine or phenylalanine, respectively) are enhanced. Only spectrum b does not show any significant IR induced change of the 106 amu channel. This indicates that the fragmentation behavior depends on the excess energy imparted to the molecule upon UV excitation. Furthermore, while the relative fragment intensities are otherwise largely similar, isomer B shows a strong relative increase of the 166 fragment, which indicates isomer specific behavior.

At a delay of about 400 ns (spectra e and f), isomers A (excitation at 38129.4 cm^{-1}) and E show a different fragmentation pattern. As in the spectra at short times, depletion of the 180 amu channel and enhancement of the 106 amu channel is observed. However, the other two channels do not show a change in fragmentation yield upon IR irradiation. It was found that the peak at 166 amu in spectrum e (marked with an asterisk) actually arises from the action of the IR laser only. At the origin of this observation seems to be a slightly higher sample concentration in this particular mass scan, which favors the formation of larger, multiply charged clusters that dissociate upon absorption of one or several IR photons. These clusters were found to be absent at the lower concentrations that were usually employed. The different fragmentation pattern

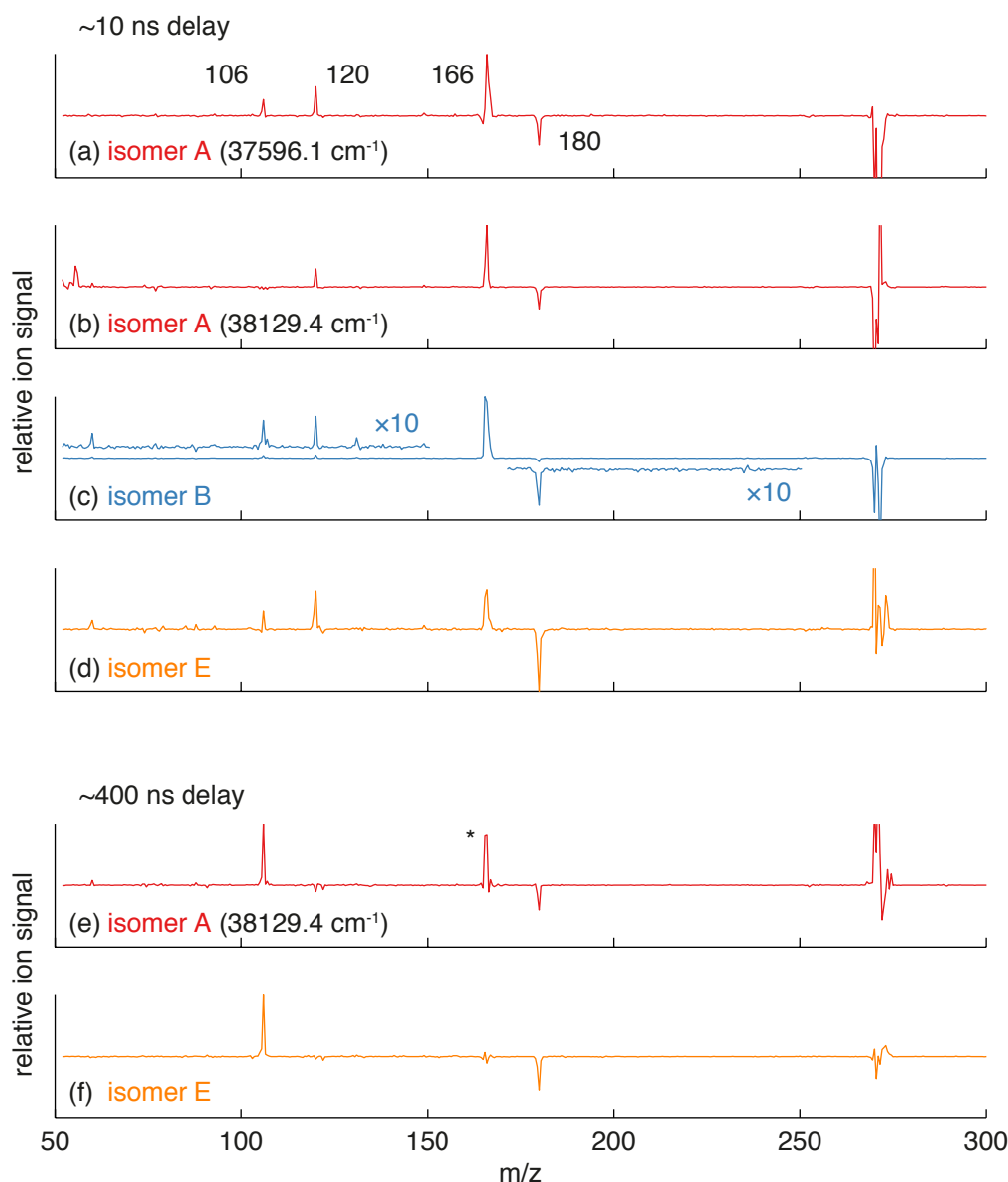


Figure 4.17: Difference photofragment mass spectra showing the enhancement or depletion of different mass channels upon IR irradiation of a UV excited species. The IR OPO is tuned to one of the carboxylic acid OH stretches and fired at a delay of about 10 ns (a-d) and 400 ns (e, f) after the UV laser. The isomers are excited at the same UV transitions as in Fig. 4.6; for isomer A, a different transition at 38129.4 cm^{-1} is also probed (b and e). In spectrum e, the peak at 166 amu (marked with an asterisk) does not originate from an electronically excited species, but probably stems from the IR only dissociation of larger, multiply charged clusters.

a) Isomer A, excitation at 37596.1 cm^{-1} , 10 ns delay, b) isomer A, excitation at 38129.4 cm^{-1} , 10 ns delay, c) isomer B, excitation at 37613.7 cm^{-1} , 10 ns delay, d) isomer E, excitation at 38432.8 cm^{-1} , 10 ns delay, e) isomer A, excitation at 38129.4 cm^{-1} , 400 ns delay, f) isomer E, excitation at 38432.8 cm^{-1} , 400 ns delay.

at $\sim 400 \text{ ns}$ indicates that the corresponding species are different from the ones giving rise to spectra a-d. This is confirmed by Fig. 4.18, which shows that the ground state IR depletion spectra as well as the spectra of the UV excited species recorded at about 10 and 400 ns are all different from one another.

The spectra b and c were recorded in the 120 amu channel after UV excitation of isomer A

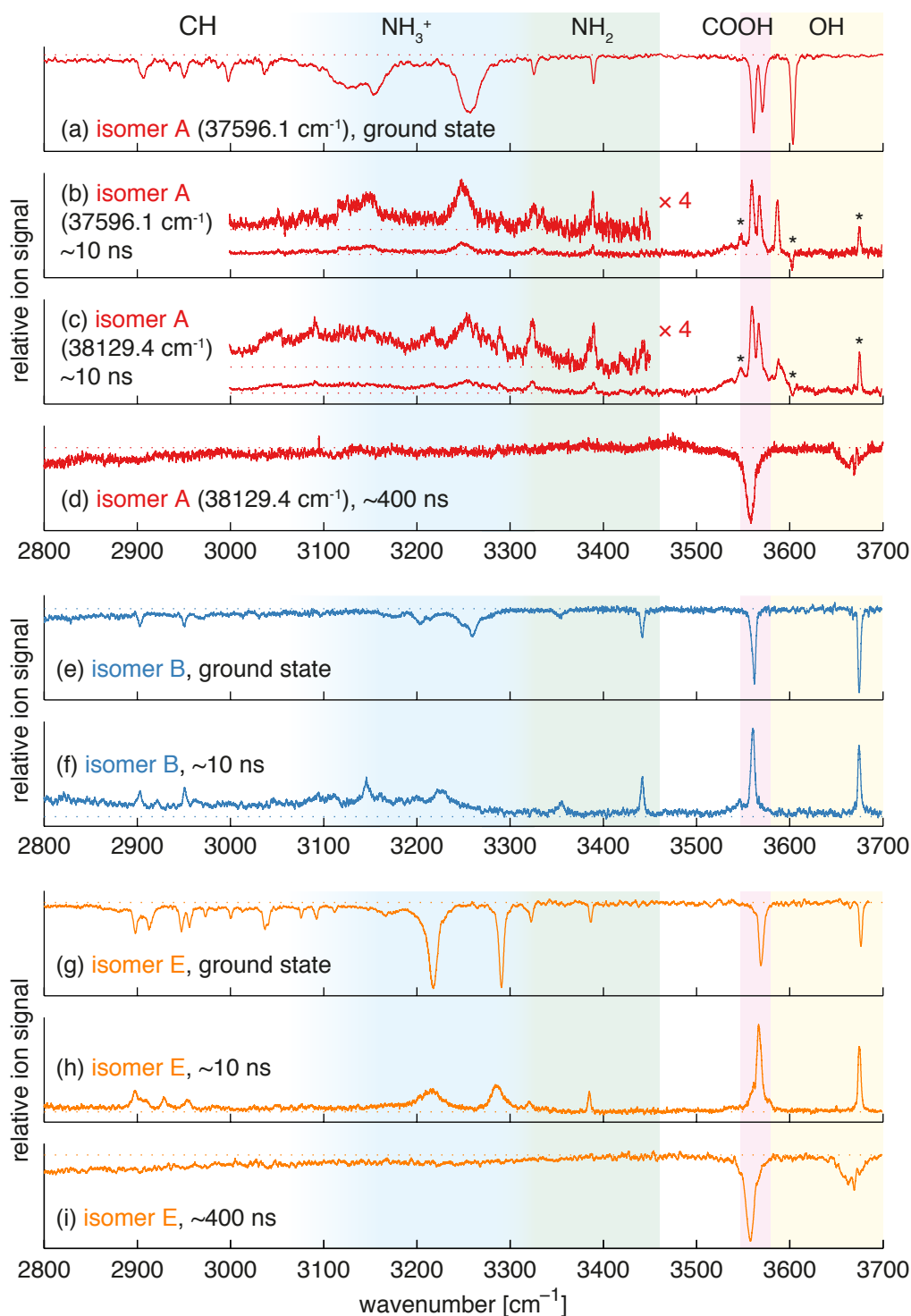


Figure 4.18: Comparison of the ground and excited state spectra of three isomers. Bands marked with an asterisk are attributed to different species than the electronically excited cluster that is being interrogated. In d and i, the structure observed on top of the band at 3666 cm^{-1} is due to water absorption in the IR beam path. a) Isomer A, UV transition at 37596.1 cm^{-1} , ground state spectrum in the 180 amu channel; b) isomer A, UV transition at 37596.1 cm^{-1} , excited state spectrum in the 120 amu channel at a delay of ~ 10 ns; c) same, UV transition at 38129.4 cm^{-1} ; d) isomer A, UV transition at 38129.4 cm^{-1} , excited state spectrum in the 120 amu channel at a delay of ~ 400 ns; e) isomer B, ground state spectrum in the 180 amu channel; f) isomer B, excited state spectrum in the 120 amu channel at a delay of ~ 10 ns; g) isomer E, ground state spectrum in the 180 amu channel; h) isomer E, excited state spectrum in the 120 amu channel at a delay of ~ 10 ns; i) isomer E, excited state spectrum in the 180 amu channel at a delay of ~ 400 ns.

at 37596.1 and 38129.4 cm^{-1} , respectively, with a delay of the IR pulse of about 10 ns. Both spectra are largely similar, but show marked differences to the ground state spectrum (a); most notably, the bands in the NH stretch range appear with much lower intensity. In spectrum c, where isomer A is excited more than 530 cm^{-1} above the band origin, a broad background signal is observed in this range, which likely points to a higher internal temperature of the ions. It has previously been reported that specific vibrations of several indole derivatives appear broadened and with lower peak intensities in the excited state IR spectra. This observation has been explained by a strong coupling of the vibrational states associated with these specific modes to a different, close-lying electronic surface that leads to a fast deactivation.⁷⁴ One might speculate that a similar mechanism could be operating here. All the fragments that are enhanced by the absorption of an IR photon are created upon intermolecular dissociation. If the ammonium hydrogens are indeed involved in several intermolecular hydrogen bonds, as suggested above, it is not unlikely that the corresponding excited NH stretch vibrational states could couple to the dissociative coordinate on a different surface. Another possible explanation for the low intensity of the NH stretch bands could be that internal conversion from the initially excited $\pi\pi^*$ state to a locally excited state occurs,²⁷⁹ during which electronic energy is converted into vibrational energy, so that a warm species is probed in the IR spectra b and c. Indeed, the room temperature IRMPD spectra of some protonated amino acid dimers show weak, broad features in the NH stretch range,⁹⁸ similar to what is observed here.

Several peaks in the OH stretch region of the spectra b and c (marked with asterisks) are attributed to different species than the excited state of isomer A that is being investigated here. The peak at 3548 cm^{-1} is not observed when the same spectrum is recorded in depletion in the 180 amu channel and is attributed to the same species that was already identified in the gain spectrum shown in Fig. 4.9. Similarly, the band at 3675 cm^{-1} is assigned to gains from the other isomers (in their ground state); and the depletion at 3604 cm^{-1} , to the depletion of the ground state of isomer A. When the laser pulses partially overlap in time, these gains and depletions arise because there is a finite probability that a molecule will absorb an IR photon before the UV photon, even though the peak of the UV pulse precedes that of the IR pulse.

The transitions at 3560 and 3567 cm^{-1} are assigned to the slightly red-shifted carboxylic acid OH stretches; and the peak at 3588 cm^{-1} , to the serine side chain OH vibration, which shows a large redshift of 16 cm^{-1} . The spectral positions of the NH_2 and OH vibrations indicate that the structure of the observed species should be close to that of the ground state. Moreover, the fact that the OH bands do not show any considerable broadening indicates that the observed species is not internally hot, which would not be expected if a large amount of electronic energy had been converted into vibrational energy in a radiationless transition. It therefore appears likely that the species probed in the spectra a and b is in the initially excited $\pi\pi^*$ state or in another excited electronic state that is close in energy. The strong shift of the alcohol OH stretch transition of the serine moiety could be explained by a hydrogen bond with the aromatic

ring. At higher internal energies (spectrum c), this band broadens, which is also in agreement with the hypothesis of a hydrogen bonded OH group.

Spectrum d, recorded in the 180 amu channel after about 400 ns (excitation at 38129.4 cm^{-1}), only shows a broad, structureless absorption below 3500 cm^{-1} . The broad peaks at 3558 cm^{-1} (half width of $\sim 11\text{ cm}^{-1}$) and at 3666 cm^{-1} (half width of $\sim 24\text{ cm}^{-1}$) are assigned to the red-shifted, free carboxylic OH stretches and the red-shifted, free serine side chain OH stretch, respectively. The broadening and redshifts are indicative of an internally hot species. The features of the species observed in spectrum c are absent. At shorter delays, both species can be simultaneously observed in the 180 amu mass channel, as demonstrated in Fig. 4.19, which shows spectra recorded at different delays.

The NH stretch region provides only a poor diagnostic tool, since it is broad for both species and shows only some structure at short delays. However, in the OH stretch range, the simultaneous disappearance of the sharp spectral features and the appearance of the broad features can be observed. This indicates that the species observed at short times undergoes a radiationless transition, yielding the species whose spectral signature appears at long delays. In this process, electronic energy is converted into vibrational energy, leading to a hot species with broad, red-shifted features. The internal energy is obviously sufficient to melt the hydrogen bonding network of the cluster, which leads to the loss of the hydrogen bond of the serine side chain OH group, so that a free alcohol OH stretch is observed. This second, internally hot species is not identical with the electronic ground state, since it shows a non-statistical fragmentation pattern (*i.e.* a pattern different from the one observed upon CID of the ground state species), which changes upon IR excitation (see Fig. 4.17). It should be noted that the structure observed on top of the band at 3666 cm^{-1} is due to water absorption in the IR beam path.

Above 3300 cm^{-1} , the IR spectrum of isomer B at a delay of $\sim 10\text{ ns}$ after UV excitation (Fig. 4.18, f) is practically identical to the ground state spectrum (e). However, the ammonium NH vibrations appear red-shifted and broadened and clearly exhibit a different spectral signature. As in the case of isomer A, it seems possible that this observation could be a consequence of a strong coupling of the ammonium NH stretch vibrational levels to another excited state surface or that a radiationless transition from the $\pi\pi^*$ state to another close-lying excited surface is involved, during which a rearrangement of the hydrogen bond network occurs.

For isomer E, a similar picture is obtained. The IR spectrum at a delay of $\sim 10\text{ ns}$ after UV excitation (Fig. 4.18, h) is similar to the spectrum in the ground state (spectrum g), indicating a similar structure in the excited state. Most bands appear red-shifted by $1\text{--}2\text{ cm}^{-1}$, and the peaks in the range of the ammonium NH stretches are broadened. Some of the CH stretch bands below 2950 cm^{-1} can still be distinguished, while others appear washed out. This provides further evidence for a mode specific coupling to another electronic surface on which fast deactivation occurs. The spectrum of isomer E recorded at $\sim 400\text{ ns}$ (spectrum i) is practically identical to the spectrum d of isomer A. This, together with the identical fragmentation pattern at long

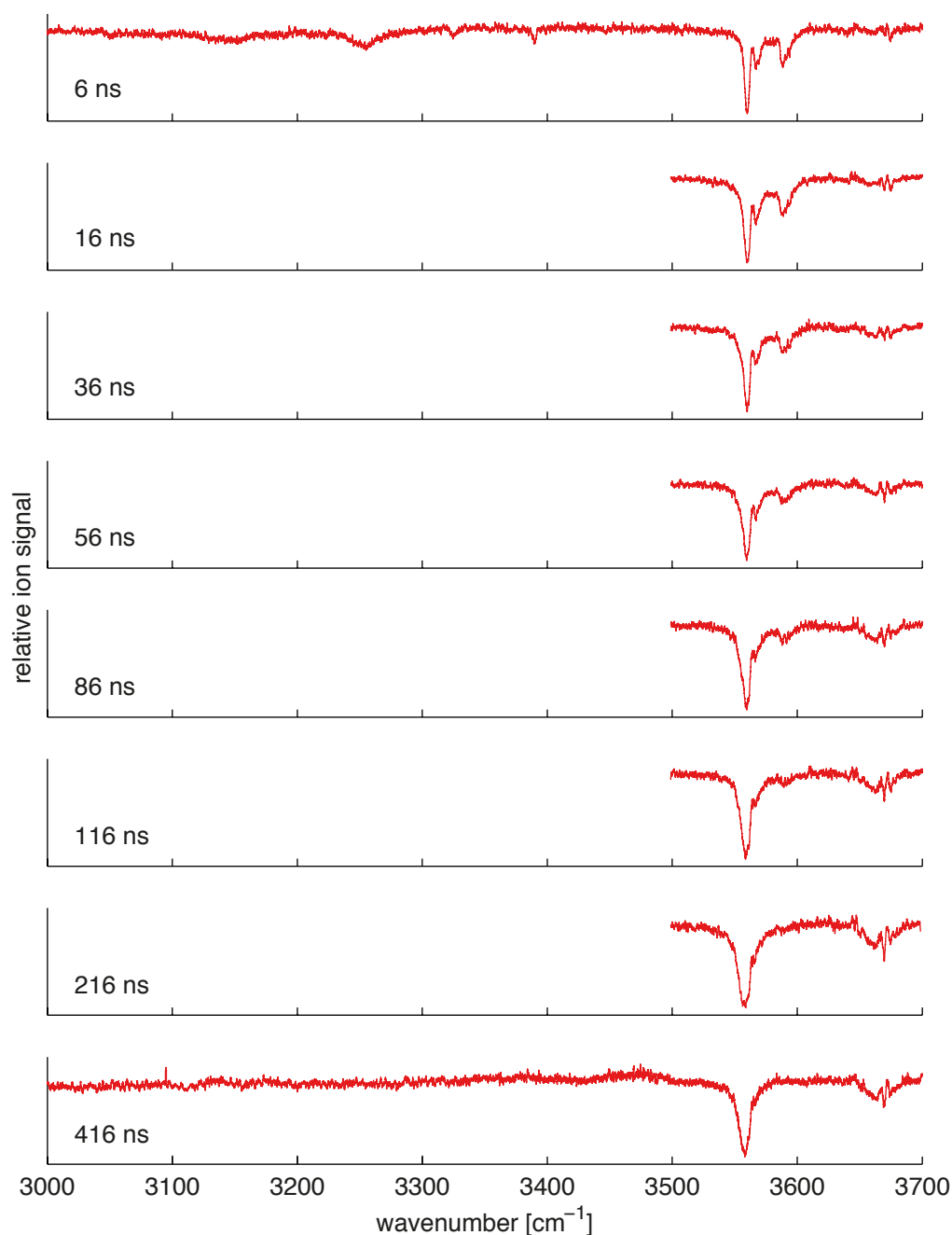


Figure 4.19: IR spectra of isomer A in the 180 amu channel at various delays after UV excitation at 38129.4 cm^{-1} . The structure observed on the band at 3666 cm^{-1} is due to a water absorption in the IR beam path.

delays, suggests that both isomers undergo a sequence of radiationless transitions that lead to vibrationally hot clusters on the same excited state surface. These clusters have sufficient internal energy to interconvert, which results in identical IR spectra.

Figure 4.20 shows the results of an experiment to determine the lifetime of the species that is initially observed after UV excitation of isomer A at 38129.4 cm^{-1} . The relative enhancement signal in the 120 amu channel is shown as a function of the delay between UV excitation and IR probe pulse at 3588 cm^{-1} , which corresponds to the serine side chain OH stretch vibration.

From the data points for delays > 18 ns, a lifetime of 63 ± 1 ns is determined, slightly shorter

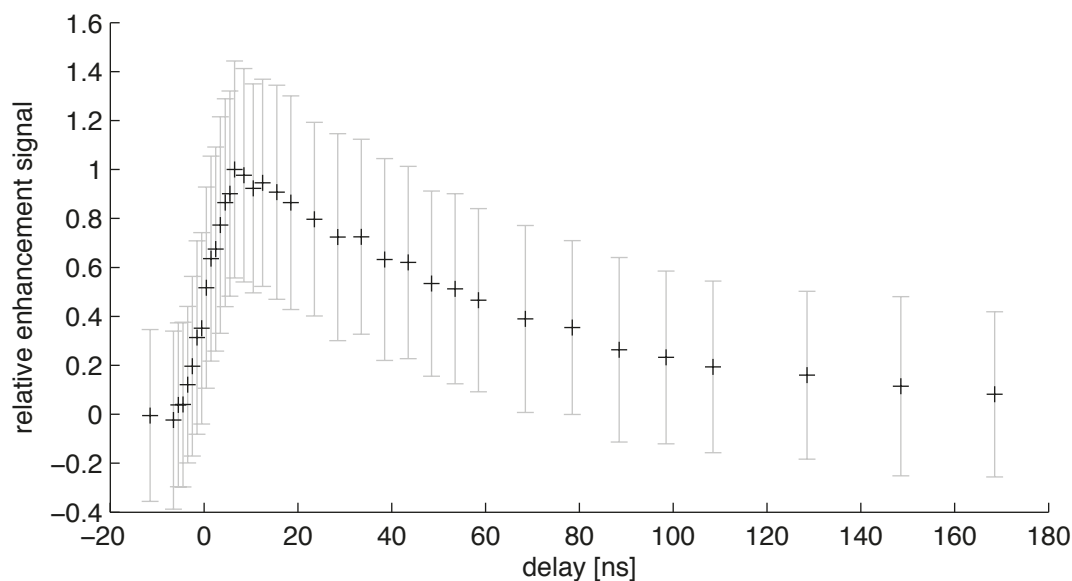


Figure 4.20: Determination of the lifetime of the short lived species that is initially created upon UV excitation of isomer A at 38129.4 cm^{-1} . The relative enhancement signal in the 120 amu channel is shown as a function of the delay between UV excitation and IR probe pulse at 3588 cm^{-1} (corresponding to the serine side chain OH stretch). From the data points for delays > 18 ns, a lifetime of 63 ± 1 ns is determined.

than the lifetime of 73 ± 3 ns that was obtained when the band origin of the same isomer at 37596.1 cm^{-1} was pumped instead. For isomers B and E, similar measurements yielded lifetimes of 112 ± 5 ns and 70 ± 2 ns, respectively.

Figure 4.21 shows the results of the analogous experiment to determine the lifetime of the species that is observed at long delays after UV excitation of isomer A at 38129.4 cm^{-1} . The relative depletion signal in the 180 amu channel is shown as a function of the delay between UV excitation and IR probe pulse at 3558 cm^{-1} , which corresponds to the broad peak assigned to the carboxylic acid OH stretches. The initial fast drop of the depletion signal is ascribed to the escape of the ions from the volume of the laser focus and their redistribution in the trap.¹²⁰ From the data points for delays $> 60 \mu\text{s}$, a lifetime of $506 \pm 62 \mu\text{s}$ is determined, considerably longer than that of the initially created species. It should also be noted that collisional deactivation and cooling due to residual helium in the trap occurs on a similar time scale, so that the value obtained above might not reflect the intrinsic lifetime of the species. A similar measurement for isomer E could provide further evidence for the identity of the species formed at long times.

In summary, the available information on the excited state properties of the protonated phenylalanine/serine dimers suggest the following picture. After UV excitation, a first species is observed whose IR spectrum is largely similar to the spectrum of the ground state, suggesting a structure with identical hydrogen bonding network. Sharp transitions are observed in the range of the amino group NH stretches and the OH stretches as well as for some CH stretches, which points to a vibrationally cold species. This renders it likely that the initially excited $\pi\pi^*$ state is

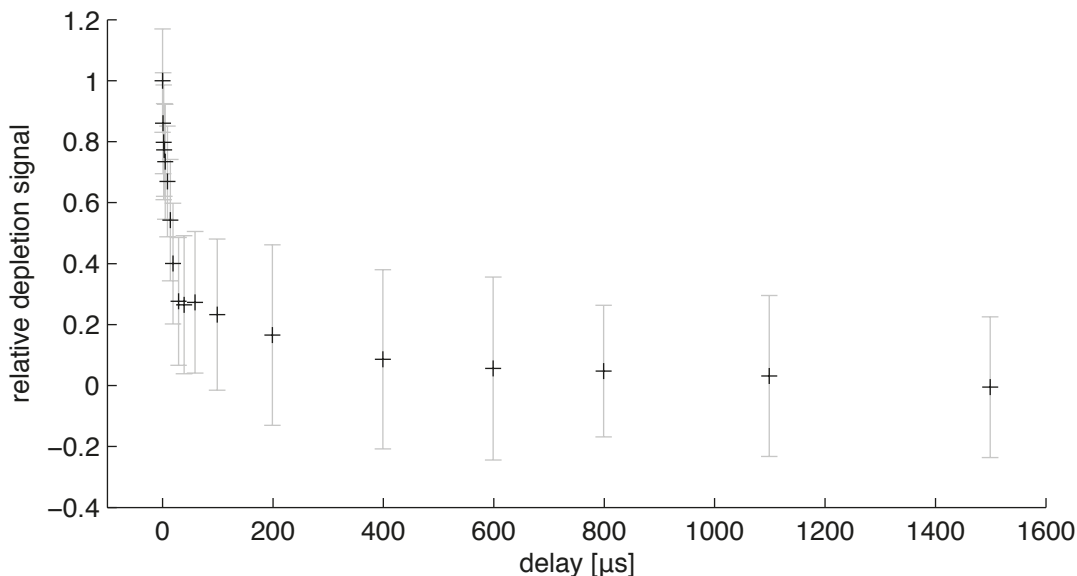


Figure 4.21: Determination of the lifetime of the long lived species that is created after UV excitation of isomer A at 38129.4 cm^{-1} and a subsequent radiationless transition. The relative depletion signal in the 180 amu channel is shown as a function of the delay between UV excitation and IR probe pulse at 3558 cm^{-1} (corresponding to the carboxylic acid OH stretches). The initial fast drop of the depletion signal is ascribed to the escape of the ions from the volume of the laser focus and their redistribution in the trap.¹²⁰ From the data points for delays $> 60\text{ }\mu\text{s}$, a lifetime of $506 \pm 62\text{ }\mu\text{s}$ is determined.

being probed. The ammonium NH stretches show considerable broadening, which is attributed to a strong coupling to a different excited state surface that leads to fast deactivation.

On a time scale on the order of 100 ns, the transition to a different excited state surface occurs. This second species possesses a lifetime of at least $\sim 500\text{ }\mu\text{s}$ and a different fragmentation pattern. Its IR spectrum is broad below 3500 cm^{-1} and shows only two broad peaks, corresponding to the free carboxylic acid OH stretches and the free OH stretch of the serine side chain. These features indicate an internally hot species with a molten structure and suggest that a considerable amount of electronic energy is converted to vibrational energy during the radiationless transition that leads to this species.

It is difficult to link these findings to any previous studies that investigated the excited state dynamics either of protonated amino acids or protonated peptides – simply because these systems are different and might be governed by different mechanisms. Most closely related are probably the investigations on the mechanism of the so-called Infrared Laser Assisted Photofragment Spectroscopy (IRLAPS) technique, which has been used to enhance the fragmentation yield of UV excited protonated peptides through subsequent irradiation with a CO_2 laser.¹¹⁹ It was found that in tyrosine or phenylalanine containing peptides, the mass channel corresponding to the loss of the aromatic side chain usually showed the strongest enhancement. This, however, suggests fragmentation on an excited state surface, since side chain loss is not observed from hot, ground state molecules.¹²⁰ IRLAPS enhancement could still be observed even at a delay of several hundred μs between the UV and CO_2 laser pulses. The similar lifetime of the long-lived

species observed here suggests that it might be related to the species whose dissociation yield can be enhanced with the IRLAPS technique and that both intermediates might be formed in a related process. The high vibrational temperature of the long-lived species could also explain the high efficiency of the IRMPD enhancement of up to two orders of magnitude.¹¹⁹ At high internal energies, the high density of states leads to efficient IRMPD, while for internally cold species, on the other hand, the multiple photon excitation with an off-resonant IR laser can be expected to be slow. Furthermore, the long-lived species observed here is in an excited electronic state, and one of its fragmentation channels corresponds to side chain loss, as observed in the IRLAPS experiments. Whereas in the IRLAPS investigations, an enhancement of this channel was observed, it is actually suppressed upon IR excitation in the present study. However, the differences in the IR excitation scheme and the molecular system might account for the different behavior. It was also reported that at long delays of several ms between UV excitation and IRMPD, a constant IRLAPS enhancement signal could be measured.¹²⁰ In the present study, the long-lived species is not detectable any more on these time scales.

Several studies have explored the UV photo induced dynamics of protonated aromatic amino acids from the fs to the ms time scale, and these efforts have been reviewed recently.²⁸³ The most detailed picture has been elaborated for protonated tryptophan, while the investigations for protonated phenylalanine generally suffer from a lower fragmentation yield.^{284, 285} The complex fragmentation behavior of protonated tryptophan arises from a coupling of the $\pi\pi^*$ state with two charge transfer states that are close in energy and lead to different fragmentation patterns. However, it is not clear whether these states and the dissociation mechanisms of protonated tryptophan are relevant to the excited state dynamics of the protonated dimers. It has, for example, been observed that microsolvation of protonated tryptophan raises the energy of the dissociative $\pi\sigma^*$ state that leads to fast H atom loss from the ammonium group. This should also be the case for the protonated dimers, since the analysis of the ground state spectra suggests that the ammonium group is involved in several hydrogen bonds. Different excited-state dynamics can therefore be expected.

The elementary steps suggested for the different fragmentation pathways of protonated tryptophan involve H atom loss from the ammonium group, intramolecular proton transfer, loss of NH_3 , and breakage of the $\text{C}_\alpha\text{-C}_\beta$ bond. For the dimers, loss of NH_3 is not observed in the photofragment mass spectra. Also, the two transient species observed here clearly have not lost the aromatic side chain – otherwise, absorption of an IR photon would not be able to deplete the yield in these channels. H atom loss or intramolecular proton transfer on a different electronic surface would likely result in a vibrationally hot species. It is therefore possible that such elementary steps are involved in the formation of the long-lived intermediate, while the low internal temperature and vibrational signature of the short-lived species suggest otherwise.

4.7 Conclusions and Outlook

The UV and IR spectra of the protonated phenylalanine/serine dimer demonstrate the presence of at least five different isomers under the experimental conditions. Non-zwitterionic structures are assigned to these isomers based on a pattern of NH stretch vibrations that is consistent with a free amino group and a hydrogen-bonded ammonium group as well as the observation of two free carboxylic OH stretches for three of the isomers. The spectra with ^{15}N labeled phenylalanine are consistent with the assignment of the bands in the NH stretch range, since they either show the redshift of the two bands assigned to the free amino group or the shift of the three ammonium stretches. Most importantly, the labeling experiments show that in two of the isomers, the excess proton is located on the amino acid with the lower proton affinity, serine.

Quantum chemical calculations have been performed with the goal to assign structures to the isomer-specific IR spectra. It is shown that the previously successful strategy of exploring the PES on the force field level and then refining the obtained structures in DFT calculations cannot be applied to the present system. A detailed analysis demonstrates that the Monte Carlo conformational search that was employed does not efficiently sample the PES. With this approach, it is therefore not possible to obtain the structures and spectra of the lowest energy isomers in a reliable and deterministic fashion. The calculations, however, support the conclusions drawn from the IR spectra about the connectivity of the hydrogen bonding network, which appears to be dominated by several intermolecular hydrogen bonds of the ammonium group.

The present investigation of the protonated phenylalanine/serine dimer leaves many questions open about the detailed structures of the observed isomers. It demonstrates the complexity of such an apparently simple system – in contrast to the simple picture that previous studies of protonated amino acid dimers using IRMPD spectroscopy have suggested. The failure of a standard computational approach to elucidate the structure of even such a small system raises questions about the applicability of these methods to much larger biological molecules. Surprisingly, it is not even possible to *a priori* predict which amino acid carries the excess proton.

The investigations of the IR spectroscopic signatures and dynamics of the excited state species are incomplete at this point. Most of all, a complete set of experiments for all isomers of the protonated dimer are missing, and several suggestions for further investigations have been made in the text. The available data, however, provide conclusive evidence for the following picture. Upon UV excitation, a short-lived species is initially created, whose IR spectrum indicates a low vibrational temperature and resembles that of the ground state. It seems likely that this species corresponds to the $\pi\pi^*$ state which, on a time scale on the order of 100 ns, converts into another electronically excited species with a lifetime on the order of 500 μs . The IR spectrum of the latter reveals a high internal temperature and a molten structure and is

identical for different isomers in the ground state. These initial investigations suggest that with the methodology used here new kinds of information about the excited state dynamics of cold ions could potentially be accessible for a large variety of systems.

Chapter 5

Conclusions

The attempt to draw a unifying conclusion from the scientific efforts described in the previous chapters meets several difficulties. The body of work presents itself as very heterogeneous, so that it seemed wise to include detailed conclusions for each experimental chapter separately. Consequently, the goal of this chapter should not be to simply repeat the separate thoughts discussed there, but rather to put the work into a larger context and discuss its implications for the field of research. However, from this larger point of view, the progress that could be achieved with the efforts of four years seems very modest, and it would appear vain to try and arrive at far reaching conclusions based on the minute contribution of the present work. One feels tempted to join Wagner in Goethe's Faust who exclaims "Ach Gott! die Kunst ist lang; / Und kurz ist unser Leben." ("Oh, God! Art is long / And life is short.")

The "spectroscopy of cold, biomolecular ions" constitutes the uniting frame of the present work, for which the introduction sets the stage. The second chapter then actually describes the construction of a mass spectrometer for the preparation of cold, biomolecular ions. Several new features were implemented that improve the performance of the instrument in comparison with the previous generation of the setup. In particular, the use of an ion funnel provides a tenfold increase in signal. At the current stage, only a few studies have been carried out on this new system. Most of all, its extended capabilities have hardly been exhausted and its limits explored. It will hopefully unfold its full potential in the future and lay the basis for many fruitful studies.

The third chapter describes the development of a planar multipole ion trap/TOF mass spectrometer. Although originally motivated in the context of the second chapter, it actually represents a work in its own right. Apart from its potential as a tool for the investigation of buffer gas cooled ions, it is also relevant as a new approach to some long standing technical challenges in TOF mass spectrometry. A number of further applications to a range of different problems are suggested. The chapter describes the evolution of the mechanical design, the development of the electronics, and the different setups in which the instrument was tested. Characterization experiments accompanied by numerical simulations shed light onto several subtleties of the principle of operation of the device. It is my hope that the planar trap/TOF instrument developed here will in the future prove a useful extension of the experimental toolbox

of mass spectrometry as well as cold ion spectroscopy.

These first two experimental chapters are technical in nature and (maybe involuntarily) shift the emphasis of the present work to the side of the instrumentation. However, as the introduction argues, the development of experimental tools to control and manipulate molecular systems and the development of concepts describing these systems depend on each other. Moreover, “[n]othing tends so much to the advancement of knowledge as the application of a new instrument.”²⁸⁶

The fourth chapter finally describes the spectroscopic investigation of a protonated amino acid dimer. The isomer specific IR spectra demonstrate that this small and apparently simple system is far more complicated than could have been anticipated from previous investigations of related systems. The greater detail of the spectroscopic information also provides more stringent criteria for the analysis of the experimental spectra by means of quantum chemical calculations. With a frequently used computational approach, the system is not tractable. Using a UV-pump/IR-probe scheme, it was demonstrated how the lifetimes and the IR spectra of several excited state species can be obtained. These investigations are certainly incomplete at the present stage. Moreover, it would be interesting to extend the studies to other amino acids and peptides and explore whether they show a similar behavior.

Again, drawing general conclusions about the entire field from the investigations on a particular system would seem a stretch. However, a few observations may still be insightful. First of all, the surprising complexity of a small amino acid dimer suggests that, maybe, our understanding of entire proteins is only superficial. Moreover, at this point, our tools seem to be insufficient to fully elucidate the problem. The appeal of the spectroscopy of cold biomolecules is to no small extent due to the fact that it has been successful in providing structural information about large and complex systems. While the nature of a single hydrogen or van der Waals bond has been subjected to detailed investigations, *e.g.* by means of gas phase spectroscopy, the complexity that arises from a large number of these fundamental interactions is hardly understood and difficult to tackle with other techniques (see chapter 1).

However, the difficulty to obtain structural information even for a small amino acid dimer may point to some limitations of the approach and raise questions about the suitability of spectroscopy as a structural probe. Unlike *e.g.* for multidimensional NMR spectroscopy, there is no direct way to obtain the structure from an IR spectrum. (While multidimensional optical techniques are being employed in the liquid phase,²⁸⁷ they are currently not sufficiently sensitive for the gas phase.) This makes it necessary to resort to quantum chemical calculations to interpret the spectra. In some cases, the calculations for the protonated phenylalanine/serine dimer predicted almost identical spectra for different isomers of largely different structures. This usually does not present a problem, since only the lowest-energy structures are considered for the comparison with the experimental spectra. However, it shows that there is no one-to-one correspondence between the IR spectrum and the structure of the molecule.

In order to study complexity, the molecular necessarily has to be large. With an increasing number of NH and OH oscillators, it will become impossible to resolve all of them. Again, NMR spectroscopy avoids this problem by using multidimensional techniques, which is prohibitive for the low sample concentrations of gas phase ions. Diffraction techniques, on the other hand, are a direct probe of the structure and could therefore in the future offer the best approach. Moreover, time-resolved diffraction experiments^{25,288} would allow one to obtain information about both structure and reactivity, the two fundamental concepts of chemistry. However, these techniques are still in their infancy and enormous technical hurdles will have to be overcome before it will actually be possible to study large and complex systems in the gas phase. No matter in which direction the field will develop, many interesting questions remain to be answered, and we can hope for many exciting discoveries to be made.

Appendix

Table 5.1 provides pinouts of the various multipin connectors of the vacuum chamber of the tandem quadrupole mass spectrometer described in chapter 2. These connectors carry the majority of the DC voltages that are applied to the various electrostatic elements. The remaining connections, including, for example, the RF connections for the multipoles, are fairly obvious.

pin	source	quadrupole 1	bender 1	octopole	bender 2
A	hexapole exit lens		B1 entrance lens		B2 entrance lens
B	ion funnel DC exit		Q1 exit lens	entrance lens	B2 inner poles
C	jet disrupter				B2 outer poles
D		Q1 entrance lens		octopole housing	B2 exit lens
E	ion funnel DC entrance				lens 1
F	ion funnel exit lens		B1 exit lens		lens 2
G			B1 outer poles		lens 3
H	gate valve blade		B1 inner poles		lens 4
I					lens 5
J				octopole exit lens	

pin	22-pole	bender 3	quadrupole 2
A	ring electrode 1	lens 10	Q2 entrance lens
B	lens 6		
C	ring electrode 2	lens 11	
D	ring electrode 3	lens 12	
E	ring electrode 4	B3 entrance lens	
F	lens 7	B3 inner poles	
G	lens 9	B3 outer poles	
H	ring electrode 5		Q2 exit lens
I	lens 8		
J		B3 exit lens	

Table 5.1: Pinout of the multipin connectors of the tandem quadrupole mass spectrometer.

Panel 1, timers, PXI 6602

Various timing tasks. Some timers are used internally to synchronize the data acquisition to the machine cycle. Their signals can be read out for diagnostic purposes.

card	pin	pin designation	function
PXI 6602	5	PFI 36/CTR 0 OUT	internal (timing of execution)
PXI 6602	9	PFI 32/CTR 1 OUT	hexapole exit lens timing
PXI 6602	32	PFI 28/P0.28/CTR 2 OUT	22-pole exit lens timing
PXI 6602	29	PFI 24/P0.24/CTR 3 OUT	broken
PXI 6602	26	CTR 4 OUT/PFI 20/P0.20	pyroelectric detector gate
PXI 6602	23	CTR 5 OUT/PFI 16/P0.16	CTR 0 gate out
PXI 6602	53	CTR 6 OUT/PFI 12/P0.12	internal (timing of execution)
PXI 6602	16	CTR 7 OUT/PFI 8/P0.8	internal (timing of execution)

Panel 2, DIO and CTR sources, PXI 6602

The output of the counting preamplifier is connected to the source of the counter CTR 0. The counter CTR 1 is currently not used. The digital lines P0.0 and P0.1 are used as inputs to synchronize the system with the BNC delay generator, which is used as the master clock of the experiment. The digital lines P0.2 and P0.3 handle the communication with the Lambda Physik dye laser.

card	pin	pin designation	function
PXI 6602	2	PFI 39/CTR 0 SOURCE	CTR 0 source (ion counting)
PXI 6602	7	PFI 35/CTR 1 SOURCE	CTR 1 source (not used)
PXI 6602	10	PFI 0/P0.0	t_0 in (clocking pulse in)
PXI 6602	44	PFI 1/P0.1	$\nu/2$ in (half frequency clocking pulse in)
PXI 6602	45	PFI 2/P0.2	Lambda burst trigger
PXI 6602	12	PFI 3/P0.3	Lambda ready
PXI 6602	13	PFI 4/P0.4	
PXI 6602	47	PFI 5/P0.5	

Panel 3, AI, PXI 6052E

Various readbacks.

card	pin	pin designation	function
PXI 6052E	28	AI 4	multiplier(+) Vmon
PXI 6052E	60	AI 5	Q1 pole bias read
PXI 6052E	25	AI 6	Q2 pole bias read
PXI 6052E	57	AI 7	broken
PXI 6052E	34	AI 8	ion funnel RF amplitude read
PXI 6052E	66	AI 9	hexapole RF amplitude read
PXI 6052E	31	AI 10	22-pole RF amplitude read
PXI 6052E	63	AI 11	needle voltage read

Panel 4, DO and AI, PXI 6052E and PXI 6711

This panel features two 15D-Sub connectors, which are used to read back the DC voltages generated by two Spectrum Solutions power supplies. Four digital lines and one analog input are used for the readback of each ten outputs. The digital lines are connected to a multiplexer that selects which output to read on the analog line.

15D-Sub A

card	pin	pin designation	function
PXI 6052E	52	P0.0	pin 1, bit 1
PXI 6052E	17	P0.1	pin 9, bit 2
PXI 6052E	49	P0.2	pin 2, bit 4
PXI 6052E	47	P0.3	pin 10, bit 8
PXI 6052E	68	AI 0	pin 3, meter channel 1-10
PXI 6052E	19	P0.4	pin 11, bit 1
PXI 6052E	51	P0.5	pin 4, bit 2
PXI 6052E	16	P0.6	pin 12, bit 4
PXI 6052E	48	P0.7	pin 5, bit 8
PXI 6052E	33	AI 1	pin 13, meter channel 11-20

15D-Sub B

card	pin	pin designation	function
PXI 6711	52	P0.0	pin 1, bit 1
PXI 6711	17	P0.1	pin 9, bit 2
PXI 6711	49	P0.2	pin 2, bit 4
PXI 6711	47	P0.3	pin 10, bit 8
PXI 6052E	65	AI 2	pin 3, meter channel 1-10
PXI 6711	19	P0.4	pin 11, bit 1
PXI 6711	51	P0.5	pin 4, bit 2
PXI 6711	16	P0.6	pin 12, bit 4
PXI 6711	48	P0.7	pin 5, bit 8
PXI 6052E	30	AI 3	pin 13, meter channel 11-20

Panel 5, fast AO, PXI 6052E and PXI 6711

Control voltages for mass command and pole bias of Q1.

card	pin	pin designation	function
PXI 6052E	22	AO 0	Q1 mass command
PXI 6052E	21	AO 1	Q1 pole bias
PXI 6711	22	AO 0	
PXI 6711	21	AO 1	
PXI 6711	57	AO 2	
PXI 6711	25	AO 3	

Panel 6, timers, PXI 6052E, PXI 6711 and PXI 6723 (a)
Various timers.

card	pin	pin designation	function
PXI 6052E	2	CTR 0 OUT	22-pole enable pulsed valve
PXI 6052E	40	CTR 1 OUT	
PXI 6711	2	CTR 0 OUT	
PXI 6711	40	CTR 1 OUT	
PXI 6723 (a)	2	CTR 0 OUT	
PXI 6723 (a)	40	CTR 1 OUT	

Panels 7 and 8, AO, PXI 6723 (a), 6723 (b), and 6704

Panels 7 and 8 each feature one 25D-Sub connector that supplies the command voltages for a Spectrum Solutions power supply.

25D-Sub A

card	pin	pin designation	function
PXI 6723 (a)	22	AO 0	pin 1, output 1
PXI 6723 (a)	21	AO 1	pin 14, output 2
PXI 6723 (a)	57	AO 2	pin 2, output 3
PXI 6723 (a)	25	AO 3	pin 15, output 4
PXI 6723 (a)	60	AO 4	pin 3, output 5
PXI 6723 (a)	28	AO 5	pin 16, output 6
PXI 6723 (a)	30	AO 6	pin 4, output 7
PXI 6723 (a)	65	AO 7	pin 17, output 8
PXI 6723 (b)	68	AO 8	pin 5, output 9
PXI 6723 (b)	33	AO 9	pin 18, output 10
PXI 6723 (b)	32	AO 10	pin 6, output 11
PXI 6723 (b)	65	AO 11	pin 19, output 12
PXI 6723 (b)	30	AO 12	pin 7, output 13
PXI 6723 (b)	29	AO 13	pin 20, output 14
PXI 6723 (b)	62	AO 14	pin 8, output 15
PXI 6723 (b)	27	AO 15	pin 21, output 16
PXI 6723 (b)	26	AO 16	pin 9, output 17
PXI 6723 (b)	59	AO 17	pin 22, output 18
PXI 6723 (b)	24	AO 18	pin 10, output 19
PXI 6723 (b)	23	AO 19	pin 23, output 20

25D-Sub B

card	pin	pin designation	function
PXI 6723 (b)	22	AO 20	pin 1, output 1
PXI 6723 (b)	21	AO 21	pin 14, output 2
PXI 6723 (b)	57	AO 22	pin 2, output 3
PXI 6723 (b)	25	AO 23	pin 15, output 4
PXI 6723 (b)	60	AO 24	pin 3, output 5
PXI 6723 (b)	28	AO 25	pin 16, output 6
PXI 6723 (b)	30	AO 26	pin 4, output 7
PXI 6723 (b)	65	AO 27	pin 17, output 8
PXI 6723 (b)	68	AO 28	pin 5, output 9
PXI 6723 (b)	33	AO 29	pin 18, output 10
PXI 6723 (b)	32	AO 30	pin 6, output 11
PXI 6723 (b)	65	AO 31	pin 19, output 12
PXI 6704	34	AO 0 (V)	pin 7, output 13
PXI 6704	66	AO 1 (V)	pin 20, output 14
PXI 6704	31	AO 2 (V)	pin 8, output 15
PXI 6704	63	AO 3 (V)	pin 21, output 16
PXI 6704	28	AO 4 (V)	pin 9, output 17
PXI 6704	60	AO 5 (V)	pin 22, output 18
PXI 6704	25	AO 6 (V)	pin 10, output 19
PXI 6704	57	AO 7 (V)	pin 23, output 20

Panel 9, slow AO, PXI 6704

Command voltages for the quadrupoles and the octopole.

card	pin	pin designation	function
PXI 6704	22	AO 8 (V)	Q2 mass command
PXI 6704	54	AO 9 (V)	Q2 pole bias
PXI 6704	52	AO 10 (V)	Q2 Δm
PXI 6704	17	AO 11 (V)	Q1 Δm
PXI 6704	15	AO 12 (V)	octopole “mass command” (<i>i.e.</i> RF amplitude)
PXI 6704	47	AO 13 (V)	octopole pole bias
PXI 6704	12	AO 14 (V)	
PXI 6704	44	AO 15 (V)	

Panel 10, DIO, PXI 6704

Digital signals for the communication with the quadrupoles and the Lumonics dye laser.

card	pin	pin designation	function
PXI 6704	2	P0.0	Q1 pole DC
PXI 6704	3	P0.1	Q1 pole DC reverse
PXI 6704	4	P0.2	Q3 pole DC
PXI 6704	5	P0.3	Q3 pole DC reverse
PXI 6704	6	P0.4	Lumonics burst trigger
PXI 6704	7	P0.5	Lumonics in position
PXI 6704	8	P0.6	broken
PXI 6704	9	P0.7	

Panel 11, DIO, PXI 6723 (a)

Digital signals for the communication with the ion funnel and hexapole RF power supplies and the high voltage power supplies for the dynode and multiplier (–). The digital line P0.6 reads the half frequency clocking pulse. This way the software can determine whether the current cycle is an “on” or “off” cycle.

card	pin	pin designation	function
PXI 6723 (a)	52	P0.0	ion funnel enable
PXI 6723 (a)	17	P0.1	hexapole enable
PXI 6723 (a)	49	P0.2	dynode polarity set
PXI 6723 (a)	47	P0.3	multiplier (–) polarity set
PXI 6723 (a)	19	P0.4	dynode polarity read
PXI 6723 (a)	51	P0.5	multiplier (–) polarity read
PXI 6723 (a)	16	P0.6	$\nu/2$ in (half frequency clocking pulse in)
PXI 6723 (a)	48	P0.7	

Panel 12, timers, AI, and DIO, PXI 6723 (c) and PXI 6052E

This panel provides two timer outputs; two analog inputs, which are used to read back the voltage outputs of two high voltage power supplies; and the 15D-Sub connector that is used to read back the DC voltages of a third Spectrum Solutions power supply (see panel 4).

card	pin	pin designation	function
PXI 6723 (c)	2	CRT 0 OUT	
PXI 6723 (c)	40	CRT 1 OUT	
PXI 6052E	58	AI 14	dynode Vmon
PXI 6052E	23	AI 15	multiplier (–) Vmon

15D-Sub C

card	pin	pin designation	function
PXI 6723 (c)	52	P0.0	pin 1, bit 1
PXI 6723 (c)	17	P0.1	pin 9, bit 2
PXI 6723 (c)	49	P0.2	pin 2, bit 4
PXI 6723 (c)	47	P0.3	pin 10, bit 8
PXI 6052E	61	AI 12	pin 3, meter channel 1-10
PXI 6723 (c)	19	P0.4	pin 11, bit 1
PXI 6723 (c)	51	P0.5	pin 4, bit 2
PXI 6723 (c)	16	P0.6	pin 12, bit 4
PXI 6723 (c)	48	P0.7	pin 5, bit 8
PXI 6052E	26	AI 13	pin 13, meter channel 11-20

Panel 13, AO, PXI 6723 (c) and 6723 (d)

Panel 13 features one 25D-Sub connector that supplies the command voltages for a third Spectrum Solutions power supply (see panels 7 and 8).

25D-Sub C

card	pin	pin designation	function
PXI 6723 (c)	22	AO 0	pin 1, output 1
PXI 6723 (c)	21	AO 1	pin 14, output 2
PXI 6723 (c)	57	AO 2	pin 2, output 3
PXI 6723 (c)	25	AO 3	pin 15, output 4
PXI 6723 (c)	60	AO 4	pin 3, output 5
PXI 6723 (c)	28	AO 5	pin 16, output 6
PXI 6723 (c)	30	AO 6	pin 4, output 7
PXI 6723 (c)	65	AO 7	pin 17, output 8
PXI 6723 (d)	68	AO 8	pin 5, output 9
PXI 6723 (d)	33	AO 9	pin 18, output 10
PXI 6723 (d)	32	AO 10	pin 6, output 11
PXI 6723 (d)	65	AO 11	pin 19, output 12
PXI 6723 (d)	30	AO 12	pin 7, output 13
PXI 6723 (d)	29	AO 13	pin 20, output 14
PXI 6723 (d)	62	AO 14	pin 8, output 15
PXI 6723 (d)	27	AO 15	pin 21, output 16
PXI 6723 (d)	26	AO 16	pin 9, output 17
PXI 6723 (d)	59	AO 17	pin 22, output 18
PXI 6723 (d)	24	AO 18	pin 10, output 19
PXI 6723 (d)	23	AO 19	pin 23, output 20

Panel 14, AO, PXI 6723 (d)

Various command voltages. The RF amplitudes of the ion funnel, hexapole, and 22-pole are indirectly controlled via DC voltages that three FUG power supplies deliver to the RF power supplies.

card	pin	pin designation	function
PXI 6723 (d)	55	AO 20	Q1 Δ_{res}
PXI 6723 (d)	20	AO 21	Q2 Δ_{res}
PXI 6723 (d)	19	AO 22	ion funnel RF amplitude
PXI 6723 (d)	52	AO 23	hexapole RF amplitude
PXI 6723 (d)	17	AO 24	22-pole RF amplitude
PXI 6723 (d)	16	AO 25	dynode Vset
PXI 6723 (d)	49	AO 26	multiplier (–) Vset
PXI 6723 (d)	14	AO 27	multiplier (+) Vset

Panel 15, AO, PXI 6723 (d)

The command voltage for the high voltage applied to the spray needle.

card	pin	pin designation	function
PXI 6723 (d)	13	AO 28	needle voltage
PXI 6723 (d)	46	AO 29	
PXI 6723 (d)	11	AO 30	
PXI 6723 (d)	10	AO 31	

The PXI 6133 card is used to record the analog ion signal and the signal of the pyroelectric detector for normalization on the laser power. These signals are directly connected to the PXI the card via a short connector bock (National Instruments).

Connections for analog ion signal and signal of the pyroelectric detector,
fast AI, PXI 6133

card	pin	pin designation	function
PXI 6133		AI 0	analog ion signal
PXI 6133		AI 1	signal of pyroelectric detector

List of Figures

1.1	The merits of curiosity-driven research (from Theodor Hänsch's Nobel lecture in 2005 ¹⁴).	3
2.1	Overview of the tandem mass spectrometer with 22-pole ion trap.	14
2.2	Time sequence of a typical experiment.	15
2.3	The ion source.	16
2.4	Illustration of the pumping stages of the tandem quadrupole mass spectrometer.	17
2.5	The ESI process.	18
2.6	Waveforms and wiring diagram for a quadrupole mass filter.	21
2.7	Stability diagram for the operation of a quadrupole mass analyzer.	22
2.8	Simulated ion trajectory in an ideal, two-dimensional octopole RF field.	23
2.9	Simulated ion trajectory in an ideal, two-dimensional octopole RF field showing non-adiabatic behavior.	25
2.10	Effective potentials V^* for quadrupoles, hexapoles, octopoles, and 22-poles.	27
2.11	Drawing of the 22-pole mounted on the cold head.	29
2.12	Schematic representation of an ion funnel.	30
2.13	Simulation of the effective potential V^* of an ion funnel.	31
2.14	Circuit diagram of the ion funnel.	33
2.15	Structure of the data acquisition software.	35
2.16	Analog ion signal versus ion counts per ms for a continuous ion beam.	38
2.17	Analog ion signal versus number of ion counts for a 2 ms ion package released from the octopole.	39
2.18	Analog signal of a short ion package and a stretched-out ion package released from the cold 22-pole.	40
2.19	Signal level of a short ion package versus signal level of a long ion package released from the 22-pole in counting and analog detection mode.	40
2.20	Mass spectrum of a mixture of protonated primary amines, demonstrating the transmission of low masses through the ion funnel.	42
2.21	Ion signal of protonated tyrosine as a function of storage time in the 22-pole.	44

2.22	Mass spectra obtained when protonated tyrosine is stored in the 22-pole at 4 K and after laser irradiation at 35081 cm^{-1}	45
2.23	UV spectrum of protonated tyrosine recorded in the $m/z = 108$ fragment channel.	46
3.1	Schematic representation of a simple two-electrode ion source and a Wiley-McLaren type acceleration region comprising three electrodes.	54
3.2	Schematic representation of a two-stage reflectron setup.	55
3.3	RF electrode geometry of the planar multipole trap of Wester and co-workers ²³⁴	57
3.4	Electrode geometry of the planar multipole trap, one set of trap electrodes as realized in the final design, scale 1:1. The interlacing RF combs (8 poles of each phase, 30 mm long, 1 mm wide, and 1 mm apart) are surrounded by DC electrodes (5 mm wide and spaced by 1 mm).	60
3.5	Exploded view of the planar multipole trap.	61
3.6	Simulated potentials of a two-dimensional planar multipole trap.	61
3.7	Comparison of the trap depths of linear multipoles and planar traps as a function of the RF amplitude.	62
3.8	Simulation of the effective potential V^* of a planar multipole trap showing a series of local minima in its center.	63
3.9	The effect of the extraction plates on the extraction fields. Simulation of the electric potential in a two-dimensional trap with different extraction voltages applied to the electrodes.	64
3.10	Simulation of the phase space distribution of an ion in the three-dimensional planar trap at 298 K.	65
3.11	The simulated mean absolute velocity components of an ion in the three-dimensional planar trap as a function of the spatial coordinates.	66
3.12	Simulation of the phase space distribution of an ion in the three-dimensional planar trap at 6 K.	67
3.13	Photograph of the prototype of the trap.	68
3.14	The second version of the trap, assembled and mounted onto a flange.	69
3.15	Schematic representation of the test setup.	71
3.16	Cross section of the tandem quadrupole mass spectrometer with the trap coupled to the second bender.	71
3.17	Photograph of the trap coupled to the tandem quadrupole mass spectrometer.	72
3.18	Schematic circuit of the RF/high voltage pulse generator used to generate the waveforms on the trap electrodes.	73
3.19	Comparison of mass spectra of aniline and its fragment ions obtained with static extraction voltages applied to the trap electrodes and after 30 ms of trapping.	76

3.20 Spectrum recorded after 10 s of trapping showing background signal of aniline and some fragments.	78
3.21 Simulation of the effective potential V^* in the center of a two-dimensional planar trap. Different positions of the local minima result when the same or the opposite RF phase are applied to opposite electrodes.	79
3.22 Mass spectra recorded with the same or the opposite RF phase applied to opposite electrodes.	79
3.23 Waveforms on one of the RF electrodes for two different extraction phases as well as their difference.	81
3.24 Dependence of the ion signal on the extraction phase.	82
3.25 Dependence of the ion signal and resolution on the delay between the short circuit and the extraction pulses.	83
3.26 Dependence of the ion signal and resolution on the delay between the short circuit and the extraction pulses at long delays.	83
3.27 Dependence of the signal intensity and resolution on the voltage on the trapping DC electrodes.	84
3.28 Simulation of the ion distribution in the three-dimensional trap for different trapping DC voltages.	85
3.29 Mass resolution of the aniline ion peak as a function of the pressure in the trap chamber.	86
3.30 Dependence of the signal intensity and resolution on the trapping time.	87
3.31 Simulation of the trajectories of ions created by laser ionization in the three-dimensional trap.	87
3.32 Dependence of the ion signal and resolution on the RF amplitude.	88
3.33 Simulated spatial distributions of the ions for different RF amplitudes.	89
3.34 Determination of the trapping time of the test setup for different pressures.	90
3.35 Comparison of mass spectra of an electrosprayed mixture of amino acids recorded with a quadrupole analyzer and with the planar trap/TOF instrument.	93
3.36 TOF mass spectrum of photofragments of protonated phenylalanine.	94
3.37 Dependence of the signal intensity and resolution on the RF amplitude.	95
3.38 Characterization of the injection efficiency as a function of the delay between the helium pulse and the moment of ion injection.	97
3.39 Dependence of the signal intensity and resolution on the trapping time.	97
3.40 Determination of the trapping time.	98
3.41 Dependence of the signal intensity on the voltage applied to the trapping DC electrodes.	99
3.42 Fringe fields in the simulated effective potential in the center plane of the trap for two alternative electrode configurations.	100

4.1	Chemical structures of the amino acids L-phenylalanine and L-serine.	106
4.2	Spectroscopic techniques used in the present work to obtain UV, IR/UV hole burning, and IR depletion spectra.	110
4.3	Spectroscopic scheme to obtain the IR spectrum of a single isomer in the excited state.	110
4.4	Mass spectrum obtained when protonated phenylalanine/serine dimer ions are stored in the 22-pole and irradiated at 38432.8 cm^{-1}	111
4.5	The UV spectrum of the protonated phenylalanine/serine dimer.	112
4.6	Isomer specific IR depletion spectra of the protonated dimer.	113
4.7	Spectra of the various isomers in the NH stretch region with ^{15}N labeled phenylalanine and natural isotope abundance.	115
4.8	The UV spectrum of the protonated phenylalanine/serine dimer together with IR/UV hole burning spectra.	118
4.9	Comparison of the UV spectra of the protonated dimer in the 180 amu and 120 amu channel.	119
4.10	IR gain spectrum in the 120 amu channel recorded with the UV laser fixed to 37521.9 cm^{-1}	119
4.11	Relative (zero point corrected) DFT energy versus relative force field energy for the lowest energy structures obtained in the initial conformational search.	121
4.12	DFT optimized structures of different isomers of the protonated dimer.	123
4.13	Relative (zero point corrected) DFT energy versus relative force field energy for the lowest energy structures obtained in the conformational search with different starting structures.	124
4.14	Comparison of experimental IR spectra with calculated spectra of structures obtained from the conformational search and by guessing.	125
4.15	DFT optimized structures of the best isomers of the protonated dimer that were obtained by guessing.	127
4.16	Structure of the dimer corresponding to the spectrum marked with an asterisk in Fig. 4.14.	127
4.17	Difference photofragment mass spectra showing the enhancement or depletion of different mass channels upon irradiation of a UV excited species with an IR laser pulse after about 10 ns and 400 ns.	129
4.18	Comparison of the ground and excited state spectra of three isomers.	130
4.19	IR spectra of isomer A in the 180 amu channel at various delays after UV excitation.	133
4.20	Determination of the lifetime of the short lived species that is initially created upon UV excitation of isomer A at 38129.4 cm^{-1}	134
4.21	Determination of the lifetime of the long lived species that is created after UV excitation of isomer A at 38129.4 cm^{-1} and a subsequent radiationless transition.	135

- 5.1 Schematic representation of the front and back panel of the connector box. . . . 144

List of Tables

2.1	Differential pumping stages of the tandem mass spectrometer with 22-pole ion trap.	18
2.2	Hardware for instrument control and data acquisition.	34
2.3	Signal to noise ratios for two different acquisition modes, using one detector or two detectors for the normalization on parent ion signal.	43
3.1	Typical voltages and timing parameters for the operation of the planar trap/TOF mass spectrometer in the test setup.	75
3.2	Typical voltages and timing parameters for the operation of the planar trap/TOF mass spectrometer when coupled to the tandem mass spectrometer described in chapter 2.	92
5.1	Pinout of the multipin connectors of the tandem quadrupole mass spectrometer.	143
5.2	Occupation of the slots in the PXI chassis by the different DAQ instruments. . .	144

List of Abbreviation

AI	Analog Input (hardware resources)
AO	Analog Output (hardware resources)
BIRD	Blackbody Infrared Radiative Dissociation
CI	Chemical Ionization
CID	Collision Induced Dissociation
CTR	Counter (hardware resources)
DC	Direct Current
DFT	Density Functional Theory
DI	Digital Input (hardware resources)
DNA	Deoxyribonucleic Acid, the macromolecule containing genetic information in living organisms
DO	Digital Output (hardware resources)
EI	Electron Impact Ionization
ESI	Electrospray Ionization
FAIMS	High-Field Asymmetric Waveform Ion Mobility Spectrometry
FEL	Free Electron Laser
FT-ICR	Fourier Transform Ion Cyclotron Resonance (Mass Spectrometer)
IC	Internal Conversion
IRLAPS	Infrared Laser Assisted Photofragment Spectroscopy
IRMPD	Infrared Multiple Photon Dissociation
IRPD	Infrared Photodissociation
IVR	Intramolecular Vibrational Energy Redistribution

LID	Laser Induced Dissociation
MALDI	Matrix Assisted Laser Desorption/Ionization
MCP	Micro Channel Plate (detector)
MEMS	Microelectromechanical Systems (devices manufactured with a range of microfabrication techniques)
MHV	Miniature High Voltage (connector)
MOSFET	Metal-Oxide-Semiconductor Field-Effect Transistor
Nd:YAG	Neodymium-doped Yttrium Aluminium Garnet (laser)
NMR	Nuclear Magnetic Resonance
OPA	Optical Parametric Amplifier
OPO	Optical Parametric Oscillator
PC	Personal Computer
PCB	Printed Circuit Board
PEEK	Polyether Ether Ketone, an organic polymer thermoplastic
PES	Potential Energy Surface
PXI	PCI Extensions for Instrumentation
R2PI	Resonance Enhanced Two Photon Ionization
REMPI	Resonance Enhanced Multi Photon Ionization
RET	Ring Electrode Trap
RF	Radio Frequency
SCSI	Small Computer System Interface (here referring to a connector)
SEP	Stimulated Emission Pumping
TOF	Time of Flight
TTL	Transistor–Transistor Logic, here referring to a standard for digital signals

Bibliography

- [1] S. French, D. Krause, *Identity in physics: a historical, philosophical, and formal analysis*, Oxford University Press Inc., New York, **2006**.
- [2] P. A. M. Dirac, *Proc. R. Soc. London Ser. A* **1929**, 123, 714.
- [3] J. Pople, *Quantum Chemical Models, Nobel Lecture*, **1998**,
URL http://nobelprize.org/nobel_prizes/chemistry/laureates/1998/pople-lecture.html.
- [4] W. Kohn, *Electronic Structure of Matter-Wave Functions and Density Functionals*, **1998**,
URL http://nobelprize.org/nobel_prizes/chemistry/laureates/1998/kohn-lecture.html.
- [5] W. Tittel, J. Brendel, H. Zbinden, N. Gisin, *Phys. Rev. Lett.* **1998**, 81, 3563–3566.
- [6] M. Arndt, O. Nairz, J. Vos-Andreae, C. Keller, G. van der Zouw, A. Zeilinger, *Nature (London, U. K.)* **1999**, 401, 680–682.
- [7] F. Jensen, *Introduction to Computation Chemistry*, John Wiley & Sons Inc., **1999**.
- [8] M. A. Nielsen, I. L. Chuang, *Quantum Computation and Quantum Information*, Cambridge University Press, **2000**.
- [9] N. S. Nagornova, T. R. Rizzo, O. V. Boyarkin, *J. Am. Chem. Soc.* **2010**, 132, 4040–4041.
- [10] S. Grimme, J. Antony, T. Schwabe, C. Mueck-Lichtenfeld, *Organic & Biomolecular Chemistry* **2007**, 5, 741–758.
- [11] D. J. Wales, *Energy Landscapes*, Cambridge University Press, **2003**.
- [12] D. J. Wales, T. V. Bogdan, *J. Phys. Chem. B* **2006**, 110, 20765–20776.
- [13] A. H. Zewail, *Chem. Phys.* **2010**, 378, 1–3.
- [14] T. W. Hänsch, *Passion for Precision, Nobel Lecture*, **2005**,
URL http://nobelprize.org/nobel_prizes/physics/laureates/2005/hansch-lecture.html.

- [15] J. M. Berg, J. L. Tymoczko, L. Stryer, *Biochemistry*, 6th edition, Palgrave MacMillan, New York, **2006**.
- [16] D. Selkoe, *Nature (London, U. K.)* **2003**, *426*, 900–904.
- [17] E. R. Kay, D. A. Leigh, F. Zerbetto, *Angew. Chem. Int. Ed.* **2007**, *46*, 72–191.
- [18] K. Wüthrich, *NMR Studies of Structure and Function of Biological Macromolecules, Nobel Lecture*, **2002**,
URL http://nobelprize.org/nobel_prizes/chemistry/laureates/2002/wuthrich-lecture.html.
- [19] J. E. Walker, *ATP Synthesis by Rotary Catalysis, Nobel Lecture*, **1997**,
URL http://nobelprize.org/nobel_prizes/chemistry/laureates/1997/walker-lecture.html.
- [20] I. Hargittai, M. Hargittai (editors), *Stereochemical Applications of Gas-Phase Electron Diffraction*, Parts A and B, VCH, **1988**.
- [21] K. Borisenko, C. Bock, I. Hargittai, *J. Phys. Chem.* **1996**, *100*, 7426–7434.
- [22] J. Hovick, L. Bartell, *J. Phys. Chem. B* **1998**, *102*, 534–539.
- [23] M. Maier-Borst, D. Cameron, M. Rokni, J. Parks, *Phys. Rev. A: At. Mol. Opt. Phys.* **1999**, *59*, R3162–R3165.
- [24] S. Kruckeberg, D. Schooss, M. Maier-Borst, J. Parks, *Phys. Rev. Lett.* **2000**, *85*, 4494–4497.
- [25] M. Chergui, A. H. Zewail, *ChemPhysChem* **2009**, *10*, 28–43.
- [26] P. Schnier, W. Price, R. Jockusch, E. Williams, *J. Am. Chem. Soc.* **1996**, *118*, 7178–7189.
- [27] W. Price, P. Schnier, E. Williams, *J. Phys. Chem. B* **1997**, *101*, 664–673.
- [28] A. Lemoff, E. Williams, *J. Am. Soc. Mass. Spectrom.* **2004**, *15*, 1014–1024.
- [29] A. Kamariotis, O. V. Boyarkin, S. R. Mercier, R. D. Beck, M. F. Bush, E. R. Williams, T. R. Rizzo, *J. Am. Chem. Soc.* **2006**, *128*, 905–916.
- [30] U. Mazurek, O. Geller, C. Lifshitz, M. McFarland, A. Marshall, B. Reuben, *J. Phys. Chem. A* **2005**, *109*, 2107–2112.
- [31] U. Mazurek, M. Engeser, C. Lifshitz, *Int. J. of Mass Spect.* **2006**, *249*, 473–476.
- [32] B. Winger, K. Lightwahl, A. Rockwood, R. Smith, *J. Am. Chem. Soc.* **1992**, *114*, 5897–5898.

- [33] M. F. Jarrold, *Annu. Rev. Phys. Chem.* **2000**, *51*, 179–207.
- [34] H. D. F. Winkler, E. V. Dzyuba, C. A. Schalley, *New Journal of Chemistry* **2011**, *35*, 529–541.
- [35] L. Konermann, J. Pan, Y.-H. Liu, *Chem. Soc. Rev.* **2011**, *40*, 1224–1234.
- [36] N. C. Polfer, R. C. Dunbar, J. Oomens, *J. Am. Soc. Mass. Spectrom.* **2007**, *18*, 512–516.
- [37] E. Robinson, E. Williams, *J. Am. Soc. Mass. Spectrom.* **2005**, *16*, 1427–1437.
- [38] F. McLafferty, Z. Guan, U. Haupts, T. Wood, N. Kelleher, *J. Am. Chem. Soc.* **1998**, *120*, 4732–4740.
- [39] G. Tsaprailis, H. Nair, Á. Somogyi, V. H. Wysocki, W. Zhong, J. H. Futrell, S. G. Summerfield, S. J. Gaskell, *J. Am. Chem. Soc.* **1999**, *121*, 5142–5154.
- [40] R. Aebersold, D. R. Goodlett, *Chem. Rev.* **2001**, *101*, 269–296.
- [41] I. Papayannopoulos, *Mass Spectrom. Rev.* **1995**, *14*, 49–73.
- [42] B. C. Bohrer, S. I. Mererbloom, S. L. Koeniger, A. E. Hilderbrand, D. E. Clemmer, *Annu. Rev. Anal. Chem.* **2008**, *1*, 293–327.
- [43] A. B. Kanu, P. Dwivedi, M. Tam, L. Matz, H. H. Hill, *J. Mass Spectrom.* **2008**, *43*, 1–22.
- [44] R. Julian, R. Hodyss, B. Kinnear, M. Jarrold, J. Beauchamp, *J. Phys. Chem. B* **2002**, *106*, 1219–1228.
- [45] T. Wyttenbach, G. vonHelden, M. Bowers, *J. Am. Chem. Soc.* **1996**, *118*, 8355–8364.
- [46] D. E. Clemmer, M. F. Jarrold, *J. Mass Spectrom.* **1997**, *32*, 577–592.
- [47] R. Hudgins, M. Jarrold, *J. Am. Chem. Soc.* **1999**, *121*, 3494–3501.
- [48] M. Kohtani, J. Schneider, T. Jones, M. Jarrold, *J. Am. Chem. Soc.* **2004**, *126*, 16981–16987.
- [49] M. F. Jarrold, *Phys. Chem. Chem. Phys.* **2007**, *9*, 1659–1671.
- [50] T. R. Rizzo, J. A. Stearns, O. V. Boyarkin, *Int. Rev. Phys. Chem.* **2009**, *28*, 481–515.
- [51] T. R. Rizzo, Y. D. Park, D. H. Levy, *J. Am. Chem. Soc.* **1985**, *107*, 277–278.
- [52] T. R. Rizzo, Y. D. Park, L. Peteanu, D. H. Levy, *J. Chem. Phys.* **1985**, *83*, 4819–4820.
- [53] T. R. Rizzo, Y. D. Park, L. A. Peteanu, D. H. Levy, *J. Chem. Phys.* **1986**, *84*, 2534–2541.
- [54] Y. D. Park, T. R. Rizzo, L. A. Peteanu, D. H. Levy, *J. Chem. Phys.* **1986**, *84*, 6539–6549.
- [55] G. Meijer, M. S. de Vries, H. E. Hunziker, H. R. Wendt, *Appl. Phys. B* **1990**, *51*, 395–403.

- [56] J. R. Cable, M. J. Tubergen, D. H. Levy, *J. Am. Chem. Soc.* **1987**, *109*, 6198–6199.
- [57] J. R. Cable, M. J. Tubergen, D. H. Levy, *J. Am. Chem. Soc.* **1988**, *110*, 7349–7355.
- [58] J. R. Cable, M. J. Tubergen, D. H. Levy, *J. Am. Chem. Soc.* **1989**, *111*, 9032–9039.
- [59] J. Bakker, C. Plutzer, I. Hunig, T. Haber, I. Compagnon, G. von Helden, G. Meijer, K. Kleinermmanns, *ChemPhysChem* **2005**, *6*, 120–128.
- [60] A. Abo-Riziq, B. O. Crews, M. P. Callahan, L. Grace, M. S. de Vries, *Angew. Chem. Int. Ed.* **2006**, *45*, 5166–5169.
- [61] B. Dian, A. Longarte, S. Mercier, D. Evans, D. Wales, T. Zwier, *J. Chem. Phys.* **2002**, *117*, 10688–10702.
- [62] I. Hunig, K. Kleinermmanns, *Phys. Chem. Chem. Phys.* **2004**, *6*, 2650–2658.
- [63] L. C. Snoek, E. G. Robertson, R. T. Kroemer, J. P. Simons, *Chem. Phys. Lett.* **2000**, *321*, 49–56.
- [64] L. C. Snoek, R. T. Kroemer, M. R. Hockridge, J. P. Simons, *Phys. Chem. Chem. Phys.* **2001**, *3*, 1819–1826.
- [65] J. M. Bakker, L. M. Aleese, G. Meijer, G. von Helden, *Phys. Rev. Lett.* **2003**, *91*, 203003.
- [66] W. Chin, J. P. Dognon, C. Canuel, F. Piuuzzi, I. Dimicoli, M. Mons, I. Compagnon, G. von Helden, G. Meijer, *J. Chem. Phys.* **2005**, *122*, 054317.
- [67] G. M. Florio, T. S. Zwier, *J. Phys. Chem. A* **2003**, *107*, 974–983.
- [68] M. N. Blom, I. Compagnon, N. C. Polfer, G. von Helden, G. Meijer, S. Suhai, B. Paizs, J. Oomens, *J. Phys. Chem. A* **2007**, *111*, 7309–7316.
- [69] W. Chin, J. P. Dognon, F. Piuuzzi, B. Tardivel, I. Dimicoli, M. Mons, *J. Am. Chem. Soc.* **2005**, *127*, 707–712.
- [70] M. Gerhards, C. Unterberg, A. Gerlach, A. Jansen, *Phys. Chem. Chem. Phys.* **2004**, *6*, 2682–2690.
- [71] C. Unterberg, A. Gerlach, T. Schrader, M. Gerhards, *J. Chem. Phys.* **2003**, *118*, 8296–8300.
- [72] M. S. de Vries, P. Hobza, *Annu. Rev. Phys. Chem.* **2007**, *58*, 585–612.
- [73] V. A. Shubert, T. S. Zwier, *J. Phys. Chem. A* **2007**, *111*, 13283–13286.
- [74] B. Dian, A. Longarte, T. Zwier, *J. Chem. Phys.* **2003**, *118*, 2696–2706.
- [75] T. Walther, H. Bitto, T. K. Minton, J. R. Huber, *Chem. Phys. Lett.* **1994**, *231*, 64–69.

- [76] B. C. Dian, A. Longarte, T. S. Zwier, *Science* **2002**, *296*, 2369–2373.
- [77] B. C. Dian, G. M. Florio, J. R. Clarkson, A. Longarte, T. S. Zwier, *J. Chem. Phys.* **2004**, *120*, 9033–9046.
- [78] B. C. Dian, A. Longarte, P. R. Winter, T. S. Zwier, *J. Chem. Phys.* **2004**, *120*, 133–147.
- [79] B. C. Dian, J. R. Clarkson, T. S. Zwier, *Science* **2004**, *303*, 1169–1173.
- [80] J. R. Clarkson, B. C. Dian, L. Moriggi, A. DeFusco, V. McCarthy, K. D. Jordan, T. S. Zwier, *J. Chem. Phys.* **2005**, *122*, 214311.
- [81] K. Tanaka, *The Origin of Macromolecule Ionization by Laser Irradiation*, Nobel Lecture, **2002**.
- [82] J. B. Fenn, *Electrospray Wings for Molecular Elephants*, Nobel Lecture, **2002**,
URL http://nobelprize.org/nobel_prizes/chemistry/laureates/2002/fenn-lecture.html.
- [83] J. Fenn, M. Mann, C. Meng, S. Wong, C. Whitehouse, *Mass Spectrom. Rev.* **1990**, *9*, 37–70.
- [84] J. B. Fenn, M. Mann, C. K. Meng, S. F. Wong, C. M. Whitehouse, *Science* **1989**, *246*, 64–71.
- [85] G. Papadopoulos, A. Svendsen, O. V. Boyarkin, T. R. Rizzo, *Faraday Discuss.* **2011**,
URL <http://dx.doi.org/10.1039/C0FD00004C>.
- [86] C. Bich, R. Zenobi, *Current Opinion In Structural Biology* **2009**, *19*, 632–639.
- [87] N. C. Polfer, J. Oomens, *Mass Spectrom. Rev.* **2009**, *28*, 468–494.
- [88] T. D. Fridgen, *Mass Spectrom. Rev.* **2009**, *28*, 586–607.
- [89] N. Polfer, J. Oomens, D. Moore, G. von Helden, G. Meijer, R. Dunbar, *J. Am. Chem. Soc.* **2006**, *128*, 517–525.
- [90] N. Polfer, J. Oomens, R. Dunbar, *Phys. Chem. Chem. Phys.* **2006**, *8*, 2744–2751.
- [91] P. B. Armentrout, M. T. Rodgers, J. Oomens, J. D. Steill, *J. Phys. Chem. A* **2008**, *112*, 2248–2257.
- [92] P. Kupser, K. Pagel, J. Oomens, N. Polfer, B. Koksche, G. Meijer, G. von Helden, *J. Am. Chem. Soc.* **2010**, *132*, 2085–2093.
- [93] M. Rossi, V. Blum, P. Kupser, G. von Helden, F. Bierau, K. Pagel, G. Meijer, M. Scheffler, *J. Phys. Chem. Lett.* **2010**, *1*, 3465–3470.

- [94] D. Scuderi, C. F. Correia, O. P. Balaj, G. Ohanessian, J. Lemaire, P. Maitre, *ChemPhysChem* **2009**, *10*, 1630–1641.
- [95] C. F. Correia, C. Clavaguera, U. Erlekam, D. Scuderi, G. Ohanessian, *ChemPhysChem* **2008**, *9*, 2564–2573.
- [96] J. Oomens, N. Polfer, D. T. Moore, L. van der Meer, A. G. Marshall, J. R. Eyler, G. Meijer, G. von Helden, *Phys. Chem. Chem. Phys.* **2005**, *7*, 1345–1348.
- [97] K. Pagel, P. Kupser, F. Bierau, N. C. Polfer, J. D. Steill, J. Oomens, G. Meijer, B. Koks, G. von Helden, *Int. J. of Mass Spect.* **2009**, *283*, 161–168.
- [98] H. Oh, C. Lin, H. Hwang, H. Zhai, K. Breuker, V. Zabrouskov, B. Carpenter, F. McLafferty, *J. Am. Chem. Soc.* **2005**, *127*, 4076–4083.
- [99] N. C. Polfer, B. Paizs, L. C. Snoek, I. Compagnon, S. Suhai, G. Meijer, G. von Helden, J. Oomens, *J. Am. Chem. Soc.* **2005**, *127*, 8571–8579.
- [100] D. Oepts, A. F. G. van der Meer, P. W. van Amersfoort, *Infrared Phys. Technol.* **1995**, *36*, 297–308.
- [101] R. Prazeres, J. M. Berset, F. Glotin, D. Jaroszynski, J. M. Ortega, *Nucl. Instrum. Methods Phys. Res., Sect. A* **1993**, *331*, 15–19.
- [102] R. Wu, T. B. McMahon, *J. Am. Chem. Soc.* **2007**, *129*, 4864–4865.
- [103] L. Mac Aleese, A. Simon, T. B. McMahon, J. M. Ortega, D. Scuderi, J. Lemaire, P. Maitre, *Int. J. of Mass Spect.* **2006**, *249*, 14–20.
- [104] J. Mino, Warren K., J. Szczepanski, W. L. Pearson, D. H. Powell, R. C. Dunbar, J. R. Eyler, N. C. Polfer, *Int. J. of Mass Spect.* **2010**, *297*, 131–138.
- [105] J. Oomens, B. G. Sartakov, G. Meijer, G. von Helden, *Int. J. of Mass Spect.* **2006**, *254*, 1–19.
- [106] O. V. Boyarkin, S. R. Mercier, A. Kamariotis, T. R. Rizzo, *J. Am. Chem. Soc.* **2006**, *128*, 2816–2817.
- [107] W. C. Stwalley, R. V. Krems, B. Friedrich (editors), *Cold Molecules*, CRC Press, **2009**.
- [108] F. Bierau, P. Kupser, G. Meijer, G. von Helden, *Phys. Rev. Lett.* **2010**, *105*.
- [109] S. Smolarek, N. B. Brauer, W. J. Buma, M. Drabbels, *J. Am. Chem. Soc.* **2010**, *132*, 14086–14091.
- [110] D. Nolting, C. Marian, R. Weinkauff, *Phys. Chem. Chem. Phys.* **2004**, *6*, 2633–2640.

- [111] S. R. Mercier, O. V. Boyarkin, A. Kamariotis, M. Guglielmi, I. Tavernelli, M. Cascella, U. Rothlisberger, T. R. Rizzo, *J. Am. Chem. Soc.* **2006**, *128*, 16938–16943.
- [112] D. Gerlich, *Adv. Chem. Phys.* **1992**, *82*, 1–176.
- [113] J. A. Stearns, S. Mercier, C. Seaiby, M. Guidi, O. V. Boyarkin, T. R. Rizzo, *J. Am. Chem. Soc.* **2007**, *129*, 11814–11820.
- [114] J. A. Stearns, M. Guidi, O. V. Boyarkin, T. R. Rizzo, *J. Chem. Phys.* **2007**, *127*, 154322.
- [115] J. A. Stearns, O. V. Boyarkin, T. R. Rizzo, *J. Am. Chem. Soc.* **2007**, *129*, 13820–13821.
- [116] J. A. Stearns, C. Seaiby, O. V. Boyarkin, T. R. Rizzo, *Phys. Chem. Chem. Phys.* **2009**, *11*, 125–132.
- [117] N. S. Nagornova, M. Guglielmi, M. Doemer, I. Tavernelli, U. Rothlisberger, T. R. Rizzo, O. V. Boyarkin, *Angew. Chem. Int. Ed.* **2011**, *50*, 5383–5386.
- [118] C. Seaiby, *Spectroscopic Probes of Conformational Isomerization of Biological Molecules in a Cold Ion Trap*, Ph.D. thesis, Ecole Polytechnique Fédérale de Lausanne, **2010**.
- [119] M. Guidi, U. J. Lorenz, G. Papadopoulos, O. V. Boyarkin, T. R. Rizzo, *J. Phys. Chem. A* **2009**, *113*, 797–799.
- [120] M. Guidi, *Spectroscopy and Dissociation Dynamics of Cold, Biomolecular Ions*, Ph.D. thesis, Ecole Polytechnique Fédérale de Lausanne, **2009**.
- [121] J. M. Lisy, *J. Chem. Phys.* **2006**, *125*, 132302.
- [122] L. I. Yeh, Y. T. Lee, *J. Am. Chem. Soc.* **1989**, *111*, 5597–5604.
- [123] M. Okumura, L. I. Yeh, Y. T. Lee, *J. Chem. Phys.* **1988**, *88*, 79–91.
- [124] M. Okumura, L. I. Yeh, Y. T. Lee, *J. Chem. Phys.* **1985**, *83*, 3705–3706.
- [125] M. A. Johnson, W. C. Lineberger, *Techniques for the study of gas-phase ion molecule reactions*, Wiley: New York, **1988**, 591–635.
- [126] M. Duncan, *Int. Rev. Phys. Chem.* **2003**, *22*, 407–435.
- [127] J. W. Shin, N. I. Hammer, E. G. Diken, M. A. Johnson, R. S. Walters, T. D. Jaeger, M. A. Duncan, R. A. Christie, K. D. Jordan, *Science* **2004**, *304*, 1137–1140.
- [128] J. Lemaire, P. Boissel, M. Heninger, G. Mauclaire, G. Bellec, H. Mestdagh, A. Simon, S. L. Caër, J. M. Ortega, F. Glotin, P. Maître, *Phys. Rev. Lett.* **2002**, *89*, 273002.
- [129] N. C. Polfer, J. Oomens, *Phys. Chem. Chem. Phys.* **2007**, *9*, 3804–3817.

- [130] U. J. Lorenz, N. Solcà, J. Lemaire, P. Maître, O. Dopfer, *Angew. Chem. Int. Ed.* **2007**, *46*, 6714–6716.
- [131] D. Gerlich, *Phys. Scr.* **1995**, *T59*, 256–263.
- [132] J. Mikosch, U. Fruehling, S. Trippel, R. Otto, P. Hlavenka, D. Schwalm, M. Weidemueller, R. Wester, *Phys. Rev. A: At. Mol. Opt. Phys.* **2008**, *78*, 023402.
- [133] S. Schlemmer, T. Kuhn, E. Lescop, D. Gerlich, *Int. J. of Mass Spect.* **1999**, *187*, 589–602.
- [134] O. Asvany, P. Kumar, B. Redlich, I. Hegemann, S. Schlemmer, D. Marx, *Science* **2005**, *309*, 1219–1222.
- [135] A. Dzhonson, D. Gerlich, E. J. Bieske, J. P. Maier, *J. Mol. Struct.* **2006**, *795*, 93–97.
- [136] A. Svendsen, U. J. Lorenz, O. V. Boyarkin, T. R. Rizzo, *Rev. Sci. Instrum.* **2010**, *81*, 073107.
- [137] J. S. Page, K. Tang, R. D. Smith, *Int. J. of Mass Spect.* **2007**, *265*, 244–250.
- [138] R. Guevremont, *J. Chromatogr.* **2004**, *1058*, 3–19.
- [139] J. Pittman, P. O'Connor, *J. Am. Soc. Mass. Spectrom.* **2005**, *16*, 441–445.
- [140] N. Cech, C. Enke, *Mass Spectrom. Rev.* **2001**, *20*, 362–387.
- [141] P. Kebarle, M. Peschke, *Anal. Chim. Acta* **2000**, *406*, 11–35.
- [142] A. Gomez, K. Tang, *Phys. Fluids* **1994**, *6*, 404–414.
- [143] M. Wilm, M. Mann, *Int. J. of Mass Spect.* **1994**, *136*, 167–180.
- [144] M. Karas, U. Bahr, T. Dulcks, *Fresenius J. Anal. Chem.* **2000**, *366*, 669–676.
- [145] R. E. March, J. F. J. Todd, *Quadrupole Ion Trap Mass Spectrometry, Chemical Analysis*, volume 165, 2nd edition, Wiley-Interscience, **2005**.
- [146] G. A. Salazar, T. Masujima, *J. Am. Soc. Mass. Spectrom.* **2007**, *18*, 413–421.
- [147] G. A. Salazar, T. Masujima, *Rapid Commun. Mass Spectrom.* **2008**, *22*, 1351–1358.
- [148] I. Cermak, *Rev. Sci. Instrum.* **2005**, *76*, 063302.
- [149] O. Asvany, S. Schlemmer, *Int. J. of Mass Spect.* **2009**, *279*, 147–155.
- [150] R. Wester, *J. Phys. B: At., Mol. Opt. Phys.* **2009**, *42*.
- [151] V. M. Doroshenko, R. J. Cotter, *J. Mass Spectrom.* **1998**, *33*, 305–318.
- [152] D. Gerlich, S. Horning, *Chem. Rev.* **1992**, *92*, 1509–1539.

- [153] J. Mikosch, H. Kreckel, R. Wester, R. Plasil, J. Glosik, D. Gerlich, D. Schwalm, A. Wolf, *J. Chem. Phys.* **2004**, *121*, 11030–11037.
- [154] D. Gerlich, *J. Chem. Soc., Faraday Trans.* **1993**, *89*, 2199–2208.
- [155] R. T. Kelly, A. V. Tolmachev, J. S. Page, K. Tang, R. D. Smith, *Mass Spectrom. Rev.* **2010**, *29*, 294–312.
- [156] S. Shaffer, K. Tang, G. Anderson, D. Prior, H. Udseth, R. Smith, *Rapid Commun. Mass Spectrom.* **1997**, *11*, 1813–1817.
- [157] D. J. Goebbert, G. Meijer, K. R. Asmis, in K. Iguchi, T. Watanabe (editor), *4th International Conference on Laser Probing, AIP Conference Proceedings*, volume 1104, Amer. Inst. Physics., Melville, 22–29.
- [158] *SIMION, version 8.0, Scientific Instrument Services, Inc., Ringoes, NJ, 2008.*
- [159] A. V. Tolmachev, T. Kim, H. R. Udseth, R. D. Smith, T. H. Bailey, J. H. Futrell, *Int. J. of Mass Spect.* **2000**, *203*, 31–47.
- [160] S. A. Shaffer, A. Tolmachev, D. C. Prior, G. A. Anderson, H. R. Udseth, R. D. Smith, *Anal. Chem.* **1999**, *71*, 2957–2964.
- [161] T. Kim, A. V. Tolmachev, R. Harkewicz, D. C. Prior, G. Anderson, H. R. Udseth, R. D. Smith, T. H. Bailey, S. Rakov, J. H. Futrell, *Anal. Chem.* **2000**, *72*, 2247–2255.
- [162] T. Kim, K. Q. Tang, H. R. Udseth, R. D. Smith, *Anal. Chem.* **2001**, *73*, 4162–4170.
- [163] J. S. Page, A. V. Tolmachev, K. Tang, R. D. Smith, *J. Mass Spectrom.* **2005**, *40*, 1215–1222.
- [164] D. Gerlich, *Hyperfine Interactions* **2003**, *146*, 293–306.
- [165] S. R. Mercier, *Electronic and Vibrational Spectroscopy of Cold Protonated Amino Acids in the Gas Phase*, Ph.D. thesis, Ecole Polytechnique Fédérale de Lausanne, **2008**.
- [166] C. Weickhardt, F. Moritz, J. Grotemeyer, *Mass Spectrom. Rev.* **1996**, *15*, 139–162.
- [167] S. McLuckey, J. Wells, *Chem. Rev.* **2001**, *101*, 571–606.
- [168] M. Hardman, A. Makarov, *Anal. Chem.* **2003**, *75*, 1699–1705.
- [169] A. Luca, S. Schlemmer, I. Cermak, D. Gerlich, *Rev. Sci. Instrum.* **2001**, *72*, 2900–2908.
- [170] H. Wollnik, M. Przewloka, *Int. J. Mass Spectrom. Ion Processes* **1990**, *96*, 267–274.
- [171] C. Piyadasa, P. Hakansson, T. Ariyaratne, *Rapid Commun. Mass Spectrom.* **1999**, *13*, 620–624.

- [172] S. Ring, H. Pedersen, O. Heber, M. Rappaport, P. Witte, K. Bhushan, N. Altstein, Y. Rudich, I. Sagi, D. Zajfman, *Anal. Chem.* **2000**, *72*, 4041–4046.
- [173] A. Verentchikov, M. Yavor, Y. Hasin, M. Gavrik, *Tech. Phys.* **2005**, *50*, 82–86.
- [174] A. Verentchikov, M. Yavor, Y. Hasin, M. Gavrik, *Tech. Phys.* **2005**, *50*, 73–81.
- [175] M. Dahan, R. Fishman, O. Heber, M. Rappaport, N. Altstein, D. Zajfman, W. van der Zande, *Rev. Sci. Instrum.* **1998**, *69*, 76–83.
- [176] H. Pedersen, D. Strasser, S. Ring, O. Heber, M. Rappaport, Y. Rudich, I. Sagi, D. Zajfman, *Phys. Rev. Lett.* **2001**, *87*.
- [177] D. Strasser, T. Geyer, H. Pedersen, O. Heber, S. Goldberg, B. Amarant, A. Diner, Y. Rudich, I. Sagi, M. Rappaport, D. Tannor, D. Zajfman, *Phys. Rev. Lett.* **2002**, *89*.
- [178] H. Pedersen, D. Strasser, B. Amarant, O. Heber, M. Rappaport, D. Zajfman, *Phys. Rev. A: At. Mol. Opt. Phys.* **2002**, *65*.
- [179] D. Zajfman, Y. Rudich, I. Sagi, D. Strasser, D. Savin, S. Goldberg, M. Rappaport, O. Heber, *Int. J. of Mass Spect.* **2003**, *229*, 55–60.
- [180] R. Wester, *unpublished results*, **2010**.
- [181] H. Pedersen, D. Strasser, O. Heber, M. Rappaport, D. Zajfman, *Phys. Rev. A: At. Mol. Opt. Phys.* **2002**, *65*.
- [182] M. Toyoda, D. Okumura, M. Ishihara, I. Katakuse, *J Mass Spectrom* **2003**, *38*, 1125–42.
- [183] J. H. J. Dawson, M. Guilhaus, *Rapid Commun. Mass Spectrom.* **1989**, *3*, 155–159.
- [184] A. F. Dodonov, I. V. Chernushevich, V. V. Laiko, *Proceedings of 12th International Mass Spectrometry Conference* **1991**, 153.
- [185] J. G. Boyle, C. M. Whitehouse, *Anal. Chem.* **1992**, *64*, 2084–2089.
- [186] A. N. Verentchikov, W. Ens, K. G. Standing, *Anal. Chem.* **1994**, *66*, 126–133.
- [187] I. V. Chernushevich, A. V. Loboda, B. A. Thomson, *J. Mass Spectrom.* **2001**, *36*, 849–865.
- [188] *Bruker Daltonics*, URL <http://www.bdal.com/products/lc-ms/uhr-tof/maxis/overview.html>.
- [189] F. J. Knorr, M. Ajami, D. A. Chatfield, *Anal. Chem.* **1986**, *58*, 690–694.
- [190] A. Brock, N. Rodriguez, R. N. Zare, *Anal. Chem.* **1998**, *70*, 3735–3741.
- [191] A. Brock, N. Rodriguez, R. Zare, *Rev. Sci. Instrum.* **2000**, *71*, 1306–1318.

- [192] F. Fernandez, J. Vadillo, F. Engelke, J. Kimmel, R. Zare, N. Rodriguez, M. Wetterhall, K. Markides, *J. Am. Soc. Mass. Spectrom.* **2001**, *12*, 1302–1311.
- [193] I. Chernushevich, *European Journal of Mass Spectrometry* **2000**, *6*, 471–479.
- [194] Y. Hashimoto, H. Hasegawa, H. Satake, T. Baba, I. Waki, *J. Am. Soc. Mass. Spectrom.* **2006**, *17*, 1669–1674.
- [195] W. Paul, W. Oberghaus, E. Fischer, *Forschungsber. Wirtsch.-Verkehrminist. Nordrhein-Westfalen* **1958**, *415*, 1.
- [196] W. Paul, *Rev. Mod. Phys.* **1990**, *62*, 531–540.
- [197] S. M. Michael, M. Chien, D. M. Lubman, *Rev. Sci. Instrum.* **1992**, *63*, 4277–4284.
- [198] J. Taniguchi, E. Katatoh, *Bunseki Kagaku* **2008**, *57*, 1–13.
- [199] B. M. Chien, S. M. Michael, D. M. Lubman, *Int. J. Mass Spectrom. Ion Processes* **1994**, *131*, 149–179.
- [200] D. Chambers, L. Grace, B. Andresen, *Anal. Chem.* **1997**, *69*, 3780–3790.
- [201] B. M. Chien, S. M. Michael, D. M. Lubman, *Anal. Chem.* **1993**, *65*, 1916–1924.
- [202] S. M. Michael, B. M. Chien, D. M. Lubman, *Anal. Chem.* **1993**, *65*, 2614–2620.
- [203] B. M. Chien, S. M. Michael, D. M. Lubman, *Rapid Commun. Mass Spectrom.* **1993**, *7*, 837–843.
- [204] B. B. Dangi, N. A. Sassin, K. M. Ervin, *Rev. Sci. Instrum.* **2010**, *81*, 063302.
- [205] L. He, D. Lubman, *Rapid Commun. Mass Spectrom.* **1997**, *11*, 1467–1477.
- [206] J. F. J. Todd, R. M. Waldren, D. A. Freer, R. B. Turner, *Int. J. Mass Spectrom. Ion Processes* **1980**, *35*, 107–150.
- [207] P. Kofel, M. Stockli, J. Krause, U. Schlunegger, *Rapid Commun. Mass Spectrom.* **1996**, *10*, 658–662.
- [208] Q. C. Ji, M. R. Davenport, C. G. Enke, J. F. Holland, *J. Am. Soc. Mass. Spectrom.* **1996**, *7*, 1009–1017.
- [209] P. Kofel, *Practical Aspects of Trapped Ion Mass Spectrometry*, volume II, chapter Injection of Mass-Selected Ions into the Radiofrequency Ion Trap, CRC Press, **2010**, 51–87.
- [210] S. A. McLuckey, G. L. Glish, K. G. Asano, *Anal. Chim. Acta* **1989**, *225*, 25–35.
- [211] J. Qin, B. Chait, *Anal. Chem.* **1996**, *68*, 2102–2107.
- [212] V. Doroshenko, R. Cotter, *J. Mass Spectrom.* **1997**, *32*, 602–615.

- [213] C. Weil, M. Nappi, C. Cleven, H. Wollnik, R. Cooks, *Rapid Commun. Mass Spectrom.* **1996**, *10*, 742–750.
- [214] I. Chernushevich, A. Verentchikov, W. Ens, K. Standing, *J. Am. Soc. Mass. Spectrom.* **1996**, *7*, 342–349.
- [215] S. Quarmby, R. Yost, *Int. J. of Mass Spect.* **1999**, *191*, 81–102.
- [216] V. M. Doroshenko, R. J. Cotter, *Rapid Commun. Mass Spectrom.* **1993**, *7*, 822–827.
- [217] G. C. Eiden, M. E. Cisper, M. L. Alexander, P. H. Hemberger, N. S. Nogar, *J. Am. Soc. Mass. Spectrom.* **1993**, *4*, 706–709.
- [218] G. G. Dolnikowski, M. J. Kristo, C. G. Enke, J. T. Watson, *Int. J. Mass Spectrom. Ion Processes* **1988**, *82*, 1–15.
- [219] J. Schwartz, M. Senko, J. Syka, *J. Am. Soc. Mass. Spectrom.* **2002**, *13*, 659–669.
- [220] A. Makarov, E. Denisov, A. Kholomeev, W. Baischun, O. Lange, K. Strupat, S. Horning, *Anal. Chem.* **2006**, *78*, 2113–2120.
- [221] J. Franzen, *Method and device for orthogonal ion injection into a time-of-flight mass spectrometer*, US patent 5,763,878, **1998**.
- [222] U. Boesl, R. Weinkauff, E. W. Schlag, *Int. J. Mass Spectrom. Ion Processes* **1992**, *112*, 121–166.
- [223] W. C. Wiley, I. H. McLaren, *Rev. Sci. Instrum.* **1955**, *26*, 1150–1157.
- [224] R. Weinkauff, K. Walter, C. Weickhardt, U. Boesl, E. W. Schlag, *Z. Naturforsch. Sect. A-J. Phys. Sci.* **1989**, *44*, 1219–1225.
- [225] B. Mamyrin, *Int. J. of Mass Spect.* **2001**, *206*, 251–266.
- [226] B. Mamyrin, *Int. J. Mass Spectrom. Ion Processes* **1994**, *131*, 1–19.
- [227] B. A. Mamyrin, V. I. Karataev, D. V. Shmikk, V. A. Zagulin, *Zhurnal Eksperimentalnoi Teor. Fiz.* **1973**, *64*, 82–89.
- [228] A. A. Makarov, *J. Phys. D: Appl. Phys.* **1991**, *24*, 533–540.
- [229] D. E. Austin, M. Wang, S. E. Tolley, J. D. Maas, A. R. Hawkins, A. L. Rockwood, H. D. Tolley, E. D. Lee, M. L. Lee, *Anal. Chem.* **2007**, *79*, 2927–2932.
- [230] D. E. Austin, Y. Peng, B. J. Hansen, I. W. Miller, A. L. Rockwood, A. R. Hawkins, S. E. Tolley, *J. Am. Soc. Mass. Spectrom.* **2008**, *19*, 1435–1441.
- [231] D. E. Austin, S. A. Lammert, *Practical Aspects of Trapped Ion Mass Spectrometry*, volume IV, chapter Ion Traps with Circular Geometries, CRC Press, **2010**, 373–398.

- [232] S. Seidelin, J. Chiaverini, R. Reichle, J. J. Bollinger, D. Leibfried, J. Britton, J. H. Wesenberg, R. B. Blakestad, R. J. Epstein, D. B. Hume, W. M. Itano, J. D. Jost, C. Langer, R. Ozeri, N. Shiga, D. J. Wineland, *Phys. Rev. Lett.* **2006**, *96*, 253003.
- [233] K. R. Brown, R. J. Clark, J. Labaziewicz, P. Richerme, D. R. Leibbrandt, I. L. Chuang, *Phys. Rev. A: At. Mol. Opt. Phys.* **2007**, *75*, 015401.
- [234] M. Debatin, M. Kroner, J. Mikosch, S. Trippel, N. Morrison, M. Reetz-Lamour, P. Woias, R. Wester, M. Weidemuller, *Phys. Rev. A: At. Mol. Opt. Phys.* **2008**, *77*, 033422.
- [235] R. Kohls, *Zulassungsarbeit, University of Freiburg*, **1974**.
- [236] E. Teloy, *Verhandl. DPG (VI)* **1980**, *15*, 567.
- [237] C. Greve, M. Kroener, S. Trippel, P. Woias, R. Wester, M. Weidemueller, *New J. Phys.* **2010**, *12*, 065035.
- [238] R. M. Jones, D. Gerlich, S. L. Anderson, *Rev. Sci. Instrum.* **1997**, *68*, 3357–3362.
- [239] R. M. Jones, S. L. Anderson, *Rev. Sci. Instrum.* **2000**, *71*, 4335–4337.
- [240] P. B. O'Connor, C. E. Costello, W. E. Earle, *J. Am. Soc. Mass. Spectrom.* **2002**, *13*, 1370–1375.
- [241] R. Mathur, P. B. O'Connor, *Rev. Sci. Instrum.* **2006**, *77*, 114101.
- [242] J. Rocher, M. Vedel, F. Vedel, *Int. J. of Mass Spect.* **1998**, *181*, 173–180.
- [243] B. T. Chang, T. B. Mitchell, *Rev. Sci. Instrum.* **2006**, *77*, 063101.
- [244] C. T. Rettner, J. H. Brophy, *Chem. Phys.* **1981**, *56*, 53–61.
- [245] K. Kato, K. Yamanouchi, *Chem. Phys. Lett.* **2004**, *397*, 237–241.
- [246] G. A. King, T. A. A. Oliver, M. N. R. Ashfold, *J. Chem. Phys.* **2010**, *132*, 214307.
- [247] R. W. Purves, L. Li, *J. Am. Soc. Mass. Spectrom.* **1997**, *8*, 1085–1093.
- [248] H. El Aribi, G. Orlova, A. Hopkinson, K. Siu, *J. Phys. Chem. A* **2004**, *108*, 3844–3853.
- [249] N. Bradbury, R. Nielsen, *Physical Review* **1936**, *49*, 0388–0393.
- [250] J. Fox, R. Saini, K. Tsui, G. Verbeck, *Rev. Sci. Instrum.* **2009**, *80*, 093302.
- [251] P. Setz, T. Schmitz, R. Zenobi, *Rev. Sci. Instrum.* **2006**, *77*, 024101.
- [252] S. Henderson, S. Valentine, A. Counterman, D. Clemmer, *Anal. Chem.* **1999**, *71*, 291–301.
- [253] J. Olsen, L. de Godoy, G. Li, B. Macek, P. Mortensen, R. Pesch, A. Makarov, O. Lange, S. Horning, M. Mann, *Molecular & Cellular Proteomics* **2005**, *4*, 2010–2021.

- [254] A. Eppink, D. Parker, *Rev. Sci. Instrum.* **1997**, *68*, 3477–3484.
- [255] S. Willitsch, M. T. Bell, A. D. Gingell, S. R. Procter, T. P. Softley, *Phys. Rev. Lett.* **2008**, *100*, 043203.
- [256] A. Fujihara, H. Matsumoto, Y. Shibata, H. Ishikawa, K. Fuke, *J. Phys. Chem. A* **2008**, *112*, 1457–1463.
- [257] F. Talbot, T. Tabarin, R. Antoine, M. Broyer, P. Dugourd, *J. Chem. Phys.* **2005**, *122*, 074310.
- [258] U. Kadhane, J. U. Andersen, A. Ehlerding, P. Hvelplund, M.-B. S. Kirketerp, M. K. Lykkegaard, S. B. Nielsen, S. Panja, J. A. Wyer, H. Zettergren, *J. Chem. Phys.* **2008**, *129*, 184304.
- [259] J. S. Kwon, C. M. Choi, H. J. Kim, N. J. Kim, J. Jang, M. Yang, *J. Phys. Chem. A* **2009**, *113*, 2715–2723.
- [260] I. Compagnon, A.-R. Allouche, F. Bertorelle, R. Antoine, P. Dugourd, *Phys. Chem. Chem. Phys.* **2010**, *12*, 3399–3403.
- [261] M. K. Drayss, P. B. Armentrout, J. Oomens, M. Schaefer, *Int. J. of Mass Spect.* **2010**, *297*, 18–27.
- [262] T. D. Vaden, T. S. J. A. de Boer, N. A. MacLeod, E. M. Marzluff, J. P. Simons, L. C. Snoek, *Phys. Chem. Chem. Phys.* **2007**, *9*, 2549–2555.
- [263] C. Coletti, N. Re, D. Scuderi, P. Maitre, B. Chiavarino, S. Fornarini, F. Lanucara, R. K. Sinha, M. E. Crestoni, *Phys. Chem. Chem. Phys.* **2010**, *12*, 13455–13467.
- [264] S. Raspopov, T. McMahon, *J. Mass Spectrom.* **2005**, *40*, 1536–1545.
- [265] K. Rajabi, T. D. Fridgen, *J. Phys. Chem. A* **2008**, *112*, 23–30.
- [266] C. G. Atkins, K. Rajabi, E. A. L. Gillis, T. D. Fridgen, *J. Phys. Chem. A* **2008**, *112*, 10220–10225.
- [267] X. Kong, I. Tsai, S. Sabu, C. Han, Y. Lee, H. Chang, S. Tu, A. Kung, C. Wu, *Angew. Chem. Int. Ed.* **2006**, *45*, 4130–4134.
- [268] R. C. Dunbar, J. D. Steill, N. C. Polfer, J. Oomens, *J. Phys. Chem. A* **2009**, *113*, 845–851.
- [269] E. Hunter, S. Lias, *J. Phys. Chem. Ref. Data* **1998**, *27*, 413–656.
- [270] G. Gorman, J. Speir, C. Turner, I. Amster, *J. Am. Chem. Soc.* **1992**, *114*, 3986–3988.
- [271] G. Bojesen, *J. Am. Chem. Soc.* **1987**, *109*, 5557–5558.

- [272] A. Harrison, *Mass Spectrom. Rev.* **1997**, *16*, 201–217.
- [273] S. Mirza, S. Prabhakar, M. Vairamani, *Rapid Commun. Mass Spectrom.* **2001**, *15*, 957–962.
- [274] C. Afonso, F. Modeste, P. Breton, F. Fournier, J. Tabet, *European Journal of Mass Spectrometry* **2000**, *6*, 443–449.
- [275] M. Meotner, E. Hunter, F. Field, *J. Am. Chem. Soc.* **1979**, *101*, 686–689.
- [276] G. von Helden, I. Compagnon, M. N. Blom, M. Frankowski, U. Erlekam, J. Oomens, B. Brauer, R. B. Gerber, G. Meijer, *Phys. Chem. Chem. Phys.* **2008**, *10*, 1248–1256.
- [277] Y. Inokuchi, Y. Kobayashi, T. Ito, T. Ebata, *J. Phys. Chem. A* **2007**, *111*, 3209–3215.
- [278] X. Cao, G. Fischer, *J. Phys. Chem. A* **1999**, *103*, 9995–10003.
- [279] A. L. Sobolewski, W. Domcke, *Conical Intersections: Theory, Computation and Experiment, Advanced Series in Physical Chemistry*, volume 17, chapter Efficient Excited-State Deactivation in Organic Chromophores and Biologically Relevant Molecules: Role of Electron and Proton Transfer Processes, World Scientific, **2011**.
- [280] E. G. Buchanan, W. H. James III, A. Gutberlet, J. C. Dean, L. Guo, S. H. Gellman, T. S. Zwier, *Faraday Discuss.* **2011**, URL <http://dx.doi.org/10.1039/C1FD00001B>.
- [281] *MacroModel, version 9.1, Schrödinger, LLC, New York*, **2005**.
- [282] Y. Zhao, D. G. Truhlar, *Theoretical Chemistry Accounts* **2008**, *120*, 215–241.
- [283] G. Gregoire, B. Lucas, M. Barat, J. A. Fayeton, C. Dedonder-Lardeux, C. Juvet, *Eur. Phys. J. D* **2009**, *51*, 109–116.
- [284] B. Lucas, M. Barat, J. A. Fayeton, M. Perot, C. Juvet, G. Gregoire, S. B. Nielsen, *J. Chem. Phys.* **2008**, *128*, 164302.
- [285] H. Kang, C. Juvet, C. Dedonder-Lardeux, S. Martrenchard, G. Gregoire, C. Desfrancois, J. Schermann, M. Barat, J. Fayeton, *Phys. Chem. Chem. Phys.* **2005**, *7*, 394–398.
- [286] H. Davy, *Elements of Chemical Philosophy, The Collected Works of Sir Humphry Davy (1839-40)*, volume 4, Smith, Elder and Co., London, **1840**, 37.
- [287] P. Hamm, J. Helbing, J. Bredenbeck, *Annu. Rev. Phys. Chem.* **2008**, *59*, 291–317.
- [288] F. Filsinger, G. Meijer, H. Stapelfeldt, H. N. Chapman, J. Kuepper, *Phys. Chem. Chem. Phys.* **2011**, *13*, 2076–2087.

Acknowledgments

A PhD thesis is a gamble in the sense that one sets out with an educated (?) guess to find something new and hopes that the project will be successful and produce results. If the project fails, one risks to lose a lot of time (and possibly one's nerves). During my PhD, I have maybe taken some chances working on long projects and following some ideas of my own that others sometimes considered risky. If some of these projects actually worked out, so that I was able to write the thesis you are holding in your hands, I owe it to some remarkable people, who I had the good fortune to work with. I would especially like to thank

My PhD supervisor, Prof. T. R. Rizzo, who I have come to know as a brilliant scientist, for his support and continuous interest in my work, the freedom he gave me to try out some ideas of my own, and many fruitful discussions.

Dr. Annette Svendsen, who was doing a post doc in our group at the time and with whom we built the tandem quadrupole instrument. I have found Annette to be an ideal combination of a smart scientist and a kind human being. I owe you a lot for everything that I learnt from you, and I would like to thank you and Kristian for the good time we spent together.

Dr. Marcel Drabbels, for the active interest that he took in my work and for numerous insightful discussions, for helping me out with equipment many times, for his great sense of humor, and for the great pleasure that it always meant to talk about science with him. I am very grateful for all your help and advice, and I am very much going to miss our discussions over a cup of coffee.

Philippe Marmillod who developed the electronics for the planar trap/TOF instrument and without whom this project would not have been a success. Working together with him and his team was one of the most delightful parts of my PhD thesis.

Our mechanical workshop, who worked long hours to help us build the tandem quadrupole instrument, and in particular Yves Morier and André Fattet, who showed great ingenuity and patience in constructing the two versions of the planar trap.

Our electronics workshops, especially Supardi Sujito, Grégoire Pasche, and Patrick Favre, who made the major part of the electronics that we needed to set up the lab.

Our secretary, Marianne Dang, the soul and heart of our group, whose kindness and moral support are invaluable.

Prof. Rainer Beck for good advice and for helping me out so many times with his equipment.

Dr. Caroline Seaiby for long conversations and mutual encouragement, her special sense of humor, and our Négoces breaks.

Yiorgos Papadopoulos for being such a good-natured person, which made it so enjoyable to spend time with him, and for many interesting conversations.

Nils Brauer for taking me along to such exciting hikes, bike trips, or ski tours and for being such a good-humored and helpful person.

Dr. Tobias Wassermann for many encouraging conversations.

Dr. O. V. Boyarkin for building the 22-pole.

Dr. K. Asmis, Dr. M. V. Gorshkov, and Kevin Kuchta for advice on building the tandem quadrupole instrument.

Prof. O. Dopfer, Prof. Y. Tsybin, Dr. C. Wandrey, and Prof. R. Wester for accepting to be members of my committee and for some interesting discussions.

The Fonds der Chemischen Industrie for a generous fellowship that supported me for two years.

My family for their support throughout the years of my PhD, that is my sister Judith, her husband Christian, and my nieces Johanna and Mathilda; most of all my parents, who deserve all my gratitude and admiration.

Curriculum Vitae

- School Education: July 2001
Abitur, Freiherr-vom-Stein-Schule Fulda
- Military Service: July 2001 – March 2002
Violinist at the German Army Music Corps in Siegburg
- Studies: April 2002 – February 2007
Chemistry at the University of Würzburg
Diploma thesis with Prof. O. Dopfer
“Infrared Spectroscopy of Protonated Aromatic Molecules”
- PhD thesis: June 2007 – September 2011
In the group of Prof. T. R. Rizzo
At the École Polytechnique Fédérale de Lausanne
“Spectroscopy of Cold, Biomolecular Ions: Instrumentation and Application”
- Publications: U. Lorenz, N. Solcà, O. Dopfer, *Chem. Phys. Lett.* **2005**, *406*, 321–326.
Y. Yu, A. D. Bond, P. W. Leonard, U. J. Lorenz, T. V. Timofeeva, K. P. C. Vollhardt, D. W. Glenn, A. A. Yakovenko, *Chem. Commun.* **2006**, 2572–2574.
U. J. Lorenz, N. Solcà, J. Lemaire, P. Maître, O. Dopfer, *Angew. Chem.* **2007**, *46*, 6714–6716.
U. J. Lorenz, J. Lemaire, P. Maître, M.-E. Crestoni, S. Fornarini, O. Dopfer, *Int. J. of Mass Spect.* **2007**, *267*, 43–53.
M. Guidi, U. J. Lorenz, G. Papadopoulos, O. V. Boyarkin, T. R. Rizzo, *J. Phys. Chem. A* **2009**, *113*, 797–799.
A. Lagutschenkov, A. Springer, U. J. Lorenz, P. Maître, O. Dopfer, *J. Phys. Chem. A* **2010**, *114*, 2073–2079.
A. Svendsen, U. J. Lorenz, O. V. Boyarkin, T. R. Rizzo, *Rev. Sci. Inst.* **2010**, *81*, 073107.
A. Lagutschenkov, U. J. Lorenz, O. Dopfer, *Int. J. Mass Spectrom.* **2011**, *accepted*.
U. J. Lorenz, T. R. Rizzo, *Analyt. Chem.* **2011**, *accepted*.

